Characterization of a Pneumatic Strain Energy Accumulator: Efficiency and First Principles Models with Uncertainty Analysis

By
Joshua Joseph Cummins

Dissertation Proposal
Submitted to the Faculty of the
Graduate School of Vanderbilt University
in partial fulfillment of the requirements
for the degree of
DOCTOR OF PHILOSOPHY
in
Mechanical Engineering
May, 2016
Nashville, Tennessee

Approved:
Douglas E. Adams, Ph.D.

Eric J. Barth, Ph.D.

Sankaran Mahadevan, Ph.D.

Thomas Withrow, Ph.D.

Florence Sanchez, Ph.D.

This work is dedicated to my beautiful bride Kimberly, parents Ed and Joanne, siblings Shaun and Ryan and has been completed for the glory of God through whom all things are possible!

ACKNOWLEDGEMENTS

I would like to start by thanking the men and women in uniform who protect and serve our country. It is through your courage and sacrifice that we have the liberty to study and advance science. I would like to thank the National Science Foundation and the Center for Compact and Efficient Fluid Power for their financial support of the work herein. I would like to thank my committee members for their support and guidance along the way to completion of this work. I would especially like to thank the chair of my committee, Doug Adams for his support, guidance and encouragement at both Purdue University and Vanderbilt University. I would like to thank my friends who provide immeasurable emotional support and encouragement on a daily basis. Specifically I would like to thank the faith communities I have been blessed to be a part of during my journey thus far. To all of my brothers and sisters in Christ, you have encouraged, inspired, and strengthened me and those around you by bringing your light and joy to the world. In a special way I would like to thank those that have dedicated their lives to serving the Lord as spiritual Fathers and religious Sisters, especially Fr. Patrick Baikauskas, Fr. Brian Doerr, Fr. Dave Wells, Fr. John O'Neill, and Fr. John Sims Baker. I would like to thank my family: my loving and faithful parents, Ed and Joanne; my awesome and inspiring siblings Shaun and Ryan; and especially my beautiful bride Kimberly not only for her support but for her loving sacrifice to make this possible. Each of you have sacrificed and loved in ways big and small, and I cannot express how truly grateful and appreciative I am of your unending selflessness. Finally and most importantly, I would like to thank our Blessed Mother for her constant intercession and love that only a mother can provide and to God, Father, Son and Holy Spirit, for His grace and strength that makes all things possible!

TABLE OF CONTENTS

Page

LIST OF TABLES

LIST OF FIGURES

CHAPTER 1

INTRODUCTION

1 Background

Fluid Power is the use of pressurized fluids to generate, control and transmit power consisting of two mediums, hydraulics and pneumatics. One of the primary advantages of using fluid power over other forms is that it offers power density that competing power sources cannot. Despite this compelling advantage, a major shortcoming of the fluid power industry is that it is largely inefficient. As a result, the Center for Compact and Efficient Fluid Power, a National Science Foundation Engineering Research Center was formed, with efficiency being one of its primary focuses. A number of efficiency concepts have been developed within the center with one, the strain energy accumulator, building off of an existing fluid power efficiency improvement device, the accumulator.

1.1 Existing Accumulator Technology

Accumulator technology has been introduced in a number of applications in the hydraulic sector to bolster energy efficiency. Traditional accumulators consist of a rigid exterior cavity that is partitioned into two regions, with gas on one side and a hydraulic fluid on the other side. The accumulator stores energy by pumping hydraulic fluid into one side of the cavity and compressing the gas on the other side of the cavity resulting in a nonlinear pressure profile. Doing so accomplishes two objectives; first it attenuates pressure spikes in the system that can cause damage to other costly fluid power components. Second, it temporarily stores energy for the system that can be used at a later point in time. While traditional accumulators isolate pressure spikes and increase efficiency there is much room for improvement as the existing technology is often big and bulky, relatively inefficient in energy storage due to heat loses and carries an additional maintenance burden due to the diffusion of gas across the bladder into the hydraulic side of the system. A device developed to address these drawbacks of traditional accumulators is the strain energy accumulator (SEA).

1.2 Strain Energy Accumulator Technology

The SEA is an energy storage device consisting of an expandable rubber bladder inside of a rigid shroud. Fundamentally, the SEA utilizes the hyperelastic behavior of rubber to store energy in the form of strain energy of the stretched rubber material and pressure energy of the stored gas within the material. The SEA comes in both a hydraulic and pneumatic version. In the hydraulic version, the application of the SEA remains largely the same as traditional accumulators while offering a more compact and efficient alternative. The pneumatic strain energy accumulator (pSEA) on the other hand, for the first time, enables the use of accumulators in pneumatic systems. The closest competing technologies in the pneumatics sector are rigid compressed air storage tanks for energy storage and pressure regulators for improved efficiency. In application, a primary method of use of the pSEA is in exhaust gas recycling.

A specific area of application is use in line with pneumatically actuated cylinders in manufacturing processes. Current standard operating procedures for pneumatic cylinders require each cylinder to be supplied with supply air. In applications where current efficiency improvement methods are employed, pressure regulators are used to regulate cylinders down to their minimum operating pressure to avoid using excessively pressurized air, equating to unnecessary energy expenditures. Even with pressure regulators in use the largest source of wasted energy comes from the exhaust stage of the operating cycle where compressed air in the cylinder is exhausted to atmosphere along with all of its usable energy. The pSEA is introduced to the system to capture those gases and their remaining useful energy, and store them for use at a later time; thus recovering and recycling the exhaust gas. The pSEA fills the accumulator technology gap in the pneumatics industry, offering the advantages of offering a constant pressure supply, being compact, lightweight, inexpensive and highly efficient.

2 Motivation

A report released in 2012 by Oak Ridge National Laboratories (ORNL) and the National Fluid Power Association (NFPA) identified the fluid power industry as being only 22 % efficient on average [1]. The pneumatic division of the fluid power industry comes in even lower at a mere 15 % average efficiency. In an era where energy consumption and efficiency are of great concern, the fluid power industry and specifically the pneumatics sector with its abysmal efficiency, is an obvious candidate offering significant room for improvement. If the efficiency of the fluid power industry can be increased, fluid power has a great potential to address an increasing energy demand and desire for energy efficiency.

2.1 Previous Work

The SEA having been identified as an improvement over existing hydraulic accumulators as well as a highly efficient device offers an opportunity to improve the fluid power industry's efficiency. Two Master's theses have been completed in advancing the body of knowledge available on the SEA. The first of these two works is by Pedchenko [2] focusing on the design and finite element modeling of the SEA. In the work Pedchenko developed the basic theory behind the operational behavior of the SEA, developed a prototype, modeled the prototype using finite element analysis to capture the fundamental behavior of the SEA and experimentally validated SEA behavior. Subsequently Tucker [3] advanced the work completed by Pedchenko and investigated a number of materials and geometries to use for the SEA. In doing so several new configurations of the SEA were developed primarily for hydraulic applications with emphasis placed on the distributed piston configuration.

The work completed by Pedchenko and Tucker identified a number of gaps that needed to be addressed including advanced materials and manufacturing design challenges to overcome high pressure challenges presented by hydraulic systems and limiting the use of elastomers in the SEA. Bing et al. [4] studied the efficiency impact a hydraulic accumulator had on a hydraulic elevator system. In the paper by Bing et al., the efficiency improvement realized by introducing the accumulator into the system was confirmed along with the ability of the accumulator to attenuate perturbations of the system allowing the elevator to follow the desired input. The work did not extend out generically to other hydraulic systems, did not develop widely applicable models and neglected any pneumatic system implications. Finally Harris et al. [5] studied energy efficiency in pneumatic production systems by evaluating current state of the art technologies and methods and identifying needs for the future. The findings included the importance of using

current efficiency methods such as eliminating leaks and using pressure regulators. In the report is was estimated that the ability to recover and recycle air could result in 12-52 % energy savings but that "recovery of exhaust air is not feasible" and that future research needs include "a lack of compressed air cost accounting and lack of awareness of potential savings," "development of integrated performance metrics" and "model-based optimization techniques with specific focus on the application side." The ensuing body of work addresses all of these gaps and needs.

3 Objectives and Contributions

Motivated by the gaps in the current state-of-the-art, the current work's objectives and resulting contributions start by identifying new materials being developed for other applications and extending them to the current application with materials modeling work [6]. Modeling efforts are continued through development of models for efficiency studies for the pneumatic strain energy accumulator [7]. Component efficiency [8] and System efficiency increases [9] are studies and reported while incorporating uncertainty analysis. Finally, the materials concepts are extended by completing conductive elastomer proof of concept work investigating the ability to monitor load and detect damage in hyperelastic materials [10].

3.1 Advanced Accumulator Materials Modeling

Due to the hyperelastic nature of the material, the identification of an appropriate elastomer and the characterization of the strength properties and energy density of this elastomer are challenging tasks. Another technical barrier is the manufacturability of these elastomers including the high cost of fabrication and the limited elastomer formulations with high strength and large energy density. A quantitative analysis of these technical barriers is needed. A comprehensive modeling effort for the strain energy accumulator in 2-D and 3-D using the hyperelastic Mooney-Rivlin model was performed to validate the behavior of the strain energy accumulator. Additionally, various multiscale modeling methods, including the Mori-Tanaka, Hashin-Shtrikman, Lielens, Voigt and Reuss Methods were investigated to estimate the homogenized elastic modulus of carbon nanotube rubber resulting in homogenized modulus estimates ranging anywhere from a few times to almost 80 times the elastic modulus of rubber.

3.2 Pneumatic Strain Energy Accumulator Model

The pneumatic Strain Energy Accumulator (pSEA), a device that stores the energy of compressed air in the strain energy of a rubber bladder, has recently undergone proof of concept testing showing promise in compact energy storage applications. An adequate model of the pneumatic strain energy accumulator on a systems level is needed to explore the design space in order to optimize the device. The recent success of the pneumatic strain energy accumulator on an Ankle Foot Orthosis (AFO) medical assist device serves as motivation for such a systems level model. In laboratory experiments the AFO medical assist device has reported from 25-75 % energy efficiency improvement when using the pSEA depending on the various parameters of the medical device. Early measurements and calculations for a single stage independent process pSEA indicated a theoretical maximum energy efficiency increase of 33 % which lies between the energy efficiency values realized on the AFO device using a single stage coupled process pSEA. A study of a lumped parameter model using measured Pressure-Volume curve data as a model input will be used to quantify energy efficiency increases for a variety of system configurations. Once complete, a set of measurement techniques and tools to successfully realize the strain energy accumulator will be ready to use in quantifying its energy savings.

3.3 Component Efficiency with Uncertainty Analysis

There is heightened interest in research to develop materials and devices that achieve greater energy storage capacity, power density and increased energy efficiency. This work analyzes the performance of a novel energy storage device, the pneumatic strain energy accumulator, which is designed to exploit the advantageous aspects of the non-linear behavior of elastomeric materials. An analytical methodology for simultaneously characterizing the pneumatic and material energy storage in a strain energy accumulator, and more general for pneumatic and strain energy systems, has been developed. Component efficiency along with the expansion and contraction pressures of the pneumatic strain energy accumulator are determined experimentally, using a combined Matlab and National Instruments data acquisition system, so that a system level efficiency calculation can be performed. Incorporating uncertainty analysis, the efficiencies of the strain energy accumulator are measured to be consistently over 93 % in over 2500 cycles of testing. The expansion and contraction pressures of the accumulator, despite the hysteretic behavior of rubber, have a fairly stable value with a standard deviation of only 0.1 % of the mean values.

3.4 System Efficiency State Models with Energy Savings Projections

A number of national organizations have recently expressed interest in research to develop materials and devices that achieve greater energy storage capacity, power density and increased energy efficiency on the heels of a report finding that the pneumatic sector of the fluid power industry averages only 15 % efficiency. One way of improving efficiency is the use of energy storage and recycling devices. The pneumatic Strain Energy Accumulator is a recently developed device that recycles exhaust gas from one pneumatic component, stores it in a highly efficient process, and reuses the stored exhaust gas at a constant pressure to power another pneumatic component. This work analyzes system efficiency increases directly attributable to the implementation of a pneumatic strain energy accumulator applying an analytical methodology for system level efficiency improvement calculations, experimental validation, and energy savings projections. Experimentally determined efficiency increases start at 36 % and be as high as over 60 %, rendering the pneumatic strain energy accumulator a viable part of the solution to the fluid power efficiency challenge.

3.5 Carbon Nanotube Reinforced Elastomers Concept

Early work on embedding CNTs in elastomers focused on strength and electrical effects including modulus, conductivity and electro-magnetic interference (EMI) shielding properties. In some of the most recent work, CNTs have been dispersed into viscous materials or spun into threads and used to measure strain in composite materials in an effort to functionalize CNTs embedded in elastomeric and carbon fiber reinforced composites respectively. Recently, carbon nanotube sensor thread was tested as a distributed sensor for the first time on IM7/977-3 composites where the sensor thread was able to monitor strain and detect damage in composite panels while not affecting the integrity of the composite material. Extending this work to conductive elastomers, CNTs in forest or ribbon form would be ideal to use in hyperelastic materials due to their ability to undergo large deformations and maintain contact with each other upon return to the original geometry. CNTs, when used as electrical sensors, can enable material state awareness through structural health monitoring (SHM) while improving strength properties. The ability to sense strain using CNTs in the form of CNT thread is extended through a proof of

concept study demonstrating the ability of conductive elastomers to monitor load and detect damage in specific directions.

References

[1] Love LJ, Lanke E and Alles P, 2012. Estimating the Impact (Energy, Emissions and Economics) of the U.S. Fluid Power Industry. *Oak Ridge National Laboratory*, Oak Ridge, TN.

[2] Pedchenko AV, 2014. Design and Finite Element Modeling of a High Energy Density Strain Energy Accumulator. *Master's thesis,* Vanderbilt University.

[3] Tucker JM, 2012. Design and Experimental Evaluation of a High Energy Density Elastomeric Strain Energy Accumulator. *Master's thesis,* Vanderbilt University.

[4] Bing X, Jian Y and Huayong Y, 2005. Comparison of energy-saving on the speed control of the VVVF hydraulic elevator with and without the pressure accumulator. *Mechatronics* 15 pp. 1159-74.

[5] Harris P, O'Donnell GE and Whelan T, 2012. Energy Efficiency in Pneumatic Production Systems: State of the Art and Future Directions. *Proceedings of the 19th CIRP International Conference on Life Cycle Engineering.* May 23rd-25th Berkeley, CA, USA.

[6] Cummins JJ, Pedchenko A, Barth E and Adams DE, 2014, Advanced Strain Energy Accumulator: Materials, Modeling and Manufacturing. *Proceedings of the 2014 Bath/ASME Symposium on Fluid Power and Motion Control.* Sept 11. Bath, England UK.

[7] Cummins JJ, Barth, EJ and Adams DE, 2015. Modeling of a Pneumatic Strain Energy Accumulator for Variable System Configurations with Quantified Projections of Energy Efficiency Increases. *Proceedings of the 2015 Bath/ASME Symposium on Fluid Power and Motion Control.* Oct 14th Chicago, IL, USA.

[8] Cummins, JJ, Thomas S, Nash CJ, et al., 2016. Experimental Evaluation of the Efficiency of a Pneumatic Strain Energy Accumulator. *International Journal of Fluid Power.* Submitted for review Feb 2016.

[9] Cummins, JJ, Nash CJ, Thomas S, Justice A, et al., 2016. Energy Conservation in Industrial Pneumatics: A State Model for Predicting Energetic Savings using a Novel Pneumatic Strain Energy Accumulator. *Applied Energy.* Submitted for review Mar 2016.

[10] Cummins, JJ, Maurice C, Song Y, et al., 2014, Elastomeric Evolution: A New Look at Carbon Nanotube Reinforced Elastomers. *Proceedings of the 2014 European Rotorcraft Forum.* Sept 4. Southampton, England UK.

CHAPTER 2

ADVANCED STRAIN ENERGY ACCUMULATOR: MATERIALS, MODELING AND MANUFACTURING

Joshua J Cummins, Alexander V Pedchenko,
Eric J Barth and Douglas E Adams

Department of Mechanical Engineering
Vanderbilt University
Nashville, TN

Published in the Proceedings of the 2014 Bath/ASME Symposium on
Fluid Power and Motion Control September 11th, 2014

Abstract

Energy efficiency is a prominent target in cost reduction efforts in a variety of machinery including manufacturing equipment and hybrid vehicles. In the course of developing a proof of concept strain energy accumulator on an Ankle Foot Orthosis (AFO) device, several technical barriers have been quantified in this device. Due to the hyperelastic nature of the material, the identification of an appropriate elastomer and the characterization of the strength properties and energy density of this elastomer are challenging tasks. Another technical barrier is the manufacturability of these elastomers including the high cost of fabrication and the limited elastomer formulations with high strength and large energy density. A quantitative analysis of these technical barriers is needed. A comprehensive modeling effort for the strain energy accumulator in 2-D and 3-D using the hyperelastic Mooney-Rivlin model was performed to validate the behavior of the strain energy accumulator. Additionally, various multiscale modeling methods, including the Mori-Tanaka, Hashin-Shtrikman, Lielens, Voigt and Reuss Methods were investigated to estimate the homogenized elastic modulus of carbon nanotube rubber resulting in homogenized modulus estimates ranging anywhere from a few times to almost 80 times the elastic modulus of rubber.

1 Introduction

Energy efficiency is an active area of research, which continues to grow as energy costs and demand increase amidst rising concerns over the depletion of natural resources. Fluid power has a great potential to address this increase in energy demand and desire for energy efficiency [1]. The main benefit of fluid power is that it has more energy density than competing power sources.

1.1 Current Accumulator Technology

In particular, fluid power energy accumulator technology has been introduced in a number of applications to bolster energy efficiency. Traditional accumulators consist of a rigid exterior cavity that is partitioned into two regions, with gas on one side and a hydraulic fluid on the other side. The accumulator stores energy by pumping hydraulic fluid into one side of the cavity and compressing the gas on the other side of the cavity.

Drawbacks of the current technology include excessive size and weight, thermal losses from the compressed gas to the environment when the energy stored is not reused soon after it is stored, and diffusion of the gas across the partition into the hydraulic fluid leading to increased maintenance requirements of the device [2]. These challenges motivated the development of a new strain energy accumulator design concept [3].

1.2 Strain Energy Accumulator Technology

The strain energy accumulator, which is illustrated in Figure 2.1, consists of a rubber bladder encased by a rigid shroud. The strain energy accumulator functions by capitalizing on the hyperelastic behavior of the rubber bladder as it stores energy in the form of strain energy in the rubber bladder. Both pneumatic and hydraulic variants of the strain energy accumulator are possible – the pneumatic proof of concept device is pictured in Figure 2.2.

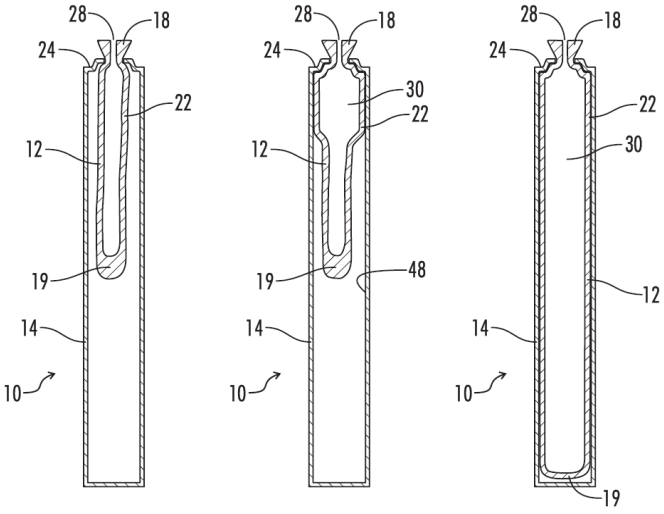

Figure 2.1: Strain energy accumulator US Patent Application US20120085449 A1

Figure 2.2: Pneumatic strain energy accumulator proof of concept

The strain energy storage of the accumulator can be understood by correlating Figure 2.3(a) and (b). In Figure 2.3(b), the stress strain curve of rubber is divided into four regions that correspond to the behavior seen in Figure 2.3(a). The rubber deforms according to the initial

modulus of the deflated rubber bladder in Region 1 in Figure 2.3(b) corresponding to the linear region of the pressure-volume diagram in Figure 2.3(a). In Region 2 shown in Figure 2.3(b), the rubber modulus begins to decrease corresponding to the rounded peak in Figure 2.3(a). At this point the bladder material undergoes hyperelastic deformation and begins to balloon resulting in a sudden increase in volume and the pressure drop seen in Figure 2.3(a).

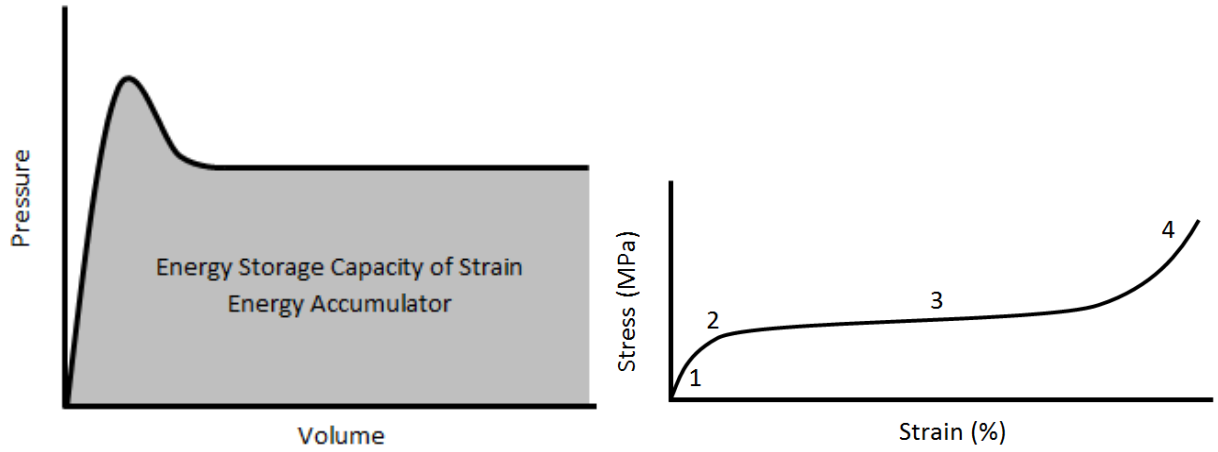

Figure 2.3: (a) typical pressure-volume diagram of strain energy accumulator (b) typical stress-strain curve of rubber

The pressure then continues to drop until the ballooning region of the rubber bladder experiences a local increase in elastic modulus in Region 4 of Figure 2.3(b) resulting in the same modulus as in Region 1 of Figure 2.3(b). The localized increase in elastic modulus is believed to be caused by a localized strain hardening of the rubber material, at which point the ballooning region of the rubber bladder starts to travel the length of the bladder at the minimum modulus of Region 3 from Figure 2.3(b). As the ballooning region travels the length of the bladder, the pressure remains constant while the volume increases which corresponds to the flat region in Figure 2.3(a).

1.3 Applications for Strain Energy Accumulator

Two specific applications that motivated the development of the strain energy accumulator are the Ankle Foot Orthosis (AFO) device for assisting patients in stroke recovery and the hydraulic hybrid vehicle shown in Figures 3.4(a) and (b), respectively.

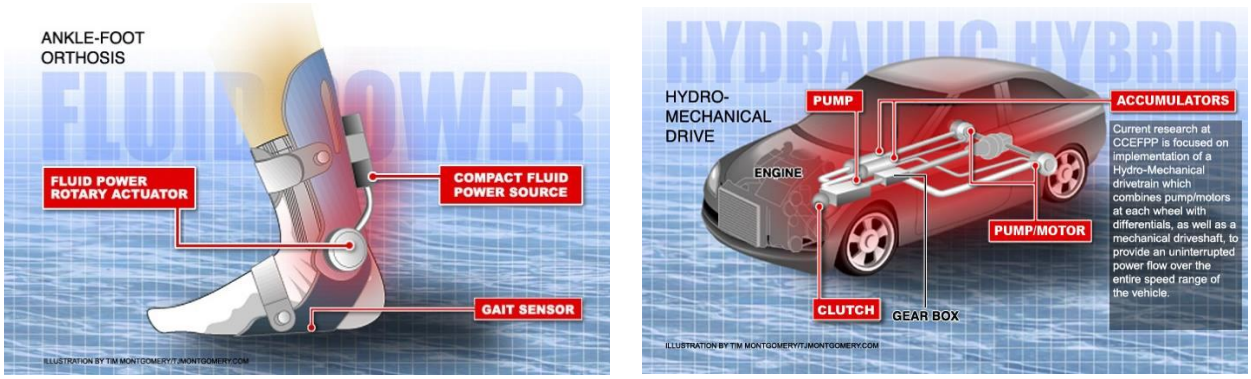

Figure 2.4: (a) Ankle Foot Orthosis [4] (AFO) and (b) hydraulic hybrid [5] concepts

Early success has been realized on the AFO using a pneumatic strain energy accumulator that takes advantage of the nearly constant pressure-volume relationship of the accumulator to recycle exhaust gases. An efficiency increase in the AFO device of over 25 % as compared to the device without the pneumatic strain energy accumulator has been demonstrated experimentally [6]. The initial success of the pneumatic strain energy accumulator has led to insights regarding the challenges in both the pneumatic and hydraulic variants of the strain energy accumulator in the areas of materials, modeling and manufacturing. A discussion of the materials challenges is presented next with proposed solutions, followed by an overview of the modeling efforts that are underway to quantify these challenges, and ending with a discussion of the manufacturing obstacles that need to be addressed to make the advanced strain energy accumulator commercially viable.

2 Materials

Several challenging material issues have been identified. Typically, rubber is used in isolation applications, e.g., bushings, in which maximum hysteresis is desirable to damp out unwanted vibrations. Additionally, the elastic modulus of rubbers that exhibit hyperelastic behavior is relatively low compared to other materials such as alloys and composites; therefore, the use of rubber in high pressure and large stress operating conditions, as are typically experienced in hydraulic systems, results in premature material failure.

2.1 Carbon Nanotube Embedded Rubber

One idea that has been proposed to improve the material properties of rubber is to add Carbon Nanotubes (CNTs) to the rubber material. The embedding of CNTs in rubber has been investigated previously primarily for its improvement in rubber's strength and electrical properties [7],[8]. The improved strength properties with increasing weight percent CNTs are illustrated conceptually in Figure 2.5.

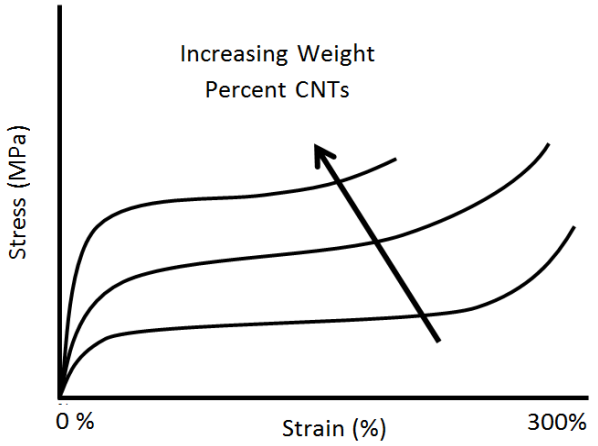

Figure 2.5: Effect of increasing weight percent of CNTs on rubber modulus

With an increase in the elastic modulus of rubber containing CNTs, this advanced concept of the strain energy accumulator has the potential to be used in higher pressure hydraulic applications. In addition to improved strength properties, a number of other material property advantages exist for CNT embedded rubber including increased conductivity and Electro Magnetic Interference (EMI) shielding capability [7] and the potential to produce functionally

graded CNT embedded rubbers. Prior to fully exploring these additional capabilities, the concept for a CNT embedded rubber must be thoroughly developed.

2.2 Advanced CNT Embedded Rubber Strain Energy Accumulator Concept

Carbon nanotubes embedded in a rubber strain energy accumulator enable advanced material properties to be achieved. A number of possibilities exist of how to incorporate CNTs into rubber including CNT powder, vertically aligned CNT sheets, and even spun CNT threads. The concept of a sheet of vertically aligned CNTs embedded in rubber is shown in Figure 2.6. Figure 2.6(a) shows the advanced strain energy accumulator in its elastic taut position with vertically aligned CNTs; Figure 2.6(b) shows the hyperelastic configuration of the advanced strain energy accumulator.

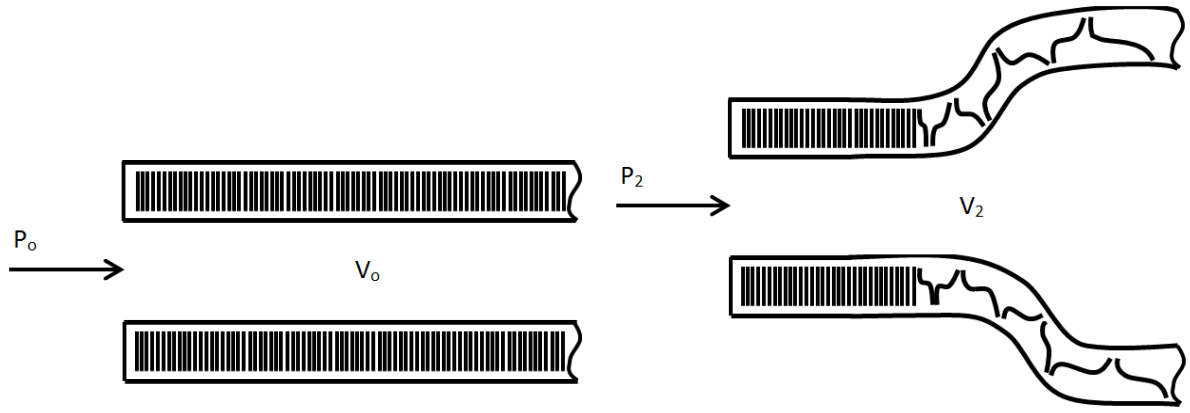

Figure 2.6: Vertically aligned CNT embedded rubber strain energy accumulator concept (a) initial (b) final/stretched configuration

Yamada et al. [9] have also demonstrated the capability of vertically aligned CNTs to be used in flexible fabrics as a strain sensing device. Kang et al. [7] have also demonstrated the strain sensing capability of CNTs in a spun thread configuration. Before a final configuration is selected, the expected properties and feasibility of each configuration must be investigated through appropriate modeling and manufacturing techniques.

3 Modeling

There are several modeling techniques available to approach the CNT embedded rubber material including multiscale modeling and analytical software packages such as Abaqus available in both 2-dimensional (2-D) and 3-dimensional (3-D) versions. All of these techniques will be considered and employed herein. Table 2-1 shows the material properties used for CNTs in the multiscale modeling homogenization techniques.

Table 2-1: CNT material properties used in homogenization methods

Direction	Young's Modulus (GPA)	Poisson's Ratio	Shear Modulus (GPA)
Longitudinal	825.0	0.28	8.0
Transverse	4.5	0.38	

The values chosen for the longitudinal and transverse Young's modulus and Poisson's ratio for CNTs reported by Montazeri et al. [11] were used and the shear modulus reported by Zeng et al. [12] was used. Since the values for rubber vary based on the type of rubber selected and also vary from one manufacturer to another, for the Abaqus modeling, a soft rubber was chosen with a Young's modulus of 28.5 MPa; for the multiscale homogenization techniques a Young's modulus representing a stiff rubber was selected to be 0.1 GPa with a corresponding Poisson's ratio of 0.4. The importance of the selection of two opposing moduli will be discussed in later sections. The aforementioned values are supplied as inputs to their respective models.

3.1 2-D Modeling of Dynamic Performance of Strain Energy Accumulator

The first step in the modeling process was to complete a 2-D analytical dynamic model in Abaqus of the strain energy accumulator to accurately capture the behavior of the device. Figure 2.7 shows the deformation predicted by Abaqus and relative stress magnitude for a rubber only, strain energy accumulator. As expected the rubber bladder ballooned and then started to travel down the length of the device with a higher stress on the inside wall and a lower stress on the outside wall of the accumulator.

Figure 2.7: 2D Abaqus dynamic model of strain energy accumulator

The 2-D Abaqus model, with a profile view shown in Figure 2.8(a), was used to generate the P-V curve shown in Figure 2.8(b) and validate the general shape of the P-V curve shown in Figure 2.3(a).

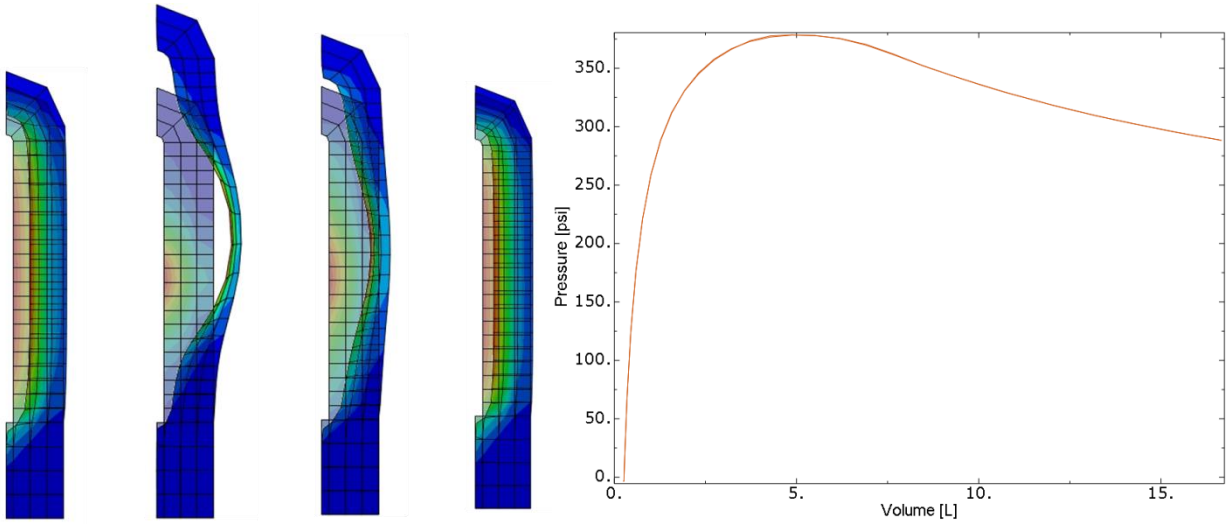

Figure 2.8: (a) Profile view of 2-D Abaqus model displaying Von Mises stress distribution for free (no shroud) expansion and contraction w/o hysteresis (b) P-V curve generated from simulation

With the behavior of the strain energy accumulator characterized in 2-D the next step was to generate a 3-D model of the strain energy accumulator.

3.2 3-D Modeling of Quasi-Static Response of Advanced Strain Energy Accumulator

The next stage of the modeling effort was to develop a 3-D rubber model for the strain energy accumulator. In the model shown in Figure 2.9, the Mooney-Rivlin hyperelastic model was selected. Required inputs to the Mooney-Rivlin hyperelasticity model are the constants C_{10}, C_{01}, and D. Constants C_{10}, C_{01}, and D are typically determined from the bulk modulus of rubber and experimental data. In the absence of experimental data, the elastic modulus of rubber selected was the softest value of initial stiffness reported by Xue and Hutchinson [13] as listed in Table 2-2 with the corresponding values for constants C_{10}, C_{01}, and D. The softest modulus was selected since softer rubbers are ideal for hyperelastic behavior in the strain energy accumulator.

Table 2-2: Mooney-Rivlin Constants

Initial Stiffness E (MPa)	C_{10} (MPa)	C_{01} (MPa)	D (1/MPa)
28.5	4.5980	-0.18392	4.2105e-3

Values for the constants were entered into the Mooney-Rivlin 3-D hyperelastic model. The dimensions used in the 3-D simulation were similar to those of the 2-D simulation from Figures 3.8(a) and (b) rounded to the nearest metric dimension for the free expansion (no shroud) configuration without hysteresis. Figure 2.9 shows the initial and final states of the strain energy accumulator.

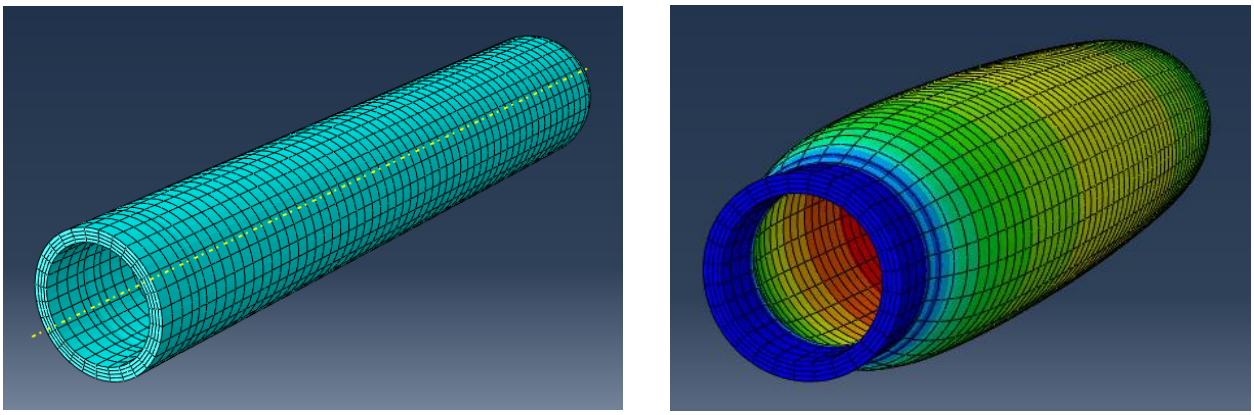

Figure 2.9: 3D Quasi-static simulation of rubber only strain energy accumulator (a) mesh used in simulation (b) Von Mises stress in final inflated stress state for constant pressure loading

The results obtained from the 3-D quasi-static model are consistent with those obtained in the 2-D model, thus serving as a form of verification of the 2-D model. It is observed that the inner surface experiences a much higher strain than the outer surface even at a relatively thin wall thickness of 2.5 mm. The final quasi-static state is in the fully ballooned configuration. The next modeling step is to develop a dynamic 3-D simulation in an effort to again validate the P-V curves in Figure 2.3(a) and Figure 2.8(b). Once the P-V curve has been validated with the 3-D model, the next step is to validate the P-V curve using the homogenized modulus value determined from multiscale modeling homogenization techniques after the value has been validated experimentally.

3.3 Multiscale Modeling Homogenization Techniques to Estimate Elastic Modulus of CNT Embedded Rubber

The models used to extrapolate macroscale properties for a carbon nanotube reinforced elastomer are the Mori-Tanaka, Hashin-Shtrikman, Lielens, Voigt and Reuss Homogenization Methods [14]. The Mori-Tanaka Homogenization method is selected because it is the most referenced homogenization technique in the literature that is used as a benchmark. Hashin-Shtrikman Homogenization was selected since it serves as an upper and lower bound for the elasticity tensor, or homogenized modulus. Once the results are obtained for the carbon nanotube reinforced elastomer a comparison of the model results will be conducted to investigate the range of predicted values. Finally, consideration will be given to the possibility of feeding these results into other models. All of the homogenization methods start with the basic stress-strain relations and their respective tensors as given in Eq. (1):

$$\sigma_{ij} = C_{ijkl}\varepsilon_{kl} \tag{1}$$

3.3.1 Voigt and Reuss Methods

The simplest of all the homogenization methods are the Voigt and Reuss methods. The homogenized modulus is determined by the effective elasticity tensor C^*. In the Voigt homogenization method the effective elasticity tensor is equivalent to springs in parallel and is defined as:

$$C^*_{(Voigt)} = \sum_{\alpha=1}^{n} c_\alpha C_\alpha \tag{2}$$

Here α is the phase (matrix or inclusion), c_α is the volume fraction or the ratio of the volume of the particular phase to the total volume and C_α is the stiffness tensor of the respective phase. In the CNT reinforced rubber there are only two phases, the CNTs and the rubber. The volume fraction is the variable input to the homogenization method and the stiffness tensor for the CNT inclusions and rubber matrix, C_i and C_m are the stiffness tensors for the inclusion and matrix material which are assumed to be transversely isotropic and isotropic respectively. The Reuss homogenization method is equivalent to springs in series with the effective elasticity tensor:

$$C^*_{(\mathrm{Re}\,uss)} = \left(\sum_{\alpha=1}^{n} c_\alpha C_\alpha^{-1} \right)^{-1} \tag{3}$$

As can be seen from Eq. (2) and Eq. (3) the Voigt method serves as an upper limit and the Reuss method serves as a lower limit. The homogenized modulus in the longitudinal direction for these two methods and all subsequent homogenization methods will be the C_{11} element of the effective elasticity tensor.

3.3.2 Mori-Tanaka Method

The Mori-Tanaka homogenization method is one of the most referenced homogenization methods in the literature to which most new methods compare their results. The Mori-Tanaka effective elasticity tensor is defined by Klusemann and Svendsen[15] as:

$$C^*_{(MT)} = C_m + \sum_i c_i (C_I - C_m) A_{I(MT),i} \tag{4}$$

Where C_I is the elasticity tensor of the inclusion, C_m the elasticity tensor of the matrix, c_i the volume fraction of the inclusion and $A_{I(MT),i}$ as defined by Klusemann and Svendsen [15]. In the case of a transversely isotropic elliptical inclusion material the Eshelby tensors are defined Weinberger and Cai.[16] When spherical isotropic inclusions are assumed, then the Eshelby tensors simplify to those provided Odegard et al. [17].

3.3.3 Hashin-Shtrikman Method

The Hashin-Shtrikman method serves as a lower and upper bound similar to the Voigt and Reuss Methods. The Hashin-Shtrikman method is included as a secondary bounding homogenization method primarily because the lower bound is similar to the Mori-Tanaka Method. The Hashin-Shtrikman upper and lower bound are defined by Klusemann and Svendsen [15] and Klusemann et al. [14] as follows:

$$\begin{aligned} C^*_{(HS^{up})} &= C_I + c_m\left[\left(C_m - C_I\right)^{-1} + c_i S_I C_I^{-1}\right]^{-1} \\ C^*_{(HS^{low})} &= C_m + c_i\left[\left(C_I - C_m\right)^{-1} + c_m S_m C_m^{-1}\right]^{-1} \end{aligned} \tag{5}$$

In the upper bound Hashin-Shtrikman method, S_I is the Eshelby tensor that uses the Poisson's ratio of the inclusion in place of that of the matrix for the lower bound.

3.3.4 Lielens Method

The final method considered in the current study is the Lielens Method since it utilizes the Mori-Tanaka method and inverse Mori-Tanaka method to obtain an interpolative elastic modulus estimate that results in a solution between the upper and lower bounds of the Hashin-Shtrikman method. In the inverse Mori-Tanaka method the matrix material becomes the inclusion material and the inclusion material becomes the matrix material and is annotated by $C^*_{(MT^{-1})}$. The Lielens homogenization method is defined by Klusemann and Svendsen [15] and Klusemann et al. [14] as:

$$C^*_{(LIL)} = \left[\left(1 - \frac{c_i + c_i^2}{2}\right)C^{*-1}_{(MT^{-1})} + \frac{c_i + c_i^2}{2} C^{*-1}_{(MT)}\right]^{-1} \tag{6}$$

3.3.5 Results and Discussion of Multiscale Modeling Homogenization Methods

The prediction of the normalized homogenized elastic modulus of the various homogenization techniques are shown in Figure 2.10. The Voigt and Upper Hashin-Shtrikman are not shown in Figure 2.10 as they predict a very large elastic modulus due to the heavy weight/influence given to the material properties of the CNTs but are presented above for completeness.

As can be seen from Figure 2.10, the various homogenization methods result in substantially different estimates for the homogenized elastic modulus of CNT embedded rubber. The Reuss method, being inversely proportional to the properties of the CNTs, results in a very small homogenized modulus estimation. The Mori-Tanaka and Lower Hashin-Shtrikman methods are in good agreement, as was observed in the literature, and start out dominated by the material properties of the rubber and slowly transition to those of the CNTs. Finally, the Lielens method attempts to give more weight to the material properties of CNTs at lower volume fractions and

then transitions to the Mori-Tanaka method at larger volume fractions of CNTs which is consistent with Eq. (6).

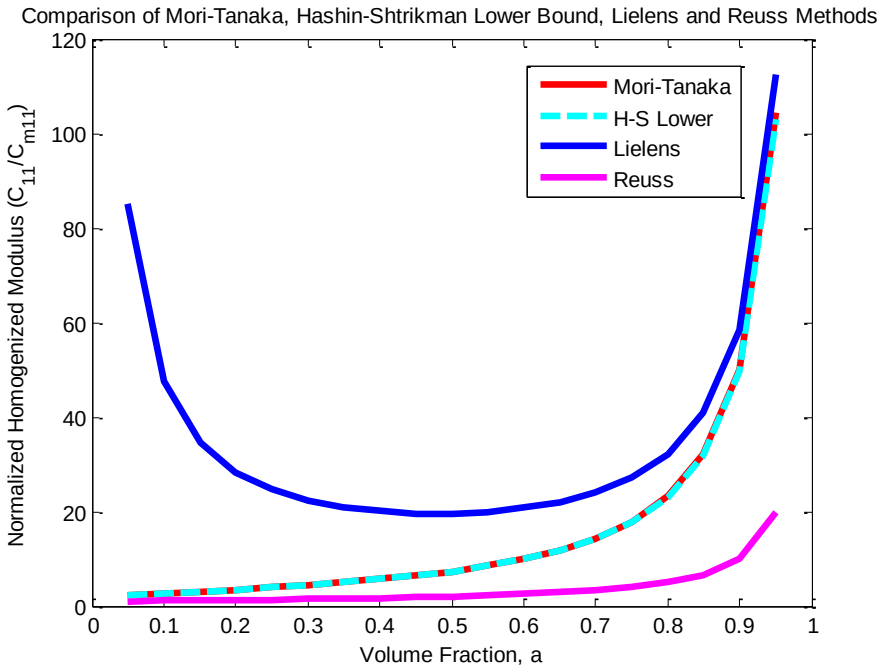

Figure 2.10: Elastic modulus homogenization results for CNT embedded rubber

Due to the large variation of predictions from the different multiscale modeling homogenization methods, these modeling techniques may not be adequate to predict the behavior of the advanced strain energy accumulator. Experimentally determined modulus values are required due to the large variation in predicted values from the multiscale methods. After the homogenized modulus values have been experimentally determined then the 2-D and 3-D models can be updated with this experimental data and the simulations can be rerun. Prior to experimental validation, the manufacturing methods used to create CNT embedded rubber are addressed.

4 Manufacturing

Similar to most research oriented programs, the first of many challenges is the cost to produce a small lot/short run accumulator samples, especially for the hydraulic accumulator which is typically larger in size. In addition to the high cost of small lot production, CNTs remain expensive and CNT manufacturers are currently working to significantly reduce the cost per gram while simultaneously greatly increasing production capability. Specific to the hydraulic accumulator is the higher pressure operating environment which has led to the desire to incorporate CNTs in the rubber material. Finding a rubber supplier with the capability of incorporating CNTs into a rubber compound is a challenge since not all rubber manufacturers have the capability. Even if they do have the capability, the knowhow is also an area that is currently at a relatively low Technology Readiness Level (TRL) for practical applications. Ways that are being considered to embed, orient, and functionally grade CNTs into rubber include vibration, magnetic fields, centrifuge, etc.

5 Conclusions and Future Work

Several key findings were put forth in the current work. The primary driver for the current work is the inability of elastomers to be applied to the high pressure hydraulic strain energy accumulator. The CNT embedded advanced strain energy accumulator was conceptualized to address this need. Hyperelastic models in both 2 and 3-D were constructed to validate the P-V curve of the strain energy accumulator and multiscale modeling homogenization techniques were employed to predict a homogenized elastic modulus of the CNT embedded strain energy accumulator. The large variation in predicted values from the existing homogenization methods indicates that the current methods may not be adequate in estimating the homogenized modulus for CNT embedded rubber. Future experimental validation will determine if new homogenization methods are required for such a material. Finally, the necessity of developing unique manufacturing methods to ensure proper dispersion of CNTs in rubber will also be explored to functionalize CNT embedded rubber in the application of the strain energy accumulator.

There is a significant potential for elastomers with improved strength properties in pneumatic and hydraulic power applications. Key industries such as manufacturing and automotive where pneumatics and hydraulics have the potential with even modest increases in efficiency, to save millions, possibly billions of dollars annually in energy costs [1]. By addressing the materials issues, gaining deeper insight through detailed modeling and improving current manufacturing techniques or developing new ones, many other industries, including the medical and aviation industries, stand to benefit from CNT embedded rubber. In the helicopter industry, as far back as 1975, bearings were identified as the number one cost driver of a helicopters transmission system [18] and remain so today. Hydraulic repair issues are well known by aircraft manufacturers as one of the top warranty drivers in new aircraft. All of these industries use elastomers, which with improved material properties, could help to achieve substantial cost reductions in material and maintenance costs [19].

Acknowledgments

This work was supported by the Center for Compact and Efficient Fluid Power, an NSF Engineering Research Center, grant EEC-0540834.

References

[1] Love, L.J., Lanke, E., Alles, P., 2012, “Estimating the Impact (Energy, Emissions and Economics) of the U.S. Fluid Power Industry.” Oak Ridge National Laboratory, Oak Ridge, TN.

[2] Pourmovahed, A., Baum, S.A., Fronczak, F.J., and Beachley, N.H., 1988, "Experimental evaluation of hydraulic accumulator efficiency with and without elastomeric foam", Journal of Propulsion and Power 4, 2, pp. 185-192.

[3] Pedchenko, A., Barth, E.J., 2009, “Design and Validation of a High Energy Density Elastic Accumulator Using Polyurethane.” Proceedings of the ASME Dynamic Systems and Control Conference, pp. 283-290.

[4] “Fluid Power Ankle-Foot Orthosis Test Bed 6: Human Assist Devices.” Center for Compact and Efficient Fluid Power. Web. 19 Apr. 2014.

[5] “Hydraulic Hybrid Passenger Vehicle Test Bed 3: Highway Vehicles.” Center for Compact and Efficient Fluid Power. Web. 19 Apr. 2014.

[6] Boes, M.K., Islam, M., Li, D., Hsiao-Wecksler, E. T., "Fuel Efficiency of a Portable Powered Ankle-Foot Orthosis". IEEE 13th International Conference on Rehabilitation Robotics (ICORR 2013). June 24-26. Seattle, WA.
[7] Kim, Y.A., Hayashi, T., Endo, M., Gotoh, Y., et al., 2006, "Fabrication of aligned carbon nanotube-filled rubber composite." Scripta Materialia 54, pp. 31-35.
[8] Bokobza, L., 2007, "Multiwall carbon nanotube elastomeric composites: A review." Polymer 48, pp. 4907-4920.
[9] Yamada, T., Hayamizu, Y., Yamamoto, Y., Yomogida, Y., et al., 2011, "A stretchable carbon nanotube strain sensor for human-motion detection." Nature Nanotechnology 6, pp. 296-301.
[10] Kang, I., Schulz, M.J., Kim, J.H., Shanov, V., et al., 2006, "A carbon nanotube strain sensor for structural health monitoring." Smart Materials and Structures 15, pp. 737-748.
[11] Montazeri, A., Sadeghi, M., Naghdabadi, R., Rafii-Tabar, H., 2010, "Computational modeling of the transverse-isotropic elastic properties of single-walled carbon nanotubes." Computational Materials Science 49, pp. 544-551.
[12] Zeng, Q.H., Yu, A.B., Lu, G.Q., 2008, "Multiscale modeling and simulation of polymer nanocomposites." Progress in Polymer Science 33, pp. 191-269.
[13] Xue, Z., Hutchinson, J.W., 2008, "Neck development in metal/elastomer bilayers under dynamic stretchings." International Journal of Solids and Structures 45, pp. 3769-3778.
[14] Klusemann, B., Bohm, H.J., Svendsen, B., 2012, "Homogenization methods for multi-phase elastic composites with non-elliptical reinforcements: Comparisons and benchmarks." European Journal of Mechanics A/Solids 34, pp. 21-37.
[15] Klusemann, B., Svendsen, B., 2010, "Homogenization methods for multi-phase elastic composites: Comparisons and benchmarks." Technische Mechanik 30, 4, pp. 374-386.
[16] Weinberger, C., Cai, W., 2004, Lecture Note 2. Eshelby's Inclusion I. Stanford University.
[17] Odegard, G.M., Clancy, T.C., Gates, T.S., 2005, "Modeling of the Mechanical Properties of Nanoparticle/Polymer Composites." Polymer 46, 2, pp. 553-562.
[18] Reddick, H.K. Jr., 1975, "Army Helicopter Cost Drivers." Army Air Mobility Research and Development Laboratory, Fort Eustis, VA.
[19] Bond, R., Underwood, S., Adams, D.E., Cummins, J.J., 2013, "Structural Health Monitoring-Based Methodologies for Managing Uncertainty in Aircraft Structural Life Assessment." Proceedings of the 9th International Workshop on Structural Health Monitoring.

CHAPTER 3

MODELING OF A PNEUMATIC STRAIN ENERGY ACCUMULATOR FOR VARIABLE SYSTEM CONFIGURATIONS WITH QUANTIFIED PROJECTIONS OF ENERGY EFFICIENCY INCREASES

Joshua J Cummins, Eric J Barth and Douglas E Adams

Department of Mechanical Engineering
Vanderbilt University
Nashville, TN

Published in the Proceedings of the 2015 Bath/ASME Symposium on
Fluid Power and Motion Control October 14th, 2015

Abstract

The pneumatic Strain Energy Accumulator (pSEA), a device that stores the energy of compressed air in the strain energy of a rubber bladder, has recently undergone proof of concept testing showing promise in compact energy storage applications. An adequate model of the pneumatic strain energy accumulator on a systems level is needed to explore the design space in order to optimize the device. The recent success of the pneumatic strain energy accumulator on an Ankle Foot Orthosis (AFO) medical assist device serves as motivation for such a systems level model. In laboratory experiments the AFO medical assist device has reported from 25-75 % energy efficiency improvement when using the pSEA depending on the various parameters of the medical device. Early measurements and calculations for a single stage independent process pSEA indicated a theoretical maximum energy efficiency increase of 33 % which lies between the energy efficiency values realized on the AFO device using a single stage coupled process pSEA. A study of a lumped parameter model using measured Pressure-Volume curve data as a model input will be used to quantify energy efficiency increases for a variety of system configurations. Once complete, a set of measurement techniques and tools to successfully realize the strain energy accumulator will be ready to use in quantifying its energy savings.

1 Introduction

Increasing energy efficiency is one of many approaches being taken to address the world's increasing energy demand. Many of the low hanging fruits in the area of energy efficiency have been realized, giving way to the next generation of devices to further increase energy efficiency and address the growing demand for energy. One such device that has been developed in recent

years to address the next wave of energy efficiency increases is the strain energy accumulator (SEA).

1.1 Previous Strain Energy Accumulator Work

There are both pneumatic (pSEA) and hydraulic (Hy-SEA) versions of the strain energy accumulator, offering high energy densities to help meet the desire for increased energy efficiency in both pneumatics and hydraulics [1],[2]. Preliminary work on the strain energy accumulator focused on proving the concept [3], developing finite element models (FEM) [4] and addressing material and manufacturing challenges [5]. The advancements in each of these previous works in the areas of proving out the concept, FEA, and materials and manufacturing challenges has indicated the need for system-level modeling for quantifying system performance in terms of the strain energy accumulator design parameters.

1.2 Current Strain Energy Accumulator Focuses

Advances in the materials used for the SEA to include carbon nanotubes (CNTs) [7]-[9], with possible self-sensing capabilities [9], continue to be pursued. Standard black latex rubber is sufficient to use on the pSEA as more advanced materials are developed to address durability and diagnostic improvements. Development efforts underway include fabricating a quick disconnect commercially viable accumulator shown in Figure 3.1, fully defining and characterizing an accumulator model, and developing a lumped parameter system model to estimate efficiency improvements for various systems utilizing the pSEA.

Figure 3.1: Quick disconnect commercially viable pSEA

1.3 Application of the Strain Energy Accumulator

The primary motivation for further developing the pSEA model is its implementation on the Ankle Foot Orthosis (AFO) device used in assisting patients in stroke recovery. Early testing with the pSEA on the AFO showed an efficiency increase in the AFO device of over 25 % [10] as compared to the device without the pneumatic strain energy accumulator. At a recent meeting with industry, efficiency increases, potentially as high as 75 %, were reported using the pSEA on

the AFO. During testing that yielded 75 % efficiency increases, multiple parameters were adjusted leading to a question of how much of the reported increase was due to the pSEA and how much was due to other system parameters. Additionally, there is also a question regarding the efficiency increase limits that can be realized for various systems while using the pSEA. Answers to these questions necessitate the development of complete component and system level models of the pSEA that can provide estimates for such limits, especially as the device is extended for use on a hydraulic hybrid vehicle. [11]

2 Accumulator Model

Before a system level model can be developed, a component level model must be completely defined as it will serve as input to the system level model.

2.1 Total Energy Stored and Extracted: Component

A first step in developing a useful component level model is to clearly define the component, including the control volume in both space and time. Figure 3.2 shows the control volume (CV) of the fully expanded pSEA demarcated by the dashed line.

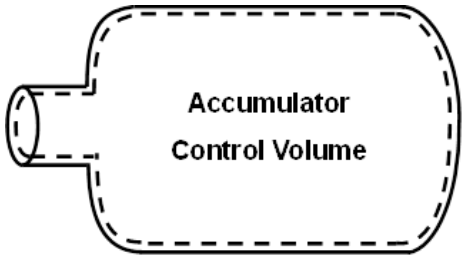

Figure 3.2: pSEA control volume

Having defined the component in space the various operating condition in time can be defined. First, the accumulator starts in the deflated state having an initial pressure of P_{atm} and an initial volume $V_{o.}$ The accumulator is then filled with a mass flow rate, $\dot{m}$, until the accumulator is full at time t_{full} having a final volume of V_{full} and a final pressure of P_{max}. The final pressure can either stop at the expansion pressure, $P_{exp,}$ or continue to rise to a higher maximum pressure, P_{max}, storing additional energy in the form of pressure. The pressure-volume curve of the fill process is shown below in Figure 3.3.

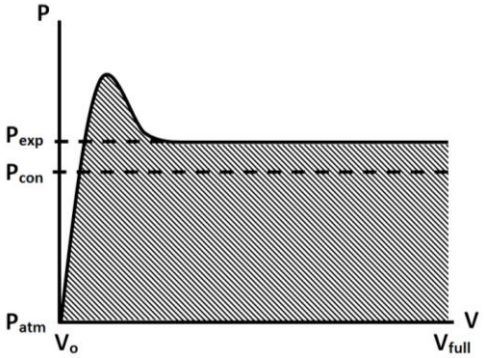

Figure 3.3: Pressure-volume curve of pSEA fill process.

A number of simplifying assumptions standard to pneumatic systems are made in order to begin the energy analysis of the device:

1. The CV is defined by the dashed line along the inner surface of the pSEA rubber bladder.
2. The accumulator is filled and exhausted rapidly; therefore, the heat loss terms are negligible so $\dot{Q} = 0.$
3. Kinetic and potential energy effects associated with the flow are neglected.
4. The thermodynamic state of the air entering and exiting the CV remains constant during the fill and exhaust processes.
5. The ideal gas model applies for air.

With the system defined in both space and time and the corresponding assumptions established, an energy rate balance analysis can be performed.

The energy rate balance equation is given in Eq. 1 when simplified for a single inlet:

$$\frac{dE_{CV}}{dt} = \dot{Q}_{CV} + \dot{W}_{CV} + \dot{m}_i(h_i + \frac{V_i^2}{2} + gz_i) \tag{1}$$

After applying assumptions two and three from above, Eq. 1 simplifies to:

$$\frac{dE_{CV}}{dt} = \dot{W}_{CV} + \dot{m}_i h_i \tag{2}$$

Multiplying both sides by *dt* and then integrating, the total energy stored in the pSEA is calculated:

$$E_{CV} = W_{CV} + \int_{t_o}^{t_{full}} \dot{m}_i h_i dt \tag{3}$$

The work done on the CV is the total boundary work, $W_{TB,}$ or strain energy, E_S, done on the strain energy accumulator. Boundary work is defined as:

$$E_S = W_{TB} = \int_{V_o}^{V_{full}} PdV \tag{4}$$

If the result of Eq. 4 is substituted into Eq. 3, an equation for the total energy of the pSEA in integral form of boundary work and mass flow rate into the accumulator is obtained:

$$E_{Tot} = \int_{V_o}^{V_{full}} PdV + \int_{t_o}^{t_{full}} \dot{m}_i h_i dt \tag{5}$$

Additionally, the second integral of Eq. 5 is the energy stored in the mass of the gas at the given pressure and volume. Once the accumulator has been filled, the final pressure and volume are set, thus fixing the mass of the system at that point. The theoretical maximum potential that the fixed mass has, at the given pressure and volume, can be determined analytically by evaluating the equivalent fixed mass control volume.

An equivalent fixed mass CV that is allowed to expand isothermally is shown in Figure 3.4. Allowing the mass at the final pressure and volume to expand isothermally yields the maximum theoretical potential energy stored in the pressure of the gas. The application of assumption five enables the analysis of the closed CV to determine the maximum potential of the compressed gas.

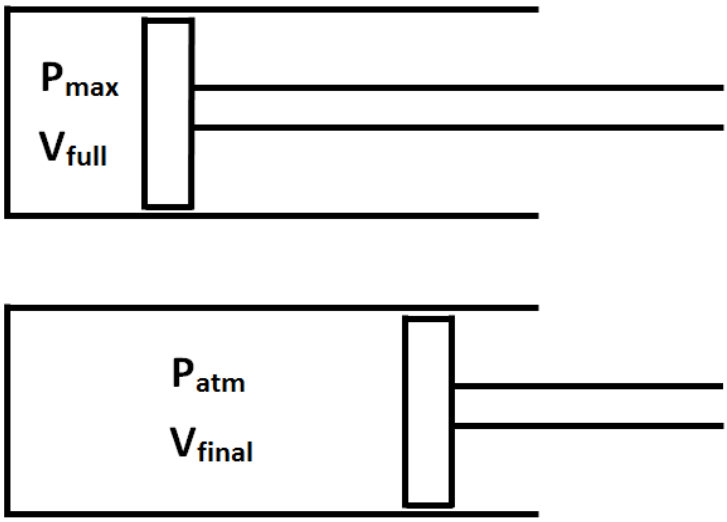

Figure 3.4: Closed system CV with constant mass allowed to expand isothermally

In an isothermal constant mass expansion, the ideal gas law results in the following expression:

$$PV = P_{\max}V_{full} = P_{atm}V_{final} = mRT = C \tag{6}$$

The above equation is rearranged by solving for P in terms of P_{max}, V_{full} and V to evaluate the integral PdV for the general pressure boundary work equation to obtain:

$$E_P = P_{\max}V_{full}\int_{V_{full}}^{V_{final}}\left(\frac{1}{V}\right)dV \tag{7}$$

Evaluating the integral in Eq. 7 the following result is obtained:

$$E_P = P_{\max}V_{full}\ln\left(\frac{V_{final}}{V_{full}}\right) \tag{8}$$

Utilizing the relationship in Eq. 6 the volume ratio is calculated inside the natural log to obtain an expression for the theoretical maximum energy stored in the pressure of the gas:

$$E_P = P_{\max}V_{full}\ln\left(\frac{P_{\max}}{P_{atm}}\right) \tag{9}$$

If the result of Eq. 9 is substituted into the second integral in Eq. 5, the end result is the total energy equation in terms of the sum of strain energy and pressure energy completely defined by pressures and volumes that are designable parameters for the strain energy accumulator:

$$E_{T\_in} = \int_{V_o}^{V_{full}} PdV + P_{\max}V_{full}\ln\left(\frac{P_{\max}}{P_{atm}}\right) \tag{10}$$

The advantage of having the equation in the form given in Eq. 10 is twofold. First, it provides a theoretical maximum stored energy value in terms of the primary forms of stored energy, strain and pressure. Next, it defines the total stored energy as a function of pressures and volumes, which are adjustable parameters for the pSEA. The equation allows for a sensitivity analysis to be discussed in more detail in Section 3.3.

2.2 Efficiency

Previous work on the strain energy accumulator has demonstrated how the device behaves under expansion and exhaust/contraction [3],[4]. Figure 3.5 shows the typical accumulator pressure-volume curve for both expansion and contraction.

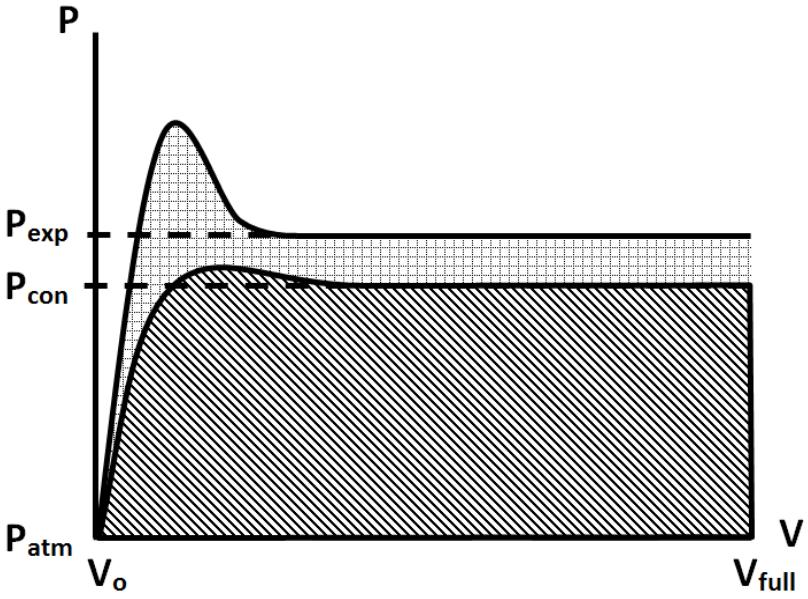

Figure 3.5: Exhaust pressure-volume curve of pSEA

The contraction of the pSEA occurs at a lower pressure and the net recoverable energy is the area under the contraction curve plus the contraction pressure energy. The total energy extracted from the pSEA can be determined from a modification to the limits of integration in Eq. 10 to get:

$$E_{T\_out} = -\int_{V_{full}}^{V_o} PdV + P_{\max} V_{full} \ln\left(\frac{P_{\max}}{P_{atm}}\right) \tag{11}$$

By taking a ratio of the energy exhausted to that input to the accumulator an efficiency of the component can be determined, η_{acc}:

$$\eta_{acc} = \frac{E_{T\_out}}{E_{T\_in}} \tag{12}$$

In long form the accumulator efficiency is:

$$\eta_{acc} = \frac{-\int_{V_{full}}^{V_o} PdV + P_{\max} V_{full} \ln\left(\frac{P_{\max}}{P_{atm}}\right)}{\int_{V_o}^{V_{full}} PdV + P_{\max} V_{full} \ln\left(\frac{P_{\max}}{P_{atm}}\right)} \tag{13}$$

This expression enables a sensitivity analysis to determine how the variation in each parameter will impact component efficiency. With the pSEA component model fully defined, including an analytical efficiency, the system model and resulting system efficiency can be determined.

3 System Model

Upon completing the component modeling, the next step is to determine the component impacts on overall system efficiency. Once a system model is complete the impact of the various parameters can be investigated, particularly the designable parameters, to minimize losses and maximize system efficiency.

3.1 Total Energy Expended: System

In order to calculate the total system efficiency with implementation of the pSEA, an energy accounting of energy expended must be performed. The motivation for this system model is the manual pSEA demonstrator shown in Figure 3.6. The manual demonstrator consists of three principal components: a primary cylinder with a volume, V_1, a pSEA, and a smaller secondary cylinder with V_2. The demonstrator receives a supply pressure of P_S and exhausts out of the valve connected to the secondary cylinder to P_{atm}.

Figure 3.6: Pneumatic Accumulator Demonstrator

The energy expended by the system is taken into account by tracking the mass used at each stage of the cycle using the following equations:

$$m_i = \frac{P_i V_i}{RT} \tag{14}$$

The above equation is used in conjunction with the following modeling assumptions:

1. The efficiency is evaluated for one complete cycle, with one cycle being one complete out stroke and one complete in stroke of both cylinders.
2. The cylinders have a set volume ratio, α.
3. The secondary cylinder in the system without an accumulator is regulated down to the same operating pressure as the secondary cylinder in the system with the accumulator.
4. Both cylinders in the system without an accumulator exhaust out to atmospheric pressure.
5. The expansion and contraction pressures of the accumulator have a ratio, β where $P_{atm}/P_S \leq \beta < 1$ and $P_{exp} > P_{con}$.
6. The shaft volume is negligible and the volume on both sides of the cylinder is the same.

7. All cylinders start at zero initial volume at the start of fill and completely fill the volume inside the cylinder.
8. The system is charged to start thus expelling mass on the first stroke of all cylinders.

Figure 3.7 shows the out-stroke flow diagram with the pSEA in line between cylinders one and two and is divided into two steps. In step one, supply pressure is input on the left side of the cylinder moving the cylinder to the right as indicated by the dashed arrow. The pressure on the outlet side of the cylinder is then exhausted into the accumulator where it stabilizes at the expansion pressure of the accumulator upon expansion thus completing step one. Step two starts with the accumulator exhausting at its contraction pressure to fill the second cylinder. The air on the other side of the second cylinder is then exhausted to the atmosphere.

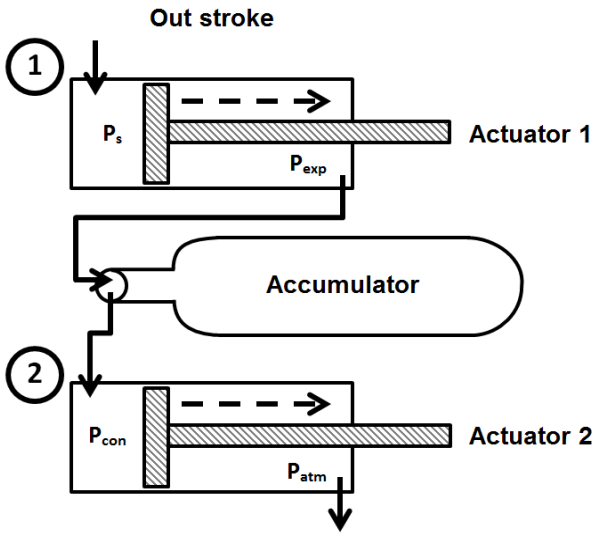

Figure 3.7: Outstroke diagram of pSEA

The in-stroke of the cylinders is essentially the reverse of the out-stroke steps and is shown in Figure 3.8 as steps three and four.

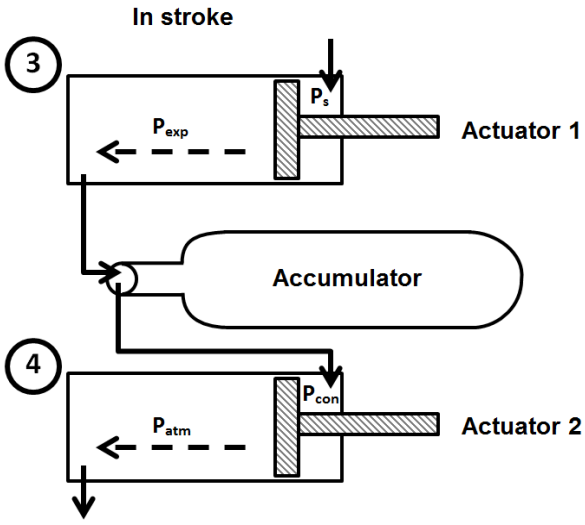

Figure 3.8: In stroke diagram of pSEA

In the case where the accumulator is not connected to the system, new mass is introduced at supply pressure to cylinder one and exhausts to atmosphere on the backside of the cylinder for each stroke of the cylinder. Cylinder two has new mass introduced at the contraction pressure as its input pressure and exhausts to atmosphere on the backside of the cylinder. Each addition of mass to the system is governed by Eq. 14. Before a system level efficiency analysis is performed a mass accounting is conducted for each step of the cycle both with and without the accumulator in line.

Starting with the system without an accumulator, the mass introduced to the system at steps one and three in Figures 4.7 and 4.8 is determined by:

$$m_{1,3\_w/o} = \frac{P_S V_1}{RT} \tag{15}$$

In steps two and four the mass introduced is the same in each step and is given by:

$$m_{2,4\_w/o} = \frac{P_{con} V_2}{RT} \tag{16}$$

Using assumptions two and five listed above, the following relations can be used in Eq. 16:

$$V_2 = \alpha V_1 \tag{17}$$

$$P_{con} = \beta P_{\exp} \tag{18}$$

By substituting Eqs. 17 and 18 into Eq. 16 the following relation is obtained:

$$m_{2,4\_w/o} = \frac{\alpha\beta P_{\exp} V_1}{RT} \tag{19}$$

The total mass used in the system without a pSEA is:

$$m_{T\_w/o} = \sum_{i=1}^{4} m_{i\_w/o} = \frac{2V_1}{RT}\left(P_S + \alpha\beta P_{\exp}\right) \tag{20}$$

Once the pSEA is introduced into the system the mass used from supply in steps one and three is the same as the case without the accumulator:

$$m_{1,3\_w} = m_{1,3\_w/o} = \frac{P_S V_1}{RT} \tag{21}$$

The energy savings in the system with the accumulator comes in subsequent steps that are powered by the energy captured by the accumulator. In these steps no additional mass from supply is required, thus in the overall mass accounting the additional mass used from supply is zero yielding:

$$m_{2,4\_w} = 0 \tag{22}$$

Summing the mass used from supply during each step of the cycle for the system with the accumulator gives:

$$m_{T\_w} = \sum_{i=1}^{4} m_{i\_w} = \frac{2V_1}{RT} P_S \tag{23}$$

With the mass used from supply accounted for in each step of the cycle for both cases, with and without the accumulator, the efficiency increase of the system can be calculated.

3.2 System Efficiency

Defining the efficiency of the system as a ratio of the mass used from supply with the accumulator to that used without the accumulator the following relation is obtained:

$$\eta_{sys} = \frac{m_{T\_w}}{m_{T\_w/o}} \tag{24}$$

If the results from Eq.'s 20 and 23 are substituted into Eq. 24, an equation for the system efficiency in terms of supply pressure and accumulator expansion pressure is given as:

$$\eta_{sys} = \frac{P_S}{P_S + \alpha\beta P_{\exp}} \tag{25}$$

Since the system efficiency is defined as how much less mass is used from supply for the system with the pSEA compared to the system without the pSEA, the percent efficiency increase can be defined as:

$$\%\,Efficiency\,Increase = \left(1 - \eta_{sys}\right) \times 100 \tag{26}$$

Having defined percent efficiency increase the accumulator provides, this result can be used to perform a sensitivity analysis of the system to determine which parameters have the greatest impact on system efficiency.

3.3 Sensitivity Analysis

In order to perform a preliminary quantitative sensitivity analysis, a sample system must be defined. Let the atmospheric pressure of the sample system be 15 psia and the primary supply pressure be 60 psia. As a first step in a complete sensitivity analysis, let the expansion pressure of the accumulator vary from atmospheric pressure way up to supply pressure. These are the two extremes that serve as an upper and lower limit of the operating range that expansion pressure could be set to by proper material and dimension selection for the system of interest.

Next let the values of α, for the volume ratio, and β for the accumulator expansion and compression ratio both be equal to one. By letting α equal one the volume of the first and second cylinder are equal. When β is equal to one then accumulator expansion and contraction pressures are equal, indicating a lossless accumulator providing an upper maximum bound of efficiency increase. Figure 3.9 shows the percent efficiency increase and how it changes with accumulator expansion pressure.

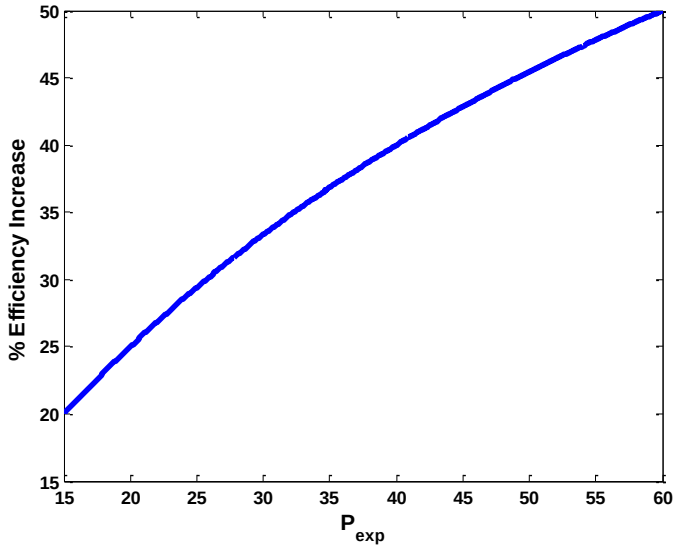

Figure 3.9: % Efficiency Increase vs Accumulator P_{exp}

Based on the specified conditions for the sample system, the percent efficiency increase that can be expected by adding a pSEA to the system ranges from 20 % to 50 %. If the input to the model is adjusted to values similar to those experienced on the manual pneumatic accumulator demonstrator from Figure 3.6, the result is that of Figure 3.10. The values for the system in Figure 3.10 are a supply pressure of 50 psia, an accumulator expansion pressure of 40 psia, a volume ratio of 0.7 and an accumulator expansion/contraction ratio of 0.95.

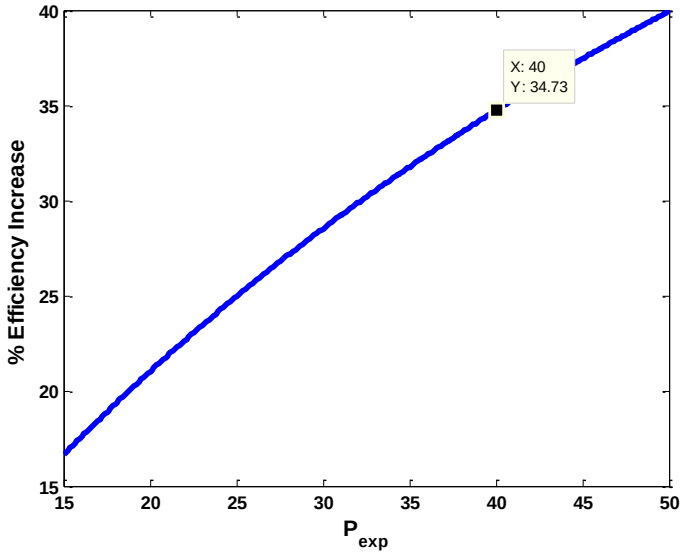

Figure 3.10: Projected % Efficiency Increase for Manual Pneumatic Accumulator Demo

It is observed in Figure 3.10 that for the manual demonstrator and for an expansion pressure of 40 psia, the maximum theoretical efficiency improvement is approximately 35 %. The theoretical maximum efficiency improvement is close to that observed in testing on the Ankle Foot Orthosis device of 27 % through the Center for Compact and Efficient Fluid Power.

4 Modeling Discussion

The modeling effort developed herein started by defining the pneumatic strain energy accumulator in both space and time. Once the accumulator had been clearly defined in space and time an energy storage balance was able to be completed. The result of the energy balance resulted in determination of energy terms for both the strain and pressure energy components stored in the pSEA. The total energy of the accumulator is a sum of the strain and pressure energies, with the final equation requiring only pressures and volumes. Some of the pressures and volumes are design parameters that can be modified to meet the system requirements.

Knowing the maximum theoretical energy input to the accumulator, along with the theoretical maximum that can be extracted, a theoretical component level efficiency can be calculated analytically. Component efficiency together with actuation work will dictate how many times the remaining energy stored in the accumulator can be reused by a system. All else being equal, the smaller the losses in the accumulator the more times the remaining energy can potentially be used down the line. The ability to store and recycle the remaining energy more than once has the potential to further boost the overall system efficiency.

Similarly to the component model, the system model was defined in space and time with a flow diagram that was used to perform an accounting of the mass consumed from the supply. Upon completion of the mass accounting, these values were used to calculate a system efficiency which was subsequently used to determine the percent efficiency increase with use of the accumulator compared to the system without an accumulator. The resulting energy saved is a function of supply pressure, accumulator expansion pressure, the volume ratio, and expansion/contraction pressure ratio of the accumulator. The percent efficiency increase equation shows a clear relationship among these parameters, allowing for the design optimization of a given application.

One of the parameters in the efficiency increase equation, the accumulator expansion pressure, was varied from atmospheric to supply pressure for a system with a cylinder volume ratio of one and an expansion/compression ratio of one to provide a maximum theoretical efficiency increase. The maximum for that system was a 50 % efficiency increase. This makes sense intuitively if the cylinders are the same size, there are no losses, and the gas from the first cylinder can be used to power the second cylinder of equal size. An analysis of the specific case approximating the manual pneumatic accumulator demonstrator was performed based on the conditions experienced with that system. The maximum theoretical efficiency increase at the given expansion pressure was 34.7 % which is comparable to the 27 % reported on the Ankle Foot Orthosis device.

5 Conclusions and Future Work

In the current work, both a component and system level energy accounting and efficiency calculation were conducted. The results of the modeling effort provide a new set of tools that can be used to analyze actual systems designed with, or retrofitted with, the accumulator. The equations clearly display the design parameters and how they impact the system performance.

An initial sensitivity analysis was conducted by varying the expansion pressure of the accumulator on the system level. Other parameters can be varied including the supply pressure, the contraction pressure, the volume ratio, the expansion/contraction pressure ratio and the volumes of the components to reveal the system's sensitivity to various parameters. Performing a sensitivity analysis will direct future work to focus on key areas for improving component and

system efficiency. An additional area that can be further investigated and developed is calculation of strain at the inner wall of the accumulator, which has been shown to be the critical stress area [4].

The analysis performed in the current work can also be extended to the hydraulic version of the accumulator. There is significant potential for strain energy accumulators to improve efficiencies in fluid power applications. Industries such as manufacturing and automotive, that use fluid power extensively, have the potential to save millions of dollars annually in energy costs [1]. By gaining deeper insight through detailed modeling, and the subsequent development of analysis tools, many other industries, such as the medical and aviation industries, stand to benefit from strain energy accumulators.

Acknowledgments

This work was supported by the Center for Compact and Efficient Fluid Power, an NSF Engineering Research Center, grant EEC-0540834.

References

[1] Love, L.J., Lanke, E., Alles, P., 2012, "Estimating the Impact (Energy, Emissions and Economics) of the U.S. Fluid Power Industry." Oak Ridge National Laboratory, Oak Ridge, TN.

[2] Uria-Martinez, R., O'Connor, P., Johnson, M.M., 2015, "2014 Hydropower Market Report." Oak Ridge National Laboratory, Oak Ridge, TN.

[3] Pedchenko, A., Barth, E.J., 2009, "Design and Validation of a High Energy Density Elastic Accumulator Using Polyurethane." Proceedings of the ASME Dynamic Systems and Control Conference, pp. 283-290.

[4] Cummins, J.J., Pedchenko, A., Barth, E., Adams, D.E., 2014, "Advanced Strain Energy Accumulator: Materials, Modeling and Manufacturing." Proceedings of the 2014 Bath/ASME Symposium on Fluid Power and Motion Control. Sept 11. Bath, England UK.

[5] Cummins, J.J., Maurice, C., Song, Y., et al., 2014, "Elastomeric Evolution: A New Look at Carbon Nanotube Reinforced Elastomers." Proceedings of the 2014 European Rotorcraft Forum. Sept 4. Southampton, England UK.

[6] Kim, Y.A., Hayashi, T., Endo, M., Gotoh, Y., et al., 2006, "Fabrication of aligned carbon nanotube-filled rubber composite." Scripta Materialia 54, pp. 31-35.

[7] Bokobza, L., 2007, "Multiwall carbon nanotube elastomeric composites: A review." Polymer 48, pp. 4907-4920.

[8] Yamada, T., Hayamizu, Y., Yamamoto, Y., Yomogida, Y., et al., 2011, "A stretchable carbon nanotube strain sensor for human-motion detection." Nature Nanotechnology 6, pp. 296-301.

[9] Kang, I., Schulz, M.J., Kim, J.H., Shanov, V., et al., 2006, "A carbon nanotube strain sensor for structural health monitoring." Smart Materials and Structures 15, pp. 737-748.

[10] Boes, M.K., Islam, M., Li, D., Hsiao-Wecksler, E. T., "Fuel Efficiency of a Portable Powered Ankle-Foot Orthosis". IEEE 13th International Conference on Rehabilitation Robotics (ICORR 2013). June 24-26. Seattle, WA.

[11] "Highway Vehicles – Hydraulic Hybrid Passenger Vehicle (Test Bed 3)." Center for Compact and Efficient Fluid Power. Web. 28 Apr. 2015.

CHAPTER 4

EXPERIMENTAL EVALUATION OF THE EFFICIENCY OF A PNEUMATIC STRAIN ENERGY ACCUMULATOR

Joshua J Cummins, Seth Thomas, Christopher Nash
Sankaran Mahadevan, Eric J Barth and Douglas E Adams

Department of Mechanical Engineering
Vanderbilt University
Nashville, TN

Submitted (In Review) for publication to the International Journal of Fluid Power in February, 2016

Abstract

There is heightened interest in research to develop materials and devices that achieve greater energy storage capacity, power density and increased energy efficiency. This work analyzes the performance of a novel energy storage device, the pneumatic strain energy accumulator, which is designed to exploit the advantageous aspects of the non-linear behavior of elastomeric materials. An analytical methodology for simultaneously characterizing the pneumatic and material energy storage in a strain energy accumulator, and more generally for pneumatic and strain energy systems, has been developed. Component efficiency along with the expansion and contraction pressures of the pneumatic strain energy accumulator are determined experimentally, using a combined Matlab and National Instruments data acquisition system, so that a system level efficiency calculation can be performed. Incorporating uncertainty analysis, the efficiencies of the strain energy accumulator are measured to be consistently over 93 % in over 2500 cycles of testing. The expansion and contraction pressures of the accumulator, despite the hysteretic behavior of rubber, have a stable value with a standard deviation of only 0.1 % of the mean values.

1 Introduction

Energy demand and the ability to meet it using efficient means are driving much of the innovation in the energy sector. One strategy to meet this demand is to develop energy storage and recovery devices. A device that has emerged recently that addresses the need for energy efficiency while also meeting power density requirements is the strain energy accumulator (SEA).

1.1 Pneumatic Strain Energy Accumulator

The pneumatic form of the strain energy accumulator (pSEA) operates by capturing and storing the exhaust gas from one component until it is needed and used by another component at a later point in time. The pSEA functions by expanding a rubber bladder at a constant pressure inside a rigid shroud, storing energy in the form of both strain and pressure energy, and then contracts at a lower constant pressure returning the energy to the system to be used for a secondary task. A 2012 Oak Ridge National Labs (ORNL) study indicates the need and importance of a device such as the pSEA. The ORNL study found that the fluid power industry uses between 2-3 % of the nation's energy and averages only 22 % efficiency (Love et al. 2012). The pneumatic sector is even less efficient averaging just 15 % efficiency, clearly indicating the need to increase efficiency and develop devices for energy storage and recovery such as the pSEA.

One such application using the pSEA is the Ankle Foot Orthosis (AFO) stroke rehabilitation device (Boes et al. 2013). The AFO uses a rotary actuator powered by a compressed gas supply, carried by the patient, that helps raise and lower a patient's foot to improve muscle memory during rehabilitation. While changing multiple system parameters, efficiency increases ranging from 25 % to 75 % when using the pSEA on the AFO were reported. With no way to directly identify the efficiency increase due solely to the pSEA, a need to quantify system performance in terms of the SEA design parameters was identified. This need has motivated the current work to fully define and characterize an accumulator component efficiency model, and develop a lumped parameter state model to estimate system level efficiency improvements. The ultimate goal for the current research is to accurately define efficiency increase limits that can be realized for various systems while using the pSEA. This paper demonstrates that the development of models for the pSEA has enabled the ability to provide estimates for efficiency limits at both the component and system level.

1.2 Pneumatic and Strain Energy Literature Survey

Initial investigation into the SEA by Pedchenko and Barth (2009) provided a proof of concept design of an energy dense SEA. In 2012, Tucker further investigated the energy density of the SEA device determining the forms of rubber that are ideal in terms of performance for use in the SEA due to their high energy density. In 2013, Boes et al. provided the first reported efficiency increases resulting from use of the pneumatic strain energy accumulator (pSEA). Equations to quantify these efficiencies are given in Cummins et al. 2015, offering the ability to characterize efficiency and how it relates to the unique material properties of rubber.

Prior to understanding the pSEA and how its performance benefits from the properties of rubber, a basic understanding of these properties is required. In his book Rubber Technology, John Dick (2009) provides a thorough overview of these properties including elasticity, tensile stress-strain behavior and fatigue resistance, hysteresis, etc. which are the underlying operating principals of the pSEA. The Mullins' effect is well documented in Mullins' original work from 1948 and explains how the strain of a rubber is dependent on previous loading, which is important for strain energy considerations. An often cited work by Cadwell et al. (1940) provides a comprehensive review of various parameters and their effect on the fatigue life of rubber showing how changing any one loading parameter can greatly affect the fatigue life of rubber. Current fatigue testing standards for rubber are given by ASTM 2011 and, specific to the SEA, understanding and characterizing the ballooning behavior of rubber tubing is presented in detail in Gent 1978 and 2005, corresponding to the behavior observed in the ballooning process of the

SEA. To obtain quantitative insights, standard uncertainty analysis such as that given in Haldar and Mahadevan (2000) can be used.

Harris et al. (2012) completed an efficiency optimization study using current technologies and identified future needs of the pneumatic industry. Within the study, energy storage was specifically identified as an area for improvement. Additionally, future directions that were identified included the development of integrated performance metrics focused on model-based optimization techniques tailored to specific applications. The three primary goals of the current research are to: (a) develop a generally applicable model-based component efficiency estimation as an integrated performance metric to the system efficiency, (b) experimentally measure the key performance parameters of the pSEA including component efficiency, and expansion and contraction pressures for the specific system of interest, and (c) perform uncertainty analysis of the component performance parameters to make uncertainty propagation an integral part of system efficiency measurements.

2 Accumulator Component Efficiency Model

Prior to system level model development, component efficiency estimates are analytically determined. In order to develop an analytical efficiency expression, an energy rate balance analysis is performed and simplified for the single inlet device shown in Figure 4.1.

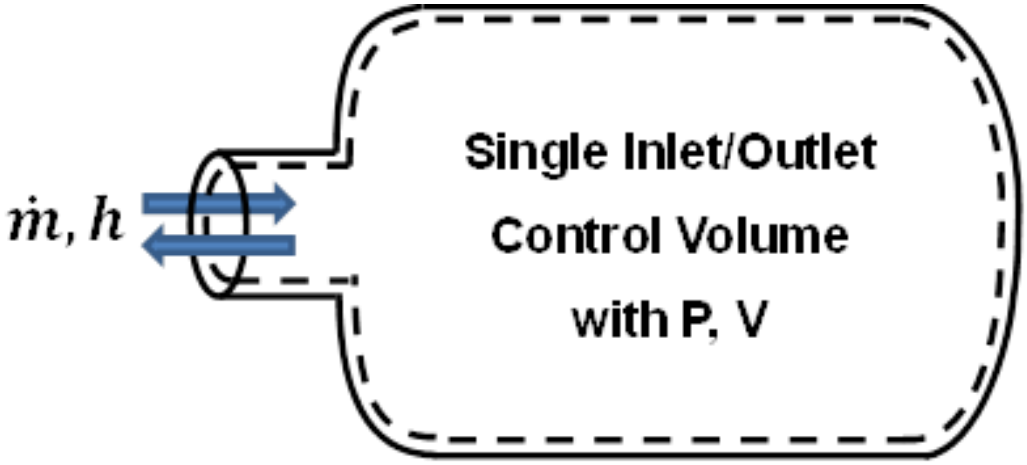

Figure 4.1: Single Inlet/Outlet Control Volume

The simplified energy balance equation for the total energy of the pSEA in integral form is developed in Cummins et al. (2015). The full details of the derivation can be found in Cummins et al. and is comprised of both boundary work and mass flow rate into the accumulator:

$$E_{Tot} = \int_{V_o}^{V_f} PdV + \int_{t_o}^{t_f} \dot{m}hdt \qquad (1)$$

where E_{Tot} is the total energy stored in the component, P is the pressure at the given volume and instant in time, V_o is the initial volume, V_f is the final volume, $\dot{m}$ is the mass flow rate in or out of the system with corresponding enthalpy, h, t_o is the initial time and t_f is the final time.

If the second integral on the right hand side of Eq.1 is evaluated, the resulting total energy equation is given in terms of the sum of the boundary work, or strain energy, and pressure energy:

$$E_{Tot} = \int_{V_o}^{V_f} PdV + P_{\max} V_{full} \ln\left(\frac{P_{\max}}{P_{atm}}\right) \tag{2}$$

Here, P_{atm} is atmospheric pressure and P_{max} is the maximum fill pressure of the accumulator with corresponding maximum volume V_{full}. The strain and pressure energy terms are completely defined by pressures and volumes that are designable parameters for the strain energy accumulator. A theoretical maximum stored energy value in terms of the primary modes of stored energy, strain and pressure, is thus given in Eq. 2.

The total energy input to and extracted from the pSEA can be determined by evaluating the total energy function in Eq. 2 at the respective limits of integration for input and exhaust. A ratio of the energy exhausted by the accumulator to the energy input into the accumulator yields the efficiency of the component, η_{acc}:

$$\eta_{acc} = \frac{-\int_{V_{full}}^{V_o} PdV + P_{\max} V_{full} \ln\left(\frac{P_{\max}}{P_{atm}}\right)}{\int_{V_o}^{V_{full}} PdV + P_{\max} V_{full} \ln\left(\frac{P_{\max}}{P_{atm}}\right)}. \tag{3}$$

With the model-based analytical pSEA component efficiency estimate defined, experiments can be conducted to determine the pSEA component efficiency.

3 Efficiency Experiments

Having developed the analytical equation necessary to determine the efficiency of the pSEA component, the necessary pressures and volumes, including the expansion and contraction pressures, can be experimentally measured and determined.

3.1 Experimental Setup

The experimental setup (Figure 4.2) consisted of a single pneumatic strain energy accumulator, Alicat M-series Mass Flow Meter, throttle valve, Festo 5-way valve bank, supply pressure regulating valve (not pictured), electrical power supply and National Instruments (NI) data acquisition (DAQ) system. The pSEA tested in each series of tests consisted of a black rubber tube encased by a polycarbonate shroud. The pSEA dimensions and volumes are proprietary as the technology is currently involved in ongoing commercialization efforts and are only provided as normalized values when necessary and where appropriate.

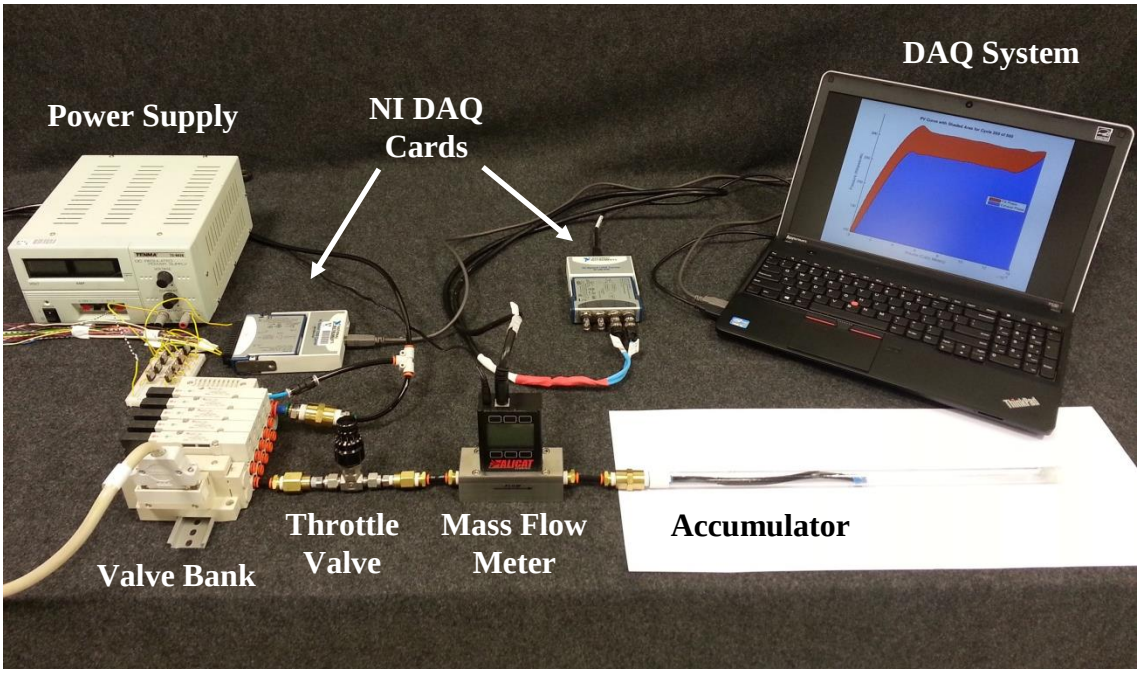

Figure 4.2: Component efficiency testing experimental test setup

Shop supply air (725 kPa) passed through the regulating valve where it was regulated down to approximately 360 kPa (denoted as P_s), which was subsequently connected to the supply port for the valve bank (port one in Figure 4.3). The upstream side of the mass flow meter was connected indirectly to port 2 on the opposite side of the bank. Between the mass flow meter and port 2 was the throttle valve. The throttle valve was placed in line to limit the fill rate of the accumulator to prevent clipping of the mass flow meter. The valve bank was modified to create a 3-way valve that could be used to control the air flow into and out of the accumulator (Figure 4.3). All pressures are reported in absolute pressure.

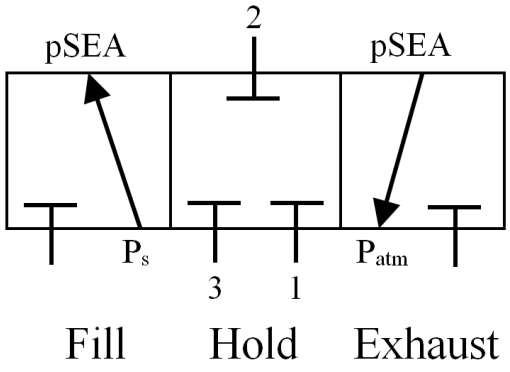

Figure 4.3: Airflow block diagram for automated valve for fill (left), hold (center) and exhaust (right) positions

In the hold phase (Figure 4.3 center) all ports remained closed. During the fill phase (Figure 4.3 left), compressed air from supply flowed into the pSEA when port 1 diverted to port 2. Upon exhausting (Figure 4.3 right), air flowed from the pSEA out to atmosphere when port 2 diverted to port 3. Throughout the cycle, the downstream side of the flow meter was connected to the

accumulator allowing the volumetric flow rate and pressure of the air flowing into and out of the accumulator to be measured. The volumetric flow and pressure data collected by the flow meter was sent to an NI input DAQ card which was then connected to the laptop computer. The valve bank positioning was controlled by a 24 V electrical power supply controlled by a NI output DAQ card connected to the laptop computer.

One full cycle of the accumulator consisted of an initial two second hold, followed by a fill stage, another two second hold, and a two second exhaust stage. A Matlab interface was used to send and receive output and input signals from the respective DAQ cards, control the number of cycles for each test, specify the sample rate at 1000 Hz and set the fill time for each test. The fill time and number of cycles were varied depending on the test. Fill time was varied from 0.30 seconds and 0.60 seconds to investigate the effect of spiking the pressure on component efficiency. Tests included a 25 cycle warmup period to minimize the Mullins effect followed by 100 cycles during which data was collected for analysis. During initial testing, tests using 500 cycles produced results consistent with the 100 cycles test. Therefore, to reduce experimental and computational time, 100 cycles were used during all subsequent tests. A recovery period of five minutes was observed between each test.

3.2 Experimental Data Collection

Pressure and volumetric-flow readings were acquired from the mass-flow meter. The resulting time histories for three cycles for pressure and volumetric flow are shown in Figure 4.4 and Figure 4.5, respectively.

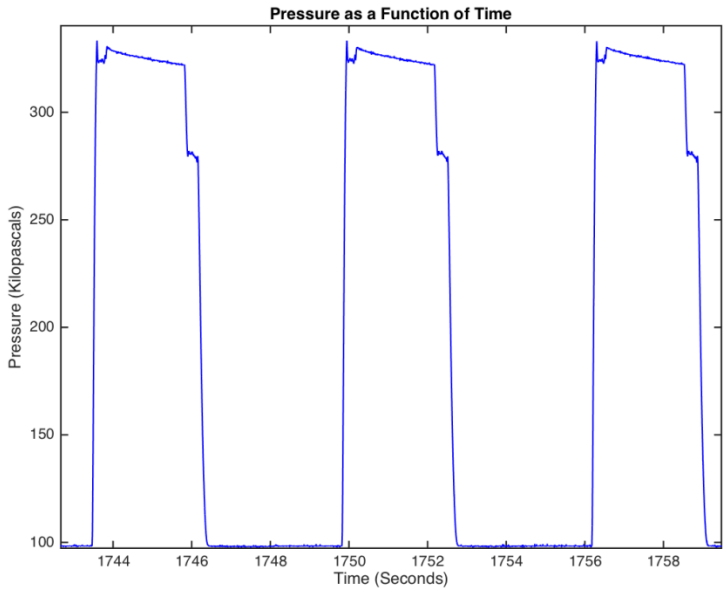

Figure 4.4: Pressure vs time from three experimental cycles

Figure 4.4 exhibits behavior similar to the results obtained in previous works (Gent 2005 and Pedchenko 2009). Initially a pressure spike is seen as the accumulator is made taut followed by a sudden drop in pressure as the accumulator balloons out. After ballooning initiates, the accumulator experiences a relatively constant pressure fill process followed by a slight pressure spike as the accumulator reaches its maximum volume. In the cases where the end of the accumulator hits the bump stop at the end of the shroud, the P-V curve experiences a slight rise in pressure. The slight decrease in pressure during the hold phase indicates a minor low flow leak

in the system. Finally the pressure experiences a relatively constant contraction stage before final exhaust to atmosphere.

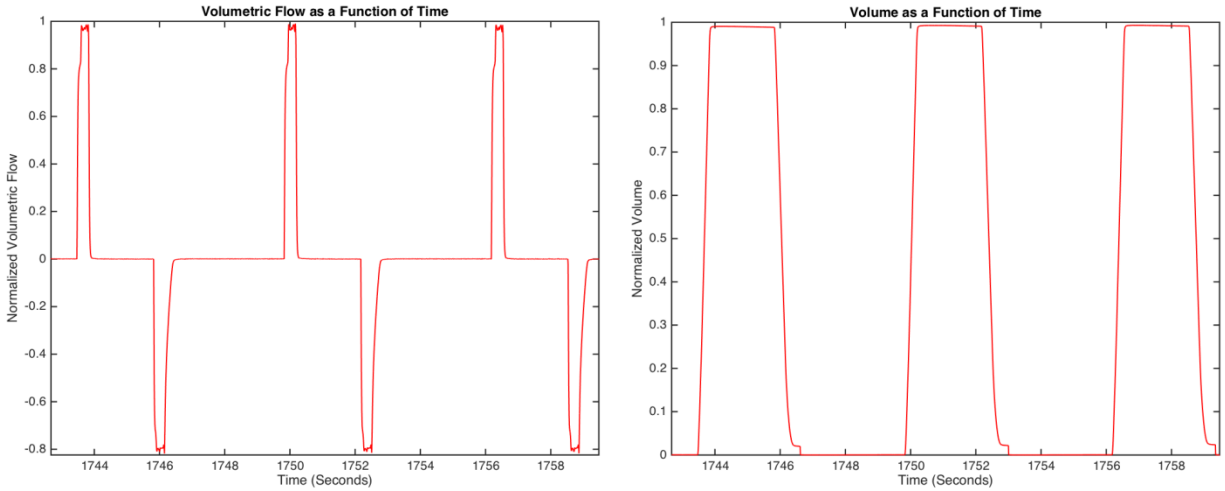

Figure 4.5: Volumetric flow vs time (left) and Volume vs time (right) from three experimental cycles

Figure 4.5a shows the volumetric flow rate as a function of time where the positive spikes correspond to the fill stage and the negative spikes the exhaust stage. When the fill cycle starts, the volumetric flow experiences a sharp rate increase before a slight levelling out as the bubble forms. A relatively constant fill rate is reached before flow into the accumulator is stopped and the volumetric flow rate returns to zero. During the hold stage when the pSEA is filled, no flow is seen by the flow meter due to the slow low-velocity leak in the system. Similar behavior is observed during exhaust of the pSEA except having a negative volumetric flow rate.

Volumetric flow rate was integrated using the trapezoidal method and detrended to obtain the accumulator volume shown in Figure 4.5b. Integration drift resulted from limitations inherent in the mass-flow meter's calibration. The data was corrected and drift was accounted for by determining a linear regression best fit line using the starting points of each cycle. Once the best fit line for the drift was found it was subtracted out from the data. The resulting volume time history is shown in Figure 4.5. Remnants of the integrator drift can be seen at the end of each cycle after the exhaust stage when the volume does not return to zero; however, this effect is negligible and is noted as a minor source of epistemic uncertainty. With the challenges associated with accurately measuring mass flow rate particularly in transient, dynamic and low flow conditions known (de Giorgi *et al.*, 2008 and Igarashi *et al.*, 2007), the transient behavior of the pSEA introduces an additional and greater source of epistemic uncertainty.

By combining pressure and volume data at each instant in time, pressure-volume curves for each cycle were generated. Data within a cycle was divided into fill and exhaust phases with respect to the cycle's maximum and minimum volumes: data produced as the system moved from a minimum volume to a maximum volume was designated as the fill phase (red), while data produced as the system moved from a maximum volume to a minimum volume was designated as the exhaust phase (blue). Sample pressure-volume curves for the beginning (cycle 1), middle (cycle 250), and end (cycle 500) cycles from a 500-cycle test are shown in Figure 4.6.

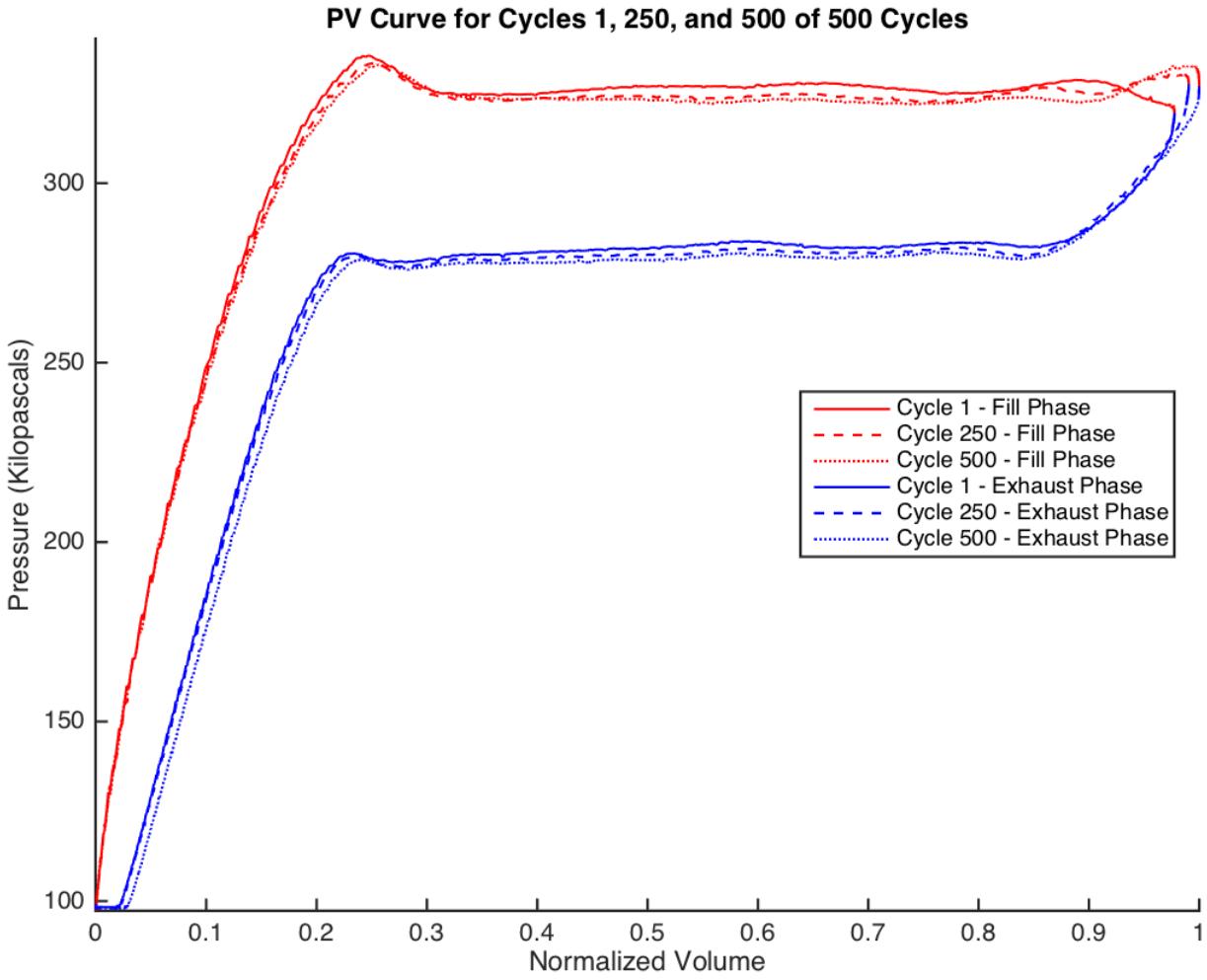

Figure 4.6: Pressure vs volume for cycles at beginning, middle and end of 500 cycle test

Several key results are observed that benefit from the hyperelastic behavior of rubber. First, as the rubber is stretched hyperelastically and softens, a slight decrease in expansion and contraction pressure is observed. This means that less work is done on stretching the rubber during steady state operation. Additionally, as the rubber softens over time the end of the accumulator reaches the bump stop at the end of the shroud thus fixing the volume and causing a slight pressure spike near the end of the fill phase.

While the pressure spike increases component efficiency, as can be seen analytically (due to domination of the pressure term in the efficiency equation) and is verified experimentally, it results in two undesired effects. First, it negates the novelty of a constant pressure device and it also degrades long term performance as it exceeds the normal operating pressure. Recurring exceedance of the design pressure causes premature failure of the accumulator as it transfers load to the end attachments. This effect was experienced during testing at excess pressures (not presented herein due to degraded pSEA life performance with current end configurations). This indicates the importance of properly designing the accumulator to the desired engineering application.

4 Results and Discussion

4.1 Component Efficiency

A cycle's efficiency is defined as the ratio between the total energy output by the pSEA to the total energy input to the pSEA as given in Eq. 3. The total energy is determined in part by calculating the area under the pressure-volume curve, or the strain energy, for both the fill and exhaust phases. This area was determined by integrating pressure with respect to volume using the trapezoidal method and is shown in Figure 4.7.

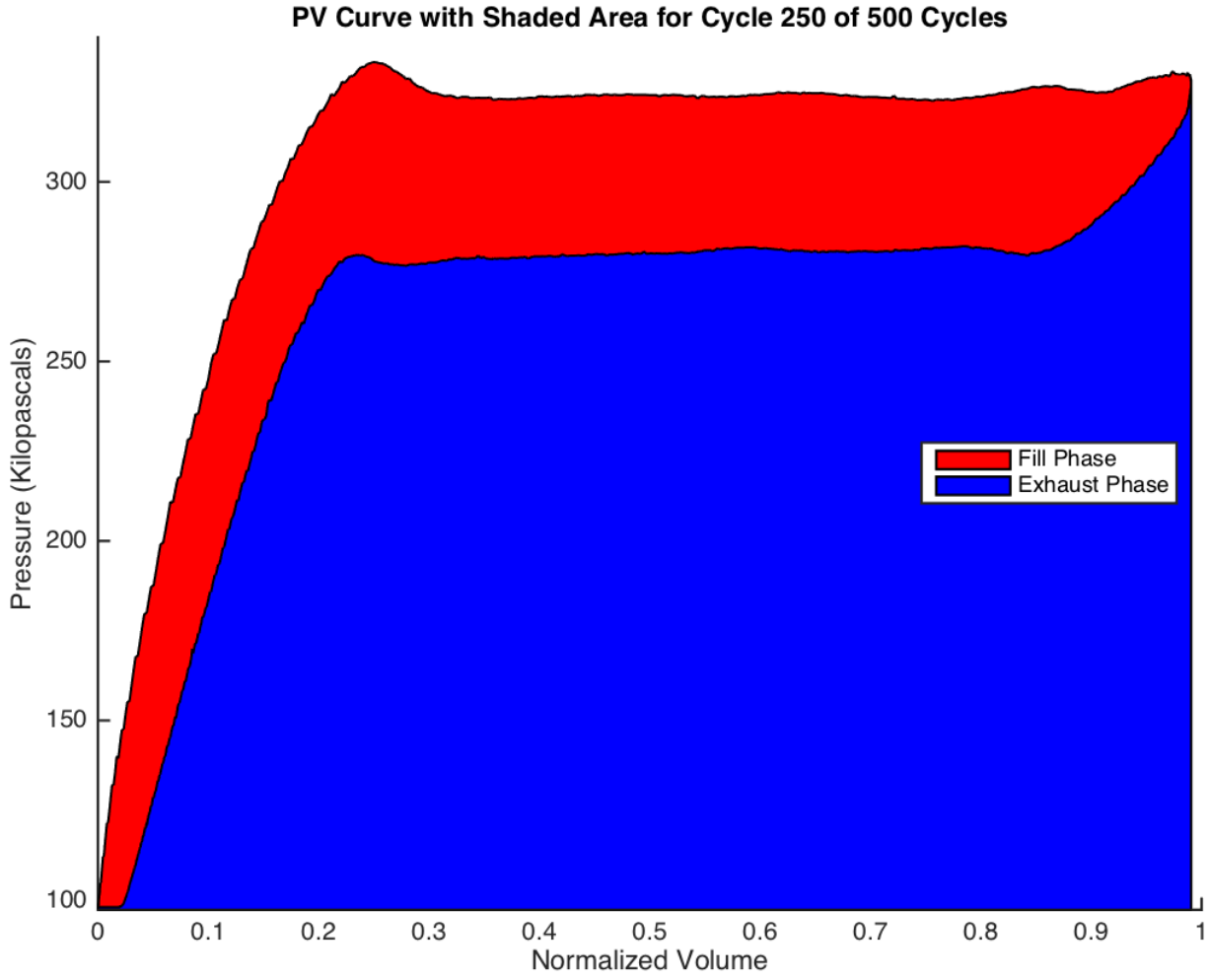

Figure 4.7: Pressure volume plot showing strain energy in (red+blue) and out (blue) of pSEA

The remainder of the total energy comes from the maximum potential of the pressurized air and is determined by measuring the cycle's maximum volume and corresponding maximum pressure at that volume. When the maximum potential of the air pressure is combined with the experimentally determined strain energy, the efficiency of the cycle is obtained. Calculated efficiency values for five, 100-cycle tests are depicted in Figure 4.8.

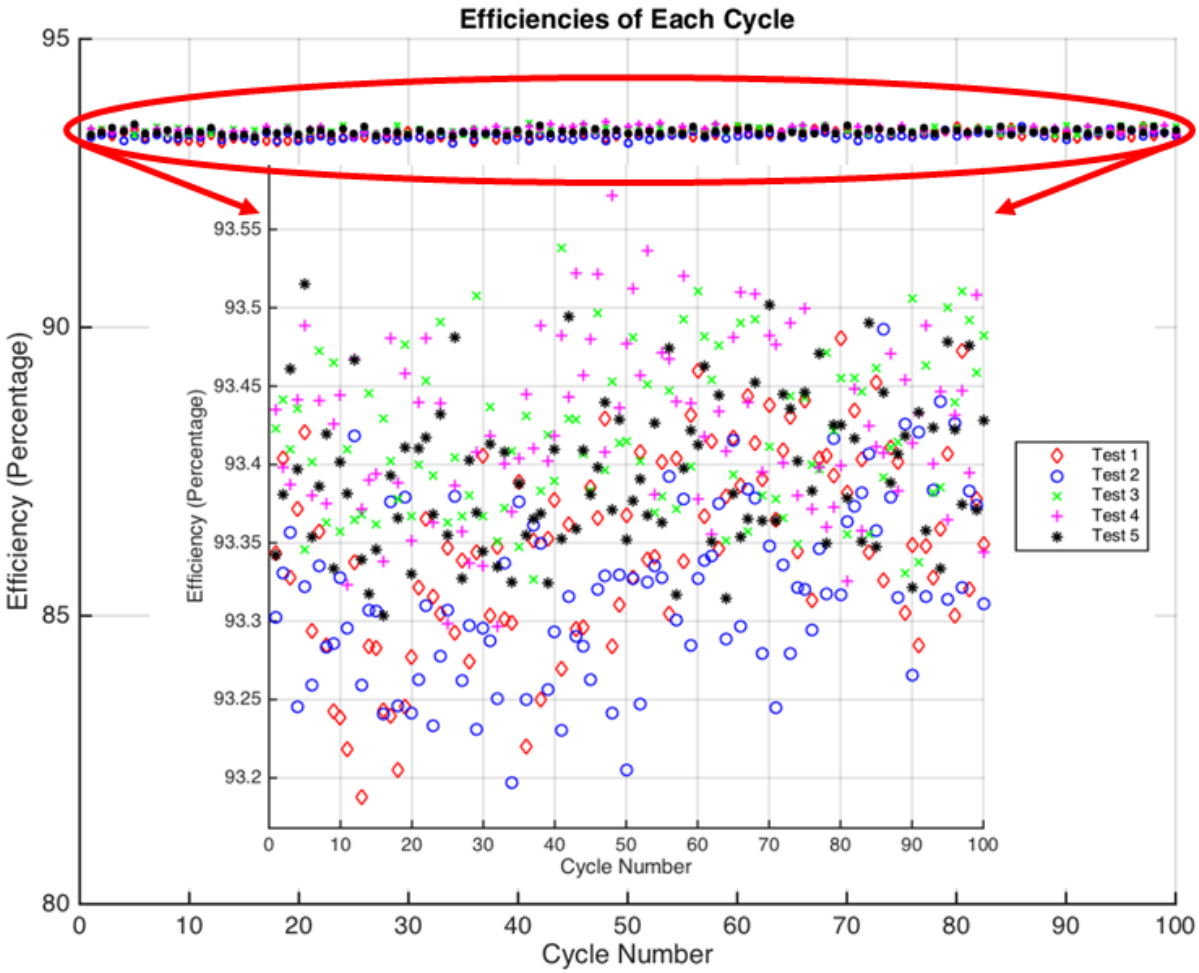

Figure 4.8: Energy efficiency of pSEA component for five, 100 cycle trials with inset zoomed-in efficiency

It is important to note the scale used for the efficiency in Figure 4.8. With the efficiency varying minimally, less than 0.3 % from max to min, the scale was chosen to identify the type of uncertainty analysis to be performed.

4.2 Component Efficiency Uncertainty Analysis

The mean value for each of the 100 cycle tests, μ, along with the standard deviation, σ, were calculated as follows:

$$\mu = \frac{1}{n}\sum_{i=1}^{n} x_i \tag{4}$$

$$\sigma = \left[\frac{1}{n-1}\sum_{i=1}^{n}(x_i - \mu_x)^2\right]^{1/2} \tag{5}$$

where n is the total number of data points and x_i is value of the i^{th} data point. Data sets that showed little to no trend in the data, such as the efficiency calculations, were analyzed using mean and standard deviation uncertainty analysis. The experimentally determined efficiency values for the pSEA component from Figure 4.8 exhibit little to no trend thus a basic mean and standard deviation analysis is given in Table 4-1.

Table 4-1: Component experimental efficiency of pSEA

Strain Energy Accumulator Component Efficiency		
Trial	Mean (%)	Standard Deviation (%)
1	93.35	0.063
2	93.32	0.057
3	93.42	0.050
4	93.42	0.056
5	93.39	0.048
5 Cycle Average	93.38	0.068

In Table 4-1, the 5 Cycle Average refers to taking all five, 100 cycle tests and treating them as a single data set. The resulting values correspond to a composite value for the pSEA component across tests. Uncertainty analysis indicates that across all tests the pSEA as a component has an average efficiency around 93.4 %. Even when the warmup cycles are taken into consideration (observed but not shown for conciseness) efficiency is still close to 92 %, and in both cases the standard deviation is less than a tenth of a percent. This indicates that in spite of hysteresis and Mullins effect, which often times negatively affect elastomer performance, the pSEA is still an energy efficient device. Furthermore, the efficiency increases with each test until it converges to a steady state efficiency of 93.4 %.

4.3 Component Key Performance Parameters

In order to study the accumulator's impact on system efficiency, it is first necessary to determine the pSEAs key performance parameters, the expansion and contraction pressures. These pressure values will serve as input parameters to the system efficiency model. The expansion pressure of the pSEA is characterized by a rapid increase in volume while the pressure remains relatively constant. Likewise, the contraction pressure corresponds to a rapid decrease in volume at a relatively constant pressure. Both of those pressures can be clearly seen on a pressure-volume diagram in Figure 4.9 as the regions where the curve is nearly linear with very little slope. In the constant pressure region, minimum and maximum volumes were set as end points for determining the expansion and contraction pressures. The pressure data between those points was averaged during each of the fill and exhaust phases. A sample determination is given in Figure 4.9. The experimentally determined expansion and contraction pressures for the five, 100 cycle tests are shown in Figure 4.10.

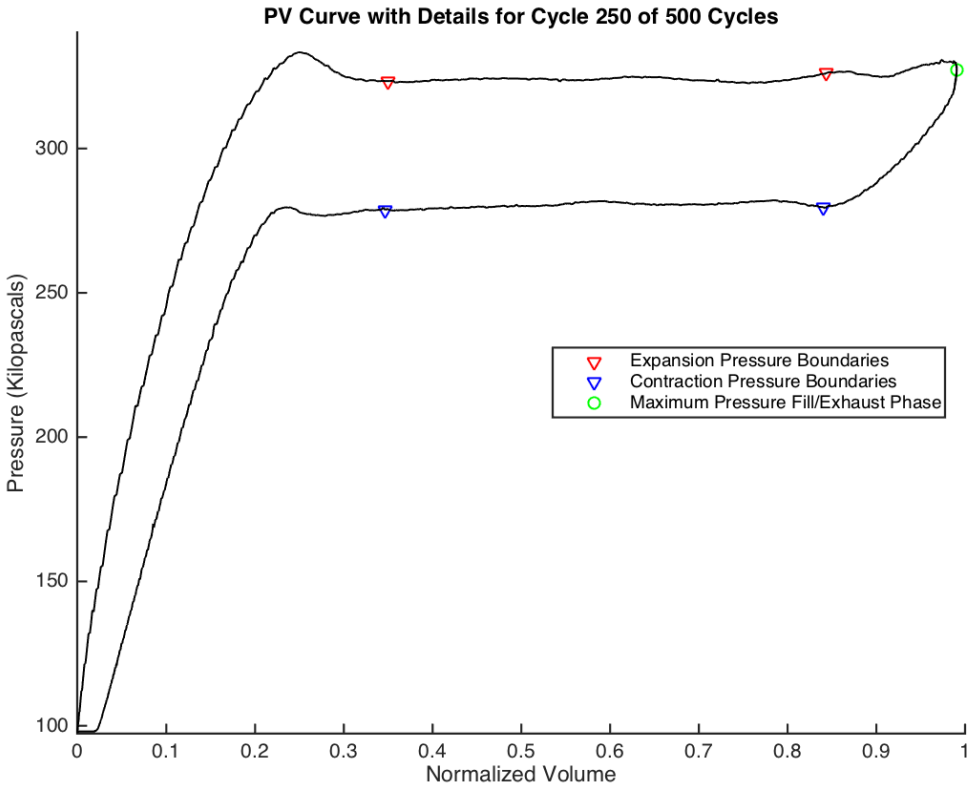

Figure 4.9: Points on P-V curve used to determine expansion, contraction, and maximum pressures

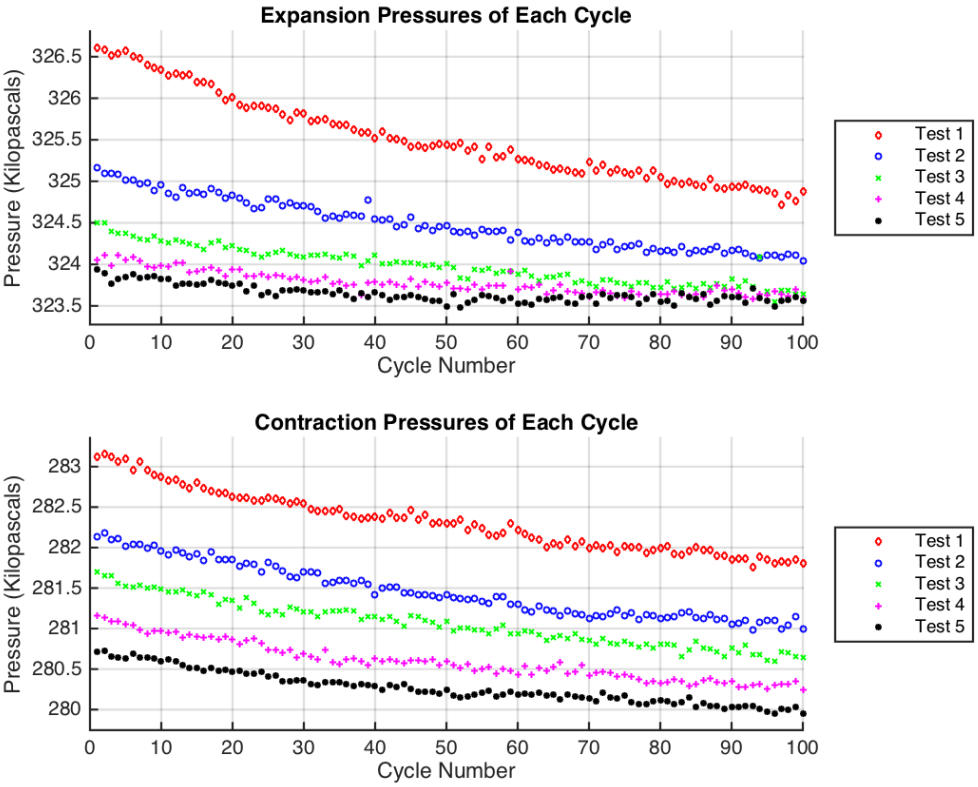

Figure 4.10: Expansion (top) and contraction (bottom) pressures for five, 100 cycle trials

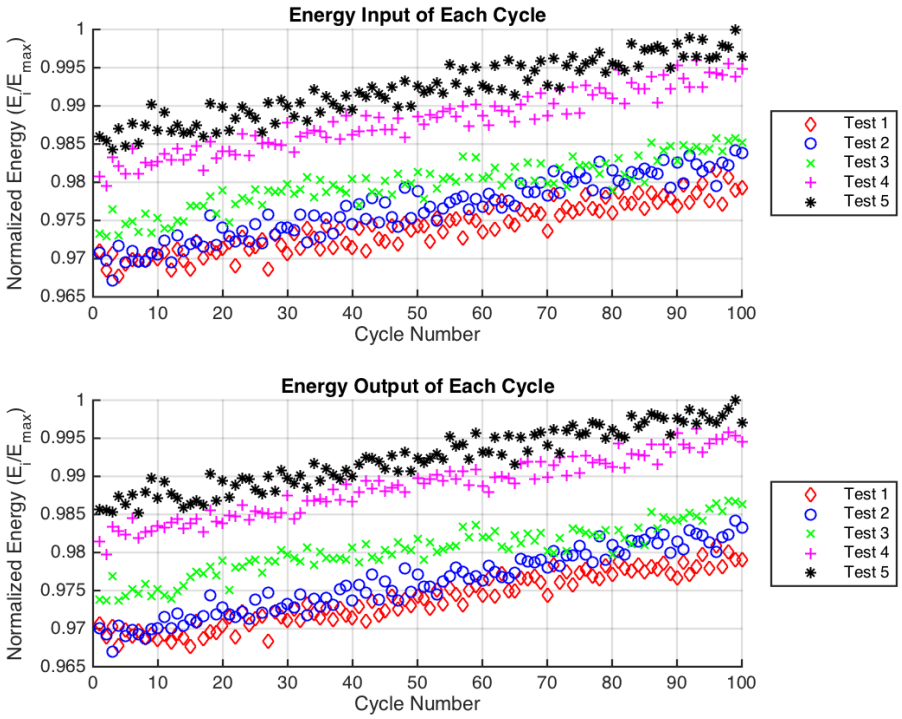

Figure 4.11: Energy into pSEA (top) and energy out of pSEA (bottom)

In Figure 4.11 the energy input to and returned by the pSEA are shown. This is done to give an idea of the order of magnitude of energy storage of a pSEA of this size. Figure 4.11 along with the expansion and contraction pressures in Figure 4.10 exhibit several of the advantageous properties of rubber. The general trend of the energy in/out is that over time the accumulator stores and returns more energy which is reflected in the higher efficiency numbers over time as noted earlier. The increase in energy and efficiency can be attributed to two primary factors. The first is that, as seen in Figure 4.10, the expansion and contraction pressures decrease over time requiring less energy to stretch the pSEA. This can be attributed to the decrease in hysteresis over time as is established and discussed in the literature. As the pSEA transitions from warm up to steady state operation and the rubber softens the pSEA stretches farther axially during steady state. This behavior resulted in the end of the pSEA hitting the bump stop at the end of the shroud leading to a slight increase in pressure, thus resulting in an increase in overall energy stored and ultimately higher component efficiency.

One difference between Figure 4.11 and Figure 4.10 is that the energy in/out appears to be constantly increasing whereas the expansion and contraction pressures appear to be asymptotically approaching a steady state value. When either the first 25 warmup cycles are included or the 500 cycle plots are considered, the energy plots also appear to be asymptotically approaching a steady state value. The asymptotic value for the expansion and contraction pressures is indicated numerically by the decreasing correlation between the values. As the data approaches its steady state value it no longer has a trend but rather a scatter about its mean value and is more pronounced in later trials. Finally, the recovery period is observed in both the energy and pressure plots as the initial value of the later trials is lower than the final value of the previous trials. This behavior indicates that starting and stopping the pSEA, as might occur in application, will decrease its efficiency and impact the other performance metrics including pressure and volume.

4.4 Key Performance Parameters Uncertainty Analysis

When trends in the data occurred, such as those observed in the expansion and contraction pressures, a linear regression analysis was performed and the resulting coefficient of determination, or R^2 values and standard error of regression ($S_{Y|x}$) values were determined. The R^2 values indicate the degree to which the linear regression equation fits the data and $S_{Y|x}$ is the conditional standard deviation of the regression or the standard error of regression.

$$E(Y \mid x) = b_0 + b_1 x \tag{6}$$

$$R^2 = \frac{\sum_{i=1}^{n} (\hat{y}_i - \bar{y})^2}{\sum_{i=1}^{n} (y_i - \bar{y})^2} \tag{7}$$

$$S_{Y|x} = \left[\frac{1}{n-2} \sum_{i=1}^{n} (y_i - \hat{y}_i)^2 \right]^{1/2} \tag{8}$$

where $E(Y \mid x)$ is the expected value of the variable of interest, Y, for a given value of x and b_0 and b_1 are the regression coefficients representing the intercept and slope respectively. In Eqs. 7 and 8, y_i is the experimentally measured value, $\hat{y}_i$ is the expected value determined by using the regression equation and $\bar{y}$ is the mean value of y. Once a linear regression is performed the 95 % confidence interval for the predicted values can be found using linear regression techniques with ± two standard errors of regression as outlined by Haldar and Mahadevan 2000.

The 95 % confidence interval of the predicted values provides a range of the values to be expected in future experiments based on analysis of the current results. Unlike the component cycle efficiency, the expansion and contraction pressures do exhibit trends in the data so a subsequent linear regression analysis is carried out with the resulting coefficient of determination, R^2, and standard error of regression, $S_{Y|x}$, values listed in Table 4-2.

Table 4-2: Linear Regression Analysis: Coefficient of Determination (R^2) and Standard Error of Regression ($S_{Y|x}$) for expansion and contraction pressures

Strain Energy Accumulator Experimental Pressures				
Trial	Expansion		Contraction	
	R^2	$S_{Y\|x}$ (kPa)	R^2	$S_{Y\|x}$ (kPa)
1	0.948	0.1176	0.952	0.0812
2	0.951	0.0673	0.944	0.0794
3	0.906	0.0680	0.960	0.0567
4	0.806	0.0603	0.920	0.0673
5	0.584	0.0656	0.928	0.0541

The corresponding 95 % confidence prediction interval using trial five R^2 values, can be seen in Figure 4.12.

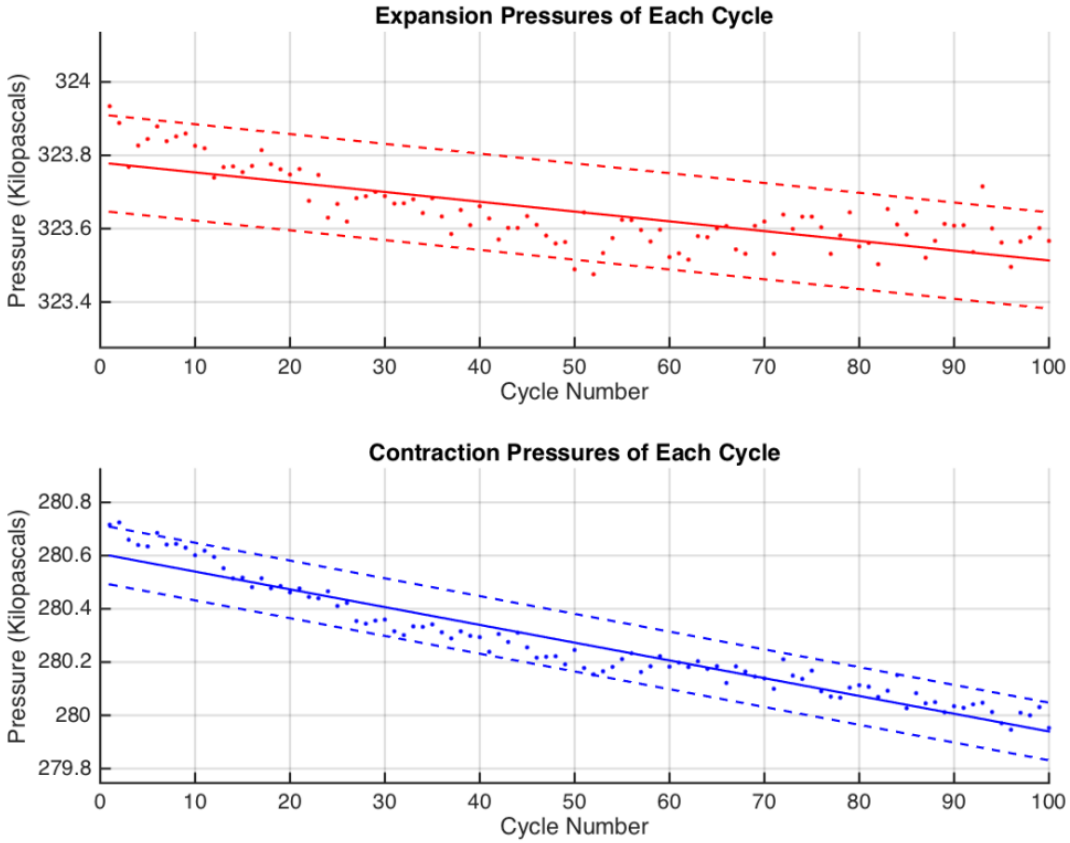

Figure 4.12: 95 % confidence interval of trial five expansion and contraction pressures

It is once again observed that the variance is minimal similar to the efficiency with the variance of the 95 % confidence interval of the expansion pressure at approximately 0.5 kPa and less than 1 kPa for the contraction pressure.

5 Conclusions and Future Work

At the commencement of the study three primary objectives were identified. The first was to develop a generally applicable model-based efficiency estimate as an integrated performance metric to the system efficiency. Starting with a simple energy balance, a model-based equation for the efficiency of the pSEA component was developed and is given in Eq. 3. This general model-based methodology enables individual component efficiency to be an integrated performance metric to system efficiency for both pneumatic and strain energy systems.

The next objective was to experimentally measure the key performance parameters of the pSEA including component efficiency, and expansion and contraction pressures specific to the system being studied herein. Key performance parameters of the pSEA including component efficiency, and expansion and contraction pressures for the specific system of interest were experimentally measured. The pSEA steady state component efficiency was experimentally determined to be consistently over 93 % and the expansion and contraction pressures were also found to asymptotically approach steady state values of 323.5 kPa and 280 kPa respectively.

The final objective was to perform uncertainty analysis of the component performance parameters to identify sources of uncertainty and make uncertainty propagation an integral part of system efficiency measurements. Mean value of the component steady state efficiency was found to have a maximum standard deviation of less than 0.1 %. Expansion and contraction pressure linear regression analysis was fit with 95 % confidence bounds and were found to have narrow confidence bounds with minimal standard errors of regression. Having obtained all three objectives, the component model, performance metrics and uncertainty analysis, enables development and testing of a system model with corresponding performance metrics using an integrated approach. With the pneumatic sector of the fluid power industry averaging only 15 % efficiency, introducing the pSEA having a 93 % efficiency into existing fluid power systems has the potential to substantially impact pneumatic systems efficiency.

Acknowledgements

This work was supported by the Center for Compact and Efficient Fluid Power, an NSF Engineering Research Center, grant EEC-0540834. The authors would like to thank SMC Corporation for their donation of equipment to improve the experimental test setup, shown in the experimental setup section, for the system efficiency testing currently underway and discussed in the future work section. Finally the authors would like to thank Dr. Janette Meyer for her review of the manuscript in preparation for submission to the journal.

References

[1] ASTM D4482-11 – Standard Test Method for Rubber Property – Extension Cycling Fatigue, 2011.

[2] Boes, M.K., Islam, M., Li, D., Hsiao-Wecksler, E.T., 2013. Fuel Efficiency of a Portable Powered Ankle-Foot Orthosis. Proceedings of the IEEE 13th International Conference on Rehabilitation Robotics (ICORR 2013). June 24th-26th Seattle, WA, USA.

[3] Cadwell, S.M., Merrill, R.A., Sloman, C.M. and Yost, F.L., 1940. Dynamic Fatigue Life of Rubber. Industrial and Engineering Chemistry 12, 19-23.

[4] Cummins, J.J., Barth, E.J., Adams, D.E., 2015. Modeling of a Pneumatic Strain Energy Accumulator for Variable System Configurations with Quantified Projections of Energy Efficiency Increases. Proceedings of the 2015 Bath/ASME Symposium on Fluid Power and Motion Control. Oct 14th Chicago, IL, USA.

[5] de Giorgi, R., Kobbi, N., Sesmat, S., and Bideaux, E., 2008. Thermal Model of a Tank for Simulation and Mass Flow Rate Characterization Purposes. Proceedings of the 7th JFPS International Symposium on Fluid Power. September 15th-18th Toyama, JA.

[6] Dick, J.S., 2009. Rubber Technology Compounding and Testing for Performance. 2nd ed. Cincinnati, OH: Hanser Publications.

[7] Gent, A.N., 1978. Rubber Elasticity: Basic Concepts and Behavior. In: F.R. Eirich, ed. Science and Technology of Rubber 3rd ed. New York, NY: Academic Press.

[8] Gent, A.N., 2005, Elastic Instabilities in Rubber. International Journal of Non-Linear Mechanics 40, 165-175.

[9] Haldar, A. and Mahadevan, S., 2000. Probability, Reliability and Statistical Methods in Engineering Design New York, NY: John Wiley and Sons Inc.

[10] Harris, P., O'Donnell G.E. and Whelan T., 2012. Energy Efficiency in Pneumatic Production Systems: State of the Art and Future Directions. Proceedings of the 19th CIRP International Conference on Life Cycle Engineering. May 23rd-25th Berkeley, CA, USA.
[11] "Highway Vehicles – Hydraulic Hybrid Passenger Vehicle (Test Bed 3)." Center for Compact and Efficient Fluid Power. Web. 28 Apr. 2015.
[12] Igarashi, K., Kawashima, K. and Kagawa, T., 2007. Development of Simultaneous Measurement System for Instantaneous Density, Viscosity and Flow Rate of Gases. Sensors and Actuators A 140, 1-7.
[13] Love, L.J., Lanke, E., Alles, P., 2012. Estimating the Impact (Energy, Emissions and Economics) of the U.S. Fluid Power Industry. Oak Ridge National Laboratory, Oak Ridge, TN.
[14] McFarland, J. M., and Mahadevan, S., 2008. Multivariate Significance Testing and Model Calibration under Uncertainty. Computer Methods in Applied Mechanics and Engineering, 197, 2467-2479.
[15] Mullins, L., 1948. Effect of Stretching on the Properties of Rubber. Rubber Chemistry and Technology 21, 281-300.
[16] Pedchenko, A., Barth, E.J., 2009. Design and Validation of a High Energy Density Elastic Accumulator Using Polyurethane. Proceedings of the ASME Dynamic Systems and Control Conference, Oct 12th-14th Hollywood, CA: 283-290.
[17] Tucker, J., 2012. Design and Experimental Evaluation of a High Energy Density Elastomeric Strain Energy Accumulator Thesis (MS). Vanderbilt University.

CHAPTER 5

ENERGY CONSERVATION IN INDUSTRIAL PNEUMATICS: A STATE MODEL FOR PREDICTING ENERGETIC SAVINGS USING A NOVEL PNEUMATIC STRAIN ENERGY ACCUMULATOR

Joshua J Cummins, Christopher Nash, Seth Thomas, Aaron Justice
Sankaran Mahadevan, Eric J Barth and Douglas E Adams

Department of Mechanical Engineering
Vanderbilt University
Nashville, TN

Submitted (In Review) for Publication to the Journal of Applied Energy March, 2016

Abstract

A number of national organizations have recently expressed interest in research to develop materials and devices that achieve greater energy storage capacity, power density and increased energy efficiency on the heels of a report finding that the pneumatic sector of the fluid power industry averages only 15 % efficiency. One way of improving efficiency is the use of energy storage and recycling devices. The pneumatic Strain Energy Accumulator is a recently developed device that recycles exhaust gas from one pneumatic component, stores it in a highly efficient process, and reuses the stored exhaust gas at a constant pressure to power another pneumatic component. This work analyzes system efficiency increases directly attributable to the implementation of a pneumatic strain energy accumulator by applying an analytical methodology for system level efficiency improvement calculations, experimental validation, and energy savings projections. Experimentally determined efficiency increases ranged between 31 % and 60 %, demonstrating that the pneumatic strain energy accumulator can be a viable part of the solution to the fluid power efficiency challenge.

1 Introduction

A report published in 2012 by Oak Ridge National Labs (ORNL), in conjunction with the National Fluid Power Association (NFPA), revealed that the operations in the fluid power industry are only 22 % efficient [1]. The pneumatic sector of the fluid power industry was found to be even worse averaging just 15 % efficiency. One technology that has been developed to improve the efficiency of the fluid power industry is the strain energy accumulator (SEA) [2]-[5].

The pneumatic version of the SEA, or the pSEA, is an energy storage device, consisting of an expandable rubber bladder inside of a rigid shroud that utilizes the hyperelastic behavior of rubber to store energy in the form of strain energy of the stretched rubber material and pressure energy of the stored compressed gas within the material as shown in Figure 5.1. The pSEA reclaims exhaust gas from pneumatic cylinders at an initial constant expansion pressure (P_{exp}), temporarily stores the exhaust gas and its accompanying energy and then recycles it at a lower constant contraction pressure (P_{con}) at a later point in time in a highly efficient process [6].

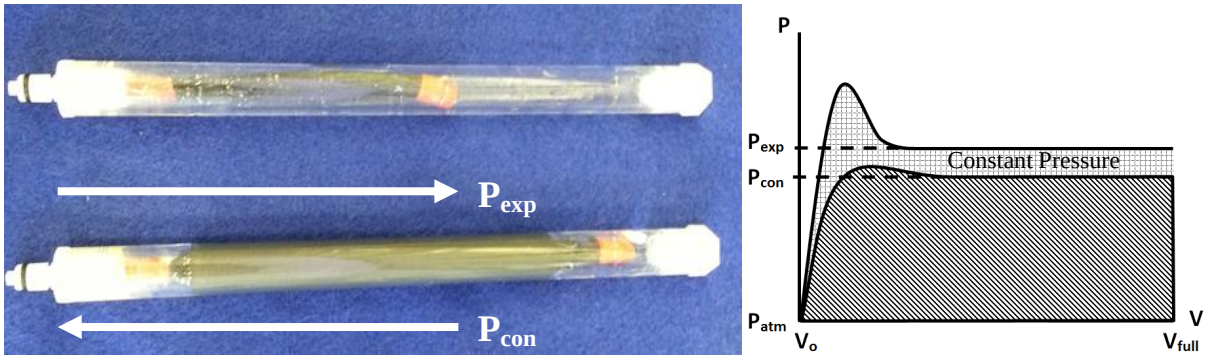

Figure 5.1: (left) Empty pSEA on top and filled pSEA on bottom; and (right) PV curve of pSEA with expansion pressure P_{exp}, contraction pressure P_{con}, and constant pressure region

Compressed air energy storage (CAES) is an active area of research. Ibrahim *et al.* [7] evaluated several types of energy storage methods, including CAES and small-scale CAES (SSCAES), in areas such as high cycle rates and energy storage capacity to meet the growing energy storage needs in managing renewable energy but did not perform an in-depth study on any one energy storage method. Raju and Khaitan [8] developed a dynamic simulation model for large scale CAES inside of caverns using mass and energy balance methods of a large scale system with a rigid boundary. Luo *et al.* [9] investigated how system efficiency is affected by component performance and parameters to help achieve higher efficiencies in adiabatic CAES systems and Zhao *et al.* [10] studied the impact of different discharge modes on CAES efficiency. Each of the modeling efforts focused on large scale compressed air storage and dynamic models which often breakdown with changes in assumptions or are difficult to implement in small scale highly transient systems.

A common source of energy loss in compressed air storage is through heat generation resulting from continuous pressure increases. Several methods to overcome heat loss have been developed and studied including the use of hybrid liquid air CAES systems [11],[12] that require long storage times for acceptable efficiencies, and the used of packed bed thermal energy storage [13],[14] which do not solve the heat generation problem but increase system complexity in an effort to mitigate heat losses. Kim *et al.* [15] developed and characterized a constant-pressure hydro CAES system to improve storage efficiency. A number studies look at the economics [16], configurations [17], performance and cost [18], role [19], market [20], and optimal operation [21] of CAES systems to estimate their impact on energy demands. While each of these studies investigated various elements of increasing efficiency on a large scale and/or the economic impact of compressed air energy storage, none combined small scale energy storage that minimizes energy loss through mechanical material properties while developing models that are used to make economic projections at both the local and national levels.

Saadat *et al.* [22] proposed and modelled an open accumulator CAES system with simulation results. Van de Ven [23] introduced a constant hydraulic pressure non-constant gas pressure energy storage hydraulic accumulator. Bing *et al.* [24] studied the efficiency increase of a hydraulic elevator applied system using a hydraulic accumulator. Finally, Harris *et al.* [25] reviewed existing industrial pneumatic efficiency increase approaches and identified the need for model-based performance metrics quantify and improve the efficiency of pneumatic systems. Even though each of these studies most closely aligns with the use of accumulators and evaluation of efficiency increase methods in pneumatics, again none combine a small scale fully pneumatic constant pressure device with simple models and energy savings projections. The gaps identified in the literature that the current work addresses, thus introducing the novelty of the work, are that the pSEA is a small-scale fully pneumatic compressed air energy storage device that operates at a constant pressure with first principles model-based performance metrics delivering experimentally validated efficiency increase projections used for energy saving projections at the local and national levels.

An application using the pSEA that serves as a motivation for the current work is the Ankle Foot Orthosis (AFO) stroke rehabilitation device (Boes *et al.* [26]). The AFO uses a rotary actuator powered by a compressed gas supply that helps raise and lower a patient's foot during rehabilitation. Similar to industrial applications, the AFO desires to minimize compressed air usage by maximizing efficiency so a patient can carry as small of a portable compressed air supply tank as possible.

During multiple trials, while changing several system parameters simultaneously, efficiency increase estimates ranging from 25 % to 75 % when using the pSEA on the AFO were reported when compared to the AFO without the pSEA. With no way to directly identify the efficiency increase attributable to the pSEA, a need to quantify the pSEAs impact is needed. This need has led to the development of a lumped parameter state model to estimate system level efficiency improvements. The ultimate goal for the current research is to accurately define efficiency increase limits that can be realized for various systems while using the pSEA and make energy savings projections based on currently available data.

One such source of available industry data is the aforementioned 2012 ORNL fluid power efficiency report. According to the ORNL report, there are over 200,000 industrial facilities in the United States that use compressed air. One tenth of all industrial energy consumption goes towards powering industrial air compressors. In some sectors, like chemical manufacturing, industrial air compressors account for over twenty percent of energy consumption. In aggregate, this amounts to 150 billion kilowatt hours ($10 billion) of electricity each year.

According to the US Department of Energy, three fourths of the total life cycle cost (capital expenditure, maintenance, and operations) of an industrial air compressor goes towards electricity. Manufacturing and material handling facilities are the biggest users of compressed air. Because of this, these end users stand to gain the most from decreased compressor demand resulting from increased pneumatic efficiency. Pneumatic technology has remained essentially unchanged for over fifty years. With rising energy costs and intense competition from international firms, companies are now more conscious of controlling costs than ever before.

2 Pneumatic System State Efficiency

Prior to conducting efficiency experiments, system level efficiency models were developed in Cummins *et al.* [27]. The purely analytical approach is presented first, followed by the practical applied model used to compare the experimental results. The analytical model lays the

foundation for the applied model which in turn will help define the efficiency increase limits and determine the efficiency increases directly attributable to the pSEA.

2.1 Pneumatic System State Efficiency: Analytical Model and Baseline Systems

Figure 5.2 shows a two cylinder pneumatic system with a pSEA. During operation the exhaust from the primary cylinder is reclaimed by the accumulator, stored, and then recycled at a later point in time to serve as the supply for the secondary cylinder.

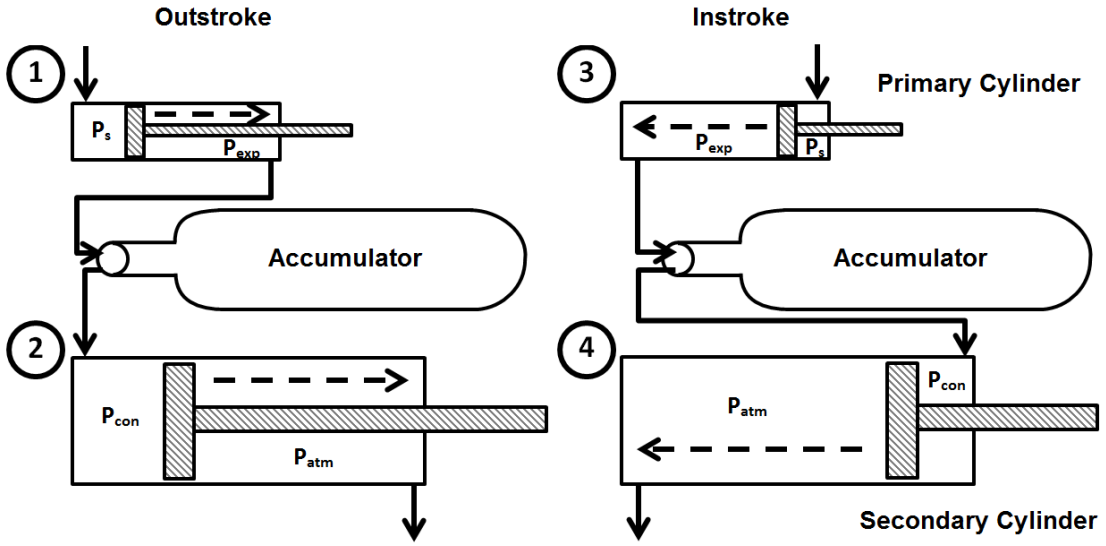

Figure 5.2: Two cylinder system with pSEA test configuration model

The system shown in Figure 5.2 has two cylinders of differing sizes operating such that for every out/instroke of the primary cylinder there is an accompanying out/instroke of the secondary cylinder, resulting in a stroke ratio of 1:1. The limitation of this model is that it assumes a 1:1 ratio is possible which for cylinders with too great of a volume difference, a complete stroke of the secondary cylinder may not be possible. As the model is developed further, and applied to experimental configurations, stroke ratios other than 1:1 will be used.

In order to compare the efficiency improvements directly attributable to the pSEA, baseline compressed air consumption of a system that does not use a pSEA is measured and serves as the foundation upon which efficiency increases are determined on a cycle by cycle basis. One complete cycle consists of an outstroke followed by an instroke, of both cylinders. In the derivation to follow, the baseline system without a pSEA assumes that the secondary cylinder supply has been regulated down to the pSEA contraction pressure. This represents a partially regulated system. This assumption introduces the ability to adjust the model for systems that employ existing energy efficiency methods by regulating down cylinder pressures with pressure regulators.

Three baseline systems will be used for comparison: an unregulated, partially regulated and fully regulated system. An unregulated system uses no pressure regulators in the system and uses supply air at whatever pressure the air is supplied to the system. A partially regulated system uses a single pressure regulator on one of the cylinders in the pair and partially reduces exhaust gas waste. The unregulated and partially regulated systems represent the most common configurations found in industrial facilities. While less common in practice, a fully regulated

system uses pressure regulators on both cylinders reducing exhaust gas waste for each. The fully regulated system is an equivalent work output system to one that uses a pSEA since all cylinders experience the same change in pressure across the cylinder. Comparison to a fully regulated system enables a comparison with current energy saving techniques and is the third baseline system that is used as a comparison to determine efficiency increases for systems that use a pSEA.

Energy is accounted for in each of the states of the system shown in Figure 5.2. Ideal gas behavior is assumed for the entire operating range of the system, an assumption that is also implemented by the flow meter in performing the necessary flow calculations. The ideal gas law is rearranged to solve for mass as follows:

$$m_i = \frac{P_i V_i}{RT} \tag{1}$$

where m_i is the mass at the respective state, P_i is the pressure, V_i is the volume, R is the ideal gas constant of air and T is the temperature of air. Only the mass is accounted for since it is conserved at each state as both the pressure and volume are allowed to change from one state to the next.

At this point a relationship between the two volumes of the cylinders is introduced where α is the ratio between the volume of the primary cylinder, V_1, and the volume of the secondary cylinder, V_2:

$$V_2 = \alpha V_1. \tag{2}$$

By substituting Eq. 2 into Eq. 1 and summing the mass introduced at each stage of the cycle, the following expressions are obtained for the system without a pSEA in line and for one that uses a pSEA:

$$m_{T\_w/o} = \sum_{i=1}^{4} m_{i\_w/o} = \frac{2V_1}{RT}\left(P_S + \alpha P_{con}\right) \tag{3}$$

$$m_{T\_w} = \sum_{i=1}^{4} m_{i\_w} = \frac{2V_1}{RT} P_S \tag{4}$$

where P_s and P_{con} are the supply pressure and pSEA contraction pressure, respectively, and the subscripts *T_w/o* and *T_w* indicate the total mass of air used from supply without the pSEA and with the pSEA, respectively. The complete derivation can be found in Cummins *et al.* 2015 [27].

A ratio of the total mass used by the system with the pSEA to that of the baseline system without the pSEA represents the model efficiency, η_{sys_ana}, and is given by:

$$\eta_{sys\_ana} = \frac{\sum m_{T\_w}}{\sum m_{T\_w/o}} \tag{5}$$

Substituting Eqs. 3 and 4 into Eq. 5 simplifies to the following:

$$\eta_{sys\_ana} = \frac{P_S}{P_S + \alpha P_{con}} \tag{6}$$

By subtracting η_{sys_ana} from 1 and converting it to percent, the analytical efficiency increase directly attributable to the pSEA is obtained:

$$\%Efficiency Increase = \left(1 - \eta_{sys\_ana}\right) \times 100 \tag{7}$$

To find the efficiency increase upper limit, P_{con} in η_{sys_ana} from Eq. 6 is replaced with P_S, the supply pressure, and the larger energy savings that can be realized in unregulated systems can be determined. Similarly, to find the efficiency increase lower limit for a fully regulated system, P_S in the denominator of Eq. 6 is replaced with P_{con}.

2.2 Pneumatic System State Efficiency: Applied Model

In the experimental application of the analytical model, the volume ratio is varied from one trial to the next, by interchanging a small, medium and large cylinder in the primary and secondary positions of the system shown in Figure 5.2. Doing so results in a number of practical implications to implementing the model presented in Subsection 2.1. The practical considerations impacting the model include:

1. pSEA length is limited to 91.5 cm as it is large enough to contain a single exhaust stroke of the large cylinder with the given geometry, and is representative of size constraints to be expected in application on actual machinery out in the field.
2. The expansion and contraction pressures of the pSEA are less than the supply pressure since the primary cylinder will perform work and experience losses in application.
3. The stroke ratio for the various cylinder combinations is determined experimentally using worst case volume stack up. This takes into account the reduced volume when the cylinder rod is fully retracted and occupying internal cylinder volume. The ratios are set so that during testing the accumulator:
    a. does not exhaust through a relief valve placed immediately before the pSEA
    b. on the last stroke of the secondary cylinder for each cycle, the accumulator is allowed to fully contract, dropping to a pressure slightly below the contraction pressure of the pSEA.
4. Each cylinder stroke results in the cylinder completing an entire stroke.
5. The number of complete total system cycles was limited so that the accumulator did not reach its maximum volume. Doing so would result in a pressure spike that would eliminate the constant pressure supply novelty of the pSEA.

Starting with Eq. 5 and applying the practical considerations above results in the following equation for the applied system efficiency, η_{sys_app}:

$$\eta_{sys\_app} = \frac{\sum_{i=1}^{p} m_{1i}}{\sum_{i=1}^{p} m_{1i} + \sum_{i=1}^{q} m_{2i}} \tag{8}$$

where p is the total number of strokes the primary cylinder undergoes, and q is the total number of strokes the secondary cylinder completes. The importance of Eq. 8, when compared to Eq. 5, is that it allows for any stroke ratio combination as it is a function of the summation of primary

and secondary cylinder strokes, making no assumption about the stroke ratio. The applied system efficiency increase is then determined by replacing η_{sys_ana} in Eq. 7 with η_{sys_app} to obtain:

$$\%EfficiencyIncrease = \left(1 - \eta_{sys\_app}\right) \times 100 \tag{9}$$

By substituting Eq. 1 into Eq. 8 for the given pressures and volumes at the respective system states, an applied efficiency increase model value is obtained that is used to compare with the experimental data. The experimentally measured mass values are substituted directly into Eq. 8 to produce an applied efficiency increase experimental value with which to compare the model values.

3 Pneumatic System Efficiency Experiments

Having developed the equations necessary to determine the efficiency increases of a system directly attributable to the pSEA, the experimental techniques used to validate these models and make energy savings projections is presented.

3.1 Experimental Setup

The experimental setup shown in Figure 5.3 consists of two pneumatic cylinders, a single pneumatic strain energy accumulator, Alicat M-series Mass Flow Meter (used to measure flow in standard litres per minute (SLPM)), throttle valve, SMC 3-way valve, two 0-10 bar pressure gages (used to monitor the accumulator pressure), supply pressure regulating valve (not pictured), accumulator overfill relief valve, electrical power supply and National Instruments (NI) data acquisition (DAQ) system. The pSEA tested in each series of tests consisted of a black rubber tube encased by a polycarbonate shroud. The pSEA dimensions are proprietary as the technology is currently involved in ongoing commercialization efforts; therefore, only the length dimension of the pSEA used for testing is provided.

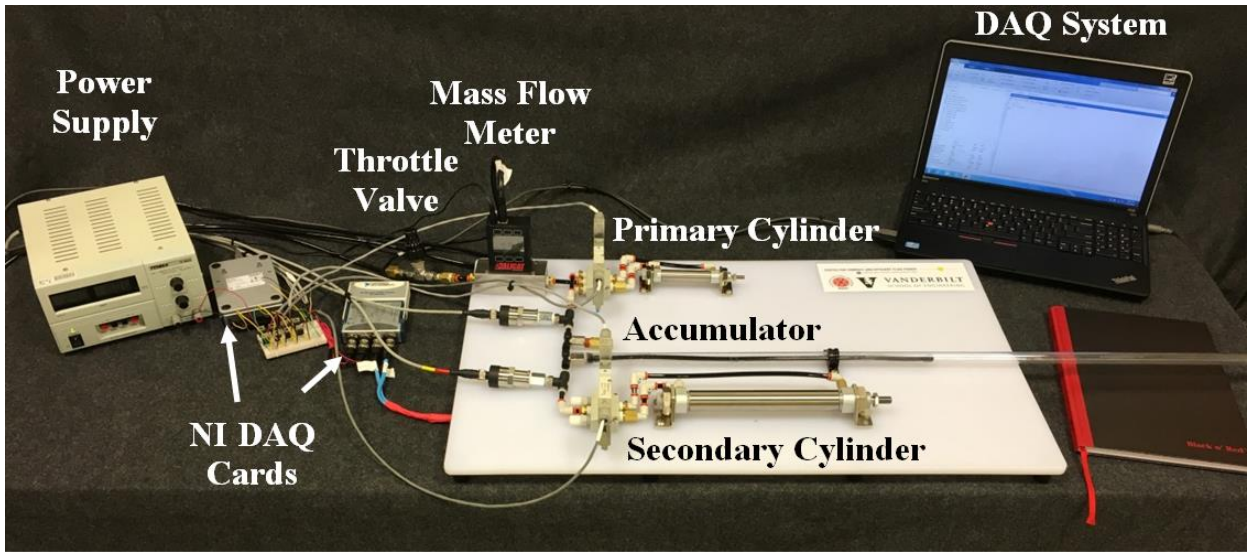

Figure 5.3: System with accumulator efficiency increase experimental test setup

Shop supply air (725 kPa) passed through the regulating valve where it was regulated down to approximately 500 kPa (denoted as P_s), which was subsequently connected to the throttle

valve just before the mass flow meter. The throttle valve was placed in line to limit the fill rate of the accumulator to prevent clipping of the mass flow meter. The downstream side of the mass flow meter was connected to the supply port of the externally piloted/actuated valve connected to the primary cylinder. This enabled the mass flow meter to measure all the air directly as it entered into the system. Two pressure gages were placed on either side of the pSEA to monitor the pressure of the accumulator and an accumulator overfill relief valve was placed just before the accumulator to exhaust the system if the accumulator reached its maximum volume. The pSEA was connected to a second externally piloted/actuated valve and served as the supply air, at the contraction pressure of the pSEA of 280 kPa, to the secondary cylinder. All pressures are absolute pressures.

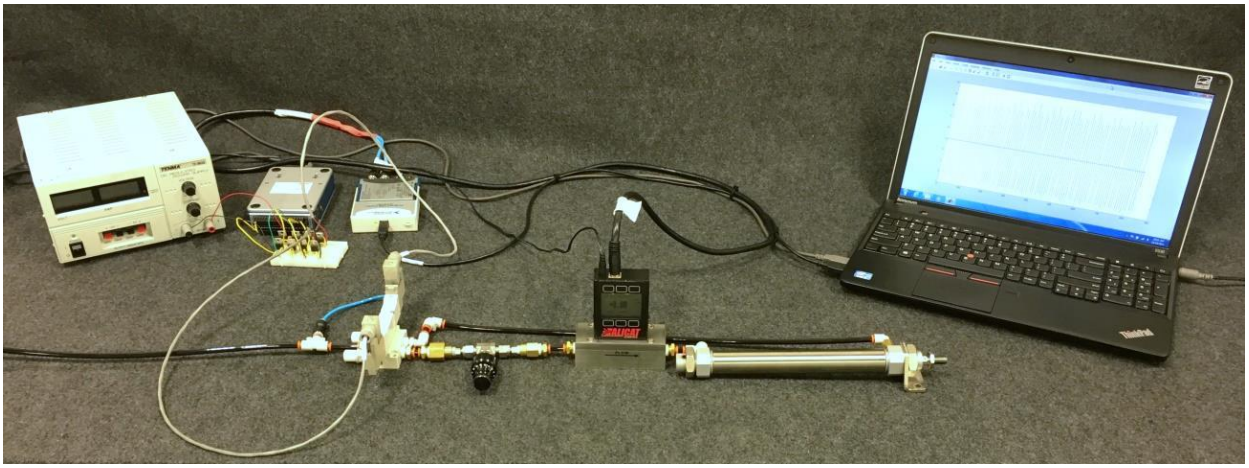

Figure 5.4: Cylinder mass flow calibration test configuration

Due to the highly transient nature of the efficiency tests and the challenges of obtaining accurate flow measurements of compressed air, which have been well documented by de Giorgi *et al.* 2008 [28] and Igarashi *et al.* 2007 [29], a series of calibration tests were conducted prior to individual cylinder or system testing. In the calibration test setup shown in Figure 5.4, the flow meter was connected to the outstroke cavity of the cylinder and the flow into the cylinder was measured. Knowing the volume, pressure and temperature of the cylinder, the theoretical mass of the cylinder is known. The measured mass value was then compared with the theoretical value and a calibration constant was calculated using a 100 cycle average for the each cylinder. Cylinders of three different sizes were used interchangeably in the primary and secondary positions and are referred to as small, medium and large. The bore and stroke dimensions along with the calibration constants of the three cylinders used in the tests are given in Table 5-1.

Table 5-1: Cylinder Dimensions and Calibration Constants

Cylinder	Bore (mm)	Stroke (mm)	Calibration Constant
Small	16	40	1.54
Medium	20	80	1.14
Large	25	160	0.71

In order to find the total mass used by a system without a pSEA, each individual cylinder was tested at supply pressures of 500 kPa and 280 kPa as shown in Figure 5.5.

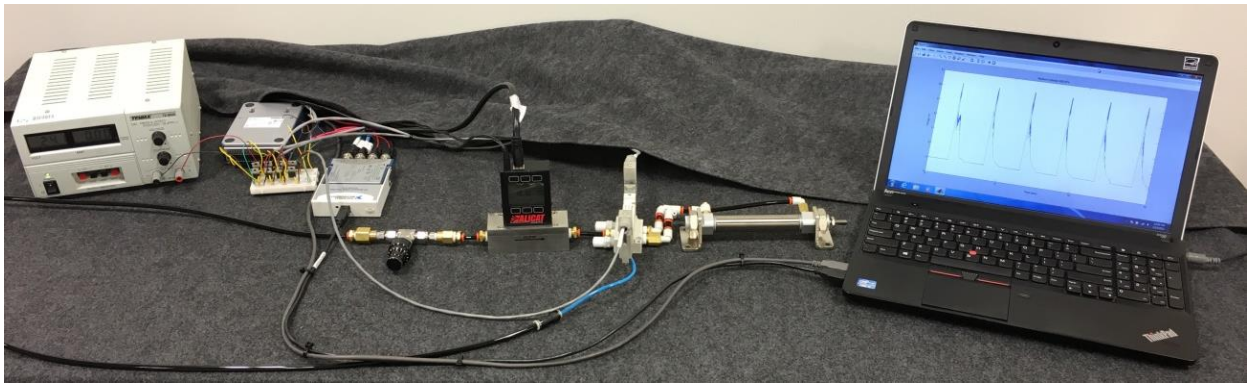

Figure 5.5: Individual Cylinder Consumption Test Setup

The flow meter was connected to the supply of the 3 way valve and 100 cycle averages were collected. The calibration factors for the respective cylinder sizes were applied and the average mass used on a single cycle, consisting of an outstroke and an instroke, of each cylinder was calculated. Collection of average cycle mass data at the two supply pressures provided the necessary data for any combination of cylinders and pressures needed for a system that does not use a pSEA that serves as the baseline to determine an efficiency increase for a system that uses a pSEA.

3.2 Experimental Data

In the system efficiency improvement experiments, the cylinder in the primary position determined the flow into the system. Consequently, the calibration factor for the primary cylinder was applied to the system flow data to improve the accuracy of the measurements. Taking into consideration the various volume and pressure combinations of the cylinders, the number of times a cylinder would need to fire to either fill or exhaust the accumulator varies. Applying worst case volume (cylinder volume less the volume of the cylinder rod) and pressure combinations, estimates for the stroke ratio were calculated and then experimentally confirmed. The ratio values used in collecting system efficiency improvement data are given in Table 5-2.

Table 5-2: Stroke/firing ratio of primary to secondary cylinder

Cylinder 1	Cylinder 2	Stroke Ratio
Small	Medium	2:1
Small	Large	5:1
Medium	Large	2:1
Medium	Medium	1:1 and 1:2
Medium	Small	1:3
Large	Small	1:8
Large	Medium	1:3 and 1:4

The first number in the ratio (x:y) indicates the number of primary cylinder strokes (x) and the second number indicates the number of secondary cylinder strokes (y). The system was run for 50 warmup cycles for each cylinder combination listed in Table 5-2 prior to data collection. The warmup period served to minimize the Mullin's effect and hysteresis during steady state operation.

Each stroke ratio in Table 5-2 was tested for the system with the pSEA and the efficiency increase was calculated for three system baseline configurations: unregulated, partially regulated and fully regulated. These three baseline systems are chosen because they are representative of actual systems encountered in application where total, partial or no pressure regulation is implemented. The total amount of mass used during operation was collected for each individual cylinder and then combined for the baseline system without the pSEA as outlined in the previous section. Total mass for the system with the pSEA was recorded at the supply of the primary cylinder for each test. In all system tests with the pSEA, the supply pressure to the primary cylinder was 500kPa.

In the unregulated baseline system, supply pressures of 500 kPa were used for both cylinders. In the case of the partially regulated system, in which the pressure of the secondary cylinder was regulated down to the contraction pressure of the pSEA, supply pressures of 500 kPa and 280 kPa were used for the primary and secondary cylinders respectively. The fully regulated system is when both cylinders perform the same amount of work and, therefore, experience the same change in pressure. In Cummins *et al.* [6] the expansion pressure of the pSEA was determined to be approximately 320 kPa. For the fully regulated system, having a supply pressure of 500 kPa and exhausting at 320 kPa, the net change in pressure for the primary cylinder in the system with the pSEA is 180 kPa. With the secondary cylinder operating at 280 kPa, and exhausting at 100 kPa, both cylinders experience a net pressure change of 180 kPa. Therefore, when compiling the individual cylinder data for the equivalent fully regulated baseline system, the 280 kPa total mass data is used for both the primary and secondary cylinders.

It is important to note that the unregulated and partially regulated systems are most representative of applied systems and offer the greatest opportunities in the field to realize energy savings with implementation of the pSEA. Application of the pSEA to these systems could be accomplished with relative ease and greatly improve their energy efficiency. A fully regulated system is most comparable to a system using a pSEA due to the fact that the two cylinders output the same work when comparing the two energy savings techniques; however, fully regulated systems are often not implemented in practice. As the results show below, all three systems show significant energy efficiency improvements when equipped with the pSEA.

The increased ratios for the medium to medium and large to medium cylinder combinations in Table 5-2 are the same systems run with an additional secondary cylinder stroke that started with a partially expanded accumulator at the constant contraction pressure supply condition and ended with the accumulator fully contracted and the final pressure of the accumulator dropping below the accumulator contraction pressure. This operating condition may not be allowable in certain applications but was included to show the potential for additional efficiency improvements if such operational environments are permissible. The results are presented in the next section.

4 Results and Discussion

4.1 Experimental System Efficiency Increases with Uncertainty Analysis

First, for the unregulated system, the pressure, volume and stroke ratio values for the test configurations listed in Table 5-2 were input into Eqs. 1, 8 and 9 to produce applied model efficiency increase projections. The experimentally measured mass flow for the same systems was input into Eqs. 8 and 9 to calculate the applied experimental efficiency increase values. The applied model and experimentally measured results from Eq. 9 are compared in Figure 5.6. The

results obtained from Eq. 9 and shown in Figure 5.6 are the efficiency increases as a percent increase for unregulated baseline systems. These efficiency increases are directly attributable to the pSEA.

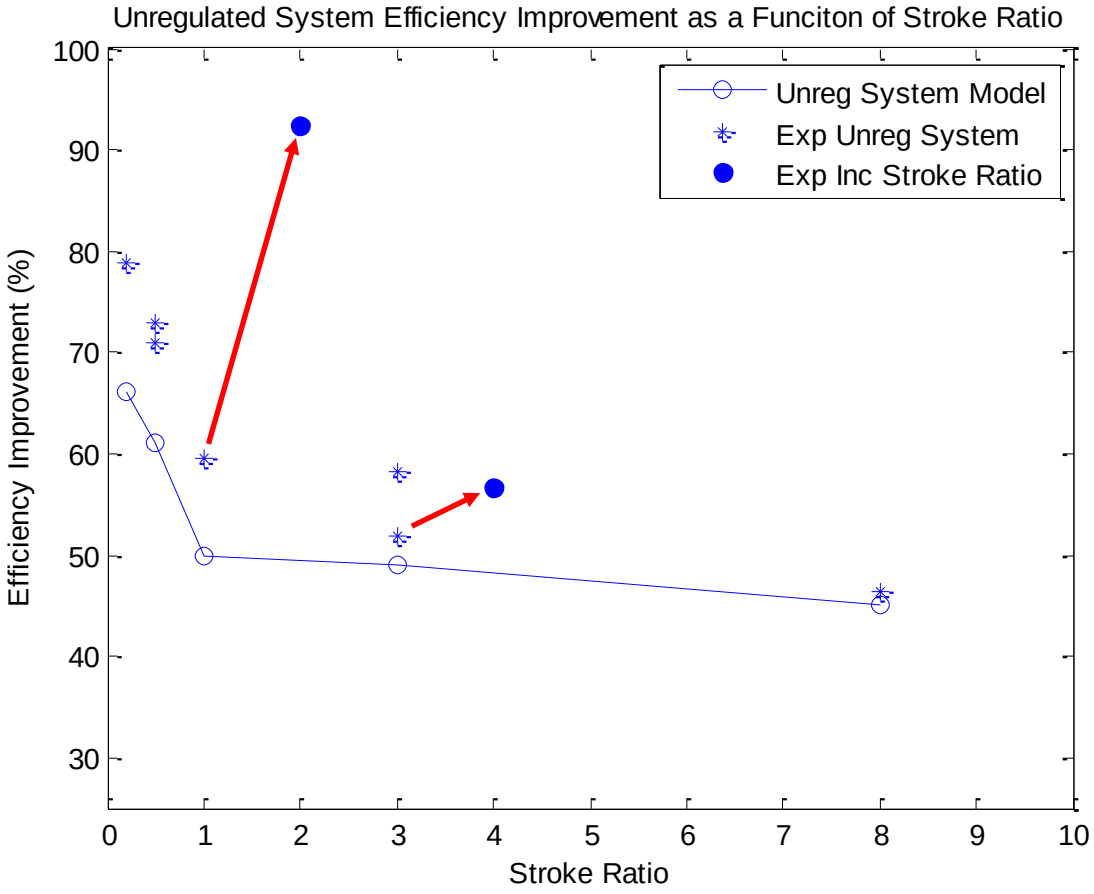

Figure 5.6: Unregulated system efficiency increase as a function of stroke ratio; red arrows indicate efficiency increase resulting from an increased stroke ratio by adding an additional stroke to the secondary cylinder

In Figure 5.6, a stroke ratio of greater than one indicates that the secondary cylinder fired more times than the primary cylinder. The increased stroke ratio data points as mentioned earlier, indicated by the bold markers, show the jump in efficiency (red arrows) that a system can experience if it is able to operate at a pressure below the contraction pressure of the pSEA. In the medium to medium and large to medium system tests an additional stroke of the secondary cylinder was added to each cycle, allowing the accumulator to fully contract and its supply pressure to the secondary cylinder to drop below the contraction pressure of the accumulator. In the large to medium case a slight increase in efficiency was noted; however, in the medium to medium case the efficiency increase jumps significantly to 89 %. This indicates that for a system using similar size cylinders, if it is allowable for the pressure to the secondary cylinder to drop to a pressure below the accumulator contraction pressure, substantially greater efficiency increases can be realized.

The standard deviation of the experimental efficiency increase resulting from mass flow measurement data and the associated error bars indicated that the variation of the flow measurements, and thus the aleatory uncertainty, was minimal. The largest source of flow measurement uncertainty likely comes from the epistemic uncertainty in the volume

approximations. The cylinder volume approximations were used to determine an experimental mass flow calibration constant. The uncertainty is greater for the smaller cylinders and smaller for the larger cylinders. Trends in the error with cylinder size are observed in the data in Figure 5.6.

Greater differences are observed between experimental efficiency increase and model prediction for the systems with a smaller primary cylinder. This is expected for two reasons; first, the uncertainty in the volume for the small cylinder is a larger percentage of the total volume, resulting in greater error in the experimental efficiency increase and larger deviation from the model prediction. The converse is true for large cylinders; the uncertainty in the volume approximation is a smaller portion of the total volume resulting in less error in the experimental efficiency increase and smaller variations from the model prediction.

A second reason the larger cylinders are expected to have less error in the mass flow measurement is that the flow conditions are closer to steady state, where the flow meters measurement is most accurate, than they are for the smaller cylinders. The flow in the smaller cylinders tends to be more transient, which introduces more error through uncertainty in the flow measurement. The greater error due to uncertainty with smaller cylinder size is observed at every point in Figure 5.6.

Starting on the left and working right, the small to large cylinder system, where the small cylinder dictated flow measurement, experiences the largest error from the model prediction. The next stroke ratio was small to medium and medium to large. The small to medium combination exhibits more error than the medium to large. Next the medium to medium experiences a similar error as the medium to large. Subsequently, medium to small and large to small have the same stroke ratio yet the medium to small experiences greater error than large to medium while large to medium approaches the model prediction. Finally the large to small experiences the least error and is closest to the model prediction.

Where the applied model predicted the same efficiency increase for the same stroke ratios, the experimental data yielded two slightly different efficiency increase numbers. With the volume uncertainty entering into the experimental data through the calibration constant, increasing error with decreasing cylinder size, it is expected that the two systems with the same stroke ratio having different cylinder size primary cylinders would exhibit different experimental efficiency increases. Therefore, it is expected that with improved volume estimates the experimental values would approach each other and converge on the model prediction.

The same results were compared for the partially regulated system as in the unregulated system and are given in Figure 5.7.

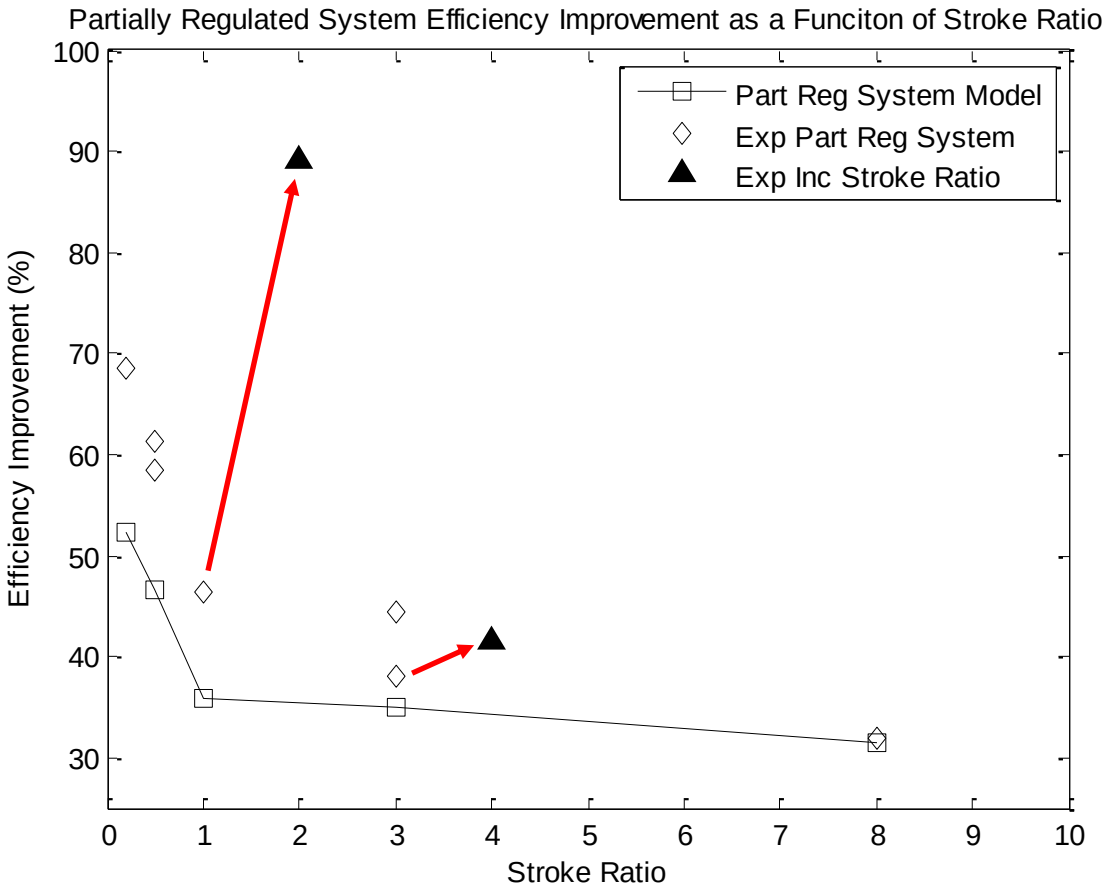

Figure 5.7: Partially regulated system efficiency increase as a function of actuation ratio; red arrows indicate efficiency increase resulting from an increased stroke ratio by adding an additional stroke to the secondary cylinder

The partially regulated system experiences lower efficiency increases than the unregulated system as expected. Regulated systems currently reduce energy waste by reducing the use of excessively pressurized air which is why unregulated system would be expected to see greater efficiency increases. In both the partially regulated and unregulated systems the model is conservative compared to the experimental results. A conservative baseline for energy savings projections is preferred since it does not over predict the savings that can be obtained by implementing the pSEA when building a business case when deciding whether or not to pursue developing the pSEA.

Efficiency increase results for the fully regulated, equal work, baseline system are shown in Figure 5.8.

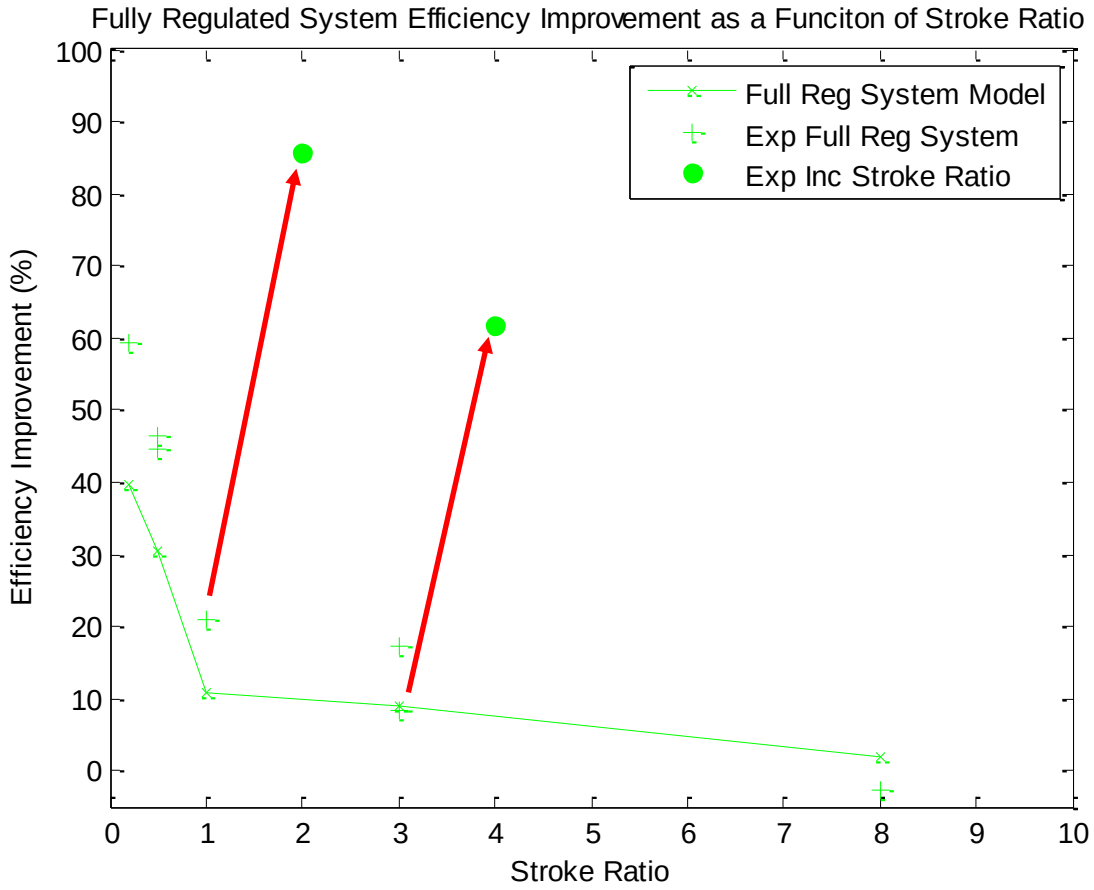

Figure 5.8: Fully regulated system efficiency increase as a function of actuation ratio; red arrows indicate efficiency increase resulting from an increased stroke ratio by adding an additional stroke to the secondary cylinder

The fully regulated system exhibits similar trends as the partially regulated and unregulated systems with a few differences. The first difference between the fully regulated system and the partially regulated and unregulated systems is a lower efficiency increase. This is expected as the fully regulated baseline system already utilizes pressure regulators that reduce pressure resulting in less exhaust waste. Another difference is that the large to small cylinder test condition with a stroke ratio of eight in Figure 5.8 shows a negative efficiency improvement while the model predicts a slight efficiency improvement. A negative efficiency improvement indicates that the pressure regulators would be more efficient in this condition; however the modeling error is too small to support such a claim. It would need to be investigated further to determine which approach is actually more efficient but the differences are expected to be negligible at high stroke ratios. Regardless of which energy saving approach is more efficient, the two are close enough that the use of the pSEA would be preferred. The pSEA offers the advantage of being able to regulate the net change in pressure of both cylinders and achieve similar energy efficiency with the use of a single accumulator where it would require two pressure regulators.

A final observation is that the increased stroke ratio for the fully regulated system results in a greater efficiency increase than either the partially regulated or unregulated systems. This result is expected as the fully regulated baseline system already implements energy saving pressure

regulators. The additional stroke is an additional energy savings technique the accumulator offers that pressure regulators are unable to offer.

All three sets of results, without the increased stroke ratio data points, are shown together in Figure 5.9 for comparison.

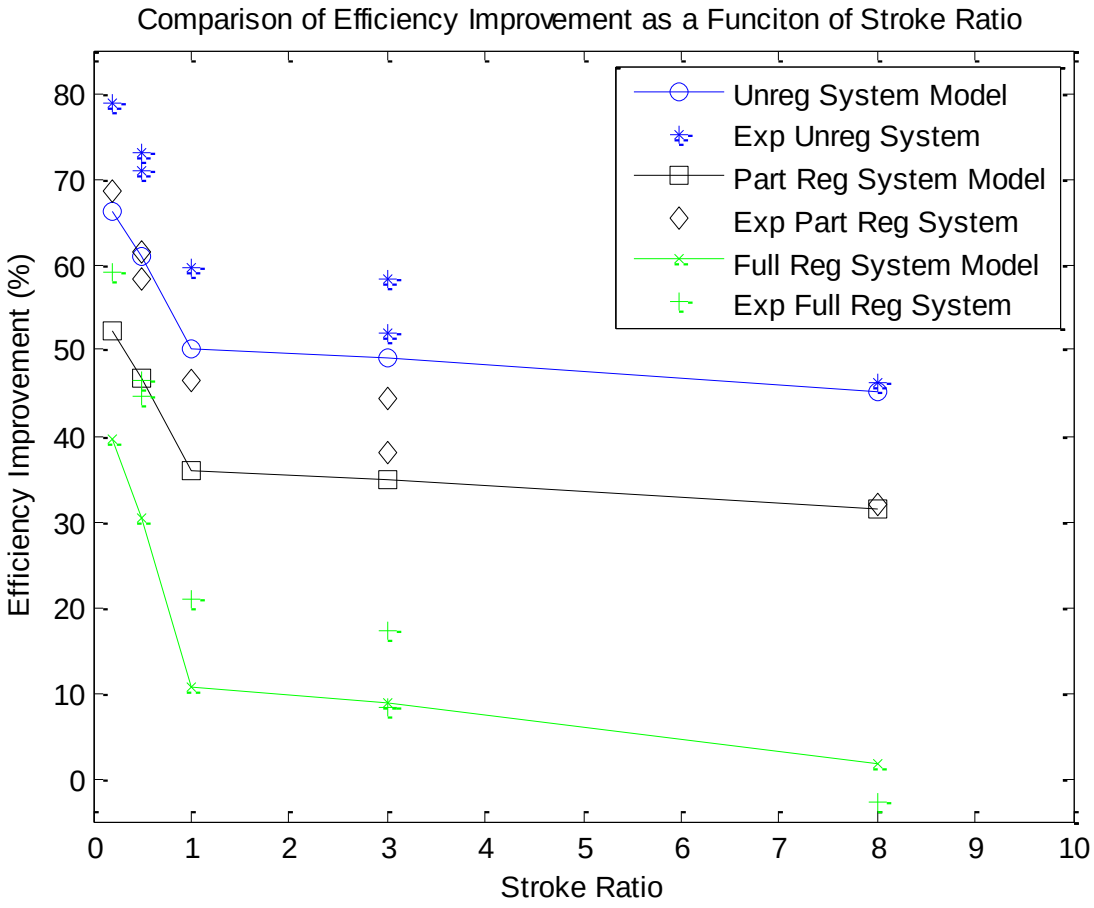

Figure 5.9: Comparison of regulated and unregulated systems model and experimental efficiency increases

The minimum and maximum numerical model and experimental results for the unregulated, partially regulated and fully regulated systems from Figure 5.9 are shown in Table 5-3.

Table 5-3: Efficiency improvement projections summary

Efficiency Improvement	Unregulated		Partially Regulated		Fully Regulated	
	Min (%)	Max (%)	Min (%)	Max (%)	Min (%)	Max (%)
Model	45.0	66.1	36.4	57.8	1.8	39.5
Experimental	47.0	78.8	41.9	76.0	-2.7	59.2

In all system configurations the greatest efficiency increases are seen when a smaller primary cylinder at a higher pressure powers a larger secondary cylinder at a lower pressure. At a stroke ratio of 1:1 the efficiency improvement returns start to level off as larger primary cylinders at a higher pressure power smaller secondary cylinders at a lower pressure. Considering systems that do not fully utilize pressure regulators, the minimum efficiency improvement for the system model is 31.4 % for a partially regulated system, and the maximum is 66.1 % for an unregulated

system. The experimental efficiency improvement values are higher and range from 31.9 % to 78.8 %. Even at the low end of the range, incorporation of the pSEA offers large improvements to an industry that currently averages just 15 % efficiency.

4.2 Energy Savings Projections

According to the US Department of Energy, from their compressed air challenge fact sheet number nine [30], "electricity costs are by far the largest expense of owning and operating a compressed air system." Many facilities are unaware of how much their compressed air systems actually cost to operate. The Department of Energy states that a single 100 horsepower air compressor can consume $50,000 in electricity each year. In using the Department of Energy's figures, with a conservative efficiency improvement of just 30% from the pSEA, would yield annual energy savings of $15,000 per compressor. This savings is realized by the compressor operating less frequently. An additional benefit is that less frequent operation would also result is a longer service life of the compressor. Facilities that use multiple, more powerful compressors would experience even greater savings. Such an increase in efficiency could reduce the total number of compressors required to meet system demand.

While Table 5-3 shows that some systems could experience substantially higher increases in efficiency, not all industrial users of compressed air will be able to integrate the pSEA into their pneumatic systems. This makes overall projections for aggregate energy savings less certain. But assuming that only ten percent of users could utilize the pSEA to increase their pneumatic system efficiency by 30%, the result would still be an aggregate energy savings in excess of $300 million in the US each year. The opportunity for such considerable cost reductions are welcome news in the face of slow industrial growth projections and increased international competition.

5 Conclusions and Future Work

A 2012 report by ORNL and NFPA on the efficiency of the fluid power industry revealed that the pneumatic division of the fluid power industry has an average efficiency of a mere 15 %. Motivated by such low efficiencies, the current work set out to: first, perform an accounting of the compressed air moving through the system; second, developed a model for applied systems that quantifies the efficiency increase directly attributable to the implementation of the pneumatic strain energy accumulator, an energy recovery, storage and recycling device; and finally, experimentally determine the efficiency increase of an applied system using a pSEA and compare that to the model predictions. In completing each of the aforementioned tasks, model predictions ranged from 31 % to 66 % efficiency increase and experimental increases ranged from 31 % to 78 %, rendering the model favorably conservative.

Starting with the conservative minimum model efficiency increase and making modest projections it is estimated that the pSEA has the potential to yield annual energy savings of $15,000 per compressor. Extrapolated out industry wide, the pSEA alone could result in industry wide annual savings in the US of $300 million. The next step will be to arrange case studies with industry partners and measure the actual energy used in a real system to see what the real energy savings turn out to be of the pSEA in an actual system, refining the model and energy savings projections as the body of knowledge around the pSEA expands. Once actual energy savings have been quantified the pSEA device will be one step closer to commercialization.

Acknowledgements

This work was supported by the Center for Compact and Efficient Fluid Power, an NSF Engineering Research Center, grant EEC-0540834. The authors would like to thank SMC Corporation for their equipment donation and Alicat Scientific for their technical support in using their M Series mass flow meter. Finally the authors would like to thank Dr. Janette Meyer for her review of the manuscript prior to submission to the journal.

References

[1] Love LJ, Lanke E and Alles P, 2012, "Estimating the Impact (Energy, Emissions and Economics) of the U.S. Fluid Power Industry." Oak Ridge National Laboratory, Oak Ridge, TN.

[2] Pedchenko A and Barth EJ, 2009, "Design and Validation of a High Energy Density Elastic Accumulator Using Polyurethane." *Proceedings of the ASME Dynamic Systems and Control Conference,* pp. 283-290.

[3] Pedchenko A, 2014, "Design and Finite Element Modeling of a High Energy Density Strain Energy Accumulator." *Master's thesis,* Vanderbilt University.

[4] Tucker J, 2012. "Design and Experimental Evaluation of a High Energy Density Elastomeric Strain Energy Accumulator." *Master's thesis.* Vanderbilt University.

[5] Tucker J and Barth EJ, 2013. "Design, Fabrication and Evaluation of a Distributed Piston Strain-Energy Accumulator." *International Journal of Fluid Power* 14(1), pp. 47-56.

[6] Cummins JJ, Thomas BS, Nash C, Mahadevan S, Barth EJ and Adams DE, 2016, "Experimental Evaluation of the Efficiency of a Pneumatic Strain Energy Accumulator." Submitted to *International Journal of Fluid Power,* Feb 26.

[7] Ibrahim H, Ilinca A and Perron J, 2008 "Energy Storage Systems – Characteristics and Comparisons." *Renewable and Sustainable Energy Reviews* 12 pp. 1221-50.

[8] Raju M and Khaitan SK, 2012 "Modeling and Simulation of Compressed Air Storage in Caverns: A Case Study of the Huntorf Plant." *Applied Energy* 89 pp. 474-81.

[9] Luo X, Wang J, Krupke C, Wang Y, Sheng Y, Li J, Yujie X, Wang D, Miao S and Chen H, 2016 "Modeling Study, Efficiency Analysis and Optimisation of Large-Scale Adiabatic Compressed Air Energy Storage Systems with Low-temperature Thermal Storage." *Applied Energy* 162 pp. 589-600.

[10] Zhao P, Gao L, Wang J and Dai Y, 2016 "Energy Efficiency Analysis and Off-design Analysis of Two Different Discharge Modes for Compressed Air Energy Storage System Using Axial Turbines." *Renewable Energy* 85 pp. 1164-77.

[11] Kantharaj B, Garvey S and Pimm A, 2015 "Compressed Air Energy Storage with Liquid Air Capacity Extension." *Applied Energy* 157 pp. 152-64.

[12] Pimm AJ, Garvey SD and Kantharaj B, 2015 "Economic Analysis of a Hybrid Energy Storage System Based on Liquid Air and Compressed Air." *Energy Storage* 4 pp. 24-35.

[13] Barbour E, Mignard D, Ding Y and Li Y, 2015 "Adiabatic Compressed Air Energy Storage with Packed Bed Thermal Energy Storage." *Applied Energy* 155 pp. 804-15.

[14] Chai L, Wang L, Liu J, Yang L, Chen H and Tan C, 2014 "Performance Study of a Packed Bed in a Closed Loop Thermal Energy Storage System." *Energy* 77 pp. 871-9.

[15] Kim YM, Shin DG and Favrat D, 2011 "Operating Characteristics of Constant-Pressure Compressed Air Energy Storage (CAES) System Combined with Pumped Hydro Storage Based on Energy and Exergy Analysis." *Energy* 36 pp. 6220-33.

[16] Madlener R and Latz J, 2013 “Economics of Centralized and Decentralized Compressed Air Energy Storage for Enhanced Grid Integration of Wind Power.” *Applied Energy* 101 pp. 299-309.
[17] Hartmann N, Vohringer O, Kruck C and Eltrop L, 2012 “Simulation and Analysis of Different Adiabatic Compressed Air Energy Storage Plant Configurations.” *Applied Energy* 93 pp. 541-8.
[18] Garvey SD, 2012 “The Dynamics of Integrated Compressed Air Renewable Energy Systems.” *Renewable Energy* 39 pp. 271-92.
[19] Lund H and Salgi G, 2009 “The Role of Compressed Air Energy Storage in Future Sustainable Energy Systems.” *Energy Conversion and Management* 50 pp. 1172-9.
[20] Swider DJ, 2007 “Compressed Air Energy Storage in an Electricity System with Significant Wind Power Generation.” *IEEE Transactions on Energy Conversion* 22 (1) pp. 95-102.
[21] Lund H, Salgi G, Elmegaard B and Andersen AN, 2009 “Optimal Operation Strategies of Compressed Air Energy Storage (CAES) on Electricity Spot Markets with Fluctuating Prices.” *Applied Thermal Engineering* 29 pp. 799-806.
[22] Saadat M, Shirazi FA and Li PY, 2015 “Modeling and Control of an Open Accumulator Compressed Air Energy Storage (CAES) System for Wind Turbines.” *Applied Energy* 137 pp. 603-16.
[23] Van de Ven JD, 2013 “Constant Pressure Hydraulic Energy Storage Through a Variable Area Piston Hydraulic Accumulator.” *Applied Energy* 105 pp. 262-70.
[24] Bing X, Jian Y and Huayong Y, 2005 “Comparison of Energy-saving on the Speed Control of the VVVF Hydraulic Elevator with and Without the Pressure Accumulator.” *Mechatronics* 15 pp. 1159-74.
[25] Harris P, O’Donnell GE and Whelan T, 2012 “Energy Efficiency in Pneumatic Production Systems: State of the Art and Future Directions.” *Proceedings of the 19th CIRP International Conference on Life Cycle Engineering,* Berkeley, CA pp. 363-8.
[26] Boes MK, Islam M, Li D and Hsiao-Wecksler ET, 2013. “Fuel Efficiency of a Portable Powered Ankle-Foot Orthosis.” *IEEE 13th International Conference on Rehabilitation Robotics (ICORR 2013).* June 24-26. Seattle, WA.
[27] Cummins JJ, Barth EJ and Adams DE, 2015, “Modeling of a Pneumatic Strain Energy Accumulator for Variable System Configurations with Quantified Projections of Energy Efficiency Increases.” *Proceedings of the 2015 Bath/ASME Symposium on Fluid Power and Motion Control,* Oct 14. Chicago, IL, USA.
[28] de Giorgi R, Kobbi N, Sesmat S and Bideaux E, 2008, “Thermal Model of a Tank for Simulation and Mass Flow Rate Characterization Purposes.” *Proceedings of the 7th JFPS International Symposium on Fluid Power,* September 15th-18th Toyama, JA.
[29] Igarashi K, Kawashima K and Kagawa T, 2007. “Development of Simultaneous Measurement System for Instantaneous Density, Viscosity and Flow Rate of Gases.” *Sensors and Actuators A* 140, 1-7.
[30] Department of Energy’s Compressed Air Challenge. “Compressed Air System Economics (Fact Sheet #9).” Web. 22 Feb. 2016.

CHAPTER 6

ELASTOMERIC EVOLUTION: A NEW LOOK AT CARBON NANOTUBE REINFORCED ELASTOMERS

Joshua J Cummins, Christopher Maurice, Yi Song, Florence Sanchez, Eric J Barth and Douglas E Adams

Department of Mechanical Engineering
Vanderbilt University
Nashville, TN

Published in the Proceedings of the 40th European Rotorcraft Forum September 5th, 2014 with an adaptation from the publication in Smart Materials and Structures October, 2014

Abstract

The use of elastomers in the rotating reference frame of helicopters is pivotal in the dissipation of vibration as a means of mitigating fatigue damage. Three of the largest cost drivers for elastomers from the perspective of design, maintenance and warranty are dampers, bearings, and hydraulic systems. One of the primary modes of failure of these components is degradation of elastomeric materials. To address these failures, elastomer compounds have been improved in conjunction with carbon nanotubes (CNTs) and structural health monitoring (SHM) technologies. Early work[7],[8] on embedding CNTs in elastomers focused on strength and electrical effects including modulus, conductivity and electro-magnetic interference (EMI) shielding properties. In some of the most recent work,[3],[7] CNTs have been dispersed into viscous materials or spun into threads and used to measure strain in composite materials in an effort to functionalize CNTs embedded in elastomeric and carbon fiber reinforced composite material respectively. The CNTs used to form CNT thread originate in sheet form. This configuration or a variant of it would be ideal to use in hyperelastic materials such as elastomers due to its ability to undergo large deformations and maintain contact upon return to its original geometry. CNTs, when used as electrical sensors, also can enable material state awareness through SHM with the added benefits of improved strength properties and EMI shielding. The ability to sense strain using CNTs in the form of CNT thread is extended through a proof of concept study demonstrating the ability of conductive elastomers to monitor load and detect damage in specific directions.

1 Introduction

Elastomers are used extensively in rotorcraft, especially in the rotating reference frame, where their applications are most critical. Rotorcraft and these elastomers experience one of the harshest environments imaginable including extreme weather, vibration and combat hazards in military applications. Billions of dollars are spent annually on detection and prevention of failure of critical rotorcraft components; among the most frequent failures are those involving bearings,[18] bushings, dampers and seals, all of which utilize elastomers.

Current detection and prevention methods rely primarily on maintenance crews and daily inspections, which are costly and time consuming. Even the most advanced decision support systems such as Health and Usage Monitoring Systems (HUMS) rely on vibration data and post processing and tend to be reactive rather than proactive, requiring clues provided by previous component failures to predict impending failures across a fleet.

One current area of active research is Integrated Structural Health Management, which utilizes structural health monitoring systems to detect and even predict component failures before they occur so that preventive maintenance actions can be taken to reduce unscheduled maintenance and improve aircraft availability.[19] Technologies being developed to address these needs include energy harvesting, wireless sensing and data analytics.

Carbon nanotubes (CNTs) are simultaneously being developed for use in other parts of the airframe, e.g., fuzzy fibers to improve the matrix/fiber interface. Additionally, CNTs are being used to improve the interfacial strength between plies of composites. CNT thread has also been developed to measure strain on composite materials.[7] Despite all of these advancements and active areas of research very few of these technologies have been considered or directly applied to elastomers. While elastomers are often times considered secondary structure, their failure often can and does lead to failure of primary structures.[8]

A concept that is currently in development that pulls from aforementioned technology development efforts is the CNT reinforced elastomer. The development of a CNT reinforced elastomer stems from the design of an advanced strain energy accumulator.[9] The advantages of CNT reinforced rubber include improved strength properties, EMI shielding, strain sensing capability, and the potential for functionally graded elastomers.

1.1 Early CNT Elastomer Work

In the early 2000's preliminary work was done to embed CNTs in various rubber materials at various volume fractions and weight percentages. The focus of these studies was to investigate the general effect on material properties including strength, conductivity, and electromagnetic shielding ability.[7],[8] At this time, carbon nanotubes were new, at a low technology readiness level (TRL), costly and were not produced in large quantities; it was also not yet possible to functionalize CNTs.

1.2 Current Measurement Techniques

Several different measurement and sensing techniques exist for obtaining material properties for elastomers but each has drawbacks. The standard load frame used in determining strength properties is accurate but lacks the ability off-the-shelf to monitor the material in situ. Standard foil strain gages are a reliable measurement technology but are subject to disbonding and also fail under the hyperelastic deformations experienced by some elastomers.

Additionally, strain gages are typically surface mounted and difficult, if not impossible in most applications, to mount inside structures. Digital Image Correlation (DIC) is another

commonly used measurement technique that uses a speckle pattern to track displacements of the material. DIC has its own challenges and drawbacks including in situ monitoring, the required speckle paint pattern that would not be feasible in most military rotorcraft applications, and the tendency of the paint specs to disbond from the elastomeric materials in high strain or hyperelastic deformation situations.[10]

1.3 New Measurement Techniques

A new measurement technique being developed at the University of Cincinnati is the used of CNT thread for integrated sensing of carbon fiber reinforced polymer (CFRP) composites. In this new sensing method, sheets of vertically aligned CNTs are woven into thread and are then integrated into CFRP composite panels for impact testing. A CFRP composite panel with an integrated CNT thread sensor system, the CNT sensor grid with impact location and measured response from an instrumented impact hammer can be seen in Figure 6.1.

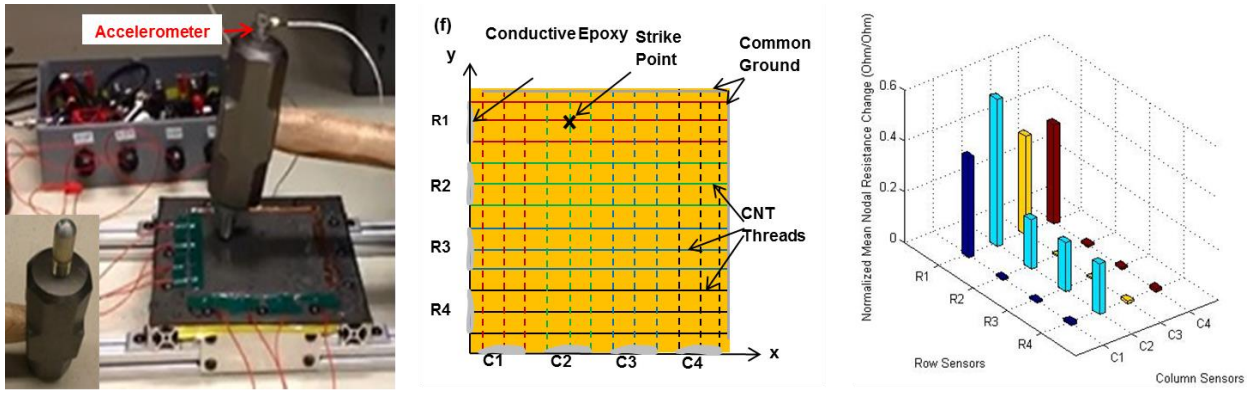

Figure 6.1: CNT thread sensor grid mounted on composite panel (left), sensor grid with impact location (center), measured response (right). Adapted from [7] included in Appendix A

The CNT sensor thread integrated on a CFRP composite panel demonstrated the ability to locate the damage and indicate the severity of the impact on the panel, the full details of which can be found in the complete manuscript in Appendix A. These results from the impact testing conducted are promising as they demonstrate the feasibility of the use of CNT thread as a viable sensor for new and advanced sensing applications. While just one version of CNTs was tested for sensing possibilities, other variations such as sheet/forest, ribbon and a combination thereof have yet to be explored and offer additional potential to advance new measurement and self-sensing techniques.

1.4 Applications of Sensor Thread

As demonstrated by the aforementioned results, the potential for CNTs to be used as sensors is greatly expanding as both the fields of SHM and CNTs continue to mature. One of the most critical applications for the use of CNTs as sensors is the Aerospace industry. As increasingly more aircraft are being made of composites due to strength and weight requirements the ability to monitor these structures is moving to the forefront. Composites typically fail suddenly and catastrophically so the ability to monitor and manage their structural integrity is of utmost importance. Since CNTs have the potential to be used as sensors and add very little weight, improve strength and are becoming affordable for use in application, they are ideal candidates for future sensors.

Another way in which CNT sensors can be used is as an enabler for condition-based

maintenance (CBM). As the cost of aircraft and other composite structures increases so does the cost to maintain and repair those structures. By implementing CNT sensors as a tool in CBM the total cost of ownership is reduced. Additionally, once CBM is implemented and acceptable levels of reliability of SHM systems are achieved, predictive maintenance can be realized. The potential of SHM systems to attain predictive maintenance not only reduces cost but also increases reliability and safety. Furthermore, where other sensors fail, due to their inferior material properties, CNT sensors can be used as complementary or redundant sensors. One such example is in monitoring hot spots or fatigue tests for composite components, where the composite part often outlasts a traditional foil strain gage, leading to increased costs of testing and the introduction of an additional source of uncertainty into results.

In addition to sensing capabilities of CNTs, there are several other properties of CNTs that can be utilized for application in other areas. CNTs offer improved strength properties which can be used in civil structures such as strengthening concrete or reinforcing elastomers. Furthermore, CNTs have resistive properties which can be used for thermography or other heating applications. The ability of CNTs embedded in rubber has also been documented [37] to provide EMI shielding capabilities, which is of great interest in defense applications. Where current measurement technologies fall short, the integration of CNTs into elastomers offers the potential to significantly advance the state-of-the-art of elastomers and measurement techniques.

2 Carbon Nanotube Elastomers

A material that has the potential to address the limitations of current measurement techniques and material properties of elastomers, and provide in situ material data for structural health monitoring of elastomers is CNT embedded elastomers. Kang and Schulz et al. first reported on the use of CNT in polymers for strain sensing but were limited at the time by the length of the CNTs.[7] One of the first reported uses of a flexible CNT sensor was by Yamada et al. in 2011 for human-motion sensing.[11] Since then Song et al. successfully utilized long, vertically aligned CNTs as shown in Figure 6.2 to create CNT thread for strain sensing in composites.[7]

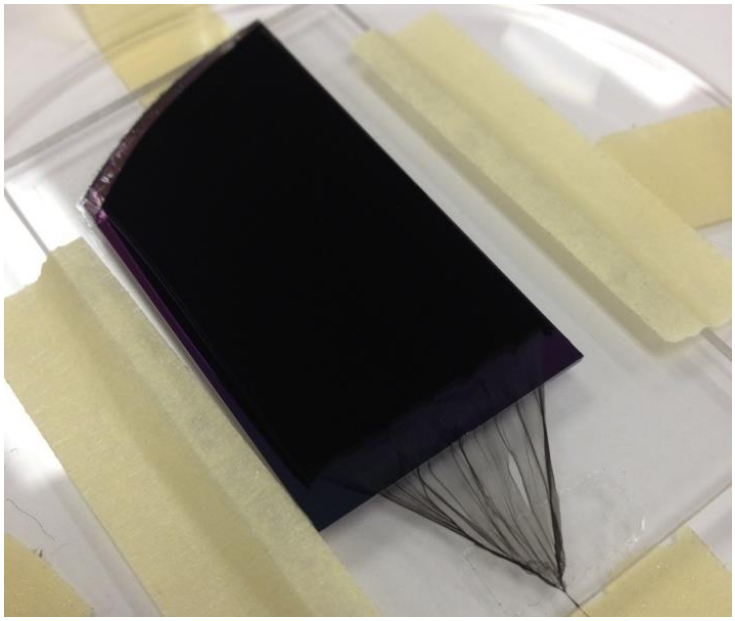

Figure 6.2: Vertically aligned spinnable CNTs.

The key findings of each of these prior works suggest the concept of a CNT embedded elastomer utilizing vertically aligned spinnable CNTs for in situ structural health monitoring of rotorcraft parts.

2.1 Carbon Nanotube Embedded Elastomers

Early investigation of CNT elastomers were focused on the mechanical and electrical properties and not on functionalizing the CNTs within the material, due to the purity and size limitations of early CNTs. Figure 6.3 shows the effect that the addition of CNTs has on the material properties of natural rubber, which is an elastomer.

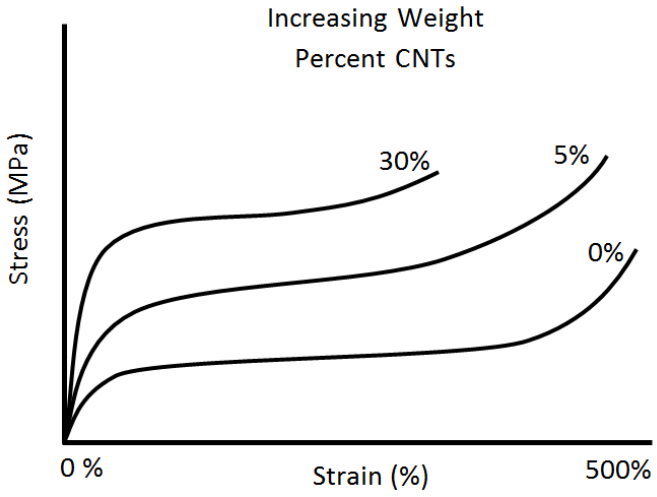

Figure 6.3: Effect of increasing weight percent of CNTs on rubber modulus. Adapted from [2].

It is observed that as the CNT percent increases, both the strength and elastic modulus increase as one would expect while the maximum strain percent obtainable decreases along with the toughness. In addition to improved strength properties, a number of other material property advantages exist for CNT embedded elastomers. Figure 6.4 shows the Electro Magnetic Interference (EMI) shielding capability of CNTs embedded in rubber that is of particular interest in military and shipboard rotorcraft applications.

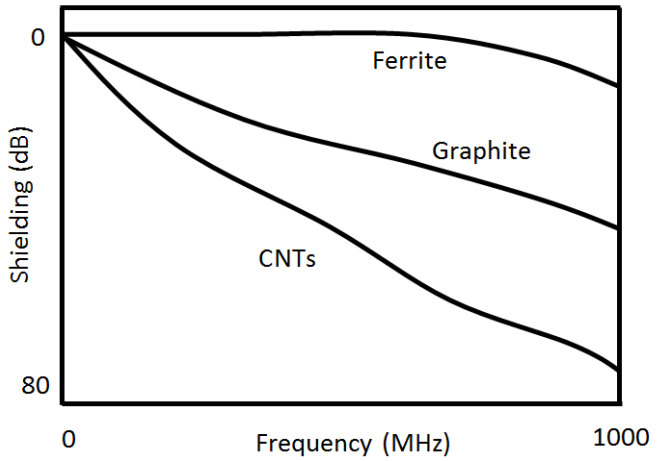

Figure 6.4: EMI shielding ability of carbon nanotubes in rubber at 30 wt%. Adapted from [2].

The ability for CNT embedded elastomers to be used for strain sensing and functionally graded materials is considered here in the context of rotorcraft elastomeric components.

2.2 CNT Embedded Elastomer Components

Degradation of elastomeric components can lead to sudden and catastrophic failure in the vibration intensive environment in which rotorcraft operate. Early detection of the degradation of elastomeric components is difficult in operation. In a ground test environment, detection is aided in the visual clues left behind in the form of pieces or residues from the degrading component. It is more challenging to detect early degradation in a flight test as the visual clues from the material that are shed are lost to the operating environment. With additional sensors and manpower available in flight tests, degradation can still be detected.

In daily operations, when maintainers perform inspections during regular intervals, and are in charge of a portion of a fleet of aircraft, early detection is challenging and early indicators of degradation can be missed. With the addition of vertically aligned CNTs in elastomers to enable strain sensing capability, early detection is possible and reductions in unscheduled maintenance or worst case scenario mishaps can be avoided.

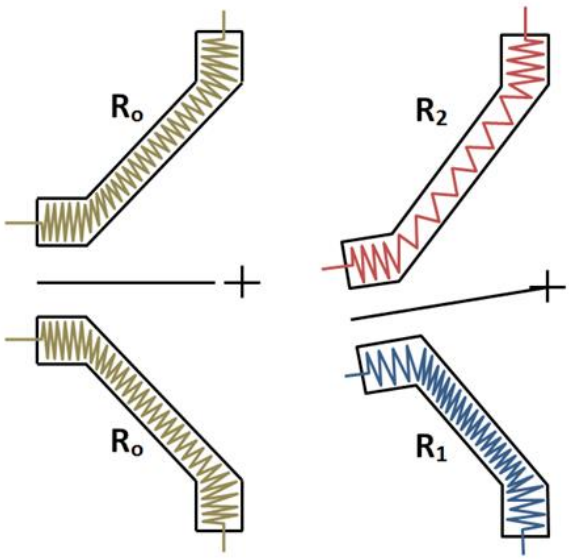

Figure 6.5: Cross sectional view of focal bearing elastomer with vertically aligned CNT embedded elastomer (a) initial/unstressed (b) final/stressed

Figure 6.5 shows a representative elastomeric component, i.e. a focal bearing, bushing, or bearing seal, with a vertically aligned CNT sheet embedded with the ends spun to form CNT thread coming out of the component serving as leads and having initial resistance, R_o. As a load is applied, the component deflects and the resistance changes to experience a compressive load/resistance, R_1, and a tensile load/resistance, R_2. As the component degrades the connections between the CNTs may be interrupted and result in a change in the initial, unstressed resistance of the material. This functionalization of the CNTs within the rubber could add the capability to monitor loads in the component and detect early signs of failure.

Similarly for functional grading of materials, vertically aligned CNT sheets can be replaced with high purity CNT powder. Again using Figure 6.5 as an example, as the component is loaded

CNTs can be dispersed to certain regions of the material depending on the load profile and where an increase, or decrease, in stiffness would be of benefit to the component.

3 Dispersion of Carbon Nanotubes in Viscous Substances

Dispersion of CNTs has been an area of research for some time and has focused on polymers, elastomers, and concrete. Lessons have been learned and new techniques developed to achieve more uniform dispersion enabling improved functionality of CNTs

3.1 Carbon Nanotube Dispersion in Polymers

Early work performed by the University of Cincinnati[7] focused on dispersion of CNTs in polymers for sensing capability, which utilized ultrasound and shear force mixing methods. One of the issues faced at the time was the inability to grow long CNTs, thereby limiting the ability to utilize them for measuring mechanical and electrical properties. While shear force mixing is the simplest, it is limited to primarily coarse dispersion where ultrasound can improve dispersion on a nanoscale. A drawback to ultrasound is that it can damage the nanotubes during the dispersion process.

3.2 Carbon Nanotube Dispersion in Concrete

The conventional approach to incorporate CNTs in concrete is to first disperse the CNTs in the mix water using a combination of superplasticizer and ultrasonication and then mix the resulting dispersion with the cement powder. Work performed at Vanderbilt University[12] has shown that while the use of polycarboxylate-based high range water reducer can help in the dispersion of CNTs in concrete, there is still evidence of the formation of sub-micron and micro-scale CNT clusters and non-uniform arrangement of individual CNTs within the cement paste leading to CNT rich and CNT poor regions. It has been demonstrated that the quantification of the agglomeration state of the CNTs by optical microscopy observation and image analysis is a useful tool to understand the structure-property relationship of concrete containing CNTs.

3.3 Magnetic Nanoparticle Dispersion

A new method that has been developed for dispersing nanoparticles in materials uses magnetic fields.[13] One of the key findings of Stuyven et al. is that magnetic fields can impact laminar flow profiles and produce velocity gradients that result in varying levels of dispersion. Given the electromagnetic properties of CNTs, magnetic fields should be able to achieve enhanced dispersion enabling functionally graded materials.

4 Carbon Nanotube Strain Sensing

Carbon nanotube materials are piezoresistive, which means the resistance of the carbon nanotube thread/ribbon changes with strain. The piezoresistive behavior can be used to sense strain and potentially damage in a host structure because local strain fields are influenced by mechanical damage. The sensitivity of strain sensing depends on the length of the sensor because average strain is measured over the length of the sensor. Carbon nanotube sensor threads are barely visible and do not add significant weight to the host composite structure.

4.1 Carbon Nanotube Thread Strain Sensing

A carbon nanotube forest was synthesized and spun into carbon nanotube sensor thread with a diameter of 20μm in the Nanoworld Laboratory at the University of Cincinnati. The sensitivity of the sensor thread was compared to the strain measured from a regular strain gage. Both sensors were bonded onto a 4-ply symmetric cross-ply laminated IM7 composite coupon for strain measurement. The tensile stress versus strain and resistance change versus strain were plotted. The gage factor of the carbon nanotube sensor thread was 0.91. The relative strain measurement error between the carbon nanotube sensor thread and regular strain gage was 5.9 %.[7]

Unlike strain gages, the carbon nanotube sensor thread could be integrated into the inner plies of a laminated composite and will not affect the integrity of the host composite structure. Therefore, carbon nanotube sensor thread provides a simple and reliable way for strain measurement and damage detection on composite structures on a near real time basis. The ability of CNT thread to measure strain on carbon fiber composites near real time can be extended to strain measurement in elastomers utilizing vertically aligned CNTs embedded in elastomers.

5 Modeling of CNT Elastomers

Homogenization models are used to extrapolate macroscale properties from their individual molecular scale material properties in this section. A brief overview of the homogenization methods is provided because it indicates a need for experimentally determined material property data. A detailed analysis is given in Cummins et al.[9]

5.1 Homogenization Techniques Estimating the Elastic Modulus of a CNT Embedded Elastomer

All homogenization methods begin with the stress-strain relations given in Eq. (1):

$$\sigma_{ij} = C_{ijkl}\varepsilon_{kl} \tag{1}$$

The homogenized modulus is determined by the effective elasticity tensor, C^*. In the upper limit Voigt homogenization method, the effective elasticity tensor is defined as:

$$C^*_{(Voigt)} = \sum_{\alpha=1}^{n} c_\alpha C_\alpha \tag{2}$$

Where α is the phase (matrix or inclusion), c_α is the volume fraction or the ratio of the volume of the particular phase to the total volume, and C_α is the stiffness tensor of the respective phase. In the CNT reinforced rubber there are only two phases, the CNTs and the rubber, where C_i and C_m are the stiffness tensors for the inclusion and matrix material respectively. The lower limit Reuss homogenization method is:

$$C^*_{(Reuss)} = \left(\sum_{\alpha=1}^{n} c_\alpha C_\alpha^{-1} \right)^{-1} \tag{3}$$

The homogenized modulus in the longitudinal direction for these two methods and the Mori-Tanaka homogenization method is the C_{11} element of the effective elasticity tensor. The Mori-Tanaka effective elasticity tensor is defined[14] as:

$$C^{*}_{(MT)} = C_m + \sum_i c_i (C_I - C_m) A_{I(MT),i} \quad (4)$$

Where C_I is the elasticity tensor of the inclusion, C_m the elasticity tensor of the matrix, c_i the volume fraction of the inclusion and $A_{I(MT),i}$ as defined by Klusemann and Svendsen.[14]

5.2 Summary of Homogenization Methods

The estimates of homogenized modulus for CNT rubber vary greatly depending on the method employed.[9] Table 6-1 shows the large variation in estimated homogenized modulus values for a soft rubber material. The homogenized elastic modulus values in Table 6-1 are normalized by the elastic modulus of the rubber material. Even at small volume fractions the methods are orders of magnitude apart. The discrepancy between the homogenization methods only increases as the volume fraction of the CNTs increases.

Table 6-1: Normalized Homogenized Modulus Values

Volume Fraction %	Homogenization Method		
	Reuss	Mori-Tanaka	Voigt
5	1.05	2.42	$1.45*10^3$
50	2.00	7.36	$14.47*10^3$
95	19.99	104.24	$27.50*10^3$

Such large discrepancies among the methods, especially with their dependence on the material properties of CNTs which can vary greatly, point to a need to obtain experimental data on the material properties of CNT elastomer samples.

6 Preliminary Testing on Metal Rubber

A first step in determining material properties of CNT elastomers, while the final formulation and construction is being finalized, is to study those of the most comparable commercially available product which in this case is a material called Metal Rubber which was used for the test specimens shown in Figure 6.6.

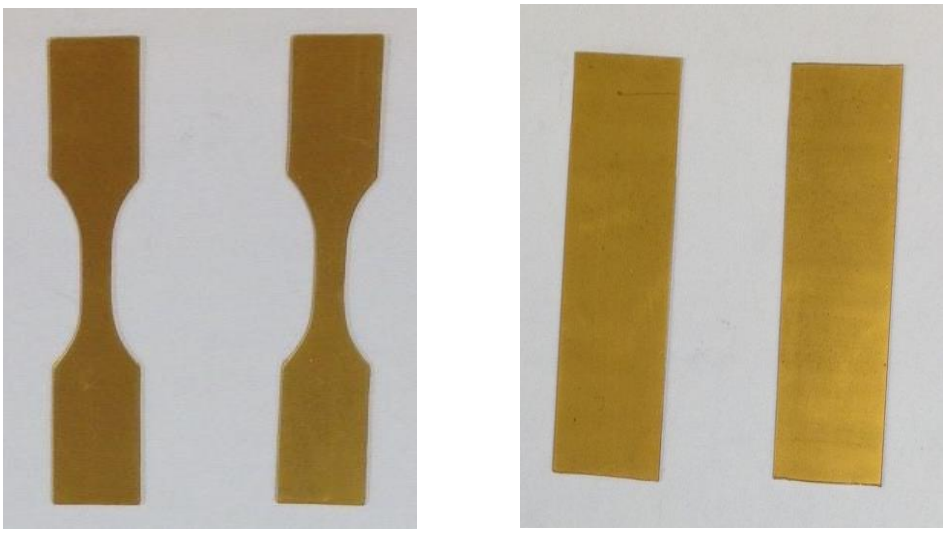

Figure 6.6: Metal Rubber test specimens: dogbone (left) and rectangular (right)

Metal Rubber consists of rubber and gold nanoclusters and exhibits the material properties of both metal and rubber. Early experiments were performed by Lalli et al.[15] measuring the resistance of the material at varying stress-strain levels. In their work they found that they were able to accurately measure strain levels up to 20 % strain but, beyond that, the metal nanoclusters lost conductance paths and resistance saturated at 75 % strain. It is believed the vertically aligned CNT elastomers, specifically rubbers in large strain deformation applications, will be able to maintain conductivity due to the large aspect ratio and van der Waals forces between the nanotubes.

One application envisioned for the CNT elastomers that can be tested on the Metal Rubber is the use on bearings and hydraulic seals to test for damage and leakage. In the current body of work, the Metal Rubber rectangular test specimens were measured for resistance values using a Fluke IV Ohmmeter. Three different damage modes were introduced to the metal rubber specimen and are labeled one through three in Figure 6.7. Damage mode one was a vertical snip using wire cutters at approximately half the vertical dimension of the Metal Rubber rectangle. The second damage mode introduced was a horizontal surface scratch and the third was a vertical surface scratch the entire vertical length of the specimen.

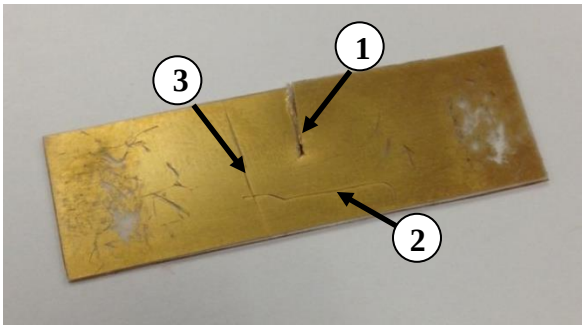

Figure 6.7: Three damage modes on Metal Rubber

Alligator clips from the Ohmmeter were vertically fixed to a bench to properly hold the specimen and reduce fluctuation in resistance due to unnecessary movement as shown in Figure 6.8.

Figure 6.8: Damaged Metal Rubber rectangular test specimen experimental test setup

Table 6-2 gives the Metal Rubber's change in resistance when physical damage is introduced to the test specimen.

Table 6-2: Change in resistance with damage

	R_1	R_2	ΔR
Half Snip	18.0	31.3	13.3
Horizontal Scratch	31.3	35.0	3.7
Vertical Scratch	35.0	Infinite*	Infinite*

***Saturation of ohmmeter resistance reached**

It is important to note that the Metal Rubber is not very durable and prone to scratching when the alligator clips are connected. The material's gold nano cluster layer is easily rubbed off by the metal alligator clips, revealing a clear non-conductive rubber layer. Once the thin layer of gold nano clusters was rubbed off, that portion of the material is no longer conductive and loses its sensing capabilities. This significantly changes the base resistance measurements throughout the experiment. Therefore, it is critical to notice the changes in resistance when the damage is induced rather than the resistance value itself.

Data from Table 6-2 indicates that vertical abrasions will significantly alter the material's conductive properties with the possibility of complete loss of conductivity. The "half-snip" and the horizontal scratches increase the resistance, but alternate conductive pathways are easily utilized by the material resulting in an increase in resistance while maintaining conductivity. The substantial decrease, or complete loss, of conductivity due to damage in a certain direction allows for directional sensing capabilities. This directional sensing capability could enable elastomers that are used for sealing applications to sense damage across the seal, severing electrical connection, and indicating a possible leak initiation site.

Subsequently, resistance changes in the Metal Rubber due to increasing load were examined through tensile testing. Vise Grip pliers were used to grip both ends of a dogbone Metal Rubber specimen while resistance changes were monitored by an Ohmmeter as weights were added to the lower Vise Grip incrementally. Figure 6.9 shows the experimental test setup used for the simple tensile test.

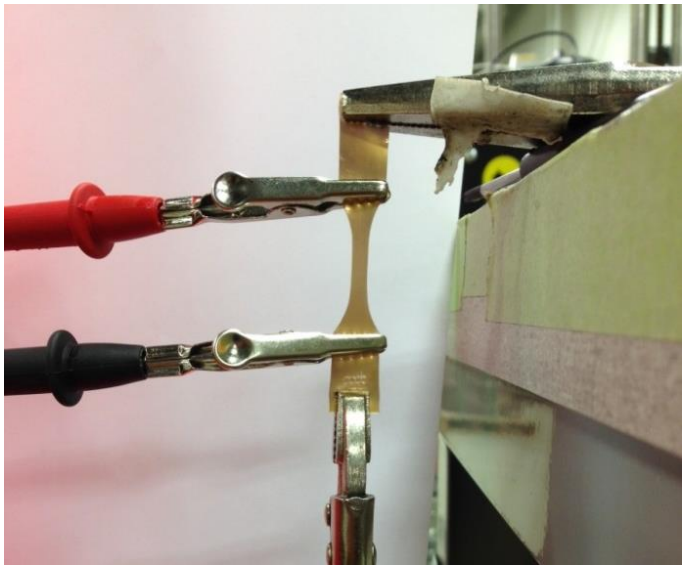

Figure 6.9: Metal Rubber dogbone specimen experimental setup for tensile test

The results of the tensile test are shown in Figure 6.10. An apparent non-linear relationship is observed between load and resistance.

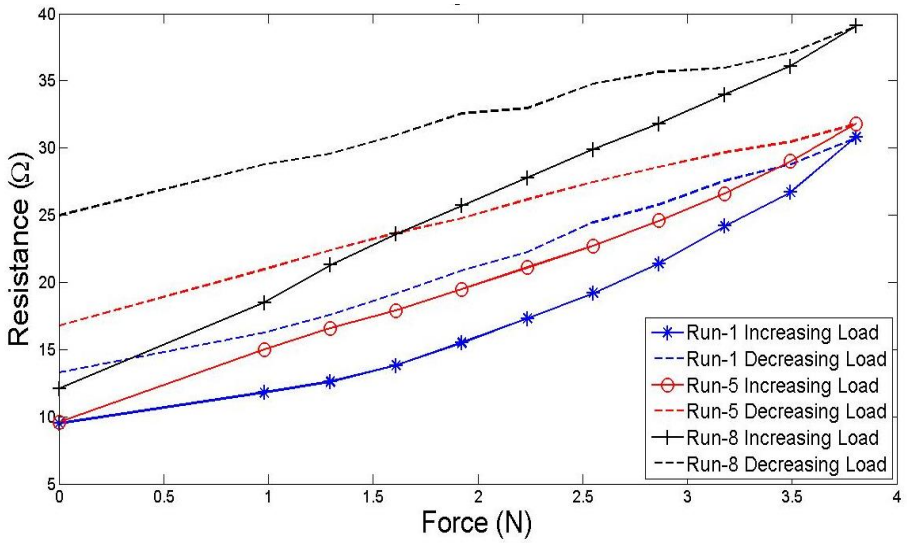

Figure 6.10: Plot of Resistance vs Load for Metal Rubber

The non-linear relationship between resistance and mass is best explained in correlation to a segmented stress-strain curve of rubber in Figure 6.11. As small amounts of weight are added, there is no significant change in resistance because the elastic modulus or slope of the line in Region 1 is large and linear. As more weight is added to the specimen, the stress-strain curve of rubber in Region 2 starts to transition into the hyperelastic regime. In this transition region, the elastic modulus starts to decreases resulting in larger deformations and therefore greater measured resistances as the gold nanoclusters in the Metal Rubber start to loose contact.

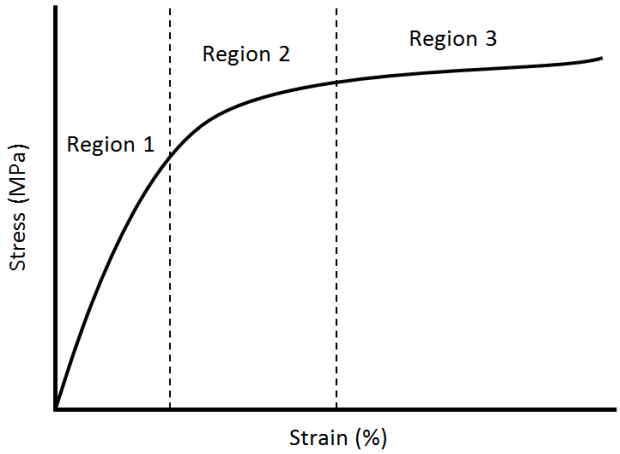

Figure 6.11: Stress-Strain Curve of Rubber

Finally, as the transition into the hyperelastic region is complete, the elastic modulus reaches a local minimum in Region 3 of Figure 6.11. This new lower elastic modulus gives way to even larger elastic deformations and measured resistance values as more electrical pathways are severed, thus resulting in the non-linear behavior that is observed. One last point worth noting is that the range of load applied herein is only 3 N. Such large changes in resistance with relatively small changes in load bode well for a sensor with great sensitivity to changes in load.

7 Conclusions and Future Work

The current work looks at the evolution of CNTs embedded in elastomers; from the early years when a simple study to investigate the impact of CNTs on mechanical and electrical properties was performed to recent years when great strides have been made to functionalize CNTs within elastomers.

Much has been learned in the area of dispersion of CNTs within materials including polymers and concrete, new methods are being investigated to achieve uniform and repeatable dispersion including the use of magnetic fields. Such methods have the potential to lead to achieving functionally graded elastomers. Realizing that the material properties and functionality of CNTs dispersed into elastomers may differ from vertically aligned CNTs embedded in elastomers, parallel paths and their corresponding results are being pursued. The functionality of each as applied to elastomeric rotorcraft components will continue to be investigated and reported.

The ability of CNT thread to measure strain has proven successful and the results of which are currently being developed and extended to vertically aligned CNTs embedded in elastomers. Preliminary multiscale modeling efforts have resulted in a wide variation of predicted material properties indicating a need to further investigate existing homogenization techniques and both verify and validate experimentally.

The nearest commercially available product to vertically aligned CNT embedded rubber is that of Metal Rubber which exhibits both hyperelastic behavior and electrical conductivity at mid-range strains. While the Metal Rubber samples tested experienced durability issues, they did allow proof of concept to both detect damage and measure load in rubber materials. Once constructed, the vertically aligned CNT embedded rubber will be compared to the results of Metal Rubber presented in the current study and extended to representative rotorcraft applications in the lab utilizing both the RC helicopter in Figure 6.12 and the in-house whirl test stand in Figure 6.13.

Figure 6.12: RC helicopter used for load/strain data acquisition testing

Figure 6.13: Whirl Test Rig

Acknowledgments

This work was supported by the Center for Compact and Efficient Fluid Power, an NSF Engineering Research Center, grant EEC-0540834.

References

[1] Kim, Y.A., Hayashi, T., Endo, M., Gotoh, Y., et al., 2006, "Fabrication of aligned carbon nanotube-filled rubber composite." Scripta Materialia 54, pp. 31-35.

[2] Bokobza, L., 2007, "Multiwall carbon nanotube elastomeric composites: A review." Polymer 48, pp. 4907-4920.

[3] Sanchez F and Sobolev K. Nanotechnology in concrete – A review. *Construction and Building Materials,* 2010; 24(11): 2060-2071.

[4] Kang, I., Schulz, M.J., Kim, J.H., Shanov, V., et al., 2006, "A carbon nanotube strain sensor for structural health monitoring." Smart Materials and Structures 15, pp. 737-748.

[5] Reddick, H.K. Jr., 1975, "Army Helicopter Cost Drivers." Army Air Mobility Research and Development Laboratory, Fort Eustis, VA.

[6] Bond, R., Underwood, S., Adams, D.E., Cummins, J.J., 2013, "Structural Health Monitoring-Based Methodologies for Managing Uncertainty in Aircraft Structural Life Assessment." Proceedings of the 9th International Workshop on Structural Health Monitoring.

[7] Song, Y., Hehr, A., Shanov, V., Alvarez, N., Kienzle, N., Cummins, J.J., Koester, D., Schulz, M, 2014, "Carbon Nanotube Sensor Thread for Distributed Strain and Damage Monitoring on IM7/977-3 Composites." Smart Materials and Structures 23, 7 pp. 5008.

[8] Calcaterra, J.R., 2009, "Common Failure Modes Affecting the Performance of Aerospace Systems." Proceedings of the 7th International Workshop on Structural Health Monitoring.

[9] Cummins, J.J., Barth, E.J., Adams, D.E., 2014, “Advanced Strain Energy Accumulator: Materials, Modeling and Manufacturing.” Proceedings of the 2014 Bath/ASME Symposium on Fluid Power and Motion Control.
[10] Moser, R. and Lightner, J.G. III., 2006, “Using 3D Digital Imaging Correlation Techniques to Validate Tire FEM.” Proceedings of the 2006 SEM Annual Conference on Experimental Mechanics.
[11] Yamada, T., Hayamizu, Y., Yamamoto, Y., Yomogida, Y., et al., 2011, “A stretchable carbon nanotube strain sensor for human-motion detection.” Nature Nanotechnology 6, pp. 296-301.
[12] Gay C, Sanchez F. Performance of carbon nanofibers/cementitious composites with a high-range water-reducer. Transp Res Record. 2010;2142(2):109-13.
[13] Stuyven, B., Chen, Q., Van de Moortel, W., et al., 2009, “Magnetic field assisted nanoparticle dispersion.” Chemical Communications 45, pp. 47-49.
[14] Klusemann, B., Bohm, H.J., Svendsen, B., 2012, “Homogenization methods for multi-phase elastic composites with non-elliptical reinforcements: Comparisons and benchmarks.” European Journal of Mechanics A/Solids 34, pp. 21-37.
[15] Lalli, J.H., Hill, A., Subrahmanyan, S., Davis, B., Mecham, J., Goff, R.M., Claus, R.O., 2005, “Metal Rubber Sensors.” Smart Structures and Materials 2005: Smart Sensor Technology and Measurement Systems 5758 pp. 333-337.

CHAPTER 7

CONCLUSION

A Department of Energy report from ORNL and NFPA estimated that the composite efficiency of the fluid power industry is 22 %, with the pneumatic division of the fluid power industry averaging a mere 15 % efficiency, providing techno-economic motivation for this work. Inspired by these low efficiencies, the strain energy accumulator (SEA) was pursued and a survey of previous work was completed. The SEA is an energy storage device consisting of an expandable rubber bladder inside of a rigid shroud that stores energy in the form of pressure and strain. In completing a survey of previous work in the areas of the SEA and fluid power component and system efficiencies, a number of knowledge and technology gaps that needed to be addressed were identified including: advanced materials modeling, uncertainty analysis, and component and system efficiency quantification through development of integrated performance metrics and model-based techniques focusing on application. Encouraged by the potential of the strain energy accumulator to improve the low efficiency of the fluid power industry, and having identified the gaps in the current state-of-the-art, the current work set out to address these deficiencies.

Efficiency of the pneumatic strain energy accumulator was studied by developing lumped parameter state efficiency models, introducing integral model-based performance efficiency metrics. The newly developed model-based performance metrics were applied in component efficiency studies with the incorporation of uncertainty analysis. Successful implementation of the efficiency metrics at the component level enabled extension of these metrics to the system level focusing on representative applied systems. After completing the efficiency studies, the research examined the advanced materials focus with conductive elastomer proof of concept work by investigating the ability of conductive nanomaterial elastomers to monitor load and detect damage while deforming hyperelastically. Multiscale modeling homogenization techniques were also used to develop a rudimentary model of CNT rubber and predict the elastic modulus of the material.

The multiscale modeling homogenized modulus effort resulted in elastic modulus estimates ranging from a few times to over 80 times the elastic modulus of rubber. A wide variation in the predicted elastic modulus was useful for assessing CNT rubber's utility in the SEA application while indicating a need for future more detailed multiscale material model development and validation. The modeling effort then transitioned into the development of models for efficiency studies for the pneumatic strain energy accumulator. The newly developed models were used to perform component efficiency studies where, in over 2500 cycles of testing, the component was found to be consistently over 93 % efficient. The incorporation of model-based performance metrics was extended through system efficiency increase studies where conservative model efficiency increase estimates ranged from 31 % to over 60 %. In applying the low end of the efficiency range, in conjunction with modest industry adoption figures of 10 %, it was determined that such efficiency increases could result in a savings of $15,000 annually per industrial compressor translating to $300 million annually across all US industries. Finally, completion of conductive elastomer proof of concept testing was successful in demonstrating the

ability of the material to both monitor load while deforming hyperelastically and detecting the presence and direction of damage.

Completion of the current research verified that the pneumatic strain energy accumulator is a highly efficient device with considerable potential to increase overall system efficiency. The stain energy accumulator as a single device has the potential to make a significant improvement in the tremendous inefficiency of the fluid power industry. Moving forward, a majority of the work will focus on commercialization efforts and development of a commercial prototype. An announcement by the Center for Compact and Efficient Fluid Power dated February 17, 2016 stated that the proposal aimed at commercializing the pneumatic strain energy accumulator was selected to be funded for a two year period. Selection of the proposal for funding will enable the development of a commercial prototype which in turn will facilitate fatigue/component life studies and case studies with industry partners quantifying the actual energy savings in application. It is anticipated that successful completion of these activities will substantially advance the pneumatic strain energy accumulator towards commercialization. Finally, while schedule and budget did not permit an in-depth study of the advanced materials development aspect of the current research, exploring the potential use of nanomaterials for the self-sensing of fluid power components helped get the need for self-sensing of fluid power components on the radar of the National Fluid Power Association, as indicated by their 2015 Technology Roadmap.

APPENDIX A

CARBON NANOTUBE SENSOR THREAD FOR DISTRIBUTED STRAIN AND DAMAGE MONITORING ON IM7/977-3 COMPOSITES

Yi Song[1], Adam Hehr[1], Vesselin Shanov[1], Noe Alvarez[1], Nicholas Kienzle[1], Joshua Cummins[3], Dave Koester[2] and Mark Schulz[1]

[1]University of Cincinnati
Cincinnati, OH

[2]Vanderbilt University
Nashville, TN

[3]Naval Air Systems Command
Patuxent River, MD

Published in Smart Materials and Structures October, 2014

Abstract

Laminated composite materials are used in applications where light weight is the key requirement. However, minor delamination damage in composites can propagate and lead to failure of components. Failure occurs because delamination reduces the local bending stiffness and increases bending stress which leads to propagation of damage and eventual failure. These failures may be avoided if the damage could be detected early and repaired. Although many damage detection methods have been investigated, none are in widespread use today to prevent failure of composites. This paper describes use of carbon nanotube sensor thread which is a new way to monitor strain and damage in composite materials. Sensor thread was bonded onto an IM7 laminated composite test coupon to measure surface strain in a quasi-static uniaxial tensile test. The sensor thread was calibrated against a strain gage also mounted to the coupon. The sensor thread measured the average strain over the length of the sample and indicated when the strain exceeded a nominal safe level. Sensor thread was also bonded to the surface of laminated composite panels in different patterns and detected, located, and partially characterized damage caused by multiple impacts to the panels. Testing showed damage must be close to the sensor thread to be detected. Summarizing what is new in this paper; (1) carbon nanotube sensor thread was tested as a distributed sensor for the first time on IM7/977-3 composites; (2) the sensor thread was able to monitor strain and detect damage in the composites with potential sensitivity down to the micro-crack level; (3) the sensor thread was barely visible on the composite and did not add significant mass or affect the integrity of the composite; (4) the data acquisition system developed was simple and reliable.

1 Introduction

Composite materials have been widely used in many advanced applications where high strength and light weight are required such as aircraft, automotive and boats. On the other hand, the main disadvantage of laminated composite materials is delamination often caused by minor impacts. Delaminations can quickly propagate along the boundary between laminae and lead to catastrophic failure of the composite as there are no fibers in the through-the-thickness direction to prevent damage propagation. Matrix cracking is also a critical failure mode because carbon fibers are brittle and susceptible to transverse cracking. Early warning of delamination and cracking can avert composite failure. Therefore, it is important for safety reasons to monitor the strain distribution and delamination in specific spots of laminated composite materials and structures.

Currently non-destructive evaluation (NDE) and structural health monitoring (SHM) are the main methods to monitor delamination of composite materials. NDE can detect local delamination effectively but it requires the composite component to be out of operation for inspection [1-4]. SHM methods include fiber optics, stress wave propagation, and piezoresistive metallic foil gages. These methods have specific disadvantages such as difficulty in making connections for a large number of fibers, low sensitivity, stress wave dispersion in complicated geometric features of composite structures, and foil gages debond from the surface of laminated composite materials due to vibration and temperature cycling [5-24]. Damage detection on polymeric materials using CNT thread under simple loading conditions is described in [1-2]. SHM application of CNT thread based on laminated glass fabric composite materials is described in [3-6]. This new manuscript presents distributed strain measurement and damage monitoring based on IM7 laminated carbon fabric composite materials. Modern NDE techniques are still the primary means of damage detection and monitoring as SHM methods are approaching the required reliability to be used in-situ. Alamusi [25] et al and Hu et al [26] reviewed the piezoresistive behaviors of strain sensors consisting of CNT/polymer nanocomposites. In the case of CNT sensor thread, the mechanism that causes piezoresistivity of CNT thread (without polymer) is not fully understood yet. Abot et al recently proposed their hypothesis regarding the mechanism of piezoresistivity for CNT thread [27]. When the CNT thread is subjected to a tensile load, the strands that comprise the CNT thread were brought together and the spacing among the strands are reduced. This leads to the overall resistance decreased as the interfacial resistance decreased when the CNT strands come in closer contact with each [27].

Recently, people have investigated new piezoresistive strain sensors based on carbon nanofiller/polymer nanocomposites for SHM applications [28-29]. B Hu and N Hu et al developed vapor grown carbon fiber (VGCF)/epoxy nanocomposite sensors to detect slight damage of a cantilever beam under bending condition. Their experimental results showed the VGCF/epoxy nanocomposite sensors are much more sensitive compared to metal-foil strain gages in terms of the variation of resistance change ratio [28]. However, the VGCF/epoxy nanocomposite sensor has a typical dimension of 13 mm × 5 mm including wire connections. It is not as flexible as carbon nanotube sensor thread to be mounted in irregular geometry structures such as holes, corners, sharp edges. The carbon nanotube sensor thread typically has a diameter in the order of 20~25 μm and can undergo large deformation and could be bonded interested target locations or irregular geometry locations. Sebastian et al grew CNTs directly on fuzzy glass fiber and the sensing elements were comprised of around 3000 such fuzzy CNT grown

glass fibers [30]. These fuzzy glass fiber sensors were integrated into IM7 composite panel to sense strain. This technique can provide sensing over large sections especially in locations that are inaccessible by conventional strain gages [30]. If the damage in the IM7 composite panel causes only small portion of glass fibers to break, the overall resistance change will not be obvious and the measurement sensitivity is relatively low. In addition, the 3000 fuzzy glass fibers with CNT grown were sandwiched between two thin layers of plain weave E2 glass fabrics for electrical isolation purpose. The two-ply isolating E2 glass fabrics will affect the integrity of the IM7 composite panel. Christner et al developed carbon fiber sensors (CFS) consisting of a 1k roving of T300B fibers to measure strain [31]. The CFS exhibits a linear piezoresistivity up to a strain level of 6000μm/m. The material property such as ultimate strain of CFS is not tailorable which limits the applications of this sensor. As a comparison, the ultimate strain of our CNT sensor thread could be adjustable by changing the twist (number of turns per unit length) and diameter of the CNT sensor thread. This is very convenient when the CNT sensor thread is used to detect damage and measure strain of different host structures with variable deformation.

Carbon nanotube (CNT) thread is a piezoresistive material which means its resistance changes due to strain caused by longitudinal loading [1-4]. CNT thread spun from vertically aligned CNT arrays [1] can be used as a sensor to measure strain similar to how strain measurement is done using conventional metallic foil strain gages. The difference is CNT thread measures distributed strain over the length of the thread. This paper demonstrates the fabrication and use of carbon nanotube thread as a sensor. The approach is to fabricate and test tensile test coupons of laminated composites with surface mounted CNT sensor thread. The gage factor of the CNT sensor thread can be determined based on tensile testing and comparison with the strain measured by conventional foil strain gages. A piezoresistive sensor grid is also constructed by bonding CNT thread onto the surface of laminated composites to detect delamination and cracking caused by impact loads.

2 Methods

The fabrication of CNT thread and the composite panels is described along with the instrumentation used in the experiments.

2.1 CNT Thread Fabrication

CNT thread is produced by pulling a web from a spinnable CNT array and simultaneously twisting [32-34] as illustrated in Figure A.0.1(a), (b). Spinnable CNT arrays have the unique property that allows assembly of the individual CNTs into continuous threads, yarns and fibers by simply grabbing one spot with forceps, and pulling and twisting in a similar manner to pulling a silk fiber from a cocoon. Due to its appropriate density and length, there are enough contact points between CNTs that allow the CNT thread to assemble due to van der Waals interactions and entanglement between the nanotubes. The as-grown CNT array has a density of 0.03 gm/cm^3 and an average CNT length of 500 μm. The diameter of single ply thread is controlled by the width of the spinnable CNT array. A 12 mm width array typically forms a 20-25 μm diameter CNT thread. By adding a weaving process into the overall spinning process with multiple spools of 1-ply thread, a variety of larger ply CNT rope may be fabricated, including 3-ply CNT rope and a 9-ply CNT rope (three 3-ply CNT ropes spun together). The different diameter rope can be used for fine or coarse resolution in measuring damage (e.g. in a polymer or cement). The fabrication process of CNT thread twists multiple CNT strands together. The twist in the CNT

thread under tension causes a radial component of the tension force that produces a high friction force among CNT strands, which substantially increases the tensile strength of the CNT thread. An SEM image of the manufactured thread is shown in Figure A.0.1(c). For the testing performed in this paper, as grown CNT thread was used. Currently, our CNT thread has strength of about 0.5-1 GPa [35-36].

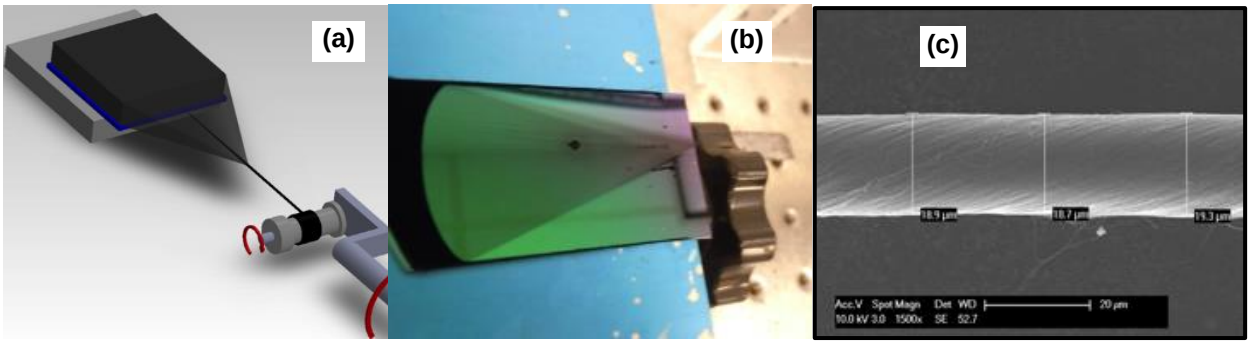

Figure A.0.1: Carbon nanotube thread fabrication technique: (a) Illustration where one side of a spinnable CNT array is pulled and collected on a spool while spinning to provide twisting; (b) photograph that shows pulling and twisting at the same time; (c) image of uniform CNT thread.

A 20 μm diameter CNT sensor thread was spun from a multi-wall CNT array without post treatment in the Nanoworld Laboratory at the University of Cincinnati [2]. CNT thread fabrication starts with the synthesis of a vertically aligned CNT array, known as a spinnable array, which contains typically double, triple and multiwall CNTs. Chemical vapor deposition (CVD) is employed to synthesize the high purity, well aligned and spinable multiwall CNT arrays. Argon is used as a carrier gas along with hydrogen and a small amount of water vapor. Ethylene is our choice for the carbon precursor gas. A low partial pressure of ethylene (~0.068) was used in order to obtain spinable CNTs arrays. The reactor pressure was nearly atmospheric. An oxidized silicon single crystal substrate was processed to form several multi-layers. An Al_2O_3 (10 nm) buffer layer and Fe alloy (2 nm) catalyst layer were formed on top of the Si/SiO_2 wafer by e-beam evaporation. All the experiments were conducted at 750ºC. The water vapor concentration in the CVD was controlled by passing argon gas through a bubbler with water. During the cooling step the system was purged with a mixture of hydrogen and argon gases until the temperature reached 300°C and finally with argon up to ambient temperature.

2.2 Composite Coupon Fabrication and Setup for Tensile Strain Measurement

A four-ply (0°,90°,90°,0°) IM7/977-3 composite panel was fabricated and consolidated at 180°C for six hours. This panel was cut into 203 mm × 12.7 mm x 1.2 mm strips for tensile testing. Fiberglass composite tabs were bonded on both ends of each test coupon with Loctite adhesive 9430 in order to protect the coupon surface for grip clamping. All the test coupons were placed in an air bag with for seven-hours under vacuum at room temperature for adhesive curing. A thin epoxy layer was spread on the test coupon surface for electrical insulation between the carbon fibers and CNT thread. In the future, electrically insulated thread will be used and the epoxy insulation layer will not be needed. Additionally, the CNT thread was bonded on the epoxy layer with another thin layer of epoxy. A Vishay strain gage was bonded in the center location of the back side of test coupon. An Instron 4206 test machine was used for uniaxial quasi-static tensile testing as shown in Figure A.0.2(a). Figure A.0.2(b) shows a tensile test coupon and Figure A.0.2(c) shows a close up view of the CNT sensor thread bonded on the test

coupon with epoxy. The two ends of the CNT threads were fixed on the thin epoxy layer with conductive epoxy (the two silver spots in Figure A.0.2(b)) for wiring connections. The loading rate was 0.05”/min and the sampling rate for data acquisition is 5 points/second. The test data was recorded by the Instron test machine. Three test coupons were characterized and the test data was analyzed and plotted.

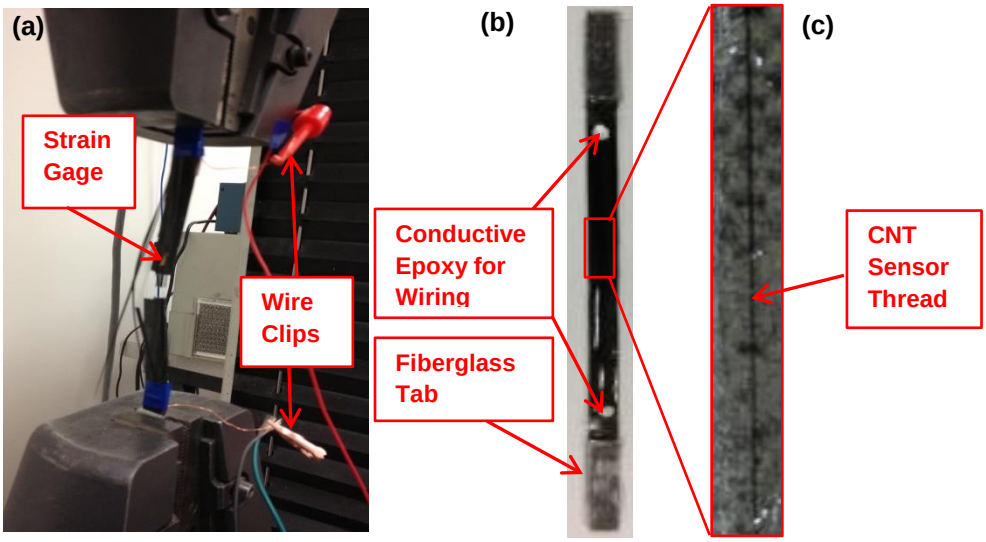

Figure A.0.2: Experimental setup for uniaxial quasi-static tensile testing: (a) a tensile test composite coupon clamped in the Instron 4206 test machine; (b) a four-ply tensile test composite coupon (a strain gage was bonded on the back surface of the coupon); (c) close up view of the CNT sensor thread bonded with epoxy on the front surface of the coupon.

2.3 Composite Panel Fabrication and Setup for Impact Testing

A symmetric eight-ply $(0°,90°,0°,90°)_s$ IM7/977-3 composite panel 200mm × 200mm x 2.4mm was fabricated using a hot press. This lay-up was heated to 180°C for six hours for consolidation. Then three fastener holes were drilled on each edge with 50.8 mm spacing between holes. A thin layer of epoxy was spread and cured on the top surface of the IM7 composite panel for electrical insulation between the carbon fiber and the CNT thread to be installed. The panel and experimental set up for impact testing are shown in Figure A.0.3. The overview of experimental set-up is shown in Figure A.0.3(a). Figure A.0.3(b) shows the CNT sensor threads bonded on the IM7 composite panel. Figure A.0.3(c) shows a close-up view of CNT sensor thread. The composite panel was mounted on an aluminum impact test rig with 12 bolts (Figure A.0.3(a), (d)). An impact rod with a tip radius of 15.875 mm was machined and mounted on the bottom side of the impact hammer (Figure A.0.3(e)). The hammer is raised to a specific angle and released during the impact test. An analog input data acquisition module (DAQ NI9205), provided by National Instruments, was adopted (Figure A.0.3(a)) for data acquisition. A Kistler type 8763B1K0AB accelerometer shown in Figure A.0.3(d) was attached to the top surface of the impact hammer to record the acceleration at the moment of impact. The eight sensor channels and the accelerometer were connected to the NI9205 data acquisition module. A Labview vi program was designed to display and save the data to a file (Figure A.0.3(a)).

A schematic of the composite panel showing the CNT sensor threads in rows and columns with the strike location is shown in Figure A.0.4(a). Twelve CNT sensor threads were bonded

with epoxy onto the panel in the longitudinal direction, Figure A.0.4(a). Every three intermediate CNT threads were connected to one signal channel of a Wheatstone bridge and a Labview data acquisition system. Another twelve CNT sensor threads were bonded with epoxy in the transverse direction. Thus eight channels of simultaneous data acquisition were used. The four channels in the longitudinal x direction were named R1, R2, R3, R4 and the four channels in the transverse y direction were named C1, C2, C3, C4 as shown in Figure A.0.4(a). Then one end of each signal channel was connected to the customized Wheatstone bridge circuit and the other end of each signal channel was connected to a common ground. Figure A.0.4(a) also shows that the strike point was located at the node between row sensor R1 and column sensor C2 on the composite panel. In order to detect and localize damage of smaller size, the number of row and column CNT sensor thread is required to increase. But this does not mean the number of communication circuits, connecting a single CNT sensor thread and DAQ, will increase correspondingly. A time-division multiplexing method will be used here shown in Figure A.0.4(b). A row and a column time-division multiplexer will connect the individual CNT sensor threads and computer via a data bus. The computer controls both time-division multiplexers to connect each individual row and column input CNT sensor threads in sequence, one after the other, to the DAQ device. The connection between one CNT sensor thread and DAQ device is very quick and then this connection is terminated. The multiplexer automatically builds another connection between the next CNT sensor thread and DAQ device similar to the previous connection.

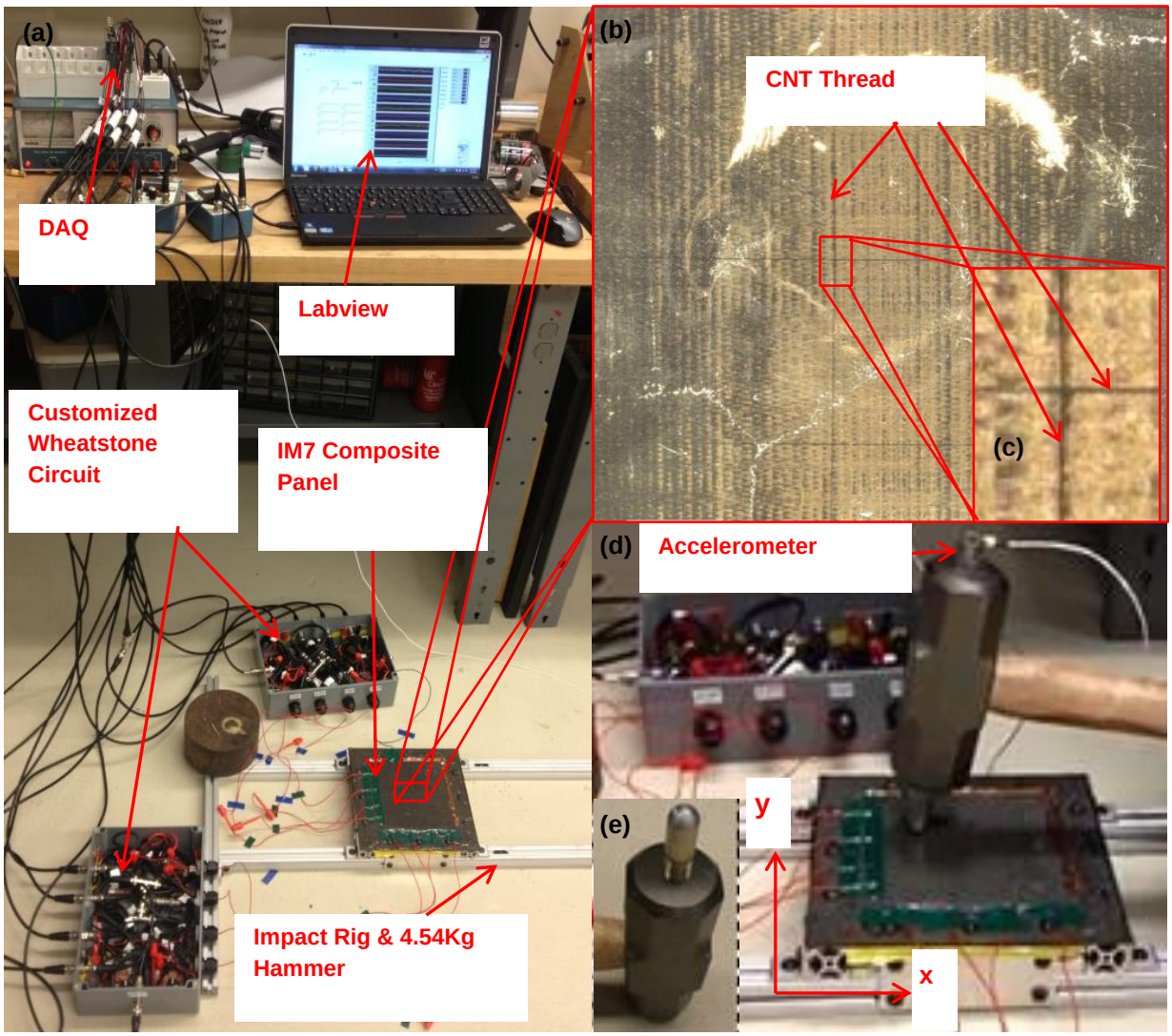

Figure A.0.3: Experimental setup for impact testing: (a) overview of the impact test set up for the composite panel; (b) CNT sensor thread bonded with epoxy on the top surface of the composite panel; (c) close-up view of the CNT sensor thread; (d) the composite panel was mounted on an aluminum impact test rig with 12 bolts. An accelerometer was mounted on the top surface of the hammer; (e) an impact tip with radius 5/8" was mounted on the bottom surface of the hammer and the hammer handle was pivoted on a shaft.

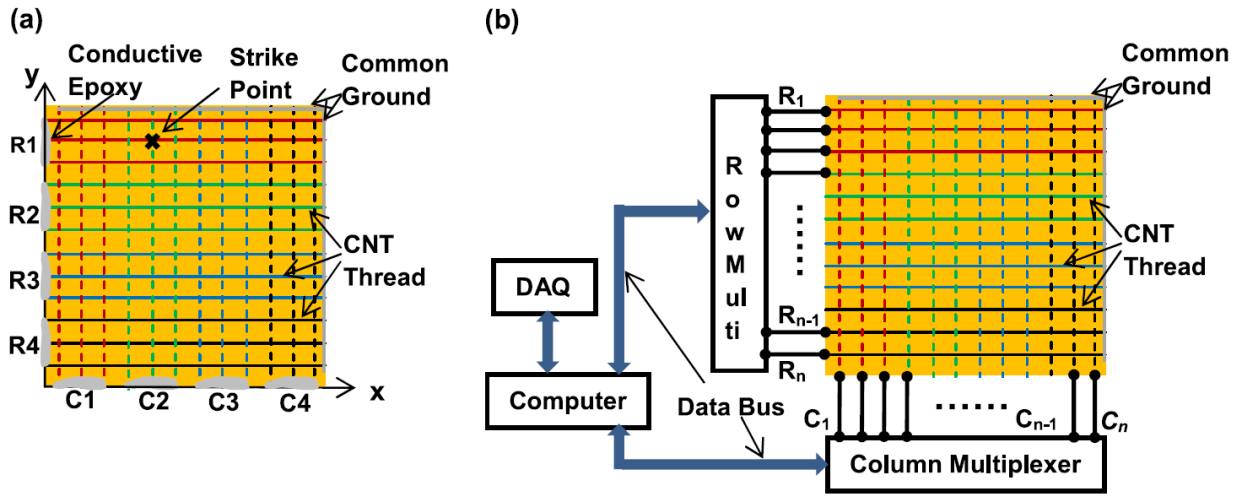

Figure A.0.4: Schematic of the composite panel shows CNT sensor threads: (a) 4x4 CNT sensor thread grid connections and the location of the strike point; (b) *nxn* CNT sensor thread grid with row and column multiplexer for time-division multiplexing.

3 Results and Analysis

The results of strain monitoring and impact testing are described in this section.

3.1 Tensile Testing

Figure A.0.2(a) showed a failed tensile test coupon that was clamped between two grips on an Instron 4206 material test machine. Figure A.0.5(a) shows the entire failed tensile test coupon. A close-up view of the failure surface is shown in Figure A.0.5(b). The failure surface of the symmetric and cross-ply tensile test coupon is perpendicular to the loading direction.

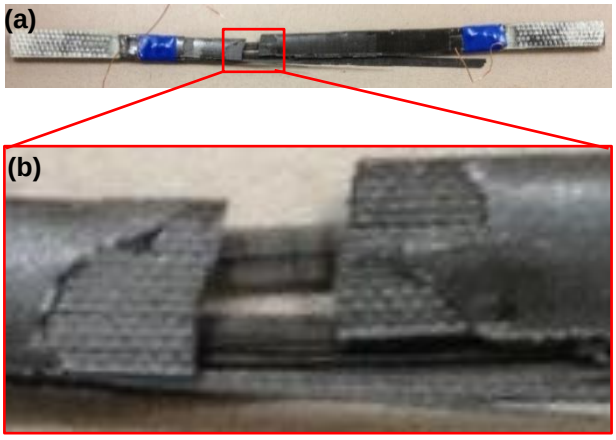

Figure A.0.5: Failed test coupon for uniaxial tensile testing and impact testing: (a) four-ply (0°,90°,90°,0°) IM7/977-3 tensile test composite coupon; (b) close-up view of the failure surface after tension testing.

Figure A.0.6(a) shows the tensile test curves for three four-ply (0°,90°,90°,0°) IM7/977-3 tensile test composite coupons. The synchronized tensile test curve and resistance response curve of the CNT sensor thread from one of the three test coupons are plotted in Figure A.0.6(b). The mean elastic modulus of the test coupons is 79.3 GPa and the mean tensile strength is 1.2 GPa.

As the tensile stress of the test coupon linearly increased, the resistance of the CNT sensor thread increased linearly up to 1.43 % tensile strain (or 1.05 GPa tensile stress). When the tensile stress is approaches the ultimate tensile strength, the resistance of the sensor thread increases dramatically. In the initial linear region, the maximum change in resistance was only around 80 Ohms. In the rapid increase region, the maximum change in resistance was around 1600 Ohms, which indicates that high strain or damage occurred in the test coupon.

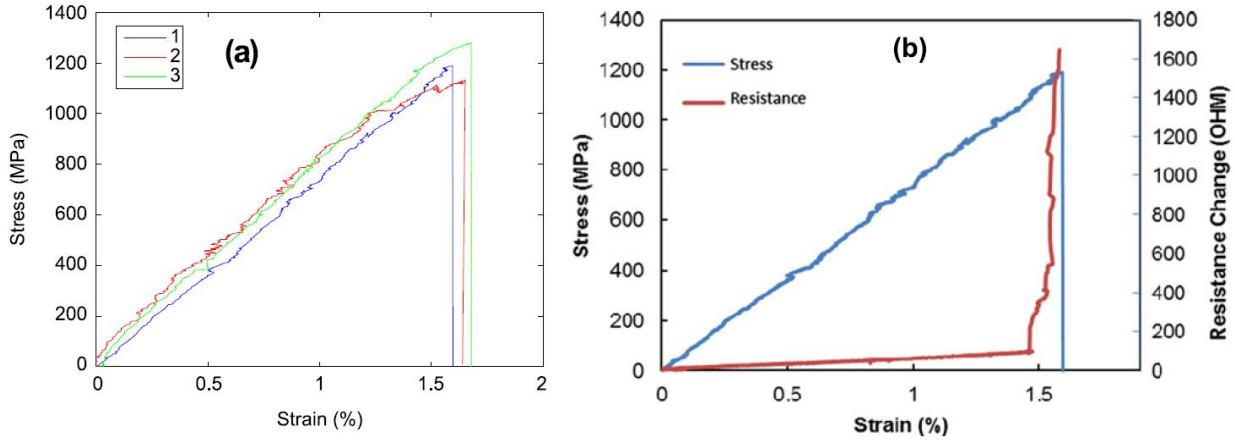

Figure A.0.6: Test curves for tensile test coupons: (a) tensile test curves for three samples; (b) synchronized tensile test curve and resistance response curve of the CNT sensor thread for one test coupon.

These tests showed that CNT thread provides a simple way to measure the tensile strain. A conventional strain gage was used to provide a baseline strain measurement to verify the accuracy of CNT thread as a strain sensor. Since the CNT sensor thread is a piezoresistive material, it is an excellent micro-sensor for measuring strain and distributed strain in composite structures. The CNT thread is either bonded on the surface of composite structures or embedded inside composite structures after being co-cured with epoxy. The typical diameter of our CNT thread is approximately 20~25 μm, only around 3 times bigger than a single carbon fiber. The integration of CNT thread onto the composite does not affect the integrity of the composite structure. The CNT thread sensor also does not debond from the host composite structure. This is important for monitoring composite structures that are operating in vibrational environments.

The gage factor of the CNT thread has to be calculated before it can be used as a strain sensor. The equation used to compute the gage factor is:

$$GF = \frac{\Delta R/R}{\varepsilon} \tag{1}$$

Here the ratio of normalized resistance (the change in resistance divided by the original resistance) to strain could be calculated from the slope of the linear portion of the resistance curve in Figure A.0.6(b) and the initial resistance. The gage factors for the three CNT sensor threads are listed in Table A-1. The mean value of the gage factor in the initial linear portion is 0.91.

The individual gage factor could be used as a material property of the CNT sensor thread. The strain that CNT sensor thread measured can be calculated with the individual gage factor via (1). Figure A.0.7 shows the comparison of strain measurement between the CNT sensor thread and the strain gage for the three test coupons separately.

The relative strain measurement errors between the CNT thread and strain gage for the three test coupons were calculated at each data point and the mean value of the relative strain

measurement error was calculated as:

$$\delta = \frac{1}{n}\sum_{i=1}^{n}\frac{\varepsilon_i^{CNT}-\varepsilon_i^{sg}}{\varepsilon_i^{sg}} \quad (2)$$

Here, δ is the mean relative strain measurement error between CNT sensor thread and strain gage, n is the number of total data points, and ε_i^{CNT} and ε_i^{sg} are individual strains measured by the CNT sensor thread and strain gage respectively. The mean relative strain error between the CNT sensor thread and strain gage is 5.9 %, and is shown in Table A-1. The strain measurement from the CNT sensor thread for the three test coupons was close to the measurement from the strain gage. The difference of the two measurements comes from the small orientation error of the CNT thread or strain gage during the bonding process and the calculation error for the mean gage factor of the CNT thread. In addition, the length of the CNT sensor thread bonded on the tensile test coupon is around 101 mm while the gage length of the strain gage is only around 10mm. The strain gage and the CNT sensor thread measure the average strain in the gage length that they cover. Therefore, the difference in gage lengths of the CNT sensor thread and strain gage contributes to the difference of the two measurements.

Overall, this result shows the potential of CNT thread to be used as a strain sensor. More tests are needed in order to determine the effective strain measurement limit of the CNT thread. In addition, the temperature compensation of CNT thread will be completed in the future. Also, the design of the sensor thread (diameter, twist angle, doping, and others) can be tailored to provide the strain to failure needed for monitoring different types of materials.

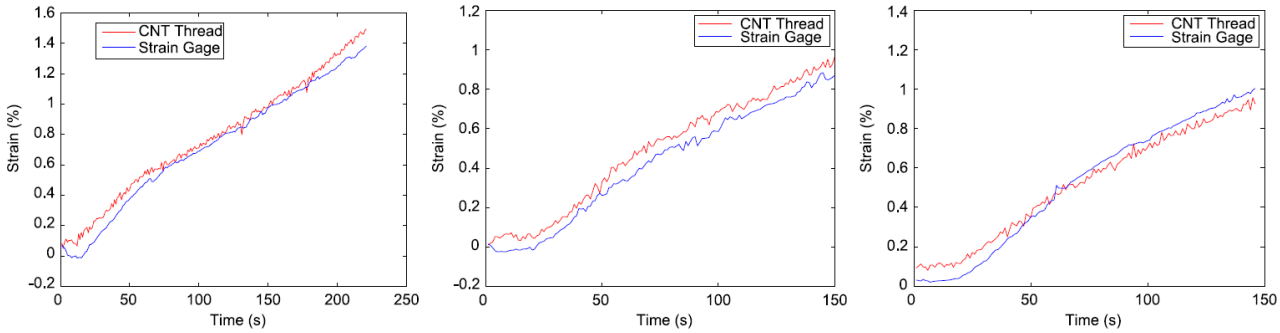

Figure A.0.7: Strain measurement of CNT sensor thread and a strain gage for three test coupons with the abscissa representing time and the ordinate representing strain in percentage.

Table A-1: Mechanical properties of IM7 composite coupons (0°, 90°)s with surface mounted CNT sensor thread

	E(GPa)	σ_u(MPa)	ε_u(%)	Gage Factor	Strain Measurement Error (%)
Sample 1	77.2	1189.0	1.58	0.79	6.0
Sample 2	79.9	1132.8	1.65	0.86	6.6
Sample 3	80.8	1279.2	1.70	1.07	5.2
Mean	79.3	1200.3	1.64	0.91	5.9
STDEV	1.87	73.9	0.06	0.15	0.7

3.2 Impact Testing

3.2.1 First Impact Test

The impact test consisted of two strikes at the same strike point from the impact hammer. The hammer was lifted at an angle of around 60° to the ground and then released for striking. The strike point for both strikes was the node formed by row sensor R1 and column sensor C2 (schematically shown in Figure A.0.4). The impact hammer was raised to the same height (0.7 m) over the impact rig for both impacts. The potential energy of the hammer was 19.6 Nm. The impact occurs directly on the sensor thread to study the sensitivity of the thread to damage. The size of a square unit cell of the grid pattern is the smallest damage that could occur without detection if the impact occurred in the center of the square which is the farthest distance away from the sensor thread. The grid size in this experiment was 10 mm x 10 mm. Even though the impact may not be directly on the sensor thread, damage could propagate either at the time of impact or later to the sensor thread and be detected. Detecting damage that occurs away from the sensor thread was not studied in this paper and is a subject for future work. Detection of arbitrarily small damage can be achieved by creating a grid pattern with as small of unit cells as desired. If only detection of damage is desired on a panel, only one signal channel is needed for an arbitrary number of sensor threads arranged in a grid pattern. To locate the damage, multiple signal channels can be used with multiplexing. Thus only one channel of data acquisition can be multiplexed over multiple sensor threads arranged in rows and columns to detect and locate damage of an arbitrary size. Future work is to automate a technique for applying the sensor thread on large structures.

Figure A.0.8(a) shows the acceleration and resistance response after the first strike. The first strike impulse duration is only 0.007 s and the maximum vertical component of the acceleration of the hammer is around 250 g. The row sensor R1 captured the first impact load with an impulse in the resistance curve (row sensor curves in Figure A.0.8(a)). Then resistance of row sensor R1 oscillated and returned to its original resistance after the impact load disappeared. All the column sensors C1-C4 captured the first impact load (column sensor curves in Figure A.0.8(a)) in a similar way to the resistance response of row sensor R1.

The normalized mean nodal resistance change, defined in equation (3), during both impact tests was calculated and plotted as a bar chart in Figure A.0.9(a). In the first impact test, the first row CNT sensor thread showed a higher normalized mean nodal resistance change than the other sensors while the column CNT sensor threads showed relatively even normalized mean nodal resistance changes. The normalized mean nodal resistance change after the first hammer strike is listed in Table A-2. Here the steady resistance instead of peak resistance at the moment of impact is used to calculate the normalized mean nodal resistance change as:

$$\overline{\Delta R_{ij}} = \frac{1}{2}\left(\frac{R_i^{steady} - R_i^{initial}}{R_i^{initial}} + \frac{R_j^{steady} - R_j^{initial}}{R_j^{initial}}\right), \quad i,j = 1,2,3,4 \tag{3}$$

Here, R^{steady} and $R^{initial}$ are the steady (final) and initial resistances of the CNT sensor thread, respectively. Subscripts *i* and *j* designate the resistances from a row of CNT sensor thread and a column of CNT sensor thread, respectively.

The maximum normalized mean nodal resistance change is only 0.035 at the node formed by

row sensor thread R1 and column sensor thread C2 as shown in Table A-2. There is no substantial increase of normalized mean nodal resistance change at each node after first impact strike thus indicating no significant damage occurred at the sensor thread.

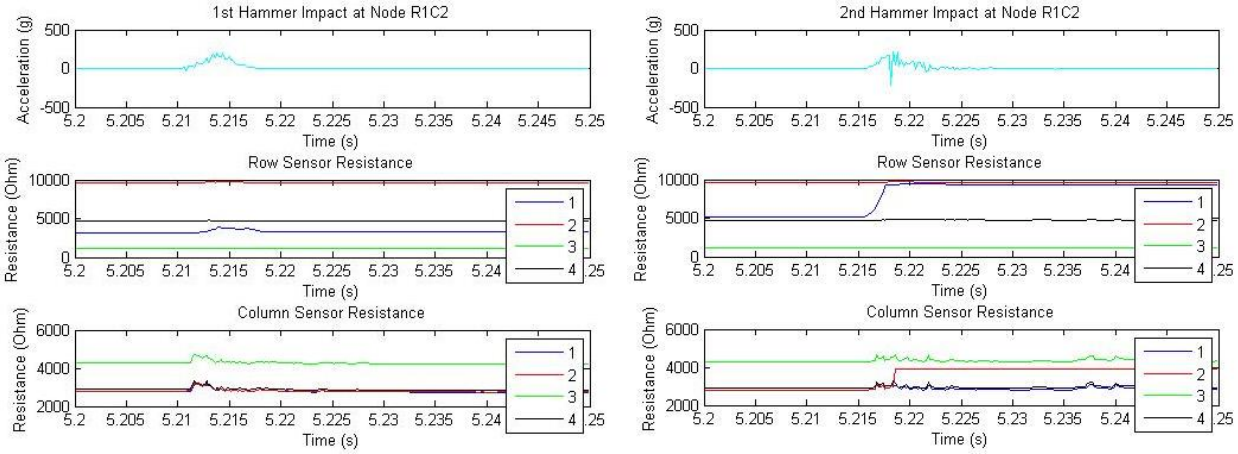

Figure A.0.8: The response of the hammer acceleration and impact resistance curves of the CNT sensor threads
after both strikes of the hammer

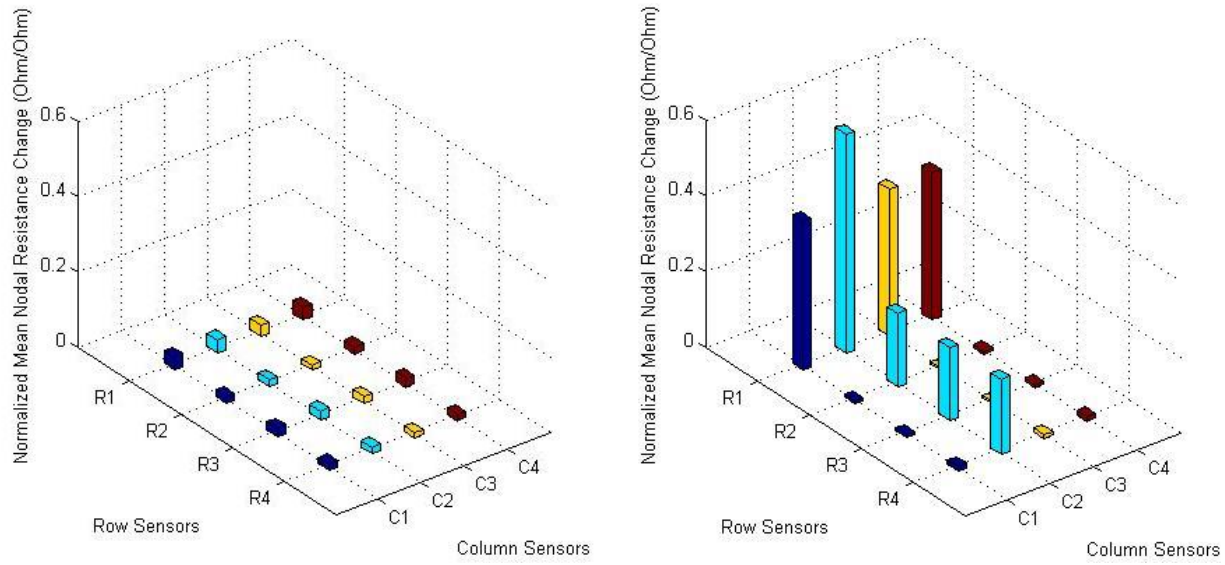

Figure A.0.9: Normalized mean nodal resistance change of the CNT sensor threads: (a) after the first hammer impact strike; (b) after the second hammer impact strike.

Table A-2: Normalized mean nodal resistance change of the CNT sensor threads after both impact strikes at all nodes

	First impact test				Second impact test			
	C1	C2	C3	C4	C1	C2	C3	C4
R1	0.034	0.035	0.030	0.035	0.390	0.576	0.388	0.390
R2	0.018	0.018	0.014	0.018	0.008	0.193	0.005	0.007
R3	0.024	0.024	0.020	0.024	0.008	0.193	0.005	0.007
R4	0.017	0.018	0.013	0.018	0.012	0.198	0.010	0.012

3.2.2 Second Impact Test

The CNT sensor threads captured the second impact. Figure A.0.8(b) shows the acceleration and resistance response curves for the second strike of the hammer. It shows that the duration of the impact load only lasts 0.012 s. There were positive and negative spikes in the acceleration response when the impact load was applied at 5.216 s. The amplitude of the acceleration spikes reduced gradually, followed by oscillation and disappearance of the spikes. The resistances of row sensor R1 and column C2 show an approximate exponential rising from initial values to infinity during the second impact process. Then both resistances of row sensor R1 and column sensor C2 remained infinite even though the impact load disappeared. This means the CNT sensor thread R1 and C2 was damaged/broken due to the second impact load.

The normalized mean nodal resistance change for the second strike of the hammer was calculated and plotted as a bar chart in Figure A.0.9(b). The first row of CNT sensor thread showed a larger change in normalized mean nodal resistance than the other row sensors during the second strike while the second column of CNT sensor thread showed a larger change in normalized mean nodal resistance than the other column sensors. The normalized mean nodal resistance change after the second strike of the hammer is listed in Table A-2. The maximum normalized mean nodal resistance change of 0.58 occurred at the node formed by row sensor thread R1 and column sensor thread C2. This value is between 3 to 115 times higher than the value of its neighboring nodes. This clearly indicates sensor thread damage/breakage at the node formed by row sensor R1 and column sensor C2, thus locating the damage. The amplitude of the resistance change at the nodes is a measure of the severity of damage. Damage can also be partially characterized by the amplitude pattern in Figure A.0.9(b), which shows whether the damage is localized or distributed. A finer grid pattern might also show the shape of the damage, e.g. an oval pattern indicating delamination or a linear pattern indicating cracking.

As confirmation of the damage, Figure A.0.10 shows the failure on the back side of the IM7 composite panel after impact testing. Both impact strikes lead to damage to the composite panel and the final damage is the accumulation of damage from both strikes. The damage to the back of the panel indicates that sensor thread placed on the back side of the panel could detect damage due to impacts on the outside surface of the panel.

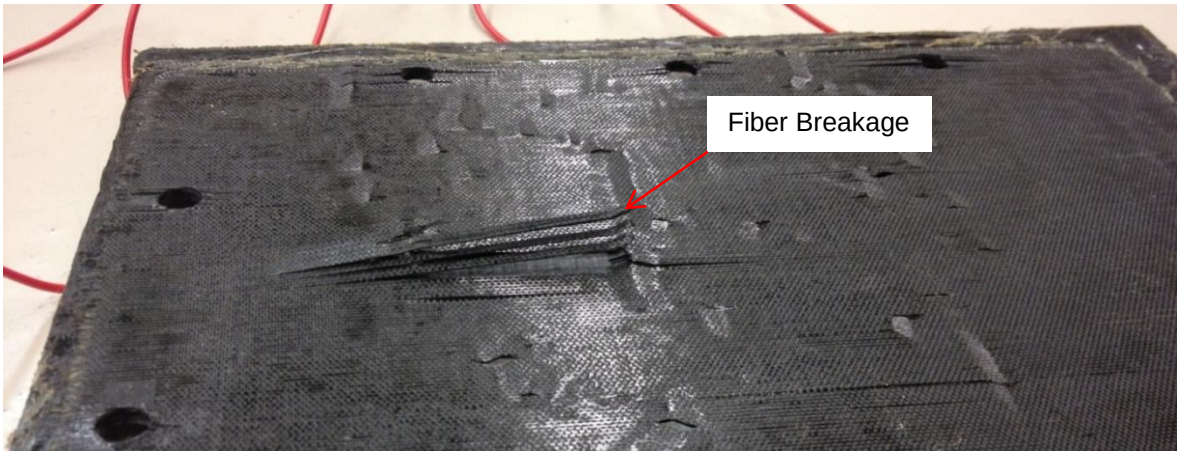

Figure A.0.10: The failure on the back surface of a symmetric eight-ply (0°,90°,0°,90°)s IM7/977-3 composite panel after impact testing. The front side of the panel does not have visual indentation damage.

The performance of the CNT sensor thread in the impact test shows it is an excellent build-in piezoimpedance sensor for SHM applications. CNT sensor thread has high sensitivity to detecting and locating damage, high accuracy for strain measurement and is low cost. There are various parameters available for design of the sensor system [1-4]. The CNT sensor thread system can be surface mounted, as in the current study, or embedded in the composite. Additionally, the architecture of the CNT sensor thread can be in the plane of the composite to detect fiber breakage or stitched through the thickness of the composite to have high sensitivity to delamination and cracking. The CNT sensor thread is a new type of distributed sensor material and there are a lot of opportunities to develop new sensor systems tailored to specific applications. The SHM sensor development process itself consists of sensor fabrication, sensor system architecture (parallel, series, channel count, multiplexing), bonding the sensor to the composite structure, data acquisition and analysis. The prototype SHM sensor system described here could be improved in all areas and in particular by eliminating the wiring to the data acquisition system, improving the tailoring of properties of the sensor material, and investigating optimizing sensor configurations for different applications.

3.3 Printed Wiring

In the current prototype SHM sensor system, all the CNT threads were soldered to conventional wires and then connected to individual Wheatstone circuit boards. This wiring method may be fine for static applications, but is not desirable for SHM applications in aircraft due to the additional weight from wires and the possible falling-off of wires in a high vibration environment. Accordingly, printed circuit wiring has been developed to replace conventional wires. All the channel terminals and common ground wiring were replaced by printed aluminum leads. An AutoCAD layout was designed for the 206 mm square IM7 composite panels as shown in Figure A.0.11(a). Each aluminum lead extends one channel terminal or common ground to one corner of the IM7 composite panel, where a 9-pin-to-socket connector is soldered. This connector is then connected to the Wheatstone circuit boards. The width of the leads is 762 microns and the spacing between leads is 1.02 mm for the purpose of even aluminum deposition. This AutoCAD layout of leads is converted to a mask for aluminum deposition by cutting on a transparent film via a 50 W laser cutting machine (Universal Laser Systems 30). The mask is bonded on the IM7 composite panel with adhesive and the aluminum deposited. The thickness of the aluminum deposition is 5 μm. The advantage of this method is that the aluminum leads are directly painted on the composite panel without any additional materials and little extra weight. Figure A.0.11(a) shows a 4x4 rectangular pattern of CNT sensor thread (8 channels of data acquisition) for locating small damage on the panel. In the case where only the detection of damage is of interest, and the location of damage is not needed or can be determined using a NDE method, a single meandering CNT sensor thread can be used with one channel of data acquisition, Figure A.0.11(b). If the dynamic response of the panel is not of interest, then the 8-channel system can be multiplexed thus requiring only one channel of data acquisition thus simplifying the data acquisition module and reducing the cost.

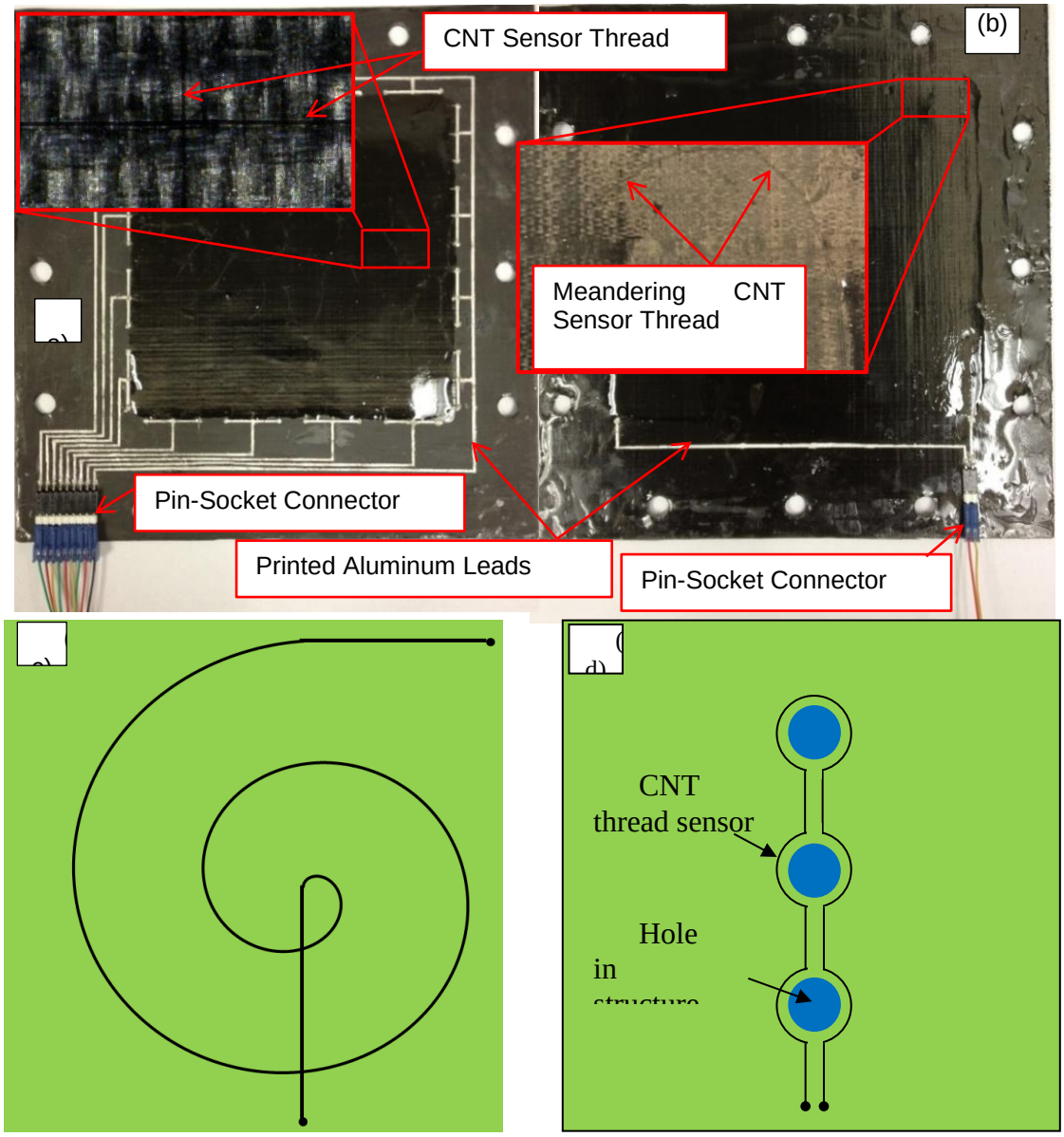

Figure A.0.11: Improvement of wiring and sensor design: (a) IM7 composite panel with printed circuit leads and surface mounted CNT sensor threads. The printed aluminum circuit leads were connected to a Wheatstone bridge circuit board via a pin-socket connector; (b) IM7 composite panel with printed circuit leads and a surface mounted meandering CNT sensor thread; (c) a spiral CNT sensor thread for large monitoring coverage; (d) a single CNT sensor thread for monitoring the integrity of multiple fastener holes.

The CNT sensor thread can be any shape and its design can be based on the target location and target structure. Figure A.0.11(c) and (d) show two examples of CNT sensor thread for damage detection. The CNT thread is curved into a spiral shape to increase the damage detection coverage in Figure A.0.11(c). In Figure A.0.11(d), the CNT thread is placed around the circumferences of three fastener holes in one composite structure. This CNT sensor thread can monitor the integrity of these three fastener holes during the operation of the composite structure. The sensor thread can also measure average strain over the length of the sensor thread. Interpreting the average strain measurement related to the distributed strain in the structure is a new area of research, especially for dynamic strain.

3.4 Suggestions for Real Life Practical Applications of Sensor Thread

The potential for CNTs to be used as sensors is greatly expanding as both the fields of SHM and CNTs continue to mature. One of the most critical applications for the use of CNTs as sensors is the Aerospace industry. As increasingly more aircraft are being made of composites due to strength and weight requirements the ability to monitor these structures is moving to the forefront. Composites typically fail suddenly and catastrophically so the ability to monitor and manage their structural integrity is of utmost importance. Since CNTs have the potential to be used as sensors and add very little weight, improve strength and are becoming affordable for use in application, they are ideal candidates for future sensors.

Another way in which CNT sensors can be used is as an enabler for condition-based maintenance (CBM). As the cost of aircraft and other composite structures increases so does the cost to maintain and repair those structures. By implementing CNT sensors as a tool in CBM the total cost of ownership is reduced. Additionally, once CBM is implemented and acceptable levels of reliability of SHM systems are achieved, predictive maintenance can be realized. The potential of SHM systems to attain predictive maintenance not only reduces cost but also increases reliability and safety.

In addition to sensing capabilities of CNTs, there are several other properties of CNTs that can be utilized for application in other areas. CNTs offer improved strength properties which can be used in civil structures such as strengthening concrete or reinforcing elastomers. Furthermore, CNTs have resistive properties which can be used for thermography or other heating applications. The ability of CNTs embedded in rubber has also been documented [37] to provide EMI shielding capabilities, which is of great interest in defense applications.

Finally, where other sensors fail, due to their inferior material properties, CNT sensors can be used as complementary or redundant sensors. One such example is in monitoring hot spots or fatigue tests for composite components, where the composite part often outlasts a traditional foil strain gage, leading to increased costs of testing and the introduction of an additional source of uncertainty to results. All the aforementioned examples only begin to scratch the surface of the applications and advantages of the use of CNTs as sensors.

4 Conclusions

The performance of CNT sensor thread in quasi-static and impact testing shows it is an excellent build-in piezoresistive sensor for SHM applications. It has high sensitivity to locate damage and detect delamination, high accuracy to measure strain and low cost. A prototype SHM system was developed that includes CNT thread, a technique for bonding CNT sensor thread to composite panel, a customized 8-channel Wheatstone bridge measurement circuit, and a Labview data analysis system and algorithm. This prototype SHM system successfully measured distributed strain and detected damage on composite panels. Sensor thread is being improved (dielectric coating) and is becoming available commercially. The overall conclusion from the work described in this paper is that carbon nanotube sensor thread is a simple, reliable, accurate, and practical technique for structural health monitoring.

Acknowledgements

The authors would like to thank the US Navy and General Nano LLC for their financial support (grant number: N683335-13) and Boeing Company for providing the IM7/977-3 prepreg materials for this research.

References

[1] Abot J L, Song Y, Sri Vatsavaya M, Medikonda S, Kier Z, Jayasinghe C, Rooy N, Shanov V N and Schulz M J 2010 Delamination detection with carbon nanotube thread in self-sensing composite materials. *Compos. Sci. Technol.* 70 1113-9

[2] Song Y, Mast D, Suberu B, Jayasinghe C, Li W, Dandino C, Abot J, Shanov V and Schulz M 2012 *Basics of Carbon Nanotube Materials for Structural Applications. Nanotechnologies and Smart Materials for SHM* ed A Catalano, G Fabbrocino and C Rainieri (Campobasso, Italy: Arti Grafiche La Regione Editrice)

[3] Hehr A, Song Y, Suberu B, Sullivan J, Shanov V and Schulz M 2013 Carbon nanotube sensor thread for structural health monitoring of composite materials *Nanotube Superfiber Materials, Changing Engineering Design* ed M J Schulz, V Shanov and J Yin (Amsterdam: Elsevier) chapter 24 pp 671-712

[4] Hehr A 2013 Embedded carbon nanotube thread strain and damage sensor for composite materials *MSc Thesis* University of Cincinnati https://etd.ohiolink.edu/

[5] Hehr A, Schulz M, Shanov V, Song Y 2014 Embedded carbon nanotube thread piezoresistive strain sensor performance *Sensor Rev.* 34 209-19

[6] Hehr A, Schulz M, Shanov V and Song A 2014 Micro-crack detection and assessment with embedded carbon nanotube thread in composite materials *Structural Health Monitoring* at press

[7] Adams D, Staszewski W, Giurgiutiu V, Boller C, Chang F-K and Fujino Y (ed) 2009 *Encyclopedia of Structural Health Monitoring* vol 3 (Chichester: Wiley) chapter 67, pp 1189-210

[8] Roach D 2006 Health monitoring of aircraft structures using distributed sensor systems. In: *Joint DoD/NASA/FAA Aging Aircraft Conf. Proc.* (Atlanta GA)

[9] Udd E (ed) 1990 *Fiber Optic Sensors: An Introduction for Engineers and Scientists* (New York: Wiley)

[10] Kim H S, Ghoshal A, Chattopadhyay A and Prosser W H 2004 Development of embedded sensor models in composite laminates in structural health monitoring *J. Reinf. Plast. Compos.* 23 1207–40

[11] Sundaresan M J, Ghoshal A and Schulz M J 2002 Sensor array system *US Patent* 6399939B1

[12] Todoroki A, Tanaka Y, Shimamura Y 2003 Luminance change method for strain and matrix cracking monitoring of glass/epoxy composites with EL backlight *Compos. Sci. Technol.* 63 273–81

[13] Schulte K and Baron C 1989 Load and failure analyses of CFRP laminates by means of electrical resistivity measurements *Compos. Sci. Technol.* 36 63–76

[14] Wang X and Chung D D L 1997 Sensing delamination in a carbon fiber polymer-matrix composite during fatigue by electrical resistance measurement *Polym. Compos.* 18 692–700

[15] Todoroki A and Suzuki H 2000 Health monitoring of internal delamination cracks for

graphite/epoxy composites by electric potential method *Appl. Mech. Eng.* 5 283–94
[16] Todoroki A, Tanaka M and Shimamura Y 2002 Measurement of orthotropic electric conductance of CFRP laminates and analysis of the effect on delamination monitoring with electric resistance change method *Compos. Sci. Technol.* 62 619–28
[17] Todoroki A, Tanaka M and Shimamura Y 2003 High performance estimations of delamination of graphite/epoxy laminates with electric resistance change method *Compos. Sci. Technol.* 63 1911–20
[18] Todoroki A, Tanaka M and Shimamura Y 2005 Electrical resistance change method for monitoring delaminations of CFRP laminates: effect of spacing between electrodes *Compos. Sci. Technol.* 65 37–46
[19] Todoroki A, Tanaka M and Shimamura Y 2007 Damage monitoring of a thick CFRP beam using electrical impedance changes *Key Eng. Mater.* 353–358 1298–301
[20] Thostenson E T and Chou T-W 2008 Real-time *in situ* sensing of damage evolution in advanced fiber composites using carbon nanotube networks *Nanotechnology* 9 215713
[21] Thostenson E T and Chou T-W 2006 Carbon nanotube networks: sensing of distributed strain and damage for life prediction and self healing *Adv. Mater.* 18 2837–41
[22] Fiedler B, Gojny F H, Wichmann M H G, Bauhofer W and Schulte K 2004 Can carbon nanotubes be used to sense damage in composites? *Ann. Chim.- Sci. Mater.* 29 81–94
[23] Muto N, Yanagida H, Nakatsuji T, Sugita M and Ohtsuka Y 1993 Preventing fatal fractures in carbon-fibre–glass-fibre-reinforced plastic composites by monitoring change in electrical resistance *J. Am. Ceram. Soc.* 76 875–9
[24] Wang X and Chung D D L 1996 Continuous carbon fibre epoxy–matrix composite as a sensor of its own strain *Smart Mater. Struct.* 5 796–800
[25] Alamusi, Hu N, Fukunaga H, Atobe S, Liu Y and Li J 2011 Piezoresistive strain sensors made from carbon nanotubes based polymer nanocomposites *Sensors* 11 10691-723
[26] Hu N, Karube Y, Arai M, Watanabe T, Yan C, Li Y, Liu Y and Fukunaga H 2010 Investigation on sensitivity of a polymer/carbon nanotube composite strain sensor *Carbon* 48 680-7
[27] Abot J, Alosh T and Belay K 2014 Strain dependence of electrical resistance in carbon nanotube yarns *Carbon* 70 95-102
[28] Hu B, Hu N, Cai Y, Yuan W, Yan C, Cai Y, Furukawa M and Matsushita M 2013 Performance characterization of VGCF/epoxy nanocomposite sensors under static load cycles and in static structural health monitoring *Smart Mater. Struct.* 22 045008
[29] Hu N *et al* 2013 Ultrasensitive strain sensors made from metal-coated carbon nanofiller/epoxy composites *Carbon* 51 202-12
[30] Sebastian J, Schehl N, Bouchard M, Boehle M, Li L, Lagounov A and Lafdi K 2014 Health monitoring of structural composites with embedded carbon nanotube coated glass fiber sensors *Carbon* 66 191-200
[31] Christner C, Horoschenkoff A and Rapp H 2012 Longitudinal and transverse strain sensitivity of embedded carbon fiber sensor *J. Compos. Mater.* 47 155-67
[32] Jakubinek M B, Johnson M B, White M A, Jayasinghe C, Li G, Cho W, Schulz M J and Shanov V 2012 Thermal and electrical conductivity of array-spun multi-walled carbon nanotube yarns *Carbon* 50 244-8
[33] Li W, Jayasinghe C, Shanov V and Schulz M 2011 Spinning carbon nanotube nanothread under a scanning electron microscope *Materials* 4 1519-27
[34] Jayasinghe C, Chakrabarti S, Schulz M J and Shanov V 2011 Spinning yarn from long

carbon nanotube array *J. Mater. Res.* 26 645-51
[35] Kluener J 2011 Characterization of CNT thread and application for firefighters garment *MSc Thesis* University of Cincinnati
[36] Nanoworld Laboratory 2014 *Carbon Naotube Thread and Sheet Available for Purchase for Applications Evaluation* (Cincinnati, OH: University of Cincinnati) http://www.min.uc.edu/nanoworldsmart/
[37] Kim Y A *et al* 2006 Fabrication of aligned carbon nanotube-filled rubber composite *Scr. Mater.* 54 31-5

APPENDIX B

MATLAB CODE FOR ANALYTICAL ANALYSIS AND EXPERIMENTAL DATA ACQUISITION AND ANALYSIS

B1: Chapter Two: Multiscale Modeling Homogenized Modulus Code

```
close all;
clear all;
clc;

%% Define material properties
%Set counter
ii=1;

%CNT size
a=10;                %nm
b=2;                 %nm

%Longitudinal Direction
Em=28.5*10^6;         %N/m^2
Ei=825*10^9;         %N/m^2
vm=0.4;
vnt=0.28;

%Transverse Direction
Eit=4.5*10^9;        %N/m^2
vntt=0.38;

%Shear Modulus
Gnt=8*10^9;          %N/m^2

%% Generate Tensor Matrices
%Matrix (Rubber)
Sm1111=1/(2*(1-vm))*((b^2+2*a*b)/(a+b)^2+(1-2*vm)*b/(a+b));
Sm2222=1/(2*(1-vm))*((a^2+2*a*b)/(a+b)^2+(1-2*vm)*a/(a+b));
Sm3333=0;
Sm1122=1/(2*(1-vm))*(b^2/(a+b)^2-(1-2*vm)*b/(a+b));
Sm2233=1/(2*(1-vm))*2*vm*a/(a+b);
Sm2211=1/(2*(1-vm))*(a^2/(a+b)^2-(1-2*vm)*a/(a+b));
Sm3311=0;
Sm3322=0;
Sm1212=1/(2*(1-vm))*((a^2+b^2)/(2*(a+b)^2)+(1-2*vm)/2);
Sm1133=1/(2*(1-vm))*2*vm*b/(a+b);
Sm2323=a/(2*(a+b));
Sm3131=b/(2*(a+b));
%Eshelby Tensor for Matrix with ellipsoidal inclusions
```

```
Sm=[Sm1111 Sm1122 Sm1133 0 0 0;Sm2211 Sm2222 Sm2233 0 0 0;Sm3311 Sm3322
Sm3333 0 0 0;0 0 0 Sm2323 0 0;0 0 0 0 Sm3131 0;0 0 0 0 0 Sm1212];
%Eshelby Tensor for Matrix with spherical inclusions
Sms1111=(7-5*vm)/(15*(1-vm));
Sms1122=(5*vm-1)/(15*(1-vm));
Sms1212=(4-5*vm)/(15*(1-vm));
Sms=[Sms1111 Sms1122 Sms1122 0 0 0;Sms1122 Sms1111 Sms1122 0 0 0;Sms1122
Sms1122 Sms1111 0 0 0;0 0 0 Sms1212 0 0;0 0 0 0 Sms1212 0;0 0 0 0 0 Sms1212];
%Stiffness Tensor for isotropic material
Cm=Em/((1+vm)*(1-2*vm))*[1-vm vm vm 0 0 0;vm 1-vm vm 0 0 0;vm vm 1-vm 0 0 0;0
0 0 (1-2*vm)/2 0 0;0 0 0 0 (1-2*vm)/2 0;0 0 0 0 0 (1-2*vm)/2];
%Stiffness Tensor for plane stress isotropic material for spherical incl
Cms=Em/((1+vm)*(1-2*vm))*[1-vm vm vm 0 0 0;vm 1-vm vm 0 0 0;vm vm 1-vm 0 0
0;0 0 0 (1-2*vm)/2 0 0;0 0 0 0 (1-2*vm)/2 0;0 0 0 0 0 (1-2*vm)/2];

%Inclusion (CNTs)
Si1111=1/(2*(1-vnt))*((b^2+2*a*b)/(a+b)^2+(1-2*vnt)*b/(a+b));
Si2222=1/(2*(1-vnt))*((a^2+2*a*b)/(a+b)^2+(1-2*vnt)*a/(a+b));
Si3333=0;
Si1122=1/(2*(1-vnt))*(b^2/(a+b)^2-(1-2*vnt)*b/(a+b));
Si2233=1/(2*(1-vnt))*2*vnt*a/(a+b);
Si2211=1/(2*(1-vnt))*(a^2/(a+b)^2-(1-2*vnt)*a/(a+b));
Si3311=0;
Si3322=0;
Si1212=1/(2*(1-vnt))*((a^2+b^2)/(2*(a+b)^2)+(1-2*vnt)/2);
Si1133=1/(2*(1-vnt))*2*vnt*b/(a+b);
Si2323=a/(2*(a+b));
Si3131=b/(2*(a+b));
%Eshelby Tensor for Inclusion with ellipsoidal inclusions
Si=[Si1111 Si1122 Si1133 0 0 0;Si2211 Si2222 Si2233 0 0 0;Si3311 Si3322
Si3333 0 0 0;0 0 0 Si2323 0 0;0 0 0 0 Si3131 0;0 0 0 0 0 Si1212];
%Stiffness Tensor for transversely isotropic ellipsoid inclusion material
S_i=[1/Ei -vnt/Eit -vnt/Eit 0 0 0;-vnt/Ei 1/Eit -vntt/Eit 0 0 0;-vnt/Ei -
vntt/Eit 1/Eit 0 0 0;0 0 0 2*(1+vntt)/Eit 0 0;0 0 0 0 1/Gnt 0;0 0 0 0 0
1/Gnt];
Ci=inv(S_i);
%Stiffness Tensor for isotropic spherical inclusion material
Cis=Ei/((1+vnt)*(1-2*vnt))*[1-vnt vnt vnt 0 0 0;vnt 1-vnt vnt 0 0 0;vnt vnt
1-vnt 0 0 0;0 0 0 (1-2*vnt)/2 0 0;0 0 0 0 (1-2*vnt)/2 0;0 0 0 0 0 (1-
2*vnt)/2];

%Mori-Tanaka Influence Tensor Calculation
I=eye(6,6);
%Ellipsiod Inclusion
Ao=inv(I+Sm*inv(Cm)*(Ci-Cm));
%Spherical Inclusion
Aos=inv(I+Sms*inv(Cms)*(Cis-Cms));
%Inverse Mori-Tanaka Influence Tensor Calculation
Aoi=inv(I+Si*inv(Ci)*(Cm-Ci));

%% Pre-allocate for speed
a=zeros(1,19);
E_mt=zeros(1,19);
E_hsu=zeros(1,19);
E_hsl=zeros(1,19);
E_l=zeros(1,19);
```

```
E_v=zeros(1,19);
E_r=zeros(1,19);
E_mts=zeros(1,19);
E_hsls=zeros(1,19);

%% Volume Fraction Iteration for all methods
for ai=0.05:0.05:0.95
    am=1-ai;
    a(ii)=ai;

    %Method 1: Mori-Tanaka Method
    Ai=inv(ai*I+am*inv(Ao)+ai*Ao*inv(Ao));
    E_hom1=Cm+ai*(Ci-Cm)*Ai;
    E_mt(ii)=E_hom1(1,1)/Em;

    %Method 2: Hashin-Shtrikman Bounds
    E_hom2=Ci+am*inv(inv(Cm-Ci)+ai*Si*inv(Ci));
    E_hsu(ii)=E_hom2(1,1)/Em;
    E_hom3=Cm+ai*inv(inv(Ci-Cm)+am*Sm*inv(Cm));
    E_hsl(ii)=E_hom3(1,1)/Em;

    %Method 3: Lielens Method
    Aii=inv(am*I+ai*inv(Aoi)+am*Aoi*inv(Aoi));
    E_hom4=Ci+am*(Cm-Ci)*Aii;
    E_hom5=inv((1-(ai+ai^2)/2)*inv(E_hom4)+(ai+ai^2)/2*inv(E_hom1));
    E_l(ii)=E_hom5(1,1)/Em;

    %Method 4: Voight/Reuss Bounds
    E_v(ii)=(ai*Ei+am*Em)/Em;
    E_r(ii)=((ai*Ei^-1+am*Em^-1))^-1/Em;
%     E_r(ii)=((ai*Ei+am*Em)^-1)/Em;

    %Method 5: Sphere vs. Ellipse Assumption Check
    Ais=inv(ai*I+am*inv(Aos)+ai*Aos*inv(Aos));
    E_hom1s=Cms+ai*(Cis-Cms)*Ais;
    E_mts(ii)=E_hom1s(1,1)/Em;
    E_hom3s=Cms+ai*inv(inv(Cis-Cms)+am*Sms*inv(Cms));
    E_hsls(ii)=E_hom3s(1,1)/Em;

    ii=ii+1;
end

%% Figure Generator
figure(1)
plot(a,E_mt,'r','LineWidth',3)
hold on
plot(a,E_hsl,'--c','LineWidth',3)
plot(a,E_l,'b','LineWidth',3)
plot(a,E_r,'m','LineWidth',3)
hold off
title('Comparison of Mori-Tanaka, Hashin-Shtrikman Lower Bound, Lielens and
Reuss Methods')
xlabel('Volume Fraction, a')
ylabel('Normalized Homogenized Modulus (C_{11}/C_{m11})')
legend('Mori-Tanaka','H-S Lower','Lielens','Reuss')
```

```
E_m=Em
E_ro=[E_r(1,1); E_r(1,10); E_r(1,19)]
E_mto=[E_mt(1,1); E_mt(1,10); E_mt(1,19)]
E_vo=[E_v(1,1); E_v(1,10); E_v(1,19)]
```

B2: Chapter Three: Analytical System Efficiency Increase Projections Code

```
close all;
clear all;
clc;

%Define System Parameters
Patm=15;
Ps=50;
Pmax=120;

%Preallocate for speed
% eta_sysa=zeros();
% eta_sysb=zeros();
% eta_sysp=zeros();

%% Efficiency as a function of alpha (Volume Ratio)
ii=1;
for alpha=0.1:0.1:10,
    Pexp=40;
    beta=0.95;
    eta_sysa(ii)=Ps/(Ps+alpha*beta*Pexp);
    eta_sysa_s(ii)=1/(1+alpha);
    ii=ii+1;
end
alpha0=0.1:0.1:10;

%% Efficiency as a function of beta (Accumulator Pressure Ratio)
jj=1;
for beta=Patm/Ps:0.01:1,
    Pexp=40;
    alpha=0.7;
    eta_sysb(jj)=Ps/(Ps+alpha*beta*Pexp);
    jj=jj+1;
end
beta0=Patm/Ps:0.01:1;

%% Efficiency as a function of p_exp
kk=1;
for p_exp=Patm:0.1:Ps,
    alpha=0.7;
    beta=.95;
    eta_sysp(kk)=Ps/(Ps+alpha*beta*p_exp);
    kk=kk+1;
end
p_exp0=Patm:0.1:Ps;

%% Efficiency as a function of Ps
ll=1;
```

```
for Ps=Patm:1:Pmax,
    alpha=0.7;
    beta=.95;
    p_exp=40;
    eta_sysps(ll)=Ps/(Ps+alpha*beta*p_exp);
    ll=ll+1;
end
Ps0=Patm:1:Pmax;

%% Efficiency Plots
figure(1)
subplot(2,2,1)
plot(p_exp0,(1-eta_sysp)*100,'LineWidth',3)
set(gca,'FontWeight','bold')
xlabel('P_e_x_p','fontweight','bold','FontSize',12)
ylabel('% Efficiency Increase','fontweight','bold','FontSize',12)
title('% Efficiency Increase vs Accumulator Expansion
Pressure','fontweight','bold','FontSize',12)

% figure(2)
subplot(2,2,2)
plot(alpha0,(1-eta_sysa)*100,'LineWidth',3)
hold on
plot(alpha0,(1-eta_sysa_s)*100,'-r','LineWidth',3)
hold off
set(gca,'FontWeight','bold')
xlabel('\alpha','fontweight','bold','FontSize',12)
ylabel('% Efficiency Increase','fontweight','bold','FontSize',12)
title('% Efficiency Increase vs Cylinder Volume Ratio
(\alpha)','fontweight','bold','FontSize',12)

% figure(3)
subplot(2,2,3)
plot(beta0,(1-eta_sysb)*100,'LineWidth',3)
set(gca,'FontWeight','bold')
xlim([min(beta0) max(beta0)])
xlabel('\beta','fontweight','bold','FontSize',12)
ylabel('% Efficiency Increase','fontweight','bold','FontSize',12)
title('% Efficiency Increase vs Accumulator Pressure Ratio
(\beta)','fontweight','bold','FontSize',12)

% figure(4)
subplot(2,2,4)
plot(Ps0,(1-eta_sysps)*100,'LineWidth',3)
set(gca,'FontWeight','bold')
xlim([min(Ps0) max(Ps0)])
xlabel('P_s','fontweight','bold','FontSize',12)
ylabel('% Efficiency Increase','fontweight','bold','FontSize',12)
title('% Efficiency Increase vs Supply
Pressure','fontweight','bold','FontSize',12)
```

B3: Chapter Four: Component Efficiency Data Acquisition and Analysis Code

B3.1: Data Acquisition Code

```
%This code controls a three-way valve that fills and exhausts a single
%accumulator and collects data from a flow meter.
%the valve holds first, then fills the accumulator, holds again, and then
exhausts
%the flowmeter collects volumetric flow rate and pressure data in volts

clear all
daq_session5 = daq.createSession('ni');

addAnalogOutputChannel(daq_session5,'cDAQ1Mod1',0:1,'Voltage'); %creates two
analog output channels for the ao0 and ao1 pins on the NI 9264
addAnalogInputChannel(daq_session5,'Dev9',0:1,'Voltage'); %creates two analog
input channels for the ai0 and ai1 pins on the NI 9215


daq_session5.Rate = 1000;

daq_session5.Channels(3).Coupling = 'DC'; %sets DC coupling for both input
channels
daq_session5.Channels(4).Coupling = 'DC';

fill_time = .5; %seconds
hold_time = 2; %seconds
exhaust_time = 2; %seconds

fill_samples = fill_time*daq_session5.Rate; %# of samples
hold_samples = hold_time*daq_session5.Rate; %# of samples
exhaust_samples = exhaust_time*daq_session5.Rate; %# of samples
cycle_samples = fill_samples + 2*hold_samples + exhaust_samples;


num_cycles = 3; %number of cycles run

sample_number = cycle_samples*num_cycles; %total number of samples

output_data = zeros(sample_number,2);
i = 0;
while cycle_samples*i < sample_number,
    for k = 1:1:cycle_samples,
        ind = k+cycle_samples*i;
        if k > hold_samples && k <= hold_samples+fill_samples %if k is in the
fill region, ao0 is set to 5 V
            output_data(ind,1) = 5;
        elseif k > 2*hold_samples+fill_samples, % if k is in the exhaust
region ao1 is set to 5 V
            output_data(ind,2) = 5;
        end % in the hold region, both channels are 0 V
    end
     i = i+1; %i essentially counts the loop iterations
end

queueOutputData(daq_session5,output_data); %assigns the output data matrix to
the session
```

```
disp('start');

[input_data, time] = daq_session5.startForeground();%starts the DAQ session
in the foreground.

exhaust_hold = zeros(exhaust_samples+1,2);
exhaust_hold(:,2) = exhaust_hold(:,2)+5;
exhaust_hold(end,2) = 0;
queueOutputData(daq_session5,exhaust_hold);
disp('exhaust');
daq_session5.startForeground();
```

B3.2: Data Analysis Code

B3.2.1: Data Analysis Fit and Analyze Raw Data Code

```
% The following function computes the mean, standard deviation, and
% polynomial of best fit of degree, d, for a data set [x, y].

function [average, standard_deviation, confidence_interval_95_percent,
curve_of_best_fit, r_squared, r_squared_adjusted] = fit_and_analyze(x, y, d)
average = mean(y);
curve_of_best_fit = polyfit(x, y, d);
sd_matrix = ones(length(x), 5); % [index, value, prediction, deviation,
deviation squared]
for i = 1:1:length(x)
    sd_matrix(i,1) = i;
    sd_matrix(i,2) = y(i);
    sd_matrix(i,3) = polyval(curve_of_best_fit, x(i));
    sd_matrix(i,4) = sd_matrix(i,2) - sd_matrix(i,3);
    sd_matrix(i,5) = (sd_matrix(i,4))^2;
end
summation = sum(sd_matrix(:,5));
standard_deviation = sqrt((1/(length(x)-2))*(summation));
standard_deviation_of_the_mean = standard_deviation/(sqrt(length(y)));
confidence_interval_95_percent = standard_deviation_of_the_mean * 1.96;
y_predict = polyval(curve_of_best_fit, x);
y_resid = y - y_predict;
sum_of_squares_resid = sum(y_resid.^2);
sum_of_squares_total = (length(y) - 1) * var(y);
r_squared = 1 - (sum_of_squares_resid/sum_of_squares_total);
r_squared_adjusted = 1 -
((sum_of_squares_resid/sum_of_squares_total)*((length(y)-1)/(length(y)-d-
1)));
end
```

B3.2.2: Data Analysis Component Efficiency Analysis Code

```
% This is the post-processing analysis script for examining the
% efficiency of the component setup for the advanced pneumatic strain
% energy accumulator.

% The following tasks are necessary in order to analyze the raw voltage
% data and produce efficiency, energy, and other plots:
```

```
%
% 1).  Translate the output voltage data into meaningful physical data.
% 2).  Integrate the volumetric flow/time data to produce volume/time data.
% 3).  Calculate the average contraction/expansion pressures of each cycle;
%      each cycle's input and output energies; and each cycle's efficiency.
% 4).  Trim the calculated data of early cycles whose
%      efficiency/energy/pressure data are not reflective of the
%      accumlator's performance as a whole.  Determine means and standard
%      deviations of the calculated data.
% 5).  Produce plots and figures of the analyzed data.

%%%%%%%%%%%%%%%%%%%%%%%%%%%%%%%%%%%%%%%%%%%%%%%%%%%%%%%%%%%%%%%%%%%%%%%%%%%%%%%

% Task 1: Translate the output voltage data into meaningful physical data.

% The necessary input data must be in the form of an nx2 matrix, where
% column 1 contains the volumetric flow data and column 2 contains the
% pressure data.

% Other necessary information include: the times and numbers of samples
% associated with each stage in the accumlator's cycle sequence (fill,
% hold, exhaust, etc.), the total number of cycles, atmospheric
% pressure relative to a vacuum, and the standard pressure from which the
% mass-flow meter is calibrated.

% Input data is translated into SI units for calculations and converted
% into Imperial units for display purposes.

disp('Start');
disp('Translating Output Data');

volumetric_flow_data = (-30 + 6*input_data(:,1)) * (0.001/60); % Standard
Cubic Meters Per Second
pressure_data = ((16*input_data(:,2)) * 6894.7573); % Pascals
p_atm = 14.696 * 6894.7573; % Pascals
cycle_time = hold_time + fill_time + hold_time + exhaust_time; % The sequence
for one cycle
sample_rate = fill_samples/fill_time; % Samples per second;
cycle_samples = cycle_time * sample_rate; % Number of samples in one cycle
sample_vector = 1:1:length(input_data(:,1));
time_vector = sample_vector * (1/sample_rate);

% pressure_standard = 101320; % Pascals
% temperature_standard = 298.15; % Kelvin
%
% % This bit of script assumes that overall temperature change while the
% % device is operating is linearly increasing.
%
% initial_temperature = 296.04; % for the 500 cycle test
% final_temperature = 297.56; % for the 500 cycle test
%
% temp_vector = zeros(length(time_vector),1);
%
% for i = 1:1:length(time_vector)
```

```
%     temperature = (((final_temperature -
initial_temperature)/(length(time_vector)))*i) + initial_temperature;
%     temp_vector(i,1) = temperature;
% end

data_1 = [time_vector', pressure_data, volumetric_flow_data]; % Compiled,
translated input data

% % Adjusting for pressure and temperature to produce a "true" volumetric
flow:
%
% for i = 1:1:length(data_1(:,3))
%     pressure_i = data_1(i,2);
%     temp_i = temp_vector(i);
%     adjusted_volume = (pressure_standard/pressure_i) *
(temp_i/temperature_standard) * data_1(i,3);
%     data_1(i,3) = adjusted_volume;
% end

%%%%%%%%%%%%%%%%%%%%%%%%%%%%%%%%%%%%%%%%%%%%%%%%%%%%%%%%%%%%%%%%%%%%%%%%%%%%

% Task 2: Integrate the volumetric flow/time data to produce volume/time
data.

% The volumetric flow data is integrated using the trapezoidal method of
% integration.  A running summation of the areas of each trapezoid outlined
% for a given point in time is recorded for that particular point in time
% to form a data set of volume with respect to time.

disp('Integrating Volumetric Flow Data');

running_volume_total = 0; % For the loop
volume_data = zeros((length(volumetric_flow_data)),1); % A blank vector for
data collection

for i = 1:1:(length(volumetric_flow_data) - 1) % The "-1" is essential for
the trapezoidal method of integration
    time_1 = data_1(i,1);
    time_2 = data_1((i+1),1);
    time_diff = abs(time_2 - time_1);
    volumetric_flow_1 = data_1(i,3);
    volumetric_flow_2 = data_1((i+1),3);
    volumetric_flow_diff = volumetric_flow_2 - volumetric_flow_1;
    if volumetric_flow_1 <= volumetric_flow_2
        area_under_curve = ((time_diff) * (volumetric_flow_1)) + ((0.5) *
(time_diff) * (volumetric_flow_diff));
        running_volume_total = running_volume_total + area_under_curve;
        volume_data(i+1,1) = running_volume_total;
    elseif volumetric_flow_1 > volumetric_flow_2
        area_under_curve = ((time_diff) * (volumetric_flow_2)) + ((0.5) *
(time_diff) * (-1)*(volumetric_flow_diff));
        running_volume_total = running_volume_total + area_under_curve;
        volume_data(i+1,1) = running_volume_total;
    else
    end
```

```
end

data_2 = [data_1(:,1), data_1(:,2), volume_data]; % Compiled, includes time,
pressure, and volume data.

% The volume data with respect to time tends to drift linearly upwards as
% time progresses due to uncertainties inherent in the volumetric-flow
% meter's calibration.  To clean the data, this drift must be eliminated.
% This is accomplished in two ways: first, each cycle is deliniated from
% the rest of the data by recording maximum and minimum volumes along a
% cycle's total time and designating each cycle as spanning from minimum
% volume to subsequent minimum volume.  Once each cycle has been
% identified, the volumetric flow data is re-integrated and the volume for
% each cycle is forced to reset to zero at the end of each cycle, thereby
% eliminating any long-term drift in the data.  Second, each cycle is
% individually analyzed using linear regression to subtract out the line of
% best fit determined from points known to be zero.

disp('Eliminating Drift')

% The following script deliniates each cycle by creating an matrix of
% indecies of minimum and maximum volumes.  Each cycle is counted from
% minimum volume to the subsequent minimum volume.

v_min_max_data_1 = zeros((num_cycles + 1), 3); % Pattern: [cycle number, min
index, max index]

for i = 1:1:(num_cycles + 1)
    if i == 1
        min_index = 1;
        v_min = data_2(min_index,3);
        [v_max,max_index] = max(data_2((min_index:1:round((min_index +
(cycle_samples)))),3));
        v_min_max_data_1(i,1) = i;
        v_min_max_data_1(i,2) = min_index;
        v_min_max_data_1(i,3) = max_index;
    elseif i > 1 && i <= (num_cycles - 1)
        previous_max_index = v_min_max_data_1((i-1),3);
        [v_min,min_index] =
min(data_2(((previous_max_index):1:round(((previous_max_index) +
(cycle_samples)))),3));
        min_index = min_index + previous_max_index - 1;
        [v_max,max_index] = max(data_2(((min_index):1:round(((min_index) +
(cycle_samples)))),3));
        max_index = max_index + min_index - 1;
        v_min_max_data_1(i,1) = i;
        v_min_max_data_1(i,2) = min_index;
        v_min_max_data_1(i,3) = max_index;
    elseif i == (num_cycles)
        previous_max_index = v_min_max_data_1((i-1),3);
        [v_min,min_index] =
min(data_2(((previous_max_index):1:(round((length(data_2(:,3))) -
(0.5*cycle_samples)))),3));
        min_index = min_index + previous_max_index - 1;
        [v_max,max_index] =
max(data_2(((min_index):1:(length(data_2(:,3)))),3));
```

```
        max_index = max_index + min_index - 1;
        v_min_max_data_1(i,1) = i;
        v_min_max_data_1(i,2) = min_index;
        v_min_max_data_1(i,3) = max_index;
    elseif i == (num_cycles + 1)
        previous_max_index = v_min_max_data_1((i-1),3);
        [v_min,min_index] =
min(data_2(((previous_max_index):1:(round((length(data_2(:,3))))))),3));
        min_index = min_index + previous_max_index - 1;
        max_index = length(data_2(:,3));
        v_max = data_2(max_index,3);
        v_min_max_data_1(i,1) = i;
        v_min_max_data_1(i,2) = min_index;
        v_min_max_data_1(i,3) = max_index;
    end
end

% The original volumetric-flow data is now re-integrated, reseting the
% running total at the beginning of each new cycle, according to the
% indecies collected in the immediate script above.  The data is
% re-integrated for one cycle, then the cycle is adjusted to account for
% linear drift along the cycle.

running_volume_total = 0;
cycle_volume_data = zeros((v_min_max_data_1((num_cycles + 1),2)),2); %
format: [re-integrated volume data, linearly-adjusted volume data]
cycle_index = 1;

while cycle_index < (num_cycles + 1)

    for i = v_min_max_data_1(cycle_index,2):1:((v_min_max_data_1((cycle_index
+ 1),2)) - 1)
        if i == v_min_max_data_1(cycle_index,2)
            cycle_volume_data(i) = 0;
            running_volume_total = 0;
            time_1 = data_1(i,1);
            time_2 = data_1((i+1),1);
            time_diff = time_2 - time_1;
            volumetric_flow_1 = data_1(i,3);
            volumetric_flow_2 = data_1((i+1),3);
            volumetric_flow_diff = volumetric_flow_2 - volumetric_flow_1;
            if volumetric_flow_1 <= volumetric_flow_2
                area_under_curve = ((time_diff) * (volumetric_flow_1)) +
((0.5) * (time_diff) * (volumetric_flow_diff));
                running_volume_total = running_volume_total +
area_under_curve;
                cycle_volume_data(i+1,1) = running_volume_total;
            elseif volumetric_flow_1 > volumetric_flow_2
                area_under_curve = ((time_diff) * (volumetric_flow_2)) +
((0.5) * (time_diff) * (-1)*(volumetric_flow_diff));
                running_volume_total = running_volume_total +
area_under_curve;
                cycle_volume_data(i+1,1) = running_volume_total;
            else
            end
        else
```

```
            time_1 = data_1(i,1);
            time_2 = data_1((i+1),1);
            time_diff = time_2 - time_1;
            volumetric_flow_1 = data_1(i,3);
            volumetric_flow_2 = data_1((i+1),3);
            volumetric_flow_diff = volumetric_flow_2 - volumetric_flow_1;
            if volumetric_flow_1 <= volumetric_flow_2
                area_under_curve = ((time_diff) * (volumetric_flow_1)) +
((0.5) * (time_diff) * (volumetric_flow_diff));
                running_volume_total = running_volume_total +
area_under_curve;
                cycle_volume_data(i+1,1) = running_volume_total;
            elseif volumetric_flow_1 > volumetric_flow_2
                area_under_curve = ((time_diff) * (volumetric_flow_2)) +
((0.5) * (time_diff) * (-1)*(volumetric_flow_diff));
                running_volume_total = running_volume_total +
area_under_curve;
                cycle_volume_data(i+1,1) = running_volume_total;
            else
            end
        end
    end

    % Now that the volumetric-flow data has been re-integrated, the small
    % drift across a cycle must be addressed.  To do so, the following
    % script identifies points along the cycle where the volumetric flow
    % should, in theory, be zero: at points before the accumulator has
    % started to fill with pressurized air.  To identify these points, the
    % script first identifies the point of maximum volumetric flow along
    % the cycle, then tests each data point from the maximum volumetric
    % flow until the start of the cycle (testing 'backwards' in time, so to
    % speak).  If the difference between the volumetric flows of the test
    % point and the start of the cycle is greater than a given threshold,
    % then the volumetric flow cannot be considered essentially zero, and
    % the next test point is evaluated.  This process continues until a
    % suitible test point has been identified.  If the number of samples
    % between the suitible test point and the start of the cycle isn't
    % significant, than linear regression analysis isn't an opiton and the
    % re-integrated data remains ultimately unchanged.

    [volumetric_flow_max, volumetric_flow_index] =
max(data_1((v_min_max_data_1(cycle_index,2):1:v_min_max_data_1(cycle_index,3)
),3)); % This is the index within the individual cycle
    volumetric_flow_index = volumetric_flow_index +
v_min_max_data_1(cycle_index,2) - 1; % Now, the index has been adjusted
within the entire data set
    minimum_difference = 10e-07;
    minimum_significant_data_points = 10;

    suitible_volumetric_flow_index = 0;

    for j = volumetric_flow_index:-1:v_min_max_data_1(cycle_index,2)
        if data_1(j,3) <= minimum_difference &&
suitible_volumetric_flow_index == 0
            suitible_volumetric_flow_index = j;
        else
```

```
            continue
        end
    end

    % Next, all points of volume data between the start of the cycle to the
    % suitible test point are considered to be of equal volume, zero.  A
    % line of best fit is evaluated through these data points, producing a
    % general trend line upon which all data within the cycle has been
    % superimposed. Expected values for each data point as a function of
    % time can be constructed from this trend line and subtracted out of
    % the data.

    linear_regression_matrix = zeros((length(data_2(:,3))),4); % [time,
volume, time^2, time * volume]

    for k = v_min_max_data_1(cycle_index,2):1:suitible_volumetric_flow_index
        t_k = (k - v_min_max_data_1(cycle_index,2))/sample_rate;
        v_k = cycle_volume_data(k,1);
        linear_regression_matrix(k,1) = t_k;
        linear_regression_matrix(k,2) = v_k;
        linear_regression_matrix(k,3) = t_k^2;
        linear_regression_matrix(k,4) = t_k * v_k;
    end

    % Linear function format: y = A + (B * x)
    A = 0;
    B = 0;
    if (suitible_volumetric_flow_index - v_min_max_data_1(cycle_index,2)) >=
minimum_significant_data_points
        B =
(sum(linear_regression_matrix(:,4)))/(sum(linear_regression_matrix(:,3)));
    end

    for l = (v_min_max_data_1(cycle_index,2) +
1):1:(v_min_max_data_1((cycle_index + 1),2) - 1)
        old_cycle_volume = cycle_volume_data(l,1);
        time_value = (l - v_min_max_data_1(cycle_index,2))/sample_rate;
        linear_volume = A + (B * time_value);
        new_cycle_volume = old_cycle_volume - linear_volume;
        cycle_volume_data(l,2) = new_cycle_volume;
    end

    % The following string script displays the real-time status of this
    % data-cleaning process.

    completed_cycle_number_tag = int2str(cycle_index);
    total_cycle_number_tag = int2str(num_cycles);
    status_tag = ['Drift removed from ' completed_cycle_number_tag ' of '
total_cycle_number_tag ' cycles'];
    disp(status_tag);

    cycle_index = cycle_index + 1;

end
```

```
% Lastly, the re-integrated cycle volume is forced to zero at the end of
% the final cycle and a new data set reflecting the cleaned volume data is
% created.

cycle_volume_data((v_min_max_data_1((num_cycles + 1),2)),1) = 0;
cycle_volume_data((v_min_max_data_1((num_cycles + 1),2)),2) = 0;

data_3 = [data_2((1:1:length(cycle_volume_data(:,2))),1),
data_2((1:1:length(cycle_volume_data(:,2))),2), cycle_volume_data(:,2)]; %
Includes time, pressure, and cleaned volume data

%%%%%%%%%%%%%%%%%%%%%%%%%%%%%%%%%%%%%%%%%%%%%%%%%%%%%%%%%%%%%%%%%%%%%%%%%%%

% Task 3:  Calculate the average contraction/expansion pressures of each
% cycle; each cycle's input and output energies; and each cycle's
% efficiency.

% The final data set is divided again into individual cycles according to
% maximum and minimum volumes before analysis for each cycle can begin.
% This is necessary because adjusting the data to account for linear drift
% isn't perfect and may result in volume values within the cycle that are
% minutely less than zero.  For efficiency calculations, it's prefferable
% to calculate from minimum volume to minimum volume, so a new cycle
% deliniation is necessary.

v_min_max_data_2 = zeros((num_cycles + 1), 3); % Pattern: [cycle number, min
index, max index]

for i = 1:1:(num_cycles + 1)
    if i == 1
        min_index = 1;
        v_min = data_3(min_index,3);
        [v_max,max_index] = max(data_3((min_index:1:round((min_index +
(cycle_samples)))),3));
        v_min_max_data_2(i,1) = i;
        v_min_max_data_2(i,2) = min_index;
        v_min_max_data_2(i,3) = max_index;
    elseif i > 1 && i <= (num_cycles - 1)
        previous_max_index = v_min_max_data_2((i-1),3);
        [v_min,min_index] =
min(data_3(((previous_max_index):1:round(((previous_max_index) +
(cycle_samples)))),3));
        min_index = min_index + previous_max_index - 1;
        [v_max,max_index] = max(data_3(((min_index):1:round(((min_index) +
(cycle_samples)))),3));
        max_index = max_index + min_index - 1;
        v_min_max_data_2(i,1) = i;
        v_min_max_data_2(i,2) = min_index;
        v_min_max_data_2(i,3) = max_index;
    elseif i == (num_cycles)
        previous_max_index = v_min_max_data_2((i-1),3);
        [v_min,min_index] =
min(data_3(((previous_max_index):1:(round((length(data_3(:,3))) -
(0.5*cycle_samples)))),3));
        min_index = min_index + previous_max_index - 1;
```

```
        [v_max,max_index] =
max(data_3(((min_index):1:(length(data_3(:,3)))),3));
        max_index = max_index + min_index - 1;
        v_min_max_data_2(i,1) = i;
        v_min_max_data_2(i,2) = min_index;
        v_min_max_data_2(i,3) = max_index;
    elseif i == (num_cycles + 1)
        previous_max_index = v_min_max_data_2((i-1),3);
        [v_min,min_index] =
min(data_3(((previous_max_index):1:(round((length(data_3(:,3))))))),3));
        min_index = min_index + previous_max_index - 1;
        max_index = length(data_3(:,3));
        v_max = data_3(max_index,3);
        v_min_max_data_2(i,1) = i;
        v_min_max_data_2(i,2) = min_index;
        v_min_max_data_2(i,3) = max_index;
    end
end

% Next, the contraction and expansion pressures of each cycle (defined as
% the stationary pressures at which the accumulator expands and contracts
% most rapidly) are determined.  The script uses user-defined minimum and
% maximum volumes within the accumlator's fill and exhaust phase and
% averages the pressure data between those volumes, for the respective fill
% and exhaust phase.

disp ('Determining Expansion/Contraction Pressures of Each Cycle')

expansion_contraction_pressures_matrix = [num_cycles,7]; % [cycle, fill MIN
boundary index, fill MAX boundary index, exhaust MAX boundary index, exhaust
MIN boundary index, expansion pressure, contraction pressure]

for i = 1:1:num_cycles

    target_min_volume = 0.35 *
max(data_3((v_min_max_data_2(i,2):1:v_min_max_data_2(i,3)),3)); % Cubic Feet
- Arbitrary, based on percentage of max volume
    target_max_volume = 0.85 *
max(data_3((v_min_max_data_2(i,2):1:v_min_max_data_2(i,3)),3)); % Cubic Feet
- Arbitrary, based on percentage of max volume

    fill_target_min_volume_index = 0;
    fill_target_max_volume_index = 0;

    exhaust_target_max_volume_index = 0;
    exhaust_target_min_volume_index = 0;

    for j = v_min_max_data_2(i,2):1:v_min_max_data_2(i,3)
       if data_3(j,3) >= target_min_volume && fill_target_min_volume_index ==
0
           fill_target_min_volume_index = j;
       elseif data_3(j,3) >= target_max_volume &&
fill_target_max_volume_index == 0
           fill_target_max_volume_index = j;
       else
```

```
            continue
        end
    end

    for k = v_min_max_data_2(i,3):1:v_min_max_data_2((i+1),2)
        if data_3(k,3) <= target_max_volume &&
exhaust_target_max_volume_index == 0
            exhaust_target_max_volume_index = k;
        elseif data_3(k,3) <= target_min_volume &&
exhaust_target_min_volume_index == 0
            exhaust_target_min_volume_index = k;
        else
            continue
        end
    end

    expansion_pressure =
mean(data_3((fill_target_min_volume_index:1:fill_target_max_volume_index),2))
;
    contraction_pressure =
mean(data_3((exhaust_target_max_volume_index:1:exhaust_target_min_volume_inde
x),2));

    expansion_contraction_pressures_matrix(i,1) = i;
    expansion_contraction_pressures_matrix(i,2) =
fill_target_min_volume_index;
    expansion_contraction_pressures_matrix(i,3) =
fill_target_max_volume_index;
    expansion_contraction_pressures_matrix(i,4) =
exhaust_target_max_volume_index;
    expansion_contraction_pressures_matrix(i,5) =
exhaust_target_min_volume_index;
    expansion_contraction_pressures_matrix(i,6) = expansion_pressure;
    expansion_contraction_pressures_matrix(i,7) = contraction_pressure;

end

% Next, the energy input and output for each cycle and the efficiency (the
% ratio of ouput energy to input energy) is calculated for each cycle.
% The energy input and energy output are largely the result of the areas
% under the PV curve for the fill and exhaust phases, respectively.  Those
% areas are determined using the trapezoidal method of integration with the
% pressure and volume data points in the matrix data_3.

disp ('Calculating Energy and Efficiencies for Each Cycle')

efficiency_mat_cycles = ones(num_cycles,4);

for i = 1:1:num_cycles

    integrated_fill_running_total = 0;
    integrated_exhaust_running_total = 0;

    for j = (v_min_max_data_2(i,2)):1:((v_min_max_data_2(i,3)) - 1)
        vol_1 = data_3(j,3);
```

```
        vol_2 = data_3((j+1),3);
        vol_diff = abs(vol_2 - vol_1);
        pressure_1 = data_3(j,2);
        pressure_2 = data_3((j+1),2);
        pressure_diff = pressure_2 - pressure_1;
        if pressure_1 <= pressure_2
            area_under_curve = ((vol_diff) * (pressure_1)) + ((0.5) *
(vol_diff) * (pressure_diff));
            integrated_fill_running_total = integrated_fill_running_total +
area_under_curve;
        elseif pressure_1 > pressure_2
            area_under_curve = ((vol_diff) * (pressure_2)) + ((0.5) *
(vol_diff) * (-1)*(pressure_diff));
            integrated_fill_running_total = integrated_fill_running_total +
area_under_curve;
        else
        end
    end

    for k = (v_min_max_data_2(i,3)):1:((v_min_max_data_2((i+1),2)) - 1)
        vol_1 = data_3(k,3);
        vol_2 = data_3((k+1),3);
        vol_diff = abs(vol_2 - vol_1);
        pressure_1 = data_3(k,2);
        pressure_2 = data_3((k+1),2);
        pressure_diff = pressure_2 - pressure_1;
        if pressure_1 <= pressure_2
            area_under_curve = ((vol_diff) * (pressure_1)) + ((0.5) *
(vol_diff) * (pressure_diff));
            integrated_exhaust_running_total =
integrated_exhaust_running_total + area_under_curve;
        elseif pressure_1 > pressure_2
            area_under_curve = ((vol_diff) * (pressure_2)) + ((0.5) *
(vol_diff) * (-1)*(pressure_diff));
            integrated_exhaust_running_total =
integrated_exhaust_running_total + area_under_curve;
        else
        end
    end

    % Having determined the areas under the PV curves for the fill and
    % exhaust phases, the final energy calculations will need to consider
    % the maximum volume of the cycle and the pressure at that volume.

    specific_max_pressure = data_3(v_min_max_data_2(i,3),2);
    specific_max_volume = data_3(v_min_max_data_2(i,3),3);

    % The final energy and efficiency calculations are derived in the
    % accompanying article.

    cycle_energy_in = integrated_fill_running_total + (specific_max_pressure
* specific_max_volume * (log(specific_max_pressure/p_atm))); % Joules
    cycle_energy_out = integrated_exhaust_running_total +
(specific_max_pressure * specific_max_volume *
(log(specific_max_pressure/p_atm))); % Joules
    cycle_efficiency = (cycle_energy_out/cycle_energy_in) * 100; % Percentage
```

```
    % The input and output energies and each cycle and the cycle's
    % efficiency are recorded in a matrix for later use.

    efficiency_mat_cycles(i,1) = i;
    efficiency_mat_cycles(i,2) = cycle_efficiency;
    efficiency_mat_cycles(i,3) = cycle_energy_in;
    efficiency_mat_cycles(i,4) = cycle_energy_out;

    % The following string script displays the real-time status of the
    % efficiency-calculating process.

    completed_cycle_number_tag = int2str(i);
    total_cycle_number_tag = int2str(num_cycles);
    status_tag = ['Energy and Efficiency Computed for '
completed_cycle_number_tag ' of ' total_cycle_number_tag ' cycles'];
    disp(status_tag);

end

%%%%%%%%%%%%%%%%%%%%%%%%%%%%%%%%%%%%%%%%%%%%%%%%%%%%%%%%%%%%%%%%%%%%%%%%%%%%

% Task 4: Trim the calculated data of early cycles whose efficiency/energy/
% pressure data are not reflective of the accumlator's performance as a
% whole. Determine means and standard deviations of the calculated data.

% Early cycles don't represent the perfomance of the elastomeric
% accumulator as a whole for a very praticle reason:  the elastic bladder
% hasn't had time to warm up and energy/efficiency data for early cycles is
% significantly lower than later ones.  After 25 cycles, the accumulator
% performs consistently and its efficiency doesn't continue to
% significantly climb.

disp('Calculating Means and Standard Deviations')

trim = 25; % number of cycles excluded from analysis taken from the beginning
of the test

% Determing the average efficiency, average input/output energy, and
% average expansion/contraction pressures over all the (trimmed) test
% cycles makes use of an external function ('fit_and_analyze'). Please
% refer to the documentation of that function's script for more
% information.

[efficiency_average_trimmed, efficiency_SD_trimmed,
efficiency_confidence_interval_trimmed, efficiency_curve_trimmed,
efficiency_curve_r_squared_trimmed,
efficiency_curve_r_squared_adjusted_trimmed] =
fit_and_analyze(efficiency_mat_cycles((1:1:num_cycles-trim),1),
efficiency_mat_cycles((trim+1:1:num_cycles),2), 1);
efficiency_data_trimmed = [efficiency_average_trimmed, efficiency_SD_trimmed,
efficiency_confidence_interval_trimmed, efficiency_curve_trimmed,
efficiency_curve_r_squared_trimmed,
efficiency_curve_r_squared_adjusted_trimmed];
```

```
[energy_in_average_trimmed, energy_in_SD_trimmed,
energy_in_confidence_interval_trimmed, energy_in_curve_trimmed,
energy_in_curve_r_squared_trimmed,
energy_in_curve_r_squared_adjusted_trimmed] =
fit_and_analyze(efficiency_mat_cycles((1:1:num_cycles-trim),1),
efficiency_mat_cycles((trim+1:1:num_cycles),3), 1);
energy_in_data_trimmed = [energy_in_average_trimmed, energy_in_SD_trimmed,
energy_in_confidence_interval_trimmed, energy_in_curve_trimmed,
energy_in_curve_r_squared_trimmed,
energy_in_curve_r_squared_adjusted_trimmed];

[energy_out_average_trimmed, energy_out_SD_trimmed,
energy_out_confidence_interval_trimmed, energy_out_curve_trimmed,
energy_out_curve_r_squared_trimmed,
energy_out_curve_r_squared_adjusted_trimmed] =
fit_and_analyze(efficiency_mat_cycles((1:1:num_cycles-trim),1),
efficiency_mat_cycles((trim+1:1:num_cycles),4), 1);
energy_out_data_trimmed = [energy_out_average_trimmed, energy_out_SD_trimmed,
energy_out_confidence_interval_trimmed, energy_out_curve_trimmed,
energy_out_curve_r_squared_trimmed,
energy_out_curve_r_squared_adjusted_trimmed];

[expansion_pressure_average_trimmed, expansion_pressure_SD_trimmed,
expansion_pressure_confidence_interval_trimmed,
expansion_pressure_curve_trimmed, expansion_pressure_curve_r_squared_trimmed,
expansion_pressure_curve_r_squared_adjusted_trimmed] =
fit_and_analyze(expansion_contraction_pressures_matrix((1:1:num_cycles-
trim),1),
expansion_contraction_pressures_matrix((trim+1:1:num_cycles),6)/1000, 1); %
data will be returned in kilopascals
expansion_pressure_data_trimmed = [expansion_pressure_average_trimmed,
expansion_pressure_SD_trimmed,
expansion_pressure_confidence_interval_trimmed,
expansion_pressure_curve_trimmed, expansion_pressure_curve_r_squared_trimmed,
expansion_pressure_curve_r_squared_adjusted_trimmed];

[contraction_pressure_average_trimmed, contraction_pressure_SD_trimmed,
contraction_pressure_confidence_interval_trimmed,
contraction_pressure_curve_trimmed,
contraction_pressure_curve_r_squared_trimmed,
contraction_pressure_curve_r_squared_adjusted_trimmed] =
fit_and_analyze(expansion_contraction_pressures_matrix((1:1:num_cycles-
trim),1),
expansion_contraction_pressures_matrix((trim+1:1:num_cycles),7)/1000, 1); %
data will be returned in kilopascals
contraction_pressure_data_1_trimmed = [contraction_pressure_average_trimmed,
contraction_pressure_SD_trimmed,
contraction_pressure_confidence_interval_trimmed,
contraction_pressure_curve_trimmed,
contraction_pressure_curve_r_squared_trimmed,
contraction_pressure_curve_r_squared_adjusted_trimmed];

%%%%%%%%%%%%%%%%%%%%%%%%%%%%%%%%%%%%%%%%%%%%%%%%%%%%%%%%%%%%%%%%%%%%%%%%%%%%%%%

% Task 5: Produce plots and figures of the analyzed data.
```

```
disp('Generating Figures');

% Converting to Standard Cubic Centimeters

for i=1:1:length(data_1(:,3))
    old_volumetric_flow = data_1(i,3);
    new_volumetric_flow = old_volumetric_flow*(10^6);
    data_1(i,3) = new_volumetric_flow;
end

for i=1:1:length(data_3(:,3))
    old_volume = data_3(i,3);
    new_volume = old_volume*(10^6);
    data_3(i,3) = new_volume;
end

% Converting to Kilopascals

for i=1:1:length(data_3(:,2))
    old_pressure = data_3(i,2);
    new_pressure = old_pressure/1000;
    data_3(i,2) = new_pressure;
end

% Determing maximum and minimum data over many variables is necessary when
% framing the presented data within proper bounds.

overall_minimum_pressure = min(data_3(:,2));
overall_maximum_pressure = max(data_3(:,2));

overall_minimum_volumetric_flow = min(data_1(:,3));
overall_maximum_volumetric_flow = max(data_1(:,3));
absolute_maximum_volumetric_flow = max(overall_minimum_volumetric_flow,
overall_maximum_volumetric_flow);

overall_minimum_volume = min(data_3(:,3));
overall_maximum_volume = max(data_3(:,3));

overall_minimum_efficiency_trimmed =
min(efficiency_mat_cycles((trim+1:1:num_cycles),2));
overall_maximum_efficiency_trimmed =
max(efficiency_mat_cycles((trim+1:1:num_cycles),2));

overall_minimum_energy_in_trimmed =
min(efficiency_mat_cycles((trim+1:1:num_cycles),3));
overall_maximum_energy_in_trimmed =
max(efficiency_mat_cycles((trim+1:1:num_cycles),3));

overall_minimum_energy_out_trimmed =
min(efficiency_mat_cycles((trim+1:1:num_cycles),4));
overall_maximum_energy_out_trimmed =
max(efficiency_mat_cycles((trim+1:1:num_cycles),4));
```

```
overall_minimum_expansion_pressure_trimmed =
min(expansion_contraction_pressures_matrix((trim+1:1:num_cycles),6))/1000;
overall_maximum_expansion_pressure_trimmed =
max(expansion_contraction_pressures_matrix((trim+1:1:num_cycles),6))/1000;

overall_minimum_contraction_pressure_trimmed =
min(expansion_contraction_pressures_matrix((trim+1:1:num_cycles),7)/1000);
overall_maximum_contraction_pressure_trimmed =
max(expansion_contraction_pressures_matrix((trim+1:1:num_cycles),7)/1000);

% Normalizing Volume Data

for i=1:1:length(data_1(:,3))
    old_volumetric_flow = data_1(i,3);
    new_volumetric_flow =
old_volumetric_flow/absolute_maximum_volumetric_flow;
    data_1(i,3) = new_volumetric_flow;
end

for i=1:1:length(data_3(:,3))
    old_volume = data_3(i,3);
    new_volume = old_volume/overall_maximum_volume;
    data_3(i,3) = new_volume;
end

% Occasionally, some of the figures require some adjustments on the bounds.

graph_adjust = 2.01; % x-axis, minimum, pressure/mass_flow/volume figures
efficiency_adjust = 0.02; % y_axis, min and max, efficiency figures
energy_adjust = 0.2; % y-axis, min and max, energy figures
pressure_adjust = 0.2; % y-axis, min and max, exp/contr pressure figures

% The following figures display pressure as a function of time, volumetric
% flow as a function of time, and volume as a function of time for some
% sample cycles within the data.  The figures are also stored to a file for
% later retrieval.

% Graphing pressure(t) (selected cycles) (pressure in kPa):
pressure_fig = figure('visible', 'off');
plot (data_3(:,1),(data_3(:,2)),'blue');
xlabel ('Time (Seconds)');
ylabel ('Pressure (Kilopascals)');
axis ([((v_min_max_data_2((round(0.5 * (num_cycles - (trim))) +
trim),2))/sample_rate)+graph_adjust ((v_min_max_data_2((round(0.5 *
(num_cycles - (trim))) + trim + 3),2))/sample_rate) overall_minimum_pressure
overall_maximum_pressure])
title ('Pressure as a Function of Time');
set(pressure_fig, 'visible', 'on');
print (pressure_fig, '-dtiff', '1_pressure_vs_time')

% Graphing volumetric-flow(t) (selected cycles) (in standard cubic meters per
second):
volumetric_flow_fig = figure('visible', 'off');
plot (data_1(:,1),data_1(:,3),'red');
xlabel ('Time (Seconds)');
```

```
ylabel ('Normalized Volumetric Flow');
axis ([((v_min_max_data_2((round(0.5 * (num_cycles - (trim))) +
trim),2))/sample_rate)+graph_adjust ((v_min_max_data_2((round(0.5 *
(num_cycles - (trim))) + trim + 3),2))/sample_rate)
overall_minimum_volumetric_flow/absolute_maximum_volumetric_flow
overall_maximum_volumetric_flow/absolute_maximum_volumetric_flow])
title ('Volumetric Flow as a Function of Time');
set(volumetric_flow_fig, 'visible', 'on');
print (volumetric_flow_fig, '-dtiff', '2_volumetric_flow_vs_time')

% Graphing volume(t) (selected cycles) (cubic meters):
volume_fig = figure('visible', 'off');
plot (data_3(:,1),data_3(:,3),'red');
xlabel ('Time (Seconds)');
ylabel ('Normalized Volume');
axis ([((v_min_max_data_2((round(0.5 * (num_cycles - (trim))) +
trim),2))/sample_rate)+graph_adjust ((v_min_max_data_2((round(0.5 *
(num_cycles - (trim))) + trim + 3),2))/sample_rate)
overall_minimum_volume/overall_maximum_volume
overall_maximum_volume/overall_maximum_volume])
title ('Volume as a Function of Time');
set(volume_fig, 'visible', 'on');
print (volume_fig, '-dtiff', '3_volume_vs_time')

% The following figure is a compilation of typical PV curves for the data
% as a whole, utilizing the beginning, middle, and end cycles of the
% trimmed data.

% Graphing PV curve - Fill and Exhaust Phases - Multiple, Selected,
Overlapping Cycles
overlapping_cycle_fig = figure('visible', 'off');
hold on
plot (data_3((v_min_max_data_2(trim + 1,2):1:v_min_max_data_2(trim +
1,3)),3), data_3((v_min_max_data_2(trim + 1,2):1:v_min_max_data_2(trim +
1,3)),2), 'r-')
plot (data_3((v_min_max_data_2(round(0.5 * (num_cycles - (trim))) +
trim,2):1:v_min_max_data_2(round(0.5 * (num_cycles - (trim))) + trim,3)),3),
data_3((v_min_max_data_2(round(0.5 * (num_cycles - (trim))) +
trim,2):1:v_min_max_data_2(round(0.5 * (num_cycles - (trim))) + trim,3)),2),
'r--')
plot
(data_3((v_min_max_data_2(num_cycles,2):1:v_min_max_data_2(num_cycles,3)),3),
data_3((v_min_max_data_2(num_cycles,2):1:v_min_max_data_2(num_cycles,3)),2),
'r:')
plot (data_3((v_min_max_data_2(trim + 1,3):1:v_min_max_data_2((trim +
1+1),2)),3), data_3((v_min_max_data_2(trim + 1,3):1:v_min_max_data_2((trim +
1+1),2)),2), 'b-')
plot (data_3((v_min_max_data_2(round(0.5 * (num_cycles - (trim))) +
trim,3):1:v_min_max_data_2((round(0.5 * (num_cycles - (trim))) +
trim+1),2)),3), data_3((v_min_max_data_2(round(0.5 * (num_cycles - (trim))) +
trim,3):1:v_min_max_data_2((round(0.5 * (num_cycles - (trim))) +
trim+1),2)),2), 'b--')
plot
(data_3((v_min_max_data_2(num_cycles,3):1:v_min_max_data_2((num_cycles+1),2))
,3),
```

```
data_3((v_min_max_data_2(num_cycles,3):1:v_min_max_data_2((num_cycles+1),2)),
2), 'b:')
hold off
cycle_title_tag = 'PV Curve for Cycles ';
cycle_1 = int2str(trim + 1 - trim);
cycle_1_tag_fill = ['Cycle ' cycle_1 ' - Fill Phase'];
cycle_1_tag_exhaust = ['Cycle ' cycle_1 ' - Exhaust Phase'];
cycle_2 = int2str(round(0.5 * (num_cycles - (trim))) + trim - trim);
cycle_2_tag_fill = ['Cycle ' cycle_2 ' - Fill Phase'];
cycle_2_tag_exhaust = ['Cycle ' cycle_2 ' - Exhaust Phase'];
cycle_3 = int2str(num_cycles - trim);
cycle_3_tag_fill = ['Cycle ' cycle_3 ' - Fill Phase'];
cycle_3_tag_exhaust = ['Cycle ' cycle_3 ' - Exhaust Phase'];
total_cycle_number_tag = int2str(num_cycles - trim);
title_tag = [cycle_title_tag cycle_1 ', ' cycle_2 ', and ' cycle_3 ' of '
total_cycle_number_tag ' Cycles'];
legend(cycle_1_tag_fill, cycle_2_tag_fill, cycle_3_tag_fill,
cycle_1_tag_exhaust, cycle_2_tag_exhaust, cycle_3_tag_exhaust, 'Location',
'East');
xlabel ('Normalized Volume');
ylabel ('Pressure (Kilopascals)');
axis ([overall_minimum_volume/overall_maximum_volume
overall_maximum_volume/overall_maximum_volume overall_minimum_pressure
overall_maximum_pressure])
title (title_tag);
set (overlapping_cycle_fig, 'visible', 'on')
print (overlapping_cycle_fig, '-dtiff', '4_overlapping_PV_cycles')

% Graphing Area under the PV Curve
area_fig = figure('visible', 'off');
hold on
area (data_3((v_min_max_data_2(round(0.5 * (num_cycles - (trim))) +
trim,2):1:v_min_max_data_2(round(0.5 * (num_cycles - (trim))) + trim,3)),3),
data_3((v_min_max_data_2(round(0.5 * (num_cycles - (trim))) +
trim,2):1:v_min_max_data_2(round(0.5 * (num_cycles - (trim))) + trim,3)),2),
'FaceColor', 'red');
area (data_3((v_min_max_data_2(round(0.5 * (num_cycles - (trim))) +
trim,3):1:v_min_max_data_2((round(0.5 * (num_cycles - (trim))) +
trim+1),2)),3), data_3((v_min_max_data_2(round(0.5 * (num_cycles - (trim))) +
trim,3):1:v_min_max_data_2((round(0.5 * (num_cycles - (trim))) +
trim+1),2)),2), 'FaceColor', 'blue');
hold off
legend('Fill Phase', 'Exhaust Phase', 'Location', 'East');
cycle_title_tag = 'PV Curve with Shaded Area for Cycle ';
cycle_2 = int2str(round(0.5 * (num_cycles - (trim))) + trim - trim);
total_cycle_number_tag = int2str(num_cycles - trim);
title_tag = [cycle_title_tag cycle_2 ' of ' total_cycle_number_tag '
Cycles'];
xlabel ('Normalized Volume');
ylabel ('Pressure (Kilopascals)');
axis ([overall_minimum_volume/overall_maximum_volume
overall_maximum_volume/overall_maximum_volume overall_minimum_pressure
overall_maximum_pressure])
title (title_tag);
set (area_fig, 'visible', 'on')
print (area_fig, '-dtiff', '5_area_PV_cycle')
```

```
% Graphing Area under the PV Curve (transparency)
area_fig = figure('visible', 'off');
hold on
fill_patch_volume_data = vertcat(data_3((v_min_max_data_2(round(0.5 *
(num_cycles - (trim))) + trim,2):1:v_min_max_data_2(round(0.5 * (num_cycles -
(trim))) + trim,3)),3), data_3((v_min_max_data_2(round(0.5 * (num_cycles -
(trim))) + trim,3)),3));
fill_patch_pressure_data = vertcat(data_3((v_min_max_data_2(round(0.5 *
(num_cycles - (trim))) + trim,2):1:v_min_max_data_2(round(0.5 * (num_cycles -
(trim))) + trim,3)),2), 0);
exhaust_patch_volume_data = vertcat(data_3(v_min_max_data_2(round(0.5 *
(num_cycles - (trim))) + trim,3),3), data_3((v_min_max_data_2(round(0.5 *
(num_cycles - (trim))) + trim,3):1:v_min_max_data_2((round(0.5 * (num_cycles
- (trim))) + trim+1),2)),3));
exhaust_patch_pressure_data = vertcat(0, data_3((v_min_max_data_2(round(0.5 *
(num_cycles - (trim))) + trim,3):1:v_min_max_data_2((round(0.5 * (num_cycles
- (trim))) + trim+1),2)),2));
fill_patch = patch (fill_patch_volume_data, fill_patch_pressure_data, 'r');
exhaust_patch = patch (exhaust_patch_volume_data,
exhaust_patch_pressure_data, 'b', 'FaceAlpha', 0.5);
hold off
legend('Fill Phase', 'Exhaust Phase', 'Location', 'East');
cycle_title_tag = 'PV Curve with Shaded Area for Cycle ';
cycle_2 = int2str(round(0.5 * (num_cycles - (trim))) + trim - trim);
total_cycle_number_tag = int2str(num_cycles - trim);
title_tag = [cycle_title_tag cycle_2 ' of ' total_cycle_number_tag '
Cycles'];
xlabel ('Normalized Volume');
ylabel ('Pressure (Kilopascals)');
axis ([overall_minimum_volume/overall_maximum_volume
overall_maximum_volume/overall_maximum_volume overall_minimum_pressure
overall_maximum_pressure])
title (title_tag);
set (area_fig, 'visible', 'on')
print (area_fig, '-dtiff', '5_transparent_area_PV_cycle')

% Graphing Details of the PV Curve
details_fig = figure('visible', 'off');
hold on
plot (data_3((expansion_contraction_pressures_matrix((round(0.5 * (num_cycles
- (trim))) + trim),2)),3),
data_3((expansion_contraction_pressures_matrix((round(0.5 * (num_cycles -
(trim))) + trim),2)),2), 'rv')
plot (data_3((expansion_contraction_pressures_matrix((round(0.5 * (num_cycles
- (trim))) + trim),4)),3),
data_3((expansion_contraction_pressures_matrix((round(0.5 * (num_cycles -
(trim))) + trim),4)),2), 'bv')
plot (data_3((v_min_max_data_2((round(0.5 * (num_cycles - (trim))) +
trim),3)),3), data_3((v_min_max_data_2((round(0.5 * (num_cycles - (trim))) +
trim),3)),2), 'go')
plot (data_3((expansion_contraction_pressures_matrix((round(0.5 * (num_cycles
- (trim))) + trim),3)),3),
data_3((expansion_contraction_pressures_matrix((round(0.5 * (num_cycles -
(trim))) + trim),3)),2), 'rv')
```

```
plot (data_3((expansion_contraction_pressures_matrix((round(0.5 * (num_cycles
- (trim))) + trim),5)),3),
data_3((expansion_contraction_pressures_matrix((round(0.5 * (num_cycles -
(trim))) + trim),5)),2), 'bv')
plot (data_3((v_min_max_data_2(round(0.5 * (num_cycles - (trim))) +
trim,2):1:v_min_max_data_2(round(0.5 * (num_cycles - (trim))) + trim,3)),3),
data_3((v_min_max_data_2(round(0.5 * (num_cycles - (trim))) +
trim,2):1:v_min_max_data_2(round(0.5 * (num_cycles - (trim))) + trim,3)),2),
'k-')
plot (data_3((v_min_max_data_2(round(0.5 * (num_cycles - (trim))) +
trim,3):1:v_min_max_data_2((round(0.5 * (num_cycles - (trim))) +
trim+1),2)),3), data_3((v_min_max_data_2(round(0.5 * (num_cycles - (trim))) +
trim,3):1:v_min_max_data_2((round(0.5 * (num_cycles - (trim))) +
trim+1),2)),2), 'k-')
hold off
legend('Expansion Pressure Boundaries', 'Contraction Pressure Boundaries',
'Maximum Pressure Fill/Exhaust Phase', 'Location', 'East');
cycle_title_tag = 'PV Curve with Details for Cycle ';
cycle_2 = int2str(round(0.5 * (num_cycles - (trim))) + trim - trim);
total_cycle_number_tag = int2str(num_cycles - trim);
title_tag = [cycle_title_tag cycle_2 ' of ' total_cycle_number_tag '
Cycles'];
xlabel ('Normalized Volume');
ylabel ('Pressure (Kilopascals)');
axis ([overall_minimum_volume/overall_maximum_volume
overall_maximum_volume/overall_maximum_volume overall_minimum_pressure
overall_maximum_pressure])
title (title_tag);
set (details_fig, 'visible', 'on')
print (details_fig, '-dtiff', '6_details_PV_cycle')

% Though not displayed individually, the following figures display the
% efficiency, energy input and output, and expansion/contraction pressures
% of each cycle within the test data.  These figures and the data used to
% produce them are compiled to present data trends across multiple data
% sets.

% Graphing Efficiency (trimmed)
efficiency_fig_trimmed = figure('visible', 'off');
hold on
plot(efficiency_mat_cycles((1:1:(num_cycles-trim)),1)',
efficiency_mat_cycles(((trim + 1):1:(num_cycles)),2), 'k.', 'MarkerSize', 10)
hold off
grid on
xlabel ('Cycle Number');
ylabel ('Efficiency (Percentage)');
axis ([0, num_cycles-trim, 85, 100])
title ('Efficiencies of Each Cycle');
set(efficiency_fig_trimmed, 'visible', 'on');
print (efficiency_fig_trimmed, '-dtiff', '7_efficiency_trimmed')

% Energy data is normalized for presentation: each data point is
% represented as a fraction of the maximum input/output energy.

% Graphing Energy (trimmed)
energy_fig_trimmed = figure('visible', 'off');
```

```
subplot (2,1,1)
plot(efficiency_mat_cycles((1:1:(num_cycles-trim)),1)',
efficiency_mat_cycles(((trim +
1):1:(num_cycles)),3)/overall_maximum_energy_in_trimmed, 'r.')
grid on
xlabel ('Cycle Number');
ylabel ('Normalized Energy (E_i/E_m_a_x)');
axis ([0, num_cycles-trim, 0.965, 1.0])
title ('Energy Input of Each Cycle');
subplot (2,1,2)
plot(efficiency_mat_cycles((1:1:(num_cycles-trim)),1)',
efficiency_mat_cycles(((trim +
1):1:(num_cycles)),4)/overall_maximum_energy_out_trimmed, 'b.')
grid on
xlabel ('Cycle Number');
ylabel ('Normalized Energy (E_i/E_m_a_x)');
axis ([0, num_cycles-trim, 0.965, 1.0])
title ('Energy Output of Each Cycle');
set(energy_fig_trimmed, 'visible', 'on');
print (energy_fig_trimmed, '-dtiff', '8_energy_trimmed')

% The plot for the expansion and contraction pressures includes a best-fit
% trend line with 95% confidence bounds.

% Graphing Expansion and Contraction Pressures (trimmed)
exp_contr_pressures_fig_trimmed = figure('visible', 'off');
subplot (2,1,1)
hold on
plot (expansion_contraction_pressures_matrix((1:1:(num_cycles-trim)),1),
expansion_contraction_pressures_matrix(((trim + 1):1:(num_cycles)),6)/1000,
'r.')
plot (expansion_contraction_pressures_matrix((1:1:(num_cycles-trim)),1),
polyval(expansion_pressure_curve_trimmed,
expansion_contraction_pressures_matrix((1:1:(num_cycles-trim)),1)), 'red')
plot (expansion_contraction_pressures_matrix((1:1:(num_cycles-trim)),1),
(polyval(expansion_pressure_curve_trimmed,
expansion_contraction_pressures_matrix((1:1:(num_cycles-trim)),1))) +
expansion_pressure_SD_trimmed*2, 'r--')
plot (expansion_contraction_pressures_matrix((1:1:(num_cycles-trim)),1),
(polyval(expansion_pressure_curve_trimmed,
expansion_contraction_pressures_matrix((1:1:(num_cycles-trim)),1))) -
expansion_pressure_SD_trimmed*2, 'r--')
hold off
grid on
xlabel ('Cycle Number');
ylabel ('Pressure (Kilopascals)');
axis ([0, num_cycles-trim, (overall_minimum_expansion_pressure_trimmed)-
pressure_adjust,
(overall_maximum_expansion_pressure_trimmed)+pressure_adjust])
title ('Expansion Pressures of Each Cycle');
subplot (2,1,2)
hold on
plot (expansion_contraction_pressures_matrix((1:1:(num_cycles-trim)),1),
expansion_contraction_pressures_matrix(((trim + 1):1:(num_cycles)),7)/1000,
'b.')
```

```
plot (expansion_contraction_pressures_matrix((1:1:(num_cycles-trim)),1),
polyval(contraction_pressure_curve_trimmed,
expansion_contraction_pressures_matrix((1:1:(num_cycles-trim)),1)), 'blue')
plot (expansion_contraction_pressures_matrix((1:1:(num_cycles-trim)),1),
(polyval(contraction_pressure_curve_trimmed,
expansion_contraction_pressures_matrix((1:1:(num_cycles-trim)),1))) +
contraction_pressure_SD_trimmed*2, 'b--')
plot (expansion_contraction_pressures_matrix((1:1:(num_cycles-trim)),1),
(polyval(contraction_pressure_curve_trimmed,
expansion_contraction_pressures_matrix((1:1:(num_cycles-trim)),1))) -
contraction_pressure_SD_trimmed*2, 'b--')
hold off
grid on
xlabel ('Cycle Number');
ylabel ('Pressure (Kilopascals)');
axis ([0, num_cycles-trim, (overall_minimum_contraction_pressure_trimmed)-
pressure_adjust,
(overall_maximum_contraction_pressure_trimmed)+pressure_adjust])
title ('Contraction Pressures of Each Cycle');
set(exp_contr_pressures_fig_trimmed, 'visible', 'on');
print (exp_contr_pressures_fig_trimmed, '-dtiff',
'9_expansion_contraction_pressures_trimmed')

disp('Finish');
```

B4: Chapter Five: System Efficiency Increase Data Acquisition and Analysis Code

B4.1: Data Acquisition Codes

B4.1.1: Data Acquisition Calibration of Flow Meter for Cylinder Size Code

```
%This code controls a three-way valve that instrokes and outstrokes a single
%cylinder and collects data from a flow meter at the inlet of a cylinder to
%calibrate the transient flow measurement to each cylinder. The valve holds
%first, then outstrokes the cylinder, holds again, and then instrokes. The
%flowmeter collects volumetric flow rate and pressure data in volts.

clear all;
close all;
clc;

daq_session5 = daq.createSession('ni');

addAnalogOutputChannel(daq_session5,'cDAQ2Mod1',0:1,'Voltage'); %creates two
analog output channels for the ao0 and ao1 pins on the NI 9264
addAnalogInputChannel(daq_session5,'Dev2',0:1,'Voltage'); %creates two analog
input channels for the ai0 and ai1 pins on the NI 9215


daq_session5.Rate = 1000;

daq_session5.Channels(3).Coupling = 'DC'; %sets DC coupling for both input
channels
daq_session5.Channels(4).Coupling = 'DC';
```

```
instroke_time = .75; %seconds
hold_time = 1.5; %seconds
outstroke_time = .375; %seconds

instroke_samples = instroke_time*daq_session5.Rate; %# of samples
hold_samples = hold_time*daq_session5.Rate; %# of samples
outstroke_samples = outstroke_time*daq_session5.Rate; %# of samples
cycle_samples = instroke_samples + 2*hold_samples + outstroke_samples;


num_cycles = 102; %number of cycles run

sample_number = cycle_samples*num_cycles; %total number of samples

output_data = zeros(sample_number,2);
i = 0;
while cycle_samples*i < sample_number,
    for k = 1:1:cycle_samples,
        ind = k+cycle_samples*i;
        if k > hold_samples && k <= hold_samples+instroke_samples %if k is in
the instroke region, ao0 is set to 5 V
            output_data(ind,1) = 5;
        elseif k > 2*hold_samples+instroke_samples, % if k is in the
outstroke region ao1 is set to 5 V
            output_data(ind,2) = 5;
        end % in the hold region, both channels are 0 V
    end
     i = i+1; %i essentially counts the loop iterations
end

queueOutputData(daq_session5,output_data); %assigns the output data matrix to
the session
disp('start');

[input_data, time] = daq_session5.startForeground();%starts the DAQ session
in the foreground.

outstroke_hold = zeros(outstroke_samples+1,2);
outstroke_hold(:,2) = outstroke_hold(:,2)+5;
outstroke_hold(end,2) = 0;
queueOutputData(daq_session5,outstroke_hold);
disp('outstroke');
daq_session5.startForeground();

plot(time,input_data(:,1));
```

B4.1.2: System Without Accumulator Data Acquisition Code

```
%This code controls a three-way valve that instrokes and outstrokes a single
%cylinder and collects data from a flow meter for individual cylinders
%simulating a system without an accumulator. The valve holds first, then
%outstrokes the cylinder, holds again, and then instrokes. The flowmeter
%collects volumetric flow rate and pressure data in volts.
```

```
clear all;
close all;
clc;

daq_session5 = daq.createSession('ni');

addAnalogOutputChannel(daq_session5,'cDAQ2Mod1',0:1,'Voltage'); %creates two
analog output channels for the ao0 and ao1 pins on the NI 9264
addAnalogInputChannel(daq_session5,'Dev2',0:1,'Voltage'); %creates two analog
input channels for the ai0 and ai1 pins on the NI 9215


daq_session5.Rate = 1000;

daq_session5.Channels(3).Coupling = 'DC'; %sets DC coupling for both input
channels
daq_session5.Channels(4).Coupling = 'DC';

instroke_time = 1; %seconds
hold_time = 1.5; %seconds
outstroke_time = 1; %seconds

instroke_samples = instroke_time*daq_session5.Rate; %# of samples
hold_samples = hold_time*daq_session5.Rate; %# of samples
outstroke_samples = outstroke_time*daq_session5.Rate; %# of samples
cycle_samples = instroke_samples + 2*hold_samples + outstroke_samples;

Ps=280; %supply pressure to store as variable in workspace in kPa
num_cycles = 102; %number of cycles run

sample_number = cycle_samples*num_cycles; %total number of samples

output_data = zeros(sample_number,2);

%initialize counters
ii = 0;

while cycle_samples*ii < sample_number,
    for k = 1:1:cycle_samples,
        ind = k+cycle_samples*ii;
        if k > hold_samples && k <= hold_samples+instroke_samples %if k is in
the instroke region, ao0 is set to 5 V
            output_data(ind,1) = 5;
        elseif k > 2*hold_samples+instroke_samples, % if k is in the
outstroke region ao1 is set to 5 V
            output_data(ind,2) = 5;
        end % in the hold region, both channels are 0 V
    end
     ii = ii+1 %i essentially counts the loop iterations
end

clc;
```

```
queueOutputData(daq_session5,output_data); %assigns the output data matrix to
the session
disp('start');

[input_data, time] = daq_session5.startForeground();%starts the DAQ session
in the foreground.

outstroke_hold = zeros(outstroke_samples+1,2);
outstroke_hold(:,2) = outstroke_hold(:,2)+5;
outstroke_hold(end,2) = 0;
queueOutputData(daq_session5,outstroke_hold);
disp('outstroke');
daq_session5.startForeground();

figure(1)
plot(time,input_data(:,1));
xlabel('Time (sec)')
ylabel('Voltage (V)')
title('Medium Cylinder P_s = 280 kPa absolute')
```

B4.1.3: System Efficiency Increase Data Acquisition Code

```
clear all;
close all;
clc;

%Create Data Acquisition Session
daqSessionsys = daq.createSession('ni');

%Specify input/output channels
addAnalogOutputChannel(daqSessionsys,'cDAQ2Mod1',0:3,'Voltage'); %creates
four analog output channels for the ao0, 1, 2,and 3 pins on the NI 9264
addAnalogInputChannel(daqSessionsys,'Dev2',0:3,'Voltage'); %creates four
analog input channels for the ai0, 1, 2,  3 channels

%Specify sampling rate for data acquisition
daqSessionsys.Rate = 1000;

%Specify voltage type for each input channel
daqSessionsys.Channels(5).Coupling = 'DC';
daqSessionsys.Channels(6).Coupling = 'DC';
daqSessionsys.Channels(7).Coupling = 'DC';
daqSessionsys.Channels(8).Coupling = 'DC';

%Volume Calculations
    %Large Cylinder Volume Calculation
    dL=25;                  %diameter in mm
    sL=160;                 %stroke length in mm
    VL=pi()*(dL/2)^2*sL;    %cylinder volume in mm^3

    %Medium Cylinder Volume Calculation
    dM=20;                  %diameter in mm
    sM=80;                  %stroke length in mm
    VM=pi()*(dM/2)^2*sM;    %cylinder volume in mm^3
```

```
    %Small Cylinder Volume Calculation
    dS=16;                  %diameter in mm
    sS=40;                  %stroke length in mm
    VS=pi()*(dS/2)^2*sS;    %cylinder volume in mm^3

    %Volume Ratio Calculations (non dimensional)
    V_lm=VL/VM;
    V_ls=VL/VS;
    V_ml=VM/VL;
    V_mm=VM/VM;
    V_ms=VM/VS;
    V_sl=VS/VL;
    V_sm=VS/VM;

%Specify # of cycles, # of fires for each cylinder, and # of sequences run
numCyl1Cycles = 3; %number of complete cyl 1 cycles (in and out stroke) to be
run, MUST BE MULTIPLE OF # OF CYL 1 FIRES
numCyl1Fires = 1; %num of times cyl 1 fires in a sequence
numCyl2Fires = 3; %num of times cyl 2 fires in a sequence
totalSequences = 2*numCyl1Cycles/numCyl1Fires; %total number of sequences to
be run

%Fire and Hold times/samples for each cylinder
    %Cylinder 1
    cyl1FireTime = .75; %seconds
    cyl1HoldTime = 1.5; %seconds, amount of time system holds before firing
2nd cyl
    cyl1FireSamp = cyl1FireTime*daqSessionsys.Rate; %# of samples per cyl 1
fire
    cyl1HoldSamp = cyl1HoldTime*daqSessionsys.Rate; %# of samples per cyl 1
hold
    cyl1StrokeSamp = cyl1FireSamp+cyl1HoldSamp; %samps per stroke (fire and
hold) for cyl 1
    cyl1SequenceSamp = numCyl1Fires*cyl1StrokeSamp; %samps per sequence for
cyl 1

    %Cylinder 2
    cyl2FireTime = .75; %seconds
    cyl2HoldTime = .5; %seconds, amount of time system holds before firing
1st cyl or ending
    cyl2FireSamp = cyl2FireTime*daqSessionsys.Rate; %# of samples per cyl 2
fire
    cyl2HoldSamp = cyl2HoldTime*daqSessionsys.Rate; %# of samples per cyl 2
hold
    cyl2StrokeSamp = cyl2FireSamp+cyl2HoldSamp; %samps per stroke (fire and
hold) for cyl 2
    cyl2SequenceSamp = numCyl2Fires*cyl2StrokeSamp; %samps per sequence for
cyl 2

%Specify initial hold time/samples before starting
startHoldTime = 1; %seconds
startHoldSamp = startHoldTime*daqSessionsys.Rate; %# of samps

%Total samples in each sequence and in the data collection,
```

```
totalSequenceSamp = cyl1SequenceSamp + cyl2SequenceSamp; %# of samps in
sequence
totalSamp = startHoldSamp + totalSequenceSamp*totalSequences - cyl2HoldSamp;
%total samps in data collection

%Define output data matrix for test
outputData = zeros(totalSamp,4); %sets entire matrix to zero (closed
position)

cycleNum = 0; %tracks how many cycles have been completed
cyl1Pos = 0; %keeps track of position of cyl 1. Even is in, Odd is out
cyl2Pos = 0; %keeps track of position of cyl 2. Even is in, Odd is out

%Beginning of loop
for sequence = 1:1:totalSequences, %tracks which overall sequence the loop is
on
    %Cylinder 1
    k = 0; %# of fires completed in this sequence for Cyl 1
    while k < numCyl1Fires,
        for j = 1:1:cyl1FireSamp,
            index1 = startHoldSamp + totalSequenceSamp*(sequence-1) + j +
k*cyl1StrokeSamp;
            %if cyclinder 1 is in, fire out
            if mod(cyl1Pos,2) == 0,
                outputData(index1,3) = 5;
            %if cylinder 1 is out, fire in
            else
                outputData(index1,4) = 5;
            end
        end
        k = k+1;
        cyl1Pos = cyl1Pos+1;
    end

    %Cylinder 2
    y = 0; %#of fires completed in this sequence for Cyl 2
    while y < numCyl2Fires
        for x = 1:1:cyl2FireSamp,
            index2 = startHoldSamp + totalSequenceSamp*(sequence-1) + x +
cyl1SequenceSamp + y*cyl2StrokeSamp;
            %if cylinder 2 is in, fire out
            if mod(cyl2Pos,2) == 0,
                outputData(index2,1) = 5;
            %if cylinder 2 is out, fire in
            else
                outputData(index2,2) = 5;
            end
        end
        y = y+1;
        cyl2Pos = cyl2Pos+1;
    end
end


%Assign the output data matrix to the session and start data collection
queueOutputData(daqSessionsys,outputData);
```

```
disp('start');
[inputData,time] = daqSessionsys.startForeground;

%Specify final exhaust time/samples after data collection
finalExhaustTime = 5; %seconds
finalExhaustSamp = finalExhaustTime*daqSessionsys.Rate; %# of samps

%Final exhaust and set every valve to closed at the end
outputEnding = zeros(finalExhaustSamp+1,4);
for z = 1:1:finalExhaustSamp,
    if mod(cyl2Pos-1,2) == 0,
        %if cyl 2 is in, exhaust in
        outputEnding(z,2) = 5;
        %if cyl 2 is out, exhaust out
    else
        outputEnding(z,1) = 5;
    end
end

queueOutputData(daqSessionsys,outputEnding);
disp('exhaust');
daqSessionsys.startForeground;

%Plot important figures after testing completed to look for anomalies
figure(1)
plot(time,inputData(:,1),'r');
xlabel('Time (s)');
ylabel('Voltage (V)');
title('Mass Flow');

figure(2)
plot(time,inputData(:,2),'b');
xlabel('Time (s)');
ylabel('Voltage (V)');
title('Source Pressure at Mass Flow Meter');

figure(3)
plot(time,inputData(:,3),'g');
xlabel('Time (s)');
ylabel('Voltage (V)');
title('Pressure Sensor 1');

figure(4)
plot(time,inputData(:,4),'c');
xlabel('Time (s)');
ylabel('Voltage (V)');
title('Pressure Sensor 2');
```

B4.2: Data Analysis Code

B4.2.1: Individual Cylinder/System Without Accumualtor Raw Data Analysis Code

```
% Based on LCat Variable Names
```

```
%%%%%%%%%%%%%%%%%%%%%%%%%%%%%%%%%%%%%%%%%%%%%%%%%%%%%%%%%%%%%%%%%%%%%%%%%%%%%%%

% Task 1: Translate the output voltage data into meaningful physical data.

disp('Start');
disp('Translating Output Data');

density_air = 1.1840; % grams/Liter (or kilograms / m^3)

mass_flow_data = (-30 + 6*input_data(:,1)) * (0.001/60) * density_air; %
Kilograms Per Second
pressure_data = ((16*input_data(:,2)) * 6894.7573); % Pascals
p_atm = 14.696 * 6894.7573; % Pascals
cycle_time = hold_time + instroke_time + hold_time + outstroke_time; % The
sequence for one cycle (Check This)!!!
sample_rate = instroke_samples/instroke_time; % Samples per second;
cycle_samples = cycle_time * sample_rate; % Number of samples in one cycle
time_vector = time;

molar_mass_air = 28.97; % grams per mol

pressure_standard = 101320; % Pascals
temperature_standard = 298.15; % Kelvin

data_1 = [time_vector, pressure_data, mass_flow_data]; % Compiled, translated
input data

%%%%%%%%%%%%%%%%%%%%%%%%%%%%%%%%%%%%%%%%%%%%%%%%%%%%%%%%%%%%%%%%%%%%%%%%%%%%%%%

% Task 2: Integrate the volumetric flow/time data to produce volume/time
data.

disp('Integrating Volumetric Flow Data');

running_mass_total = 0; % For the loop
mass_data = zeros((length(mass_flow_data)),1); % A blank vector for data
collection

for i = 1:1:(length(mass_flow_data) - 1) % The "-1" is essential for the
trapezoidal method of integration
    time_1 = data_1(i,1);
    time_2 = data_1((i+1),1);
    time_diff = abs(time_2 - time_1);
    mass_flow_1 = data_1(i,3);
    mass_flow_2 = data_1((i+1),3);
    mass_flow_diff = mass_flow_2 - mass_flow_1;
    if mass_flow_1 <= mass_flow_2
        area_under_curve = ((time_diff) * (mass_flow_1)) + ((0.5) *
(time_diff) * (mass_flow_diff));
        running_mass_total = running_mass_total + area_under_curve;
        mass_data(i+1,1) = running_mass_total;
    elseif mass_flow_1 > mass_flow_2
```

```
        area_under_curve = ((time_diff) * (mass_flow_2)) + ((0.5) *
(time_diff) * (-1)*(mass_flow_diff));
        running_mass_total = running_mass_total + area_under_curve;
        mass_data(i+1,1) = running_mass_total;
    else
    end
end

data_2 = [data_1(:,1), data_1(:,2), mass_data]; % Compiled, includes time,
pressure, and mass data.

disp('Eliminating Drift')

m_min_max_data_1 = zeros((num_cycles + 1), 3); % Pattern: [cycle number, min
index, max index]

for i = 1:1:(num_cycles + 1)
    if i == 1
        min_index = 1;
        m_min = data_2(min_index,3);
        [m_max,max_index] = max(data_2((min_index:1:round((min_index +
(cycle_samples)))),3));
        m_min_max_data_1(i,1) = i;
        m_min_max_data_1(i,2) = min_index;
        m_min_max_data_1(i,3) = max_index - 1;
    elseif i > 1 && i <= (num_cycles - 1)
        previous_max_index = m_min_max_data_1((i-1),3);
        [m_min,min_index] =
min(data_2(((previous_max_index):1:round(((previous_max_index) +
(cycle_samples)))),3));
        min_index = min_index + previous_max_index - 1;
        [m_max,max_index] = max(data_2(((min_index):1:round(((min_index) +
(cycle_samples)))),3));
        max_index = max_index + min_index - 1;
        m_min_max_data_1(i,1) = i;
        m_min_max_data_1(i,2) = min_index + 1;
        m_min_max_data_1(i,3) = max_index;
    elseif i == (num_cycles)
        previous_max_index = m_min_max_data_1((i-1),3);
        [m_min,min_index] =
min(data_2(((previous_max_index):1:(round((length(data_2(:,3))) -
(0.5*cycle_samples)))),3));
        min_index = min_index + previous_max_index - 1;
        [m_max,max_index] =
max(data_2(((min_index):1:(length(data_2(:,3)))),3));
        max_index = max_index + min_index - 1;
        m_min_max_data_1(i,1) = i;
        m_min_max_data_1(i,2) = min_index + 1;
        m_min_max_data_1(i,3) = max_index;
    elseif i == (num_cycles + 1)
        previous_max_index = m_min_max_data_1((i-1),3);
        [m_min,min_index] =
min(data_2(((previous_max_index):1:(round((length(data_2(:,3)))))),3));
        min_index = min_index + previous_max_index - 1;
        max_index = length(data_2(:,3));
        m_max = data_2(max_index,3);
```

```
        m_min_max_data_1(i,1) = i;
        m_min_max_data_1(i,2) = min_index;
        m_min_max_data_1(i,3) = max_index;
    end
end

% The original volumetric-flow data is now re-integrated, reseting the
% running total at the beginning of each new cycle, according to the
% indecies collected in the immediate script above.  The data is
% re-integrated for one cycle, then the cycle is adjusted to account for
% linear drift along the cycle.

running_mass_total = 0;
cycle_mass_data = zeros((m_min_max_data_1((num_cycles + 1),2)),2); % format:
[re-integrated volume data, linearly-adjusted volume data]
cycle_index = 1;

while cycle_index < (num_cycles + 1)

    for i = m_min_max_data_1(cycle_index,2):1:((m_min_max_data_1((cycle_index
+ 1),2)) - 1)
        if i == m_min_max_data_1(cycle_index,2)
            cycle_mass_data(i) = 0;
            running_mass_total = 0;
            time_1 = data_1(i,1);
            time_2 = data_1((i+1),1);
            time_diff = time_2 - time_1;
            mass_flow_1 = data_1(i,3);
            mass_flow_2 = data_1((i+1),3);
            mass_flow_diff = mass_flow_2 - mass_flow_1;
            if mass_flow_1 <= mass_flow_2
                area_under_curve = ((time_diff) * (mass_flow_1)) + ((0.5) *
(time_diff) * (mass_flow_diff));
                running_mass_total = running_mass_total + area_under_curve;
                cycle_mass_data(i+1,1) = running_mass_total;
            elseif mass_flow_1 > mass_flow_2
                area_under_curve = ((time_diff) * (mass_flow_2)) + ((0.5) *
(time_diff) * (-1)*(mass_flow_diff));
                running_mass_total = running_mass_total + area_under_curve;
                cycle_mass_data(i+1,1) = running_mass_total;
            else
            end
        else
            time_1 = data_1(i,1);
            time_2 = data_1((i+1),1);
            time_diff = time_2 - time_1;
            mass_flow_1 = data_1(i,3);
            mass_flow_2 = data_1((i+1),3);
            mass_flow_diff = mass_flow_2 - mass_flow_1;
            if mass_flow_1 <= mass_flow_2
                area_under_curve = ((time_diff) * (mass_flow_1)) + ((0.5) *
(time_diff) * (mass_flow_diff));
                running_mass_total = running_mass_total + area_under_curve;
                cycle_mass_data(i+1,1) = running_mass_total;
            elseif mass_flow_1 > mass_flow_2
```

```
                area_under_curve = ((time_diff) * (mass_flow_2)) + ((0.5) *
(time_diff) * (-1)*(mass_flow_diff));
                running_mass_total = running_mass_total + area_under_curve;
                cycle_mass_data(i+1,1) = running_mass_total;
            else
            end
        end
    end

    % Now that the volumetric-flow data has been re-integrated, the small
    % drift across a cycle must be addressed.  To do so, the following
    % script identifies points along the cycle where the volumetric flow
    % should, in theory, be zero: at points before the accumulator has
    % started to fill with pressurized air.  To identify these points, the
    % script first identifies the point of maximum volumetric flow along
    % the cycle, then tests each data point from the maximum volumetric
    % flow until the start of the cycle (testing 'backwards' in time, so to
    % speak).  If the difference between the volumetric flows of the test
    % point and the start of the cycle is greater than a given threshold,
    % then the volumetric flow cannot be considered essentially zero, and
    % the next test point is evaluated.  This process continues until a
    % suitible test point has been identified.  If the number of samples
    % between the suitible test point and the start of the cycle isn't
    % significant, than linear regression analysis isn't an opiton and the
    % re-integrated data remains ultimately unchanged.

    [mass_flow_max, mass_flow_index] =
max(data_1((m_min_max_data_1(cycle_index,2):1:m_min_max_data_1(cycle_index,3)
),3)); % This is the index within the individual cycle
    mass_flow_index = mass_flow_index + m_min_max_data_1(cycle_index,2) - 1;
% Now, the index has been adjusted within the entire data set
    minimum_difference = 10e-07;
    minimum_significant_data_points = 100000; % Originally 10, high number
prevents this second linear drift function

    suitible_mass_flow_index = 0;

    for j = mass_flow_index:-1:m_min_max_data_1(cycle_index,2)
        if data_1(j,3) <= minimum_difference && suitible_mass_flow_index == 0
            suitible_mass_flow_index = j;
        else
            continue
        end
    end

    % Next, all points of volume data between the start of the cycle to the
    % suitible test point are considered to be of equal volume, zero.  A
    % line of best fit is evaluated through these data points, producing a
    % general trend line upon which all data within the cycle has been
    % superimposed. Expected values for each data point as a function of
    % time can be constructed from this trend line and subtracted out of
    % the data.

    linear_regression_matrix = zeros((length(data_2(:,3))),4); % [time,
volume, time^2, time * volume]
```

```
    for k = m_min_max_data_1(cycle_index,2):1:suitible_mass_flow_index
        t_k = (k - m_min_max_data_1(cycle_index,2))/sample_rate;
        m_k = cycle_mass_data(k,1);
        linear_regression_matrix(k,1) = t_k;
        linear_regression_matrix(k,2) = m_k;
        linear_regression_matrix(k,3) = t_k^2;
        linear_regression_matrix(k,4) = t_k * m_k;
    end

    % Linear function format: y = A + (B * x)
    A = 0;
    B = 0;
    if (suitible_mass_flow_index - m_min_max_data_1(cycle_index,2)) >=
minimum_significant_data_points
        B =
(sum(linear_regression_matrix(:,4)))/(sum(linear_regression_matrix(:,3)));
    end

    for l = (m_min_max_data_1(cycle_index,2) +
1):1:(m_min_max_data_1((cycle_index + 1),2) - 1)
        old_cycle_mass = cycle_mass_data(l,1);
        time_value = (l - m_min_max_data_1(cycle_index,2))/sample_rate;
        linear_volume = A + (B * time_value);
        new_cycle_mass = old_cycle_mass - linear_volume;
        cycle_mass_data(l,2) = new_cycle_mass;
    end

    % The following string script displays the real-time status of this
    % data-cleaning process.

    completed_cycle_number_tag = int2str(cycle_index);
    total_cycle_number_tag = int2str(num_cycles);
    status_tag = ['Drift removed from ' completed_cycle_number_tag ' of '
total_cycle_number_tag ' cycles'];
    disp(status_tag);

    cycle_index = cycle_index + 1;

end

% Lastly, the re-integrated cycle volume is forced to zero at the end of
% the final cycle and a new data set reflecting the cleaned volume data is
% created.

cycle_mass_data((m_min_max_data_1((num_cycles + 1),2)),1) = 0;
cycle_mass_data((m_min_max_data_1((num_cycles + 1),2)),2) = 0;

data_3 = [data_2((1:1:length(cycle_mass_data(:,2))),1),
data_2((1:1:length(cycle_mass_data(:,2))),2), cycle_mass_data(:,2)]; %
Includes time, pressure, and cleaned volume data

%%%%%%%%%%%%%%%%%%%%%%%%%%%%%%%%%%%%%%%%%%%%%%%%%%%%%%%%%%%%%%%%%%%%%%%%%%%%
```

```
% Task 3: Find and average the maximum volumes per each cycle.

m_max_data = zeros(length(m_min_max_data_1(:,1))-3,2); % [cycle, max_volume]

for i = (1:1:length(m_min_max_data_1(:,1))-3)
    cycle = i;
    max_volume = data_3((m_min_max_data_1(i+1,3)),3);
    m_max_data(i,1) = cycle;
    m_max_data(i,2) = max_volume;
end

average_max_mass = mean(m_max_data(:,2));

%%%%%%%%%%%%%%%%%%%%%%%%%%%%%%%%%%%%%%%%%%%%%%%%%%%%%%%%%%%%%%%%%%%%%%%%%%%%%%%

% Task 4: Produce plots and figures of the analyzed data.

disp('Generating Figures');

% Determing maximum and minimum data over many variables is necessary when
% framing the presented data within proper bounds.

overall_minimum_pressure = min(data_3(:,2));
overall_maximum_pressure = max(data_3(:,2));

overall_minimum_mass_flow = min(data_1(:,3));
overall_maximum_mass_flow = max(data_1(:,3));

overall_minimum_mass = min(data_3(:,3));
overall_maximum_mass = max(data_3(:,3));

% The following figures display pressure as a function of time, volumetric
% flow as a function of time, and volume as a function of time for some
% sample cycles within the data.  The figures are also stored to a file for
% later retrieval.

% Graphing pressure(t) (pressure in kPa):
pressure_fig = figure('visible', 'off');
plot (data_3(:,1),(data_3(:,2))/1000,'blue');
xlabel ('Time (Seconds)');
ylabel ('Pressure (Kilopascals)');
axis ([0 max(time) overall_minimum_pressure/1000
overall_maximum_pressure/1000])
title ('Pressure as a Function of Time');
set(pressure_fig, 'visible', 'on');
print (pressure_fig, '-dtiff', '1_b_pressure_vs_time')

% Graphing mass-flow(t) (selected cycles) (in kilograms per second):
volumetric_flow_fig = figure('visible', 'off');
plot (data_1(:,1),data_1(:,3),'red');
xlabel ('Time (Seconds)');
ylabel ('Mass Flow (Kilograms Per Second)');
axis ([0 max(time) overall_minimum_mass_flow overall_maximum_mass_flow])
title ('Mass Flow as a Function of Time');
```

```
set(volumetric_flow_fig, 'visible', 'on');
print (volumetric_flow_fig, '-dtiff', '2_b_mass_flow_vs_time')

% Graphing volume(t) (kilograms):
volume_fig = figure('visible', 'off');
plot (data_3(:,1),data_3(:,3),'red');
xlabel ('Time (Seconds)');
ylabel ('Mass (Kilograms)');
axis ([0 max(time) overall_minimum_mass overall_maximum_mass])
title ('Mass as a Function of Time');
set(volume_fig, 'visible', 'on');
print (volume_fig, '-dtiff', '3_b_mass_vs_time')

% Graphing volume(t) - m_max check (kilograms):
volume_fig = figure('visible', 'off');
hold on
plot (data_2(:,1),data_2(:,3),'black');
plot
(data_2((m_min_max_data_1(:,3)),1),data_2((m_min_max_data_1(:,3)),3),'go');
hold off
xlabel ('Time (Seconds)');
ylabel ('Mass (Kilograms)');
title ('Mass as a Function of Time');
set(volume_fig, 'visible', 'on');
print (volume_fig, '-dtiff', '3_f_mass_vs_time')

% Graphing mass(t) - m_max check (kilograms):
volume_fig = figure('visible', 'off');
hold on
plot (data_3(:,1),data_3(:,3),'black');
plot
(data_3((m_min_max_data_1(:,3)),1),data_3((m_min_max_data_1(:,3)),3),'go');
hold off
xlabel ('Time (Seconds)');
ylabel ('Mass (Kilograms)');
axis ([0 max(time) overall_minimum_mass overall_maximum_mass])
title ('Mass as a Function of Time');
set(volume_fig, 'visible', 'on');
print (volume_fig, '-dtiff', '3_d_mass_vs_time')

% Graphing max masses:
max_volume_fig = figure('visible', 'off');
plot (m_max_data(:,1), m_max_data(:,2), 'o')
xlabel ('Cycle');
ylabel ('Maximum Mass (Kilograms)');
axis ([0 max(m_max_data(:,1)) overall_minimum_mass overall_maximum_mass])
title ('Maximum Mass of Each Cycle');
set(max_volume_fig, 'visible', 'on')
print(max_volume_fig, '-dtiff', '3_e_max_masses')

disp('Finish');
```

B4.2.2: System Efficiency Raw Data Analysis Code

```
% Based on LCat Variable Names
```

```
%%%%%%%%%%%%%%%%%%%%%%%%%%%%%%%%%%%%%%%%%%%%%%%%%%%%%%%%%%%%%%%%%%%%%%%%%%%%

% Task 1: Translate the output voltage data into meaningful physical data.

disp('Start');
disp('Translating Output Data');

density_air = 1.1840; % grams/Liter (or kilograms / m^3)
molar_mass_air = 28.97; % grams per mol
pressure_standard = 101320; % Pascals
temperature_standard = 298.15; % Kelvin
p_atm = 14.696 * 6894.7573; % Pascals

mass_flow_data = (-30 + 6*inputData(:,1)) * (0.001/60) * density_air; %
Kilograms Per Second
pressure_data = ((16*inputData(:,2)) * 6894.7573); % Pascals
% cycle_time = hold_time + instroke_time + hold_time + outstroke_time; % The
sequence for one cycle (Check This)!!!
sample_rate = 1000; % Samples per second;
cycle_samples = totalSequenceSamp; % Number of samples in one cycle
time_vector = time;
num_cycles = totalSequences;

startHoldSamp_edit = 0;

adjusted_mass_flow_data =
mass_flow_data((startHoldSamp_edit+1:1:length(mass_flow_data)),1);
adjusted_pressure_data =
pressure_data((startHoldSamp_edit+1:1:length(pressure_data)),1);
adjusted_time_vector =
time_vector((startHoldSamp_edit+1:1:length(time_vector)),1);

data_1 = [adjusted_time_vector, adjusted_pressure_data,
adjusted_mass_flow_data]; % Compiled, translated input data

%%%%%%%%%%%%%%%%%%%%%%%%%%%%%%%%%%%%%%%%%%%%%%%%%%%%%%%%%%%%%%%%%%%%%%%%%%%%

% Task 2: Integrate the volumetric flow/time data to produce volume/time
data.

disp('Integrating Volumetric Flow Data');

running_mass_total = 0; % For the loop
mass_data = zeros(length(adjusted_mass_flow_data),1); % A blank vector for
data collection

for i = 1:1:(length(adjusted_mass_flow_data) - 1) % The "-1" is essential for
the trapezoidal method of integration
    time_1 = data_1(i,1);
    time_2 = data_1((i+1),1);
    time_diff = abs(time_2 - time_1);
    mass_flow_1 = data_1(i,3);
    mass_flow_2 = data_1((i+1),3);
```

```
    mass_flow_diff = mass_flow_2 - mass_flow_1;
    if mass_flow_1 <= mass_flow_2
        area_under_curve = ((time_diff) * (mass_flow_1)) + ((0.5) *
(time_diff) * (mass_flow_diff));
        running_mass_total = running_mass_total + area_under_curve;
        mass_data(i+1,1) = running_mass_total;
    elseif mass_flow_1 > mass_flow_2
        area_under_curve = ((time_diff) * (mass_flow_2)) + ((0.5) *
(time_diff) * (-1)*(mass_flow_diff));
        running_mass_total = running_mass_total + area_under_curve;
        mass_data(i+1,1) = running_mass_total;
    else
    end
end

data_2 = [data_1(:,1), data_1(:,2), mass_data]; % Compiled, includes time,
pressure, and mass data.

disp('Eliminating Drift')

m_min_max_data_1 = zeros((num_cycles), 3); % Pattern: [cycle number, min
index, max index]

for i = 1:1:(num_cycles)
    if i == 1
        min_index = 1;
        m_min = data_2(min_index,3);
        [m_max,max_index] = max(data_2((min_index:1:(min_index +
(cycle_samples))),3));
        m_min_max_data_1(i,1) = i;
        m_min_max_data_1(i,2) = min_index;
        m_min_max_data_1(i,3) = max_index - 1;
    elseif i > 1 && i <= (num_cycles - 1)
        previous_max_index = m_min_max_data_1((i-1),3);
        [m_min,min_index] =
min(data_2(((previous_max_index):1:((previous_max_index) +
(cycle_samples))),3));
        min_index = min_index + previous_max_index - 1;
        [m_max,max_index] = max(data_2(((min_index):1:((min_index) +
(cycle_samples))),3));
        max_index = max_index + min_index - 1;
        m_min_max_data_1(i,1) = i;
        m_min_max_data_1(i,2) = min_index + 1;
        m_min_max_data_1(i,3) = max_index;
    elseif i == (num_cycles)
        previous_max_index = m_min_max_data_1((i-1),3);
        min_index = previous_max_index;
        max_index = length(mass_data);
        m_min_max_data_1(i,1) = i;
        m_min_max_data_1(i,2) = min_index + 1;
        m_min_max_data_1(i,3) = max_index;
    end
end

% The original volumetric-flow data is now re-integrated, reseting the
% running total at the beginning of each new cycle, according to the
```

```
% indecies collected in the immediate script above.  The data is
% re-integrated for one cycle, then the cycle is adjusted to account for
% linear drift along the cycle.

running_mass_total = 0;
cycle_mass_data = zeros((m_min_max_data_1((num_cycles),3)),2); % format: [re-
integrated volume data, linearly-adjusted volume data]
cycle_index = 1;

while cycle_index < (num_cycles + 1)

    for i =
m_min_max_data_1(cycle_index,2):1:((m_min_max_data_1((cycle_index),3)) - 1)
        if i == m_min_max_data_1(cycle_index,2)
            cycle_mass_data(i) = 0;
            running_mass_total = 0;
            time_1 = data_1(i,1);
            time_2 = data_1((i+1),1);
            time_diff = time_2 - time_1;
            mass_flow_1 = data_1(i,3);
            mass_flow_2 = data_1((i+1),3);
            mass_flow_diff = mass_flow_2 - mass_flow_1;
            if mass_flow_1 <= mass_flow_2
                area_under_curve = ((time_diff) * (mass_flow_1)) + ((0.5) *
(time_diff) * (mass_flow_diff));
                running_mass_total = running_mass_total + area_under_curve;
                cycle_mass_data(i+1,1) = running_mass_total;
            elseif mass_flow_1 > mass_flow_2
                area_under_curve = ((time_diff) * (mass_flow_2)) + ((0.5) *
(time_diff) * (-1)*(mass_flow_diff));
                running_mass_total = running_mass_total + area_under_curve;
                cycle_mass_data(i+1,1) = running_mass_total;
            else
            end
        else
            time_1 = data_1(i,1);
            time_2 = data_1((i+1),1);
            time_diff = time_2 - time_1;
            mass_flow_1 = data_1(i,3);
            mass_flow_2 = data_1((i+1),3);
            mass_flow_diff = mass_flow_2 - mass_flow_1;
            if mass_flow_1 <= mass_flow_2
                area_under_curve = ((time_diff) * (mass_flow_1)) + ((0.5) *
(time_diff) * (mass_flow_diff));
                running_mass_total = running_mass_total + area_under_curve;
                cycle_mass_data(i+1,1) = running_mass_total;
            elseif mass_flow_1 > mass_flow_2
                area_under_curve = ((time_diff) * (mass_flow_2)) + ((0.5) *
(time_diff) * (-1)*(mass_flow_diff));
                running_mass_total = running_mass_total + area_under_curve;
                cycle_mass_data(i+1,1) = running_mass_total;
            else
            end
        end
    end
```

```
    % Now that the volumetric-flow data has been re-integrated, the small
    % drift across a cycle must be addressed.  To do so, the following
    % script identifies points along the cycle where the volumetric flow
    % should, in theory, be zero: at points before the accumulator has
    % started to fill with pressurized air.  To identify these points, the
    % script first identifies the point of maximum volumetric flow along
    % the cycle, then tests each data point from the maximum volumetric
    % flow until the start of the cycle (testing 'backwards' in time, so to
    % speak).  If the difference between the volumetric flows of the test
    % point and the start of the cycle is greater than a given threshold,
    % then the volumetric flow cannot be considered essentially zero, and
    % the next test point is evaluated.  This process continues until a
    % suitible test point has been identified.  If the number of samples
    % between the suitible test point and the start of the cycle isn't
    % significant, than linear regression analysis isn't an opiton and the
    % re-integrated data remains ultimately unchanged.

    [mass_flow_max, mass_flow_index] =
max(data_1((m_min_max_data_1(cycle_index,2):1:m_min_max_data_1(cycle_index,3)
),3)); % This is the index within the individual cycle
    mass_flow_index = mass_flow_index + m_min_max_data_1(cycle_index,2) - 1;
% Now, the index has been adjusted within the entire data set
    minimum_difference = 10e-07;
    minimum_significant_data_points = 100000; % Originally 10, high number
prevents this second linear drift function

    suitible_mass_flow_index = 0;

    for j = mass_flow_index:-1:m_min_max_data_1(cycle_index,2)
        if data_1(j,3) <= minimum_difference && suitible_mass_flow_index == 0
            suitible_mass_flow_index = j;
        else
            continue
        end
    end

    % Next, all points of volume data between the start of the cycle to the
    % suitible test point are considered to be of equal volume, zero.  A
    % line of best fit is evaluated through these data points, producing a
    % general trend line upon which all data within the cycle has been
    % superimposed. Expected values for each data point as a function of
    % time can be constructed from this trend line and subtracted out of
    % the data.

    linear_regression_matrix = zeros((length(data_2(:,3))),4); % [time,
volume, time^2, time * volume]

    for k = m_min_max_data_1(cycle_index,2):1:suitible_mass_flow_index
        t_k = (k - m_min_max_data_1(cycle_index,2))/sample_rate;
        m_k = cycle_mass_data(k,1);
        linear_regression_matrix(k,1) = t_k;
        linear_regression_matrix(k,2) = m_k;
        linear_regression_matrix(k,3) = t_k^2;
        linear_regression_matrix(k,4) = t_k * m_k;
    end
```

```
    % Linear function format: y = A + (B * x)
    A = 0;
    B = 0;
    if (suitible_mass_flow_index - m_min_max_data_1(cycle_index,2)) >=
minimum_significant_data_points
        B =
(sum(linear_regression_matrix(:,4)))/(sum(linear_regression_matrix(:,3)));
    end

    for l = (m_min_max_data_1(cycle_index,2) +
1):1:(m_min_max_data_1((cycle_index),3) - 1)
        old_cycle_mass = cycle_mass_data(l,1);
        time_value = (l - m_min_max_data_1(cycle_index,2))/sample_rate;
        linear_volume = A + (B * time_value);
        new_cycle_mass = old_cycle_mass - linear_volume;
        cycle_mass_data(l,2) = new_cycle_mass;
    end

    % The following string script displays the real-time status of this
    % data-cleaning process.

    completed_cycle_number_tag = int2str(cycle_index);
    total_cycle_number_tag = int2str(num_cycles);
    status_tag = ['Drift removed from ' completed_cycle_number_tag ' of '
total_cycle_number_tag ' cycles'];
    disp(status_tag);

    cycle_index = cycle_index + 1;

end

% Lastly, the re-integrated cycle volume is forced to zero at the end of
% the final cycle and a new data set reflecting the cleaned volume data is
% created.

data_3 = [data_2((1:1:length(cycle_mass_data(:,2))),1),
data_2((1:1:length(cycle_mass_data(:,2))),2), cycle_mass_data(:,2)]; %
Includes time, pressure, and cleaned volume data

%%%%%%%%%%%%%%%%%%%%%%%%%%%%%%%%%%%%%%%%%%%%%%%%%%%%%%%%%%%%%%%%%%%%%%%%%%%

% Task 3: Find and average the maximum volumes per each cycle.

m_max_data = zeros(length(m_min_max_data_1(:,1))-3,2); % [cycle, max_volume]

for i = (1:1:length(m_min_max_data_1(:,1))-3)
    cycle = i;
    max_volume = data_3((m_min_max_data_1(i+1,3)),3);
    m_max_data(i,1) = cycle;
    m_max_data(i,2) = max_volume;
end

average_max_mass = mean(m_max_data(:,2));
```

```
%%%%%%%%%%%%%%%%%%%%%%%%%%%%%%%%%%%%%%%%%%%%%%%%%%%%%%%%%%%%%%%%%%%%%%%%%%%%

% Task 4: Produce plots and figures of the analyzed data.

disp('Generating Figures');

% Determing maximum and minimum data over many variables is necessary when
% framing the presented data within proper bounds.

overall_minimum_pressure = min(data_3(:,2));
overall_maximum_pressure = max(data_3(:,2));

overall_minimum_mass_flow = min(data_1(:,3));
overall_maximum_mass_flow = max(data_1(:,3));

overall_minimum_mass = min(data_3(:,3));
overall_maximum_mass = max(data_3(:,3));

% The following figures display pressure as a function of time, volumetric
% flow as a function of time, and volume as a function of time for some
% sample cycles within the data.  The figures are also stored to a file for
% later retrieval.

% Graphing volume(t) - m_max check (kilograms):
volume_fig = figure('visible', 'off');
hold on
plot (data_2(:,1),data_2(:,3),'black');
plot
(data_2((m_min_max_data_1(:,3)),1),data_2((m_min_max_data_1(:,3)),3),'go');
hold off
xlabel ('Time (Seconds)');
ylabel ('Mass (Kilograms)');
title ('Mass as a Function of Time');
set(volume_fig, 'visible', 'on');
print (volume_fig, '-dtiff', '3_f_mass_vs_time')

disp('Finish');
```

B4.2.3: System Efficiency Increase Analysis Code

```
clear all;
close all;
clc;

%% Constant and System Test Parameter Definitions

%Constants used in ideal gas equation set to 1 since they cancel in mass
%ratio when calculating efficiency improvements (CHANGE IF ACT MASS USED)
R=1;
T=1;

%System Test Parameters from system efficiency testing
```

```
%MAKE SURE TO CHECK THESE MATCH SYSTEM TESTING PARAMETERS

%Test 1: Small To Medium Cylinder
n1=10;                  %number of cycles used for data analysis
r1=2;                   %fire ratio value here 2:1
T1Cyl1Fires=2*n1;       %total number of fires for cylinder 1 in test 1
T1Cyl2Fires=2*n1/r1;    %total number of fires for cylinder 2 in test 1

%Test 2: Small To Large Cylinder
n2=10;                  %number of cycles used for data analysis
r2=5;                   %fire ratio value here 5:1
T2Cyl1Fires=2*n2;       %total number of fires for cylinder 1 in test 2
T2Cyl2Fires=2*n2/r2;    %total number of fires for cylinder 2 in test 2

%Test 3: Medium To Small Cylinder
n3=10;                  %number of cycles used for data analysis
r3=3;                   %fire ratio value here 1:3
T3Cyl1Fires=2*n3;       %total number of fires for cylinder 1 in test 3
T3Cyl2Fires=2*n3*r3;    %total number of fires for cylinder 2 in test 3

%Test 4: Medium to Medium Cylinder
n41=10;                 %number of cycles used for data analysis
r41=2;                  %fire ratio value here 1:2
n42=3;                  %number of cycles used for data analysis
r42=1;                  %fire ratio value here 1:1
T4Cyl1Fires1=2*n41;     %total number of fires for cylinder 1 in test 4
condition 1
T4Cyl2Fires1=2*n41*r41; %total number of fires for cylinder 2 in test 4
condition 1
T4Cyl1Fires2=2*n42;     %total number of fires for cylinder 1 in test 4
condition 2
T4Cyl2Fires2=2*n42*r42; %total number of fires for cylinder 2 in test 4
condition 2

%Test 5: Medium to Large Cylinder
n5=10;                  %number of cycles used for data analysis
r5=2;                   %fire ratio value here 2:1
T5Cyl1Fires=2*n5;       %total number of fires for cylinder 1 in test 5
T5Cyl2Fires=2*n5/r5;    %total number of fires for cylinder 2 in test 5

%Test 6: Large to Small Cylinder
n6=10;                  %number of cycles used for data analysis
r6=8;                   %fire ratio value here 1:8
T6Cyl1Fires=2*n6;       %total number of fires for cylinder 1 in test 6
T6Cyl2Fires=2*n6*r6;    %total number of fires for cylinder 2 in test 6

%Test 7: Large to Medium Cylinder
n71=3;                  %number of cycles used for data analysis
r71=4;                  %fire ratio value here 1:4
n72=3;                  %number of cycles used for data analysis
r72=3;                  %fire ratio value here 1:3
T7Cyl1Fires1=2*n71;     %total number of fires for cylinder 1 in test 7
condition 1
T7Cyl2Fires1=2*n71*r71; %total number of fires for cylinder 2 in test 7
condition 1
```

```
T7Cyl1Fires2=2*n72;     %total number of fires for cylinder 1 in test 7
condition 2
T7Cyl2Fires2=2*n72*r72; %total number of fires for cylinder 2 in test 7
condition 2

% Tests=[SL SM_ML MM1 MS_LM3 LS]
F_Ratio=[1/r2 1/r1 r42 r3 r6];
% Tests=[SL SM ML MM1 MS LM3 LS]
F_Ratio2=[1/r2 1/r1 1/r5 r42 r3 r72 r6];
% Tests=[MM2 LM4]
F_Ratio3=[r41 r71];

%% Volume Calculations

%Large Cylinder Volume Calculation
dL=25;                  %diameter in mm
sL=160;                 %stroke length in mm
VL=pi()*(dL/2)^2*sL;    %cylinder volume in mm^3

%Medium Cylinder Volume Calculation
dM=20;                  %diameter in mm
sM=80;                  %stroke length in mm
VM=pi()*(dM/2)^2*sM;    %cylinder volume in mm^3

%Small Cylinder Volume Calculation
dS=16;                  %diameter in mm
sS=40;                  %stroke length in mm
VS=pi()*(dS/2)^2*sS;    %cylinder volume in mm^3

%Volume Ratio Calculations (non dimensional)
V_lm=VL/VM;
V_ls=VL/VS;
V_ml=VM/VL;
V_mm=VM/VM;
V_ms=VM/VS;
V_sl=VS/VL;
V_sm=VS/VM;

%% Pressure Values

Ps=500;                 %Supply pressure in kPa
Pexp=323.5;             %Accumulator expansion pressure in kPa
Pcon=280;               %Accumulator contraction pressure in kPa

%% Analytical Mass Calculations

%Supply Pressure
mLs=Ps*VL/(R*T);
mMs=Ps*VM/(R*T);
mSs=Ps*VS/(R*T);

%Accumulator Contraction Pressure
mLc=Pcon*VL/(R*T);
mMc=Pcon*VM/(R*T);
mSc=Pcon*VS/(R*T);
```

```
%Post script on variables:
%R indicates partially regulated pressure system
%U indicates unregulated pressure system
%W indicates fully regulated, equal work system

%Test 1: Small to Medium
T1TotMW=T1Cyl1Fires*mSs;
T1TotMWOR=T1Cyl1Fires*mSs+T1Cyl2Fires*mMc;
T1EffImpR=(1-T1TotMW/T1TotMWOR)*100;
T1TotMWOU=T1Cyl1Fires*mSs+T1Cyl2Fires*mMs;
T1EffImpU=(1-T1TotMW/T1TotMWOU)*100;
T1TotMWOW=T1Cyl1Fires*mSc+T1Cyl2Fires*mMc;
T1EffImpW=(1-T1TotMW/T1TotMWOW)*100;

%Test 2: Small to Large
T2TotMW=T2Cyl1Fires*mSs;
T2TotMWOR=T2Cyl1Fires*mSs+T2Cyl2Fires*mLc;
T2EffImpR=(1-T2TotMW/T2TotMWOR)*100;
T2TotMWOU=T2Cyl1Fires*mSs+T2Cyl2Fires*mLs;
T2EffImpU=(1-T2TotMW/T2TotMWOU)*100;
T2TotMWOW=T2Cyl1Fires*mSc+T2Cyl2Fires*mLc;
T2EffImpW=(1-T2TotMW/T2TotMWOW)*100;

%Test 3: Medium to Small
T3TotMW=T3Cyl1Fires*mMs;
T3TotMWOR=T3Cyl1Fires*mMs+T3Cyl2Fires*mSc;
T3EffImpR=(1-T3TotMW/T3TotMWOR)*100;
T3TotMWOU=T3Cyl1Fires*mMs+T3Cyl2Fires*mSs;
T3EffImpU=(1-T3TotMW/T3TotMWOU)*100;
T3TotMWOW=T3Cyl1Fires*mMc+T3Cyl2Fires*mSc;
T3EffImpW=(1-T3TotMW/T3TotMWOW)*100;

%Test 4: Medium to Medium
T4TotMW1=T4Cyl1Fires1*mMs;
T4TotMWO1R=T4Cyl1Fires1*mMs+T4Cyl2Fires1*mMc;
T4EffImp1R=(1-T4TotMW1/T4TotMWO1R)*100;
T4TotMWO1U=T4Cyl1Fires1*mMs+T4Cyl2Fires1*mMs;
T4EffImp1U=(1-T4TotMW1/T4TotMWO1U)*100;
T4TotMWO1W=T4Cyl1Fires1*mMc+T4Cyl2Fires1*mMc;
T4EffImp1W=(1-T4TotMW1/T4TotMWO1W)*100;
T4TotMW2=T4Cyl1Fires2*mMs;
T4TotMWO2R=T4Cyl1Fires2*mMs+T4Cyl2Fires2*mMc;
T4EffImp2R=(1-T4TotMW2/T4TotMWO2R)*100;
T4TotMWO2U=T4Cyl1Fires2*mMs+T4Cyl2Fires2*mMs;
T4EffImp2U=(1-T4TotMW2/T4TotMWO2U)*100;
T4TotMWO2W=T4Cyl1Fires2*mMc+T4Cyl2Fires2*mMc;
T4EffImp2W=(1-T4TotMW2/T4TotMWO2W)*100;

%Test 5: Medium to Large
T5TotMW=T5Cyl1Fires*mMs;
T5TotMWOR=T5Cyl1Fires*mMs+T5Cyl2Fires*mLc;
T5EffImpR=(1-T5TotMW/T5TotMWOR)*100;
T5TotMWOU=T5Cyl1Fires*mMs+T5Cyl2Fires*mLs;
T5EffImpU=(1-T5TotMW/T5TotMWOU)*100;
T5TotMWOW=T5Cyl1Fires*mMc+T5Cyl2Fires*mLc;
```

```
T5EffImpW=(1-T5TotMW/T5TotMWOW)*100;

%Test 6: Large to Small
T6TotMW=T6Cyl1Fires*mLs;
T6TotMWOR=T6Cyl1Fires*mLs+T6Cyl2Fires*mSc;
T6EffImpR=(1-T6TotMW/T6TotMWOR)*100;
T6TotMWOU=T6Cyl1Fires*mLs+T6Cyl2Fires*mSs;
T6EffImpU=(1-T6TotMW/T6TotMWOU)*100;
T6TotMWOW=T6Cyl1Fires*mLc+T6Cyl2Fires*mSc;
T6EffImpW=(1-T6TotMW/T6TotMWOW)*100;

%Test 7: Large to Medium
T7TotMW1=T7Cyl1Fires1*mLs;
T7TotMWO1R=T7Cyl1Fires1*mLs+T7Cyl2Fires1*mMc;
T7EffImp1R=(1-T7TotMW1/T7TotMWO1R)*100;
T7TotMWO1U=T7Cyl1Fires1*mLs+T7Cyl2Fires1*mMs;
T7EffImp1U=(1-T7TotMW1/T7TotMWO1U)*100;
T7TotMWO1W=T7Cyl1Fires1*mLc+T7Cyl2Fires1*mMc;
T7EffImp1W=(1-T7TotMW1/T7TotMWO1W)*100;
T7TotMW2=T7Cyl1Fires2*mLs;
T7TotMWO2R=T7Cyl1Fires2*mLs+T7Cyl2Fires2*mMc;
T7EffImp2R=(1-T7TotMW2/T7TotMWO2R)*100;
T7TotMWO2U=T7Cyl1Fires2*mLs+T7Cyl2Fires2*mMs;
T7EffImp2U=(1-T7TotMW2/T7TotMWO2U)*100;
T7TotMWO2W=T7Cyl1Fires2*mLc+T7Cyl2Fires2*mMc;
T7EffImp2W=(1-T7TotMW2/T7TotMWO2W)*100;

% Tests=[SL SM_ML MM1 MS_LM3 LS]
EffImpR=[T2EffImpR T1EffImpR T4EffImp2R T3EffImpR T6EffImpR]

% Tests=[SL SM_ML MM1 MS_LM3 LS]
EffImpU=[T2EffImpU T1EffImpU T4EffImp2U T3EffImpU T6EffImpU]

% Tests=[SL SM_ML MM1 MS_LM3 LS]
EffImpW=[T2EffImpW T1EffImpW T4EffImp2W T3EffImpW T6EffImpW]

%% Mass and Efficiency Values from Test Data (manually input from data
analysis code results/excel spreadsheet)

% Tests=[SL (SM ML) MM1 (MS LM3) LS]
ExpEffImpR=[68.6 61.4 58.4 46.4 44.4 38 31.9] %Used Manual Seq Cycle Avg from
excel
% Tests=[MM2 LM4]
ExpEffImpR2=[89.1 41.6] %Used final-initial from excel

% Tests=[SL (SM ML) MM1 (MS LM3) LS]
ExpEffImpU=[78.8 72.9 70.9 59.5 58.2 51.9 46.3] %Used Manual Seq Cycle Avg
from excel
% Tests=[MM2 LM4]
ExpEffImpU2=[92.5 56.7] %Used final-initial from excel

% Tests=[SL (SM ML) MM1 (MS LM3) LS]
ExpEffImpW=[59.2 46.5 44.5 20.9 17.3 8.4 -2.7] %Used Manual Seq Cycle Avg
from excel
% Tests=[MM2 LM4]
```

```
ExpEffImpW2=[85.8 61.9] %Used final-initial from excel

%% Plots of Efficiency Improvements

%Unregulated Efficiency Increases
figure(1)
plot(F_Ratio,EffImpU,'bo-')
xlabel('Stroke Ratio')
ylabel('Efficiency Improvement (%)')
title('Unregulated System Efficiency Improvement as a Funciton of Stroke
Ratio')
xlim([0 10])
ylim([25 100])
hold on
plot(F_Ratio2,ExpEffImpU,'b*')
plot(F_Ratio3,ExpEffImpU2,'b.','linewidth',3,'markersize',20)
legend('Unreg System Model','Exp Unreg System','Exp Inc Stroke Ratio')
hold off

%Partially Regulated Efficiency Increases
figure(2)
plot(F_Ratio,EffImpR,'ks-')
xlabel('Stroke Ratio')
ylabel('Efficiency Improvement (%)')
title('Partially Regulated System Efficiency Improvement as a Funciton of
Stroke Ratio')
xlim([0 10])
ylim([25 100])
hold on
plot(F_Ratio2,ExpEffImpR,'kd')
plot(F_Ratio3,ExpEffImpR2,'k^','linewidth',3,'markersize',5)
legend('Part Reg System Model','Exp Part Reg System','Exp Inc Stroke Ratio')
hold off

%Fully Regulated Efficiency Increases
figure(3)
plot(F_Ratio,EffImpW,'gx-')
xlabel('Stroke Ratio')
ylabel('Efficiency Improvement (%)')
title('Fully Regulated System Efficiency Improvement as a Funciton of Stroke
Ratio')
xlim([0 10])
ylim([-5 100])
hold on
plot(F_Ratio2,ExpEffImpW,'g+')
plot(F_Ratio3,ExpEffImpW2,'g.','linewidth',3,'markersize',20)
legend('Full Reg System Model','Exp Full Reg System','Exp Inc Stroke Ratio')
hold off

%Efficiency Increase Comparison
figure(4)
plot(F_Ratio,EffImpU,'bo-')
xlabel('Stroke Ratio')
ylabel('Efficiency Improvement (%)')
title('Comparison of Efficiency Improvement as a Funciton of Stroke Ratio')
xlim([0 10])
```

```
ylim([-5 85])
hold on
plot(F_Ratio2,ExpEffImpU,'b*')
plot(F_Ratio,EffImpR,'ks-')
plot(F_Ratio2,ExpEffImpR,'kd')
plot(F_Ratio,EffImpW,'gx-')
plot(F_Ratio2,ExpEffImpW,'g+')
legend('Unreg System Model','Exp Unreg System','Part Reg System Model','Exp
Part Reg System','Full Reg System Model','Exp Full Reg System')
hold off
```